ELECTROOSMOTIC FLOW MIXING AND MASS TRANSFER IN MICRO AND NANO FLUIDIC SYSTEMS

Ph. D. THESIS

by

ABHISHEK BANERJEE

DEPARTMENT OF MATHEMATICS
INDIAN INSTITUTE OF TECHNOLOGY ROORKEE
ROORKEE – 247 667 (INDIA)
JANUARY, 2019

ELECTROOSMOTIC FLOW MIXING AND MASS TRANSFER IN MICRO AND NANO FLUIDIC SYSTEMS

A THESIS

Submitted in partial fulfilment of the requirements for the award of the degree

of

DOCTOR OF PHILOSOPHY

in

MATHEMATICS

by

ABHISHEK BANERJEE

DEPARTMENT OF MATHEMATICS
INDIAN INSTITUTE OF TECHNOLOGY ROORKEE
ROORKEE - 247 667 (INDIA)
JANUARY, 2019

INDIAN INSTITUTE OF TECHNOLOGY ROORKEE
ROORKEE

CANDIDATE'S DECLARATION

I hereby certify that the work which is being presented in the thesis entitled "**ELECTROOSMOTIC FLOW MIXING AND MASS TRANSFER IN MICRO AND NANO FLUIDIC SYSTEMS**" in partial fulfilment of the requirements for the award of the Degree of Doctor of Philosophy and submitted in the Department of Mathematics of the Indian Institute of Technology Roorkee, Roorkee is an authentic record of my own work carried out during a period from July, 2014 to January, 2019 under the supervision of Dr. Ameeya Kumar Nayak, Associate Professor, Department of Mathematics, Indian Institute of Technology Roorkee, Roorkee.

The matter presented in this thesis has not been submitted by me for the award of any other degree of this or any other Institution.

(Abhishek Banerjee)

This is to certify that the above statement made by the candidate is correct to the best of my knowledge.

(**Ameeya Kumar Nayak**)
Supervisor

The Ph.D Viva-Voce Examination of **Mr. Abhishek Banerjee**, Research Scholar, has been held on **11-07-2019.**

Chairperson, SRC **Signature of External Examiner**

This is to certify that the student has made all the corrections in the thesis.

Signature of Supervisor **Head of the Department**

Dated:_____

Dedicated

to

My Parents and Grandmother

Abstract

This thesis addresses the feasibility of introducing geometric variations and surface potential heterogeneity in micro and nano fluidic systems to create effects other than pure molecular diffusion to enhance mixing efficiency. Geometric modulations are included by considering different shapes and designs of micro channel with embedded obstacles along the walls. In performing chemical or biological analysis, samples and reagents need to be mixed together thoroughly and this is an important flow aspect in miniaturized Total Analysis Systems (μTAS), where mixing plays a vital role for system analysis. In scaling down dimensions of micro-devices, flow driving through diffusion process becomes an efficient method to achieve homogenous solutions as the characteristic length scale becomes sufficiently small.

In this thesis, passive mixing, using geometric modulations with surface potential non-homogeneity in micro/ nano channels is studied due to its advantage over active mixing in terms of simplicity and ease of fabrication. The mathematical model is based on the coupling between Maxwell's equation for electric potential, Nernst-Planck equation for ion transfer and Navier-Stokes equation for momentum transport. A control volume based algorithm is used for the numerical solution of the flow governing equations. Chapter 1 contains the basic definitions and various solution approaches used for the electrokinetic flow governing equations.

The Chapter 2 deals with electrokinetic transport and species mixing analysis in a nano-channel under an externally applied steady electric field which are applicable in micro electrical mechanical systems. The channel geometry is modulated by introducing a non-conducting obstacle on the bottom wall. In addition to geometric modulation, surface potential heterogeneity is created by putting an overpotential patch on the upper face of the rectangular obstacle. The effect of block height, block position, strength of the patch potential and external electric field are analyzed and it is found that mixing length may be significantly reduced by introducing the heterogeneity in the flow structure. Chapter 3 is concerned with the combined theoretical

and numerical study of two comparative nano-structured domains with surface potential heterogeneity and wall corrugation. The comparative study of mixing analysis is demonstrated in terms of pressure gradient, electric potentials and average flow rate for a wide range of flow controlling parameters. Irrespective of all the physical parameters used it can be concluded that mixing efficiency along the downstream is enhanced with the decrement in electric field strength and Debye-H*ü*ckel parameter.

Electrokinetic flow reversal and its impact on mixing enhancement in a symmetric wavy micro channel is concerned in Chapter 4. The combined effect of wave amplitude and electric field strength is studied to predict the threshold parametric relationship between wave amplitude, external electric field strength, and the ratio of Debye length and channel height. In addition to flow reversal, a significant contribution of flow separation on mixing efficiency enhancement is analyzed. Chapter-5 presents the study of electrokinetic flow reversal and its impact on mixing with periodically distributed zeta potential in asymmetrically arranged corrugated domains with different phase shifts which is an extension of chapter-4. Choosing the best possible phase shift for Newtonian fluid model in terms of maximum mixing efficiency together with minimum pressure drop, the model is extended for power-law fluid.

Subsequently, a comparative study on non-Newtonian flow mixing and pressure drop in circular micro fluidic domains with sudden constriction/ expansion is studied in Chapter 6. The impact of surface roughness, potential heterogeneity and power-law index is discussed for two different configurations. A suitable arrangement of flow parameters are considered to estimate a suitable balance between the mixing efficiency and pressure drop for both the configurations to propose an efficient and effective cylindrical micromixer which can produce maximum possible mixing efficiency with minimum pressure drop.

Keywords: Electroosmosis, Poisson-Nernst-Planck model, Mixing efficiency, Pressure drop, Finite volume method, Mixing performance factor, Power-law fluid, Corrugated channel.

List of Publications

1. Nayak, A. K., **Banerjee, A.**, & Weigand, B. (2018). Mixing and charge transfer in a nanofluidic system due to a patterned surface. *Applied Mathematical Modelling*, 54, 483–501.

2. **Banerjee, A.**, Nayak, A. K., Haque, A., & Weigand, B. (2018). Induced mixing electrokinetics in a charged corrugated nano-channel: towards a controlled ionic transport. *Microfluidics and Nanofluidics*, 22(10), 115.

3. **Banerjee, A.**, Nayak, A. K., & Weigand, B. (2019). Enhanced mixing and flow reversal in a modulated microchannel. *International Journal of Mechanical Sciences*, 155, 430–439.

4. **Banerjee, A.**, & Nayak, A. K. (2019). Influence of varying zeta potential on non-Newtonian flow mixing in a wavy patterned microchannel. *Journal of Non-Newtonian Fluid Mechanics*, 269, 17–27.

5. **Banerjee, A.**, & Nayak, A. K. A comparative analysis of mixing performance of power-law fluid in cylindrical micro-channels with sudden contraction / expansion (Communicated).

6. Nayak, A. K., Haque, A., **Banerjee, A.**, & Weigand, B. (2017). Flow mixing and electric potential effect of binary fluids in micro/nano channels. *Colloids and Surfaces A: Physicochemical and Engineering Aspects*, 512, 145–157.

7. Nayak, A. K., Haque, A., & **Banerjee, A.** (2017). Thermosolutal mixed convection of a shear thinning fluid due to partially active mixed zones within a lid-driven cavity. *International Journal of Heat and Mass Transfer*, 106, 686–707.

8. **Banerjee, A.**, & Nayak, A. K. (2018, July). Electroosmotic Flow Separation in a Corrugated Micro-Channel: A Numerical Study. In ASME 2018 5th Joint US-European Fluids Engineering Division Summer Meeting (pp. V003T21A001-V003T21A001). American Society of Mechanical Engineers.

9. **Banerjee, A.**, & Nayak, A. K. (2017, July). Assessment and Prediction of EOF Mixing in Binary Electrolytes. In ASME 2017 Fluids Engineering Division Summer Meeting (pp. V01BT10A016-V01BT10A016). American Society of Mechanical Engineers.

Acknowledgements

First and foremost, I express my heartiest thanks to the God Almighty and his blessings to write and complete this thesis. It gives me immense pleasure to express my deep sense of gratitude and sincere thanks to my supervisor Dr. Ameeya Kumar Nayak, Associate Professor, Department of Mathematics, Indian Institute of Technology Roorkee, India who introduced me to this subject and from whom I learned a lot about mathematics. Apart from his excellent supervision, his moral support, wonderful wisdom, remarkable suggestions and encouragement made the task enjoyable and rewarding.

I never forget to thank my collaborator Professor B. Weigand, University of Stuttgart Germany. I feel fortunate to have joint research work with him during my PhD. I would like to give a huge thanks to Prof. Prasanta Kumar Mandal and Prof. Santabrata Chakravarty, Visva Bharati University, India for their encouragement and motivation to do Mathematics.

I am also indebted to the Department of Mathematics, Indian Institute of Technology Roorkee, to all its faculty and staff for their academic support and encouragement. My sincere thanks to research committee members Dr. Arup Kumar Das, Assistant Professor, Department of Mechanical and Industrial Engineering, Prof. V. K. Katiyar and Prof. Sunita Gakkhar, Department of Mathematics for their critic views that helped me in improving the quality of my research work. I owe my sincere gratitude to Dr. N. Sukavanam, Head of the Department, Dr. V. K. Katiyar and Dr. R. C. Mittal former Heads of the Department, who provided me with requisite facilities to carry out my doctoral research. I gratefully acknowledge the financial support given by Ministry of Human Resource Development (MHRD), Government of India (Grant No. OH-31-23-200-428).

Collective and individual acknowledgements are also owed to my colleagues at IIT Roorkee. The inspiration support and cooperation that I have received from them are beyond the scope

of my acknowledgement. I would like to acknowledge my sincere thanks to my research group Dr. Venkat, Dr. Sumit, Ainul, Minakshmi, Neha, Bharat and Lokesh for providing me a helping hand whenever I asked for. Moreover, I must not forget to thank P. S. Rosnara who encourages me a lot to do good research. Many thanks goes, in particular, to Sumana, Neethu, Bimal, Prasanta, Vivek, Vishnu, Jagannath, Hemant, Shubham and Savita for their cooperation and support, and making my stay at IIT Roorkee a memorable one. In addition, I want to thank also my friends and colleagues Riddhick, Firoz, Subrata Da, Simanta Da, Partha Da, Sanjib, Naren, Partha during the stay at IIT Kharagpur, India

I make an effort to record my affectionate thanks to my parents, sister and all of my family members for having faith in me, their unconditional love and support during all my studies. Their encouragement has always given me the strength to move ahead in my life. Without their care and support, this thesis would not have been possible.

Finally, this piece of acknowledgement is incomplete without the name of God, who is supreme authority behind everything. I thank Him for blessing me with the people around me that helped me at various steps of my life.

At last, I am thankful to everyone including those whose name might have missed from the list.

Roorkee (Abhishek Banerjee)

January 25, 2019

Table of Contents

List of Figures

Nomenclature

H	channel height $[m]$
W	channel width $[m]$
L	channel length $[m]$
r_0	radius of the cylindrical channel $[m]$
D_i	diffusivity of the i^{th} sample species $[m^2\ s^{-1}]$
D_s	diffusivity of the uncharged eluted species $[m^2\ s^{-1}]$
z_i	valence of the i^{th} ion species (+1 for cation and -1 for anion)
$\mathbf{q}$	mass average velocity vector of the sample electrolyte $[m\ s^{-1}]$
U_{HS}	Helmholtz-Smolouchowski velocity (velocity scale) $[m\ s^{-1}]$
$\mathbf{E}$	electric field vector
$\mathbf{N}_i$	molar flux of the i^{th} species
F	Faraday's constant $[C\ mol^{-1}]$
k_B	Boltzmann's constant $[m^2\ kg\ s^{-2}K^{-1}]$
e	elementary charge $[C]$
n_0	bulk ionic number concentration $[ions\ m^{-3}]$
R	universal gas constant $[J\ mol^{-1}\ K^{-1}]$
T	fluid sample's absolute room temperature $[K]$
n_1, n_2	mole-fractions of counter-ion and co-ion species
E_0	external electric field $[V\ m{-}1]$
Re	Reynolds number, $U_{HS}H/\nu$
Sc	Schmidt number, $\frac{\nu}{D_i}$
Pe	Peclet number, $U_{HS}H/D_i$
Pe_s	uncharged eluted species's Peclet number, $U_{HS}H/D_s$
p	scaled pressure, $p^*/(\mu U_{HS}/H)$
u, v	scaled velocity components in x, y direction, $u^*/U_{HS}, v^*/U_{HS}$
C	scaled concentration of the uncharged eluted species, C^*/C_{ref}

Greek

κ	Debye-H$\ddot{u}$ckel parameter (reciprocal of EDL tickness) $[m^{-1}]$
λ	EDL tickness $[m]$
μ	viscosity of the fluid $[kg\ m^{-1}s^{-1}]$
ρ	density of the fluid $[kg\ m^{-3}]$
ϵ_e	permittivity of the medium $[C\ m^{-1}\ V^{-1}]$
ν	kinematic viscosity of the fluid $[m^2\ s^{-1}]$
ϕ_0	potential scale $[V]$
ρ_e	scaled net charge density
ζ	scaled zeta potential, ζ^*/ϕ_0
α_1, α_2	dimensionless wave amplitudes, α_1^*/H,α_2^*/H
R_α	amplitude ratio, $\frac{\alpha_1}{\alpha_2}$
Λ	scaled external electric field, $E_0/(\phi_0/H)$
$\boldsymbol{\tau}$	shear stress tensor
$\dot{\boldsymbol{\gamma}}$	shear stress tensor

Abbreviations

EOF	Electro osmotic flow
EDL	Electric double layer
PB	Poisson Boltzmann
NP	Nernst Planck

Superscript

$*$	dimensional quantity

Chapter 1

Introduction

1.1 Fundamentals of Fluid Mechanics

One of the key aspects in studying fluid dynamics is to determine the velocity field and the characteristics of the fluid. The governing equations describing the fluid flow are build on the conservation principles. In general fluid flows are described through two ways; Lagrangian and Eulerian description. The individual fluid particles are tracked in case of Lagrangian description whereas, in case of Eulerian description, a fixed control volume is considered in space through which the fluid flows with the increment of time. Thus, the Eulerian description of flow is to describe the fluid properties as a function of spatial location and time. This can be described by sitting on a over-bridge of a river and watching the water passing a fixed location. The Lagrangian description can be considered as an observer sitting in a boat and drifting down the river. Most of the theories of fluid mechanics are based on the Eulerian approach due to its simplicity from the Lagrangian way of describing the fluid flow. We have considered the Eulerian approach throughout the thesis. To describe the basic properties of fluid mechanics in mathematical form the material derivative is frequently used. The material derivative represents the time rate of change of a physical quantity of a material along a path moving with the fluid velocity and can serve as a link between the Lagrangian and the Eulerian descriptions of continuum deformation.

$$\underbrace{\frac{D}{Dt}}_{\text{Lagrangian}} = \underbrace{\frac{\partial}{\partial t} + \mathbf{q}.\nabla}_{\text{Eularian}} \tag{1.1}$$

where $\mathbf{q}$ is the fluid velocity vector and $\nabla = \hat{\mathbf{i}}\frac{\partial}{\partial x} + \hat{\mathbf{j}}\frac{\partial}{\partial y} + \hat{\mathbf{k}}\frac{\partial}{\partial z}$. In the above equation, the partial derivative $\frac{\partial}{\partial t}$ measures the time rate of change at a fixed spatial location, whereas $\mathbf{q} \cdot \nabla$, called

the convective derivative, measures the time rate of change due to the movement of the fluid element from one location to another in the flow domain.

The equations which speak the physics of fluid mechanics are based on three fundamental principles namely, conservation of mass, momentum and energy. These fundamental principles can be described mathematically as follows.

1.1.1 Conservation of Mass

The continuity equation based on the conservation of mass principle states that the net flow rate of mass through a control volume equals zero, i.e., the time rate of change of mass in the control volume is equal to the difference in cumulative mass in flow and out flow from the control surfaces of the control volume. The differential form of the continuity equation can be written as follows.

$$\frac{\partial \rho}{\partial t} + \nabla.(\rho \mathbf{q}) = 0 \tag{1.2}$$

where ρ, $\mathbf{q}$ and t are the density of the fluid, velocity field and time respectively. In case of incompressible flow (i.e. ρ is constant), the continuity equation reduces to

$$\nabla.\mathbf{q} = 0 \tag{1.3}$$

1.1.2 Conservation of Momentum

The Newton's second law of motion for a system implies that the time rate of change of the linear momentum of the system is equal to the sum of the external forces acting on the system. This equation was derived in the early 18^{th} century by Claude-Louis Navier [187] and George Gabriel Stokes [248] independently. Using Reynolds transport theorem, the momentum equation in vector notations can be written as follows

$$\underbrace{\frac{\partial}{\partial t}(\rho \mathbf{q}) + \nabla.(\rho \mathbf{q}\mathbf{q})}_{\text{Time and Advective acceleration}} = \underbrace{-\nabla p}_{\text{Isotropic pressure stress}} + \underbrace{\nabla \cdot \boldsymbol{\tau}}_{\text{Anisotropic viscous stress}} \tag{1.4}$$

where $\boldsymbol{\sigma} = -p\boldsymbol{I} + \boldsymbol{\tau}$ is the stress tensor and $\boldsymbol{\tau} = \mu\left[(\nabla \mathbf{q}) + (\nabla \mathbf{q})^T - \frac{2}{3}(\nabla \cdot \mathbf{q})\boldsymbol{I}\right]$ is the viscous stress. Using the equation of continuity for an incompressible fluid, the constitutive equation for a Newtonian, viscous, incompressible fluid takes the form

$$\rho\left[\frac{\partial \mathbf{q}}{\partial t}+(\mathbf{q}\cdot\nabla)\mathbf{q}\right]=-\nabla p+\mu\nabla^2\mathbf{q}, \tag{1.5}$$

where p, ρ and μ denote the pressure, density and the viscosity of the fluid respectively. At very low Reynolds number the convective acceleration term of the Navier-Stokes equation can be neglected and under steady state condition, the equation becomes Stokes equation i.e.,

$$-\nabla p+\mu\nabla^2\mathbf{q}=0. \tag{1.6}$$

Besides the governing equation, the Reynolds number (Re), a dimensionless number is traditionally necessary for fluid flow which quantifies the relative importance of inertial forces and viscous forces. The dimensionless number (Re) is named after Osborne Reynolds (1883) while investigating the flow in pipes. The Reynolds number can be written as

$$Re=\frac{\text{Inertial forces}}{\text{Viscous forces}}=\frac{\rho UL}{\mu}, \tag{1.7}$$

where U and L denote characteristic velocity scale and length scale respectively. This relation was discovered by Reynolds [226].

1.1.3 Conservation of Energy

The conservation of energy principle can be deduced from the first law of thermodynamics, which states that energy cannot be created or destroyed. If quantity of heat dQ added to volume ΔV during time Δt serves to increase internal energy by an amount of dE_T and to perform work dW, then by the first law of thermodynamics:

$$dQ=dE_T+dW \quad \text{or} \quad \frac{dQ}{dt}=\frac{dE_T}{dt}+\frac{dW}{dt} \tag{1.8}$$

In other words

$$\begin{bmatrix} Rate\ \ of \\ heat\ \ transfer \\ into\ \ the\ \ system \end{bmatrix}=\begin{bmatrix} Rate\ \ of \\ increase\ \ of \\ internal\ \ energy \\ of\ \ the\ \ system \end{bmatrix}=\begin{bmatrix} Rate\ \ of \\ work\ \ done \\ by\ \ surface\ \ force \end{bmatrix}$$

Therefore, the energy equation can be written for viscous incompressible fluid as

$$\frac{\partial T}{\partial t} + u\frac{\partial T}{\partial x} + v\frac{\partial T}{\partial y} + w\frac{\partial T}{\partial z} = \alpha\left(\frac{\partial^2 T}{\partial x^2} + \frac{\partial^2 T}{\partial y^2} + \frac{\partial^2 T}{\partial z^2}\right) + \phi \tag{1.9}$$

where the viscous dissipation function ϕ is given by

$$\begin{aligned}\phi = 2\frac{\mu}{\rho C_p}&\left[\left(\frac{\partial u}{\partial x}\right)^2 + \left(\frac{\partial v}{\partial y}\right)^2 + \left(\frac{\partial w}{\partial z}\right)^2\right] \\ +\frac{\mu}{\rho C_p}&\left[\left(\frac{\partial u}{\partial y} + \frac{\partial v}{\partial x}\right)^2 + \left(\frac{\partial u}{\partial z} + \frac{\partial w}{\partial x}\right)^2 + \left(\frac{\partial v}{\partial z} + \frac{\partial w}{\partial y}\right)^2\right]\end{aligned} \tag{1.10}$$

Here T, α and C_p are the temperature, thermal diffusivity and heat capacity at a constant pressure per unit mass, respectively.

1.2 Electrokinetic Phenomena

Electrokinetics refers to the the relative motion between two charged phases [115, 169, 219]. According to electrokinetic theory, there are several ways in which a surface acquires net charge, such as ionization or ion absorption and ion dissociation. Due to the occurrence of surface charge, counter ions are attracted to the surface and co-ions are repelled from it which leads to a redistribution of ions in the vicinity of the charged surface. As a result an induced electric field is developed close to the charged surface. Under an externally imposed electric field, the mobile counter ions move towards the electrodes of opposite charge and induce a momentum in the medium. The charged particles experience electrostatic force and the phenomena that might take place as a result of relative movement between two charged phases are classified into four types of electrokinetic phenomena and are most commonly encountered which are briefly described below.

- Electrophoresis: The movement of charged particles relative to the liquid, when the particle is suspended under the influence of an applied electric field.

- Electroosmosis: The movement of liquid relative to the stationary charged surface under the influence of an applied electric field.

- Streaming potential: Electric field generated, when the liquid is forced to flow past a stationary charged surface.

- Sedimentation potential: Electric field generated when the charged particle moves relative to a stationary liquid.

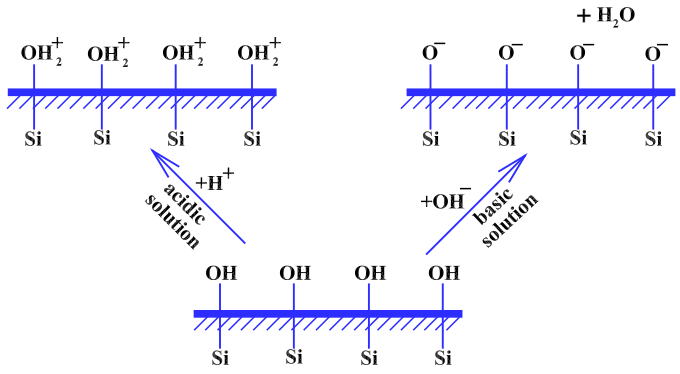

Figure 1.1: Schematic of chemical reactions in silicon wall in aqueous mediums for different pH.

1.3 Electric Double Layer (EDL)

Most oxide surfaces, which are commonly found in microfluidic devices exhibits a surface charge when immersed in aqueous solutions. The surface charges are mainly generated due to the dissociation of surface hydroxyl groups and readsorption of metal hydroxocomplexes [79]. Both these processes involve H^+ and OH^- ions which can be controlled by the pH of the solution. In acidic solutions, the surface is most likely positively charged due to the excess of bound protons and preferably adsorbs anions, whereas in alkaline solutions, the surface is negatively charged and preferably adsorbs cations. At some intermediate pH value, the surface acquires a zero net charge which is called point of zero charge (PZC) or isoelectric point (IEC). If silicon oxide is immersed in water, the silanol groups $SiOH$ react with water and transform into either $SiOH_2^+$ (pH $<$ PZC) or SiO^- (pH $>$ PZC) depending on the buffer pH value (Fig. 1.1).

Electric double layer (EDL) [96, 129] plays a key role in electrokinetic phenomena, which forms as a result of the interaction of an ionized solution with static charges on dielectric surfaces (Hunter, 2001). If the channel wall is charged (Fig. 1.2), the ions of opposite charge to that of the surface (counterions) are attracted towards the surface while the ions of like charge (coins) are repelled from it, keeping the bulk liquid electrically neutral. The attraction and repulsion combined with the thermal motion of the ions lead to the formation of a charged layer, named as electric double layer (EDL). Several theoretical studies have been done and a number of models have been proposed to describe the ion distribution near the charged

surface quantitatively. One of the earliest model used for electrokinetic phenomena is Helmholtz Double Layer model [105]. In this model it is assumed that electrically balanced counter ions are concentrated on a plane parallel to the uniformly charged surface within a small distance. Therefore, the electric potential is maximum at the wall surface and decreases linearly with the distance from the surface. The influence of the mobile layer of counter ions in the bulk fluid has been recognised by Gouy [99] and Chapman [48]. The charged surface and the mobile counter ions in the bulk region are together termed as the Gouy-Chapman Diffuse Double Layer. The model assumes that the total electric charges on the channel surface are considered to be balanced by excess counterions, so the electric potential is maximum at the surface and decreases exponentially with the distance from the surface. The Gouy-Chapman model fails in the case of a highly charged double layer. Stern [247] made corrections in the Gouy-Chapman model by taking the ion size into account. The model assumes that the electric double layer consists of two regions where ions adhere to the charge surface giving an internal Stern layer and the ions are distributed under the influence of the interparticle forces in the outer region to form a Gouy-Chapman diffuse layer. The electric double layer is separated by the Stern plane, located at surface is on the order of the ionic radius. The Stern layer is tightly packed with counterions, and the electric potential decreases linearly with the distance from the surface, according to the Helmholtz model. In the diffuse layer, the electric potential decreases exponentially with the distance from the surface. The charged ions present in the diffuse layer can move under the influence of tangential stress. The junction between fixed and mobile ions is called slipping plane (shear plane) and the potential at the edge of slipping plane is known as zeta (ζ) potential or surface potential [219].

1.4 Governing Equations for Electrokinetics

The electric field $\boldsymbol{E}$ in the steady flow case satisfy the Maxwell's equation in the form $\nabla \times \boldsymbol{E} = 0$. The Gauss's law, which relates the electrical field ($\boldsymbol{E}$) and the net electric charge density per unit volume (ρ_e) can be expressed as

$$\nabla \cdot (\epsilon_e \boldsymbol{E}) = \rho_e \tag{1.11}$$

where ϵ_e is the dielectric permittivity of the medium. Since the electric field is curl free, one can define it by a scalar electric potential ϕ, i.e., $\boldsymbol{E} = -\nabla\phi$. Substituting this into Gauss's law and assuming that the medium is isotropic, the Eq. 1.11 becomes the Poisson's equation for electric potential, i.e.,

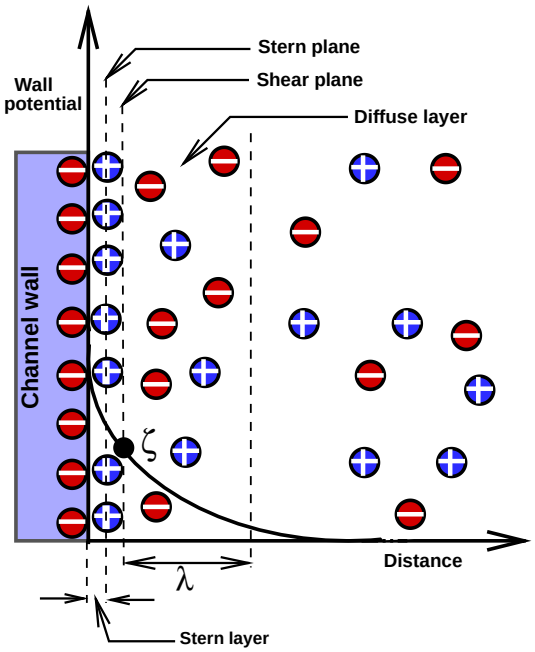

Figure 1.2: Schematic of the electric double layer (EDL) formed around a negatively charged capillary wall.

$$-\epsilon_e \nabla^2 \phi = \rho_e \tag{1.12}$$

The Boltzmann distribution is usually used to predict the distribution of ions. It is based on the condition that the electrochemical potential (μ_i) of the ions must be constant everywhere at equilibrium which implies that the electrical force and diffusion of the ion must balance out:

$$\nabla \mu_i = -z_i e \nabla \phi \tag{1.13}$$

where μ_i is the chemical potential and $e = 1.602 \times 10^{-19}\ C$ is the charge on a single electron or proton. For a flat double layer the electrostatic potential and the chemical potential are constant in planes parallel to the wall so that Eq. 1.13 can be written as

$$\frac{d\mu_i}{dy} = -z_i e \frac{d\phi}{dy} \tag{1.14}$$

and the chemical potential is defined in the form

$$\mu_i = \mu_i^0 + k_B T \ln(n_i), \tag{1.15}$$

where n_i is the number density of i^{th} ion, μ_i^0 is the chemical potential in the standard state,

i.e., when n_i assume a value of unity, k_B is the Boltzmann constant and T is the absolute temperature of the solution. From Eq. 1.14 and Eq. 1.15, we have

$$\frac{d}{dy}(\ln n_i) = \frac{1}{n_i}\frac{dn_i}{dy} = \frac{z_i e}{k_B T}\frac{d\phi}{dy} \tag{1.16}$$

Integrating this equation from a point in the bulk solution where $\phi = 0$ and $n_i = n_i^0$, yields

$$n_i = n_i^0 exp\left(-\frac{z_i e\phi}{k_B T}\right), \tag{1.17}$$

where n_i^0 is the bulk ionic concentration. Eq. 1.17 is known as Boltzmann distribution for ionic species which gives the local concentration of each species in the double layer region.
Substituting Eq. 1.17 in Eq. 1.12 gives

$$-\epsilon_e \nabla^2\phi = \sum_i z_i e n_i^0 exp\left(-\frac{z_i e\phi}{k_B T}\right) \tag{1.18}$$

Debye-Hückel approximation is a linearization of the function on the right hand side of the Poisson-Boltzmann equation (Eq. 1.18). It is based on the assumption that the electrostatic energy is far less than the thermal energy, i.e., $\phi \ll k_B T/z_i e$ for which $exp\,(-z_i e\phi/k_B T) \approx 1 - z_i e\phi/k_B T$. With this assumption Eq. 1.18 can be written in linearized form as

$$\begin{aligned}
\nabla^2\phi &= -\frac{1}{\epsilon_e}\sum_i z_i e n_i^0\left(1 - \frac{z_i e\phi}{k_B T}\right) \\
&= -\frac{1}{\epsilon_e}\left(\sum_i z_i e n_i^0 - \sum_i z_i^2 e^2 n_i^0 \frac{\phi}{k_B T}\right) \\
&= \frac{e^2}{\epsilon_e k_B T}\left(\sum_i z_i^2 n_i^0\right)\phi \\
&= \kappa^2\phi
\end{aligned} \tag{1.19}$$

In Eq. 1.17, the first sum is zero because of the electro neutrality in the bulk region. Here, $\kappa^{-1} = (\epsilon_e k_B T/e^2\sum_i z_i^2 n_i^0)^{1/2}$ is EDL thickness or Debye length. For binary and symmetric electrolyte ($z_1 = z_2 = Z$) containing two species, a cation with concentration n_1 and an anion with concentration n_2 with identical bulk concentration n_0 , the Debye length can be simplified as $\kappa^{-1} = (\epsilon_e k_B T/2e^2 Z n_0)^{1/2}$.

The Boltzmann distribution (Eq. 1.19) for ionic species near a charged surface is based on the assumptions that the ions are point-like, the solid surface are microscopically homogenous

and the system is in equilibrium i.e., under no convective movement of charged species or diffusion. The Poisson-Boltzmann description of EDL may not be appropriate for non-neutral core and for electrolytes containing multivalent ionic species [292].

By applying an external electric field to an electrolyte solution, the free charges in the electric double layer interact with the electric field and experience an electric body force ($\rho_e \boldsymbol{E}$) close to the channel walls and provokes fluid motion which is gradually transmitted to the adjacent fluid layers through viscous drag. Thus, incorporating the electrokinetic body force term, the modified Cauchy Momentum equation for the electroosmotic flow of a general non-Newtonian fluid can be written as [287]

$$\rho\left[\frac{\partial \mathbf{q}}{\partial t} + (\mathbf{q}\cdot\nabla)\mathbf{q}\right] = -\nabla p + \nabla\cdot\boldsymbol{\tau} + \rho_e \mathbf{E}, \tag{1.20}$$

where electric field $\boldsymbol{E}$ is determined by the linear superposition of external electric field and the induced electric field. Here $\boldsymbol{\tau}$ denotes the shear stress tensor. For power-law fluid, the constitutive relation between shear stress tensor and the rate of strain tensor can be written as [101,164]

$$\boldsymbol{\tau} = 2\mu(\dot{\gamma})\dot{\boldsymbol{\gamma}} = \mu(\dot{\gamma})\left(\nabla\mathbf{q} + \left(\nabla\mathbf{q}\right)^T\right) \tag{1.21}$$

where $\nabla\mathbf{q}$ and $\left(\nabla\mathbf{q}\right)^T$ denote the velocity gradient tensor and its transpose respectively. Here $\dot{\gamma}$ is the magnitude of the shear strain tensor $\dot{\boldsymbol{\gamma}}$, defined as [192,193] $\dot{\gamma} = \sqrt{\frac{1}{2}\left(\dot{\boldsymbol{\gamma}} : \dot{\boldsymbol{\gamma}}\right)}$. The apparent viscosity (μ_a) can be expressed as a function of $\dot{\gamma}$ and is denoted by $\mu_a(\dot{\gamma})$. For power-law fluid, the expression for μ_a is given by [17]

$$\mu_a(\dot{\gamma}) = m\left(\dot{\gamma}\right)^{n-1} \tag{1.22}$$

where m, called flow consistency index is a constant relative to the fluid properties and n is the fluid behavior index, according to which shear thinning or shear thickening behavior is regarded when $n < 1$ or $n > 1$, respectively. For $n = 1$, the model shows Newtonian characteristics. The expressions of μ_a for cartesian and cylindrical coordinates are represented in the corresponding chapters. For Newtonian model (i.e. for $n = 1$ and $m = \mu$), the Cauchy-Momentum equation reduces to [169]

$$\rho\left[\frac{\partial \mathbf{q}}{\partial t} + (\mathbf{q}\cdot\nabla)\mathbf{q}\right] = -\nabla p + \mu\nabla^2\mathbf{q} + \rho_e \mathbf{E}. \tag{1.23}$$

Under the application of an external electric field, the ionic species in an electrolyte can move due to the coupling effect between EDL and external potential and the fluid streams move due to viscous drag. The total number flux $\boldsymbol{N}_i$ of the i^{th} ionic species is given by [33]

$$\boldsymbol{N}_i = -D_i \nabla n_i + \frac{z_i e n_i D_i}{k_B T} \boldsymbol{E} + n_i \mathbf{q}, \tag{1.24}$$

where k_B is the Boltzmann constant, T is the absolute temperature, e is the elementary charge. Here D_i, n_i, z_i are the diffusivity, number concentration and valance of i^{th} ionic species respectively. The first term on the right hand side of Eq. 1.24 represents species transport due to molecular diffusion, the second term is due to electromigration and the third term arises due to bulk fluid advection $n_i\mathbf{q}$ with speed $\mathbf{q}$. The governing equation for the transport of ionic species based on the conservation of number flux in steady flow is given by

$$\nabla . \boldsymbol{N}_i = 0 \tag{1.25}$$

This equation is known as the Nernst-Planck equation for ionic concentration distribution. It may be noted that throughout the study we have neglected the production of the ionic species and reaction into the system. A Poisson-Nernst-Planck model is valid for potential as well as concentration distribution near the charged surface in any physical circumstances.

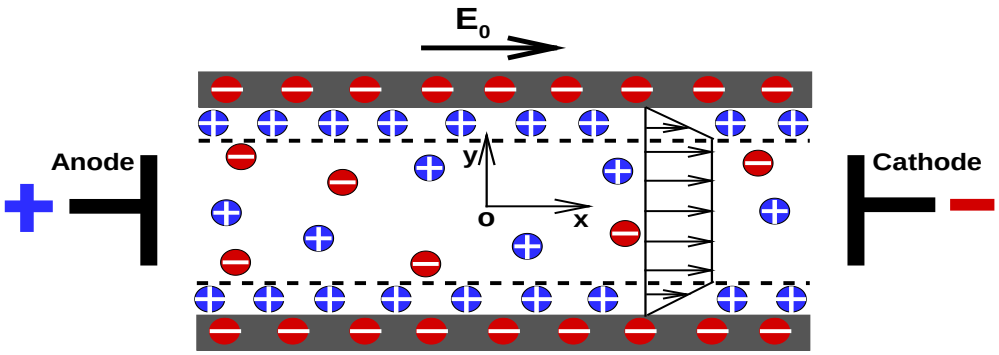

Figure 1.3: Schamatic diagram of electroosmotic flow through a rectangular capillary of height $2H$. The dotted lines represent the edge of the EDL where the velocity attains its maximum value.

1.5 Electroosmosis of Newtonian/ Power-Law Fluid in a Rectangular Micro/Nano-Channel

We consider an infinitely long rectangular channel filled with power-law fluid under the influence of a constant electric field parallel to the axis of the capillary (Fig. 1.3). The inner surface of the capillary is considered to be negatively charged. The mobile ions in the diffuse part of the EDL

experiences the Lorentz force in response to the applied field. This resulting motion of charged layer together with fluid layers is known as electroosmotic flow (EOF). This kind of flows find a wide application in micro- and nanofluidic systems, such as capillary electrophoresis [29,136], drug delivery and screening [70,271], separation of proteins [285] liquid pumps [176] and several other fields [46,51,83]. The electrokinetic force per unit volume is given by [169,219]

$$\mathbf{F}_e = \rho_e \mathbf{E} \tag{1.26}$$

Using Debye-Hückel approximation, the induced potential distribution of a binary symmetric monovalent electrolyte solution can be written as

$$\phi(y) = \zeta \frac{cosh(\kappa y)}{cosh(\kappa H)} \tag{1.27}$$

where $\phi = \zeta$ on $y = H$ (i.e. at channel wall) and $\frac{d\phi}{dy} = 0$ on $y = 0$ (i.e. at centerline).

The simplified Cauchy momentum equation for a steady, incompressible, one-dimensional flow ($u = u(y)$, $v = 0$) with no pressure gradient (i.e. $\nabla p = 0$) takes the form [287]

$$\frac{d}{dy}\left[m\left(-\frac{du}{dy}\right)^{n-1}\frac{du}{dy}\right] = \epsilon_e \mathbf{E}, \tag{1.28}$$

where $\rho_e = -\epsilon_e \nabla^2 \phi = -\epsilon_e \frac{d^2\phi}{dy^2}$ and $\mathbf{E} = E_0$, the Reynolds number (Re) is also very small. Integrating Eq. 1.28 with no-slip boundary condition along the channel wall ($y = H$) and symmetric boundary condition along the line of symmetry ($y = 0$), yields the velocity field as

$$u(y) = \kappa^{\frac{1-n}{n}}\left(-\frac{\epsilon_e \zeta E_0}{m}\right)^{1/n} \frac{\int_{\kappa y}^{\kappa H} \sinh^{1/n}(\kappa y)\ d(\kappa y)}{\cosh^{1/n}(\kappa H)}, \tag{1.29}$$

where n is the flow behaviour index and m is the flow consistency index. For Newtonian fluids $n = 1$ and $m = \mu$ [17,293]. Here κ denotes the Debye-Hückel parameter (inverse of debye layer thickness) and is defined as $\kappa = \sqrt{\frac{2n_0 e^2 z^2}{\epsilon_e k_B T}}$, where n_0 is the bulk ionic number concentration, e is the elementary charge, z is the valance of the binary monovalent ions, and T is the absolute temperature of the sample electrolyte.

- For $n = 1$ (Newtonian fluid) the representation for flow velocity is

$$u(y) = \left(-\frac{\epsilon_e \zeta E_0}{\mu}\right)\left[1 - \frac{\cosh(\kappa y)}{\cosh(\kappa H)}\right] \tag{1.30}$$

which is the well known electroosmotic velocity distribution of Newtonian fluids [169].

- For $n = \frac{1}{2}$ the representation for flow velocity is

$$u(y) = \frac{1}{2}\kappa\left(-\frac{\epsilon_e \zeta E_0}{m}\right)^2 \frac{\sinh(2\kappa H) - \sinh(2\kappa y) - 2(\kappa H - \kappa y)}{2\cosh^2(\kappa H)} \tag{1.31}$$

- For $n = \frac{1}{3}$ the representation for flow velocity is

$$u(y) = \frac{1}{3}\kappa^2\left(-\frac{\epsilon_e \zeta E_0}{m}\right)^3 \frac{\sinh(3\kappa H) - \sinh(3\kappa y) + 9\sinh(\kappa H) - 9\sinh(\kappa y)}{4\cosh^3(\kappa H)}. \tag{1.32}$$

The term $(-\frac{\epsilon_e \zeta E_0}{m})^{1/n}$ is called the generalized Helmholtz-Smoluchowski velocity and is denoted as U_s [254, 287]. For Newtonian case ($n = 1$), it represents the Helmholtz-Smoluchowski velocity which is defined as $U_{HS} = -\frac{\epsilon \zeta E_0}{\mu}$ [169]. As the integral in Eq. 1.29 can be analytically evaluated only under some special circumstances. In order to obtain the velocity distribution of an arbitrary value of flow behaviour index (n), the hyperbolic sine function can be approximated as [215]

$$\sinh(\kappa y) = \begin{cases} \kappa y \ ; & 0 < \kappa y \leq 1, \\ \frac{1}{2}e^{\kappa y} \ ; & \kappa y > 1. \end{cases}$$

Using this approximation in Eq. 1.29, analytic solution can be obtained for two different cases : (i) $\kappa H > 1$ and (ii) $0 < \kappa H \leq 1$ [287].

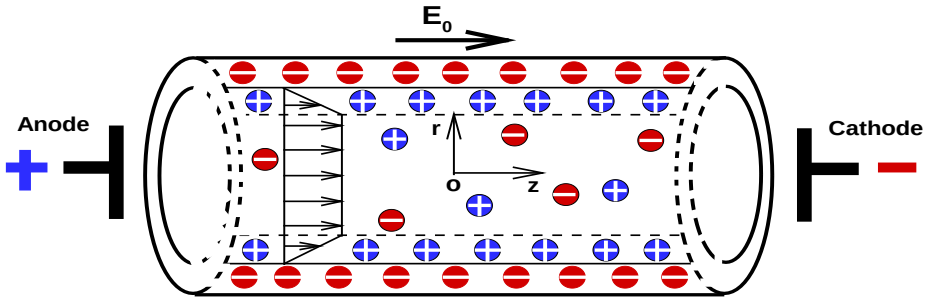

Figure 1.4: Schamatic diagram of electroosmotic flow through a cylindrical capillary of radius r_0. The dotted lines represent the edge of the EDL where the velocity attains its maximum value.

1.6 Electroosmosis of Newtonian/ Power-Law Fluid in a Cylindrical Micro/Nano-Channel

The electroosmotic flow of non-Newtonian fluid (power-law) is considered in a cylindrical microchannel with radius r_0, presented in Fig. 1.4. The external electric field is considered along

the streamwise direction (with magnitude E_0) and the wall surface is considered to possess a uniform ζ potential. The flow field is considered as unidirectional ($u_r = 0 = u_\theta$) and only the axial velocity component ($u_z = u_z(r)$) is present.

Under above mentioned conditions, the Poisson's equation of induced potential and the Cauchy's equation for momentum transport for power-law fluid takes the form

$$\epsilon_e \frac{1}{r}\frac{d}{dr}\left(r\frac{d\phi}{dr}\right) = -\rho_e \tag{1.33}$$

$$m\frac{1}{r}\frac{d}{dr}\left\{r\left(-\frac{du_z}{dr}\right)^n\right\} = \rho_e E_0 \tag{1.34}$$

For binary and monovalent electrolyte, under small surface potential assumption, the charge density due to EDL can be expressed as $\rho_e = -\kappa^2\epsilon_e\phi$, which is substituted in the Eq. 1.33 to get the distribution of induced potential due to EDL with the following boundary conditions :

$$\left.\frac{d\phi}{dr}\right|_{r=0} = 0 \qquad and \qquad \phi|_{r=r_0} = \zeta. \tag{1.35}$$

The solution of the induced potential with the prescribed boundary conditions, reduces to [259, 290]

$$\phi(r) = \zeta\frac{I_0(\kappa r)}{I_0(\kappa r_0)}, \tag{1.36}$$

where $I_0(r)$ denotes the zero-order modified Bessel function and κ is the inverse of debye length which is defined in the previous section.

Using $u_z = 0$ along $r = r_0$ (no-slip at channel walls) and $\frac{du_z}{dr} = 0$ along $r = 0$ (centerline symmetry) boundary conditions and substituting the Eq. 1.36 in Eq. 1.34, the distribution of electroosmotic velocity takes the form [290]

$$u_z(r) = \frac{\kappa^{\frac{1-n}{n}}\left(-\frac{\epsilon_e E_0\zeta}{m}\right)^{\frac{1}{n}}}{I_0^{\frac{1}{n}}(\kappa r_0)}\int_{\kappa r}^{\kappa r_0}[I_1(r)]^{\frac{1}{n}}\,dr. \tag{1.37}$$

Here $I_1(r)$ denotes the modified Bessel's function of first order. For $n = 1$ and $m = \mu$, power-law model shows Newtonian characteristic.

- For $n = 1$ (Newtonian fluid), the representation of velocity is

$$u_z(r) = \left(-\frac{\epsilon_e \zeta E_0}{\mu}\right)\left[1 - \frac{I_0(\kappa r)}{I_0(\kappa r_0)}\right] \tag{1.38}$$

which refers the commonly used EOF velocity scale for Newtonian fluids in cylindrical channels [169,224].

- For $n = \frac{1}{2}$, the representation of velocity is

$$u_z(r) = \frac{\kappa\left(-\frac{\epsilon_e E_0 \zeta}{m}\right)^2}{12 I_0^2(\kappa r_0)}\Bigg[(\kappa r_0)^3\ {}_2F_3\left\{\frac{3}{2},\frac{3}{2};2,\frac{5}{2},3;(\kappa r_0)^2\right\} - (\kappa r)^3\ {}_2F_3\left\{\frac{3}{2},\frac{3}{2};2,\frac{5}{2},3;(\kappa r)^2\right\}\Bigg]. \tag{1.39}$$

Here ${}_2F_3[x_1, x_2; \gamma_1, \gamma_2, \gamma_3; z]$ is one of the generalized hypergeometric functions [1,290]. To get the EOF velocity distribution in a closed form for an arbitrary value of flow behaviour index, the approximation used for the first-order modified Bessel function of the first kind is [1]

$$I_1(r) = \begin{cases} \frac{r}{2}; & 0 \le r < 1, \\ \frac{e^x}{(2\pi r)^{\frac{1}{2}}}\left(1 - \frac{3}{8r}\right); & r \ge 1. \end{cases}$$

With the use of the above mentioned approximation, the EOF velocity in a uniform cylindrical tube can be found for two different domains of κr_0 ($0 \le \kappa r_0 \le 1$ and $\kappa r_0 > 1$) [290].

1.7 Transport of Eluted Species and Mixing efficiency

Mixing of fluids at the microscale poses a variety of challenges, many of which arise from the fact that molecular diffusion is the dominant transport mechanism in the laminar flow regime. The unfavorable combination of low Reynolds numbers and high Peclet numbers implies that cumbersomely long microchannels are required to achieve efficient levels of micromixing. In general, mixing strategies can be classified as either active or passive, depending on the operational mechanism. Active micromixers employ external forces beyond the energy associated with the flow in order to perform mixing, whereas passive micromixers rely on chaotic advection and molecular diffusion. Out of these two types of micromixing strategies, passive one is widely used, since it is easy to handle and it does not require any external stirring agents, easy to integrate with other devices and has a greater reliability due to lack of moving parts [39,143]. The equation for transportation of the uncharged eluted species is governed by convection-diffusion equation. In the absence of species absorption and chemical reaction the species transport equation takes the form

$$\frac{\partial C^*}{\partial t^*} + (\mathbf{q}^* \cdot \nabla)C^* = D_s \nabla^2 C^*, \tag{1.40}$$

where D_s denotes the diffusion coefficient for the uncharged species with concentration C^*. By scaling the the species concentration by C_{ref}, space coordinates by characteristic channel height H and time by $\frac{H^2}{D_s}$, species transport equation can be written as

$$\frac{\partial C}{\partial t} + (\mathbf{q} \cdot \nabla)C = \frac{1}{Pe_S} \nabla^2 C. \tag{1.41}$$

Here Pe_s stands for the Peclet number for the mixing species which measures the ratio of advective to diffusion transport.

A measure of species mixing at different levels of the channel is defined by a (mixing efficiency) parameter, σ, as [84,190]

$$\sigma = \left[1 - \frac{\int_{lower\ \ surface}^{upper\ \ surface} |C - C_\infty| dy}{\int_{lower\ \ surface}^{upper\ \ surface} |C_0 - C_\infty| dy}\right] \times 100\% \tag{1.42}$$

Here C_∞ and C_0 represent the concentrations at the fully mixed and totally unmixed states, respectively. Mixing efficiency is 100% when the two species are in fully mixed condition, whereas a completely unmixed mode signifies 0% mixing efficiency.

1.8 Navier Stokes Solver

It is generally observed that the Navier-Stokes (N-S) equations provide a complete description of fluid flow problems in different branches of science, engineering and technology. Implementation of various initial and boundary conditions and the approximated solutions provide the important flow phenomena and their effects. The unsteady compressible Navier-Stokes equations are a mixed set of hyperbolic- parabolic equations, while the unsteady incompressible Navier-Stokes equations for Reynolds can be treated as a mixed set of elliptic-parabolic equations. However, Navier-Stokes equations show hyperbolic characteristics for convection dominated flow. Existence and uniqueness of the solution of Navier-Stokes equation are one of the important issues. As a consequence, different numerical techniques are used to solve the Navier-Stokes equations in the compressible and incompressible flow regimes. In practice, all efficient numerical methods for compressible Navier-Stokes equations have employed the unsteady form of the equations.

This is because of the fact that if the unsteady terms are dropped from these equations, the resulting equations become a mixed set of hyperbolic-elliptic equations which are difficult to solve because of the differences in numerical techniques required for hyperbolic and elliptic type equations. Both explicit and implicit finite-difference or finite-volume schemes are used to solve the compressible Navier-Stokes equations. As the effect of diffusion is usually small in compressible flows because of high Reynolds number, there may occur certain discontinuities such as shock wave in the flow. Several upwind methods have been developed to solve the compressible Navier-Stokes equations in conservative law forms such as the MacCormack method, Beam-Warming method, flux vector splitting scheme, total variation diminishing scheme (TVD), etc. A detailed description of these methods are discussed in by Peyret et al. [213], Fletcher [89], Anderson Jr. [10], Anderson et al. [9], Ferziger and Peric [88].

1.8.1 Numerical Methods

To obtain the solution of the Navier-Stokes equation numerically, the equations need to be discretized. The discretized equations are usually obtained with three commonly used approaches such as derived by

- **Finite difference method**
- **Finite element method**
- **Finite volume method**

1.8.1.1 Finite Difference Method

The basic idea of finite difference method (FDM) is to replace the partial derivatives by Taylor series approximation. There are the explicit and implicit schemes to approximate derivatives by using finite difference method. Incorporating the boundary conditions in this equation, the resulting algebraic system of equations are solved. This gives the approximate numerical solutions of boundary value problems. One of the main advantages of using FDM compared to other methods is its ease of implementation. But, on the other hand this method has several drawbacks such as, low order accuracy in the derivative evaluation, difficulty in managing with irregular geometries and in implementation of unusual boundary conditions.

1.8.1.2 Finite Element Method

The finite element method (FEM) is a numerical technique which gives approximate solutions to differential equations that model problems arising in physics and engineering. In contrast to finite difference method, the governing equations in the finite element method are integrated over each finite element and the solutions are summed over the entire problem domain. As a consequence of these operations, a set of finite linear equations obtained in terms of a set of unknown parameters over each element. The solution of these equations is achieved using linear algebra techniques. The most commonly used finite element approximations are least square method and Galerkin method. The most significant characteristics of FEM is the ability to handle the solution domains having irregular geometry. In general it requires fewer grid points for a given accuracy of solution as compared to FDM. The main drawback of FEM is its complex algorithmic approach of solution and it continue to retain a low-order method. Some of the recent studies made using finite element method consists of [140,170,171].

1.8.1.3 Finite Volume Method

For the study of electrokinetic flow, finite volume method (FVM) is one of the most frequently used numerical techniques. This technique is used for solving the governing equations for mass, momentum and energy conservation. In this method, the equations justify the conservation law and are integrated over a control volume. The variables on the control volume interface are estimated by a linear interpolation between the two neighboring cells to either side of the control volume interface. Here we have used the staggered grid arrangement for allocating the variables because of its advantages in considering the influence of the pressure gradients on fluid flow. A detailed description of this method is discussed by Patankar [210], Versteeg and Malalasekera [261], Fletcher [89], Lomax et al. [155] and Pletcher et al. [216].

To explain the finite volume method we consider the two dimensional convection- diffusion equation with the generic variable c as

$$\frac{\partial c}{\partial t} + \nabla.(c\boldsymbol{u}) = \nabla^2 c + S_c \tag{1.43}$$

Here, $\boldsymbol{u}$ represents the corresponding flux tensor and S_c is the source term and to proceed for the technique, we sub-divide the spatial domain into finite volumes or cells. For a particular cell (Fig. 1.6), we take the volume integral over the total volume of the cell, V_P , which gives

$$\int_{V_P} \frac{\partial c}{\partial t} dV + \int_{V_P} \nabla.(c\boldsymbol{u}) dV = \int_{V_P} \nabla^2 c dV + \int_{V_P} S_c dV \tag{1.44}$$

On integrating the first term to get the volume average and applying the Gausss divergence theorem to the second, this yields

$$\int_{V_P} \frac{\partial c}{\partial t} dV + \oint_{S_P} c(\boldsymbol{u}.\boldsymbol{n}) = \oint_{S_P} \nabla c.\boldsymbol{n} dS + \int_{V_P} S_c dV \tag{1.45}$$

where S_P represents the total surface area of the cell and $\boldsymbol{n}$ is a unit vector normal to the surface and pointing outward. This integrals are approximated as

$$\left(\frac{\partial c}{\partial t}\right)_P V_P + \oint_{S_P} c(\boldsymbol{u}.\boldsymbol{n}) dS = \oint_{S_P} \nabla c.\boldsymbol{n} dS + (S_c)_P V_P \tag{1.46}$$

The unsteady term, the fluxes, the diffuse and the source term are further discretized using various schemes.

1.8.2 Differencing Schemes for Convection and Diffusion Terms

The governing equations for EOF and solute transport consist of various terms namely, temporal, convective, diffusive, electromigration and source terms. Each terms can be approximated by various formula depending on the accuracy of the schemes. The convective term, specially for high Reynolds number flows, leads a non-physical oscillation if we discretize it by using the central difference scheme. The Nernst-Planck equation shows hyperbolic characteristics due to the presence of the convection and electromigration term. Discretization of convective and electromigration terms through central difference scheme produce wiggles near the sharpness in solutions [118,256]. To overcome this problem, generally higher order upwind scheme is used. Commonly used higher order upwind schemes are the Second order upwind scheme [74,124,240,274] and the QUICK (Quadratic Upwind Interpolation for Convective Kinematics) [104,145] scheme.

We consider one-dimensional control volume as shown in Fig. 1.5. The boundary of the control volume is positioned mid-way between the adjacent nodes. A general node point is denoted by 'P' and its neighbor points are the nodes to the west and east are identified by 'W' and 'E' respectively. The west and east side face of the control volume is referred by 'w' and 'e' respectively. For the simplicity of the presentation, we have considered the uniformly spaced nodes and the distance between them is δx. The distance between the point 'P' and its east face 'e' is $\delta x/2$ and that of west face is $\delta x/2$.

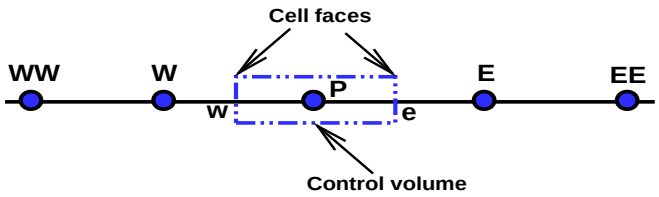

Figure 1.5: Schamatic diagram of the control volume in one dimension.

To illustrate various upwind schemes, we consider one dimensional Convective-Diffusion equations for the generic variable c, i.e.,

$$uc_x = \alpha c_{xx} \tag{1.47}$$

Using the central inferencing scheme the approximations of c at cell face e and w is given by

$$c_e = \frac{c_E + c_P}{2} \qquad \text{and} \qquad c_w = \frac{c_P + c_W}{2} \tag{1.48}$$

The major disadvantage of the central differencing scheme are its inability to identify the flow direction. In a strongly convective flow, the central differencing approximation for the convective terms is not suitable as it does not account for the flow velocities. However, the upwind differencing scheme takes into account the flow direction when determining the value at a cell face, i.e., the convected values of c at cell faces depend on the upstream and downstream node depending on the flow direction.

1.8.2.1 Second Order Upwind Scheme

Using the second order upwind scheme the convected values of c at cell face e is given by

$$c_e = \begin{cases} (\frac{3}{2}c_P + \frac{4}{2}c_W - \frac{1}{2}c_{WW}), & u_e > 0 \\ (-\frac{3}{2}c_P + \frac{4}{2}c_E - \frac{1}{2}c_{EE}), & u_e < 0. \end{cases}$$

Similar procedure is adopted to estimate c_w at cell face w.

1.8.2.2 QUICK Scheme

QUICK scheme uses the 3 point upstream weighted quadratic interpolation for the cell face values. Using the QUICK scheme the convected values of c at cell face e is given by

$$c_e = \begin{cases} (\frac{3}{8}c_E + \frac{3}{4}c_P - \frac{1}{8}c_W)), & u_e > 0 \\ (-\frac{3}{4}c_P + \frac{3}{8}c_E - \frac{1}{8}c_{EE}), & u_e < 0. \end{cases}$$

Similar procedure is adopted to estimate c_w at cell face w.

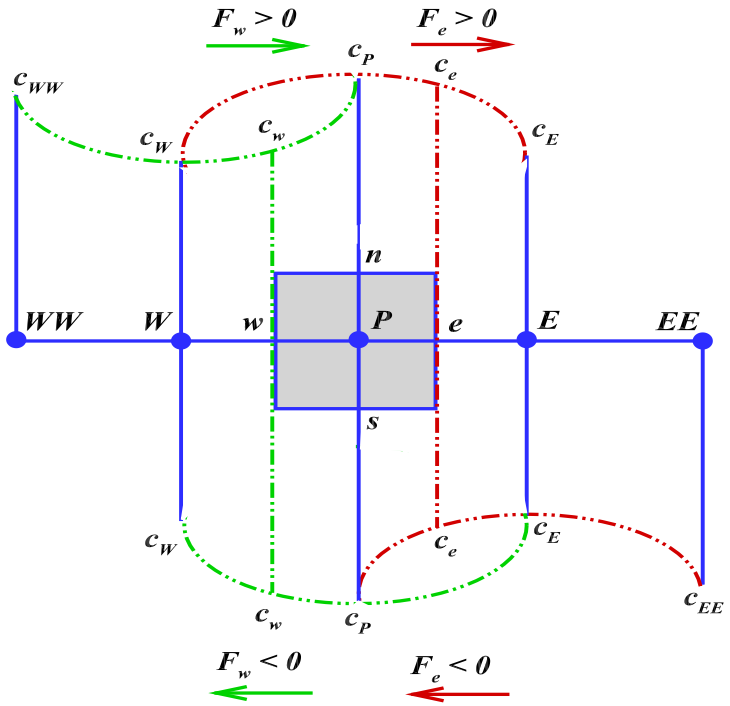

Figure 1.6: Schamatic diagram for control volume V_P where P is the center and e, w, n, s denote the cell faces. The interpolation for a variable c based on QUICK scheme

1.8.2.3 Implementation of QUICK Scheme

We consider the general Convective-Diffusion equations for the generic variable c, with some boundary condition i.e.,

$$\frac{\partial c}{\partial t} + \left[\frac{\partial}{\partial x}(uc) + \frac{\partial}{\partial y}(vc)\right] - \nabla^2 c = 0 \tag{1.49}$$

where the first term is due to the time dependency and the last term is the diffusion term. The computational domain is subdivided into a number of elementary sub cells V_P with area

dV whose sides are dx and dy. On integration of Eq. 1.49 over a cell V_P (Fig. 1.6) yields the discretization as

$$\frac{c_P^{n+1} - c_P^n}{dt} dxdy + [u_e c_e - u_w c_w]^{n+1} dy_P + [v_n c_n - v_s c_s]^{n+1} dx = \left[\left. \frac{\partial c}{\partial x} \right|_e - \left. \frac{\partial c}{\partial x} \right|_w \right]^{n+1} dy_P + \left[\left. \frac{\partial c}{\partial y} \right|_n - \left. \frac{\partial c}{\partial y} \right|_s \right]^{n+1} dx + (S_c)_P dxdy \quad (1.50)$$

Here n, s, e and w, refers to the north, south, east, west face of the cell (Fig. 1.6). An implicit first-order scheme is used to discretize the time derivatives present. The diffusion terms are discretized through central difference scheme.

The diffusion flux at interfaces 'e' and 'w' are evaluated as

$$\left. \frac{\partial c}{\partial x} \right|_e = \frac{c_E - c_P}{dx}$$

and

$$\left. \frac{\partial c}{\partial x} \right|_w = \frac{c_P - c_W}{dx}$$

Similar procedure is adopted to estimate the diffusion flux at the other cell faces 'n' and 's'. Note that the capital letter subscripts denote the cell centers in which variables are stored and small letter subscripts denote the corresponding cell faces. Using the QUICK scheme for the convective terms and central differencing scheme for the diffusion terms, the discretized equation (Eq. 1.50) can be written as

$$a_P c_P^{k+1} = a_E c_E^{k+1} + a_W c_W^{k+1} + a_N c_N^{k+1} + a_S c_S^{k+1} + a_P^0 c_P^k, \quad (1.51)$$

where the coefficients a_i ($i = E$, W, P, N and S) are as follows

$$a_E = D_e - min(u_e, 0), a_W = D_w + max(u_w, 0),$$

$$a_N = D_n - min(v_n, 0), a_S = D_s + max(v_s, 0),$$

$$a_P = D_e + max(u_e, 0) + D_w - min(u_w, 0) + D_n + max(v_n, 0) + D_s - min(v_s, 0) + a_P^0$$

The contribution of the diffusion terms are included in D.

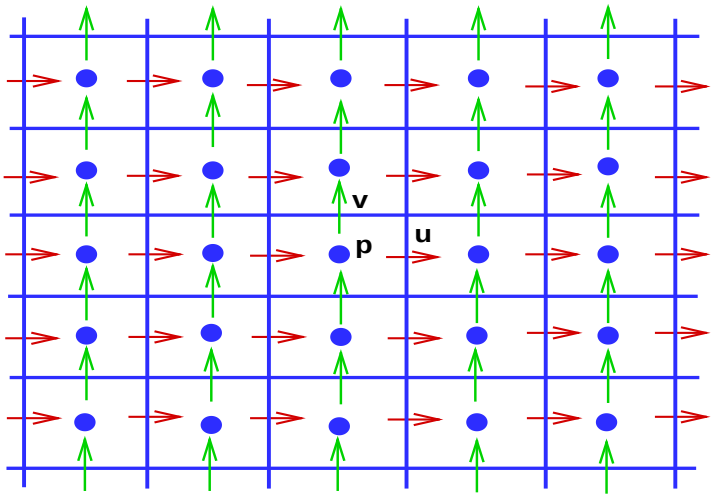

Figure 1.7: Staggered arrangement for scalar and vector components.

1.8.3 Choice of Variable Arrangement on Grid

The first issue in discretization is to select the points in the domain at which the values of the unknown dependent variables are to be computed. The obvious choice is to store all the variables at the same set of grid points and to use the same control volumes for all variables; such arranged grids is called collocated grid. Since, many of the terms in each of the equations are essentially identical, the number of coefficients that must be computed and stored is simplified by their choice. But the collocated arrangement has significant drawbacks in complicated solution domains, especially when the boundaries have slope discontinuities or the boundary conditions are discontinuous. The collocated arrangement was out of favor for a long time for incompressible flow computation due to the difficulties with pressure-velocity coupling and the occurrence of oscillations in the pressure. It can be shown that if the velocity components and the pressure are calculated for the same points, some physically unrealistic fields arise as solutions. A detailed discussion regarding these difficulties is made by Patankar [210]. A remedy for this is to use the staggered grid for velocity components [102]. Fig. 1.7 shows a portion of a two-dimensional grid. In the staggered grid, the scalar variables, including pressure, are stored at the nodes marked (•), whereas the velocity components (horizontal and vertical) are defined at the cell faces in between the nodes and are indicated by arrows. Horizontal (→) arrows indicate the locations for the u-velocities and vertical (↑) ones denote those for v-velocities.

1.8.4 Pressure Calculation

Solution of incompressible Navier-Stokes (N-S) equations is complicated due to the lack of independent equations for pressure, whose gradient contributes to each of the momentum equations. In incompressible flow, the density is constant and hence not linked to the pressure. Due to which a coupling between the pressure and velocity introduces a constraint on the solution of the flow field i.e., if the corrected pressure field is applied in the momentum equation, the resulting velocity field should satisfy the continuity equation.

Three approaches are usually adopted to calculate pressure in incompressible flow:

- **Artificial compressibility approach**
- **Pressure poisson approach**
- **Pressure correction approach**

A brief description of these schemes are presented below.

1.8.4.1 Artificial Compressibility Approach

This is one of the earlier proposed technique for solving the incompressible Navier- Stokes equations in primitive variable approach due to Chorin [69]. In this method, the continuity equation was modified by adding an artificial compressibility term which vanishes when the steady solution is reached. The continuity equation then becomes an evaluation equation for pressure. The introduction of the compressibility parameter in the continuity equation helps in the application of compressible flow solvers for the solution purpose and enhance the convergence characteristics of the solution.

1.8.4.2 Pressure Poisson Approach

The most common way to combine the continuity and momentum equations is by taking the divergence of the momentum equations. For the incompressible fluid with constant viscosity, the viscous and unsteady terms disappear by the virtue of continuity equation, resulting in the following equation

$$\frac{\partial}{\partial x_i}\left(\frac{\partial p}{\partial x_i}\right) = -\frac{\partial}{\partial x_i}\left(\frac{\partial}{\partial x_j}(\rho u_i u_j)\right) \tag{1.52}$$

The above equation for pressure can be solved by any numerical method for elliptic equations. A pressure equation of this kind is used to calculate the pressure for both explicit and implicit type solution techniques. To maintain consistency among the approximations used, it is best to derive the equation for the pressure from the discretized momentum and continuity equations rather than by approximating the Poisson equation.

One of the earliest and most widely used methods for solving the incompressible N-S equations in primitive variable form is the Marker and Cell (MAC) methods by Harlow and Welch [102]. The method is characterized by the use of staggered grid and the solution of a Poisson equation for pressure at every time step. This method makes use of FTCS (Forward Time Centered Space) finite difference scheme for the discretization of the governing equations in an explicit manner. After solving the Poisson equation for pressure, the momentum equations are solved to update the velocity field using the pressure field obtained from the pressure equation. Although the original form of MAC method has certain weakness, the use of a staggered grid and a Poisson equations for pressure has been retained in many modern methods derived from the MAC method. A simplified Marker and Cell (SMAC) method has been developed by Amsden and Harlow [8] in which a second Poisson equation for an auxiliary velocity potential is solved to satisfy continuity equation more directly. However the explicit treatment of the momentum equations puts unnecessary restriction on the time step. The extension of MAC formulation to allow the momentum equations to be marched in time with implicit approximation factorization of the velocity term is provided by Ghia et al. [93] for high Reynolds number.

1.8.4.3 Pressure Correction Approach

A number of methods have been developed based on pressure correction approach out of which SOLA, SIMPLE and PISO are worth mentioning. In the methods known as SOLA, by Hirt [108] the convective terms are discretized by a combined scheme of central and second upwinding formulation.

The family of SIMPLE algorithm is based on a finite volume dicretization on a staggered grid. This method, introduced by Patankar and Spalding [211] is essentially a guess-and- correct procedure for the calculation of pressure on the staggered grid arrangements. The acronym, SIMPLE stands for Semi-Implicit Method for Pressure-Linked Equations and describes the iterative procedure by which the solutions to the discretized equations are obtained. Here the

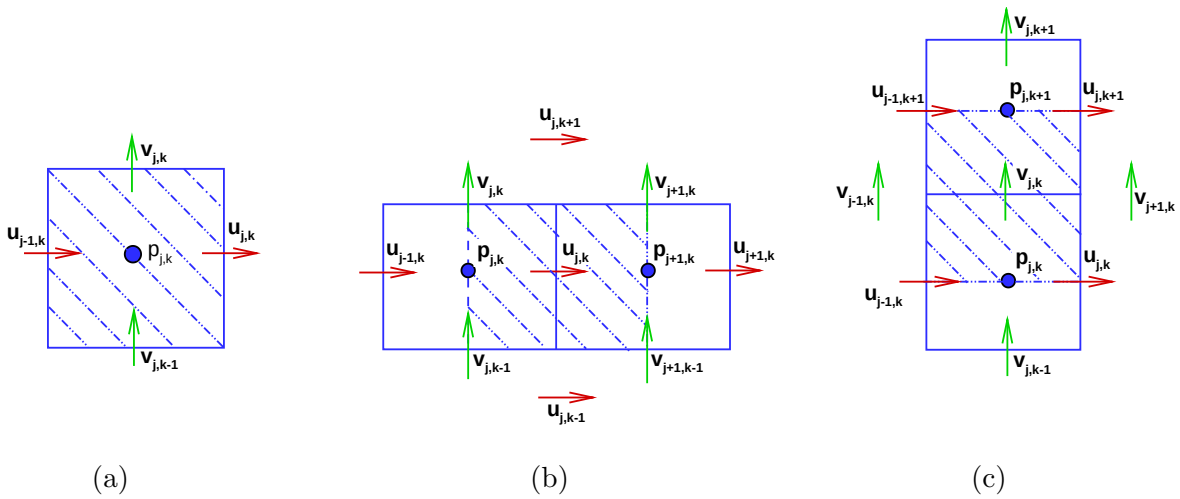

(a) (b) (c)

Figure 1.8: (a) Scalar control volume, (b) u -control volume, (c) v -control volume.

continuity equation is converted to an equation for pressure. It starts with a guessed pressure field which is used in solving the discretized momentum equation and the pressure correction equation, deduced from the continuity equation which is in turn used to update the velocity and pressure fields. The velocity field so obtained does not satisfy the continuity equation. Therefore, the pressure and velocity are corrected to satisfy the continuity equation. The other variations of SIMPLE algorithm (SIMPLER, SIMPLEC) can produce savings in computational effort due to improved convergence.

1.9 Implementation of SIMPLE Algorithm for EOF in a Slit Micro-Channel

The detail analysis of numerical scheme based on SIMPLE algorithm for a rectangular slit microchannel is briefly stated in this section. The integration of the equations for horizontal and transverse velocity components at the $(n+1)^{th}$ time step over the $(j,k)^{th}$ control volumes for u and v respectively (Fig. 1.8), yields

$$a_j^u u_{j-1,k}^{n+1} + b_j^u u_{j,k}^{n+1} + c_j^u u_{j+1,k}^{n+1} = d_j^u - \left(p_{j+1,k}^{n+1} - p_{j,k}^{n+1}\right)\Delta y \tag{1.53}$$

$$a_j^v v_{j-1,k}^{n+1} + b_j^v v_{j,k}^{n+1} + c_j^v v_{j+1,k}^{n+1} = d_j^v - \left(p_{j,k+1}^{n+1} - p_{j,k}^{n+1}\right)\Delta x \tag{1.54}$$

The mole-fraction equations for the species (counter ion and co-ion) at the $(n+1)^{th}$ time

step over the $(j,k)^{th}$ scalar control volume gives

$$a_j^{n_1} n_{1_{j-1,k}}^{n+1} + b_j^{n_1} n_{1_{j,k}}^{n+1} + c_j^{n_1} n_{1_{j+1,k}}^{n+1} = d_j^{n_1} \tag{1.55}$$

$$a_j^{n_2} n_{2_{j-1,k}}^{n+1} + b_j^{n_2} n_{2_{j,k}}^{n+1} + c_j^{n_2} n_{2_{j+1,k}}^{n+1} = d_j^{n_2} \tag{1.56}$$

Here n_1 and n_2 stand for mole-fraction for counter and co-ions respectively. For a fixed value of k, the system of equations can be expressed in a matrix form as

$$A_j X_{j-1}^{n+1} + B_j X_j^{n+1} + C_j X_{j+1}^{n+1} = D_j, \tag{1.57}$$

where the coefficient matrices A_j, B_j, C_j are given by

$$A_j = \begin{bmatrix} a_j^u & 0 & 0 & 0 \\ 0 & a_j^v & 0 & 0 \\ 0 & 0 & a_j^{n_1} & 0 \\ 0 & 0 & 0 & a_j^{n_2} \end{bmatrix};\ B_j = \begin{bmatrix} b_j^u & 0 & 0 & 0 \\ 0 & b_j^v & 0 & 0 \\ 0 & 0 & b_j^{n_1} & 0 \\ 0 & 0 & 0 & b_j^{n_2} \end{bmatrix};\ C_j = \begin{bmatrix} c_j^u & 0 & 0 & 0 \\ 0 & c_j^v & 0 & 0 \\ 0 & 0 & c_j^{n_1} & 0 \\ 0 & 0 & 0 & c_j^{n_2} \end{bmatrix}$$

with the vector of unknown variables and vector of known variables are

$$X_j = \begin{bmatrix} u_{j,k}^{n+1} \\ v_{j,k}^{n+1} \\ n_{1_{j,k}}^{n+1} \\ n_{2_{j,k}}^{n+1} \end{bmatrix}; \qquad D_j = \begin{bmatrix} d_j^u - \left(p_{j+1,k}^{n+1} - p_{j,k}^{n+1}\right)\Delta y \\ d_j^v - \left(p_{j,k+1}^{n+1} - p_{j,k}^{n+1}\right)\Delta x \\ d_j^{n_1} \\ d_j^{n_2} \end{bmatrix}.$$

Thus the system of equation can be written in a matrix from as

$$\mathbf{AX} = \mathbf{D}, \tag{1.58}$$

where $\mathbf{A}$ represents a block tridiagonal matrix, each element of which is a square matrix of order four and $\mathbf{X}$, $\mathbf{D}$ stand for the vector of unknown variables and the vector of known quantities respectively.

Integrating the continuity equation at $(n+1)^{th}$ time level over $(j,k)^{th}$ scalar control volume, we have

$$\left(u_{j,k}^{n+1} - u_{j-1,k}^{n+1}\right)\Delta y + \left(v_{j,k}^{n+1} - v_{j,k-1}^{n+1}\right)\Delta x = 0. \tag{1.59}$$

The pressure link between the continuity and momentum equations are accomplished by transforming the discretized continuity equation (Eq. 1.59) into a Poisson's equation for pressure correction. This pressure correction equation implements a divergence free velocity field.

At each control volume, pressure $p_{j,k}$ is unknown at the initial stage. To get a solution for Eq. 1.53 and Eq. 1.54, we guess a pressure field $p^c_{j,k}$. Corresponding to this guessed pressure field $p^*_{j,k}$, the velocity field $(u^*_{j,k}, v^*_{j,k})$ is determined form Eq. 1.58. Since $u^*_{j,k}, v^*_{j,k}$ satisfy Eq. 1.53 and Eq. 1.54 respectively, then

$$a^u_j u^*_{j-1,k} + b^u_j u^*_{j,k} + c^u_j u^*_{j+1,k} = d^u_j - \left(p^*_{j+1,k} - p^*_{j,k}\right)\Delta y \tag{1.60}$$

$$a^v_j v^*_{j-1,k} + b^v_j v^*_{j,k} + c^v_j v^*_{j+1,k} = d^v_j - \left(p^*_{j,k+1} - p^*_{j,k}\right)\Delta x \tag{1.61}$$

Since the velocity field $(u^*_{j,k}, v^*_{j,k})$ at intermediate stage may not form a divergence free velocity field, a correction of velocity field is needed. The correction of the velocity field can be made through a pressure correction. The pressure link between the momentum and continuity equations is accomplished by transforming the continuity equation into a pressure Poisson equation. Let $p^c_{j,k}$ be the pressure correction at $(j,k)^{th}$ cell and $(u^c_{j,k}, v^c_{j,k})$ be the corresponding correction in velocity field. Thus the updated pressure and velocity field can be expressed as

$$p^{n+1}_{j,k} = p^*_{j,k} + p^c_{j,k} \tag{1.62}$$

$$u^{n+1}_{j,k} = u^*_{j,k} + u^c_{j,k} \tag{1.63}$$

$$v^{n+1}_{j,k} = v^*_{j,k} + v^c_{j,k} \tag{1.64}$$

Subtracting Eq. 1.60 from Eq. 1.53 and Eq. 1.61 from Eq. 1.54, we get a relation between pressure correction and velocity correction as

$$a^u_j u^c_{j-1,k} + b^u_j u^c_{j,k} + c^u_j u^c_{j+1,k} = -\left(p^c_{j+1,k} - p^c_{j,k}\right)\Delta y \tag{1.65}$$

$$a^v_j v^c_{j-1,k} + b^v_j v^c_{j,k} + c^v_j v^c_{j+1,k} = -\left(p^c_{j,k+1} - p^c_{j,k}\right)\Delta x \tag{1.66}$$

Ignoring, the neighboring small correction terms $u^c_{j-1,k}$, $u^c_{j+1,k}$ and $v^c_{j-1,k}$, $v^c_{j+1,k}$, the correction of velocity components can be expressed as

$$u^c_{j,k} = -\left(\frac{\Delta t}{\Delta x}\right)\left(p^c_{j+1,k} - p^c_{j,k}\right) \tag{1.67}$$

$$v^c_{j,k} = -\left(\frac{\Delta t}{\Delta y}\right)\left(p^c_{j,k+1} - p^c_{j,k}\right) \tag{1.68}$$

Substituting the corrected velocity field $(u_{j,k}, v_{j,k})$ into the discretized continuity equation (Eq. 1.59), the following Poisson's equation for pressure corection is obtained.

$$\left[2\left(\frac{\Delta t\Delta y}{\Delta x}\right) + 2\left(\frac{\Delta t\Delta x}{\Delta y}\right)\right]p^c_{j,k} = -div^* + \left(\frac{\Delta t\Delta y}{\Delta x}\right)\left(p^c_{j-1,k} + p^c_{j+1,k}\right) + \left(\frac{\Delta t\Delta x}{\Delta y}\right)\left(p^c_{j,k-1} + p^c_{j,k+1}\right) \tag{1.69}$$

where

$$div^* = \left(u^*_{j,k} - u^*_{j-1,k}\right)\Delta y + \left(v^*_{j,k} - v^*_{j,k-1}\right)\Delta x$$

Here α_u and α_v are relaxation factors corresponding to axial and transverse velocity corrections respectively. The Eq. 1.69 is solved using a Gauss-Seidel iterative method to achieve the pressure correction $(p^c_{j,k})$ at each cell of the flow domain. For rapid convergence, the pressure field is under-relaxed as

$$p^{n+1}_{j,k} = p^*_{j,k} + \alpha_p p^c_{j,k}, \tag{1.70}$$

where α_p is the under-relaxation factor. The relaxation factor is taken between 0 and 1, so that guessed pressure field is added in a fraction of the corrected pressure field p^c, in order to improve iteration process to carry forward. Similarly, the velocity components $u^{n+1}_{j,k}$ and $v^{n+1}_{j,k}$ are under-relaxed in the following manner:

$$\left.\begin{aligned} u^{n+1}_{j,k} &= u^*_{j,k} + \alpha_u u^c_{j,k} \\ v^{n+1}_{j,k} &= v^*_{j,k} + \alpha_v v^c_{j,k} \end{aligned}\right\}. \tag{1.71}$$

Any time step of the algorithm consists of the following sequential steps:

1. Start the iteration by guessed pressure, velocity, ionic concentration and electric potential.
2. Discritized ionic concentration and momentum equations are solved by block elimination method (Appendix C) using the guessed values of the corresponding variables.
3. Solve the pressure correction equation with SOR method (Appendix A).
4. Update the velocity and pressure fields at each cell using pressure correction.
5. At each time step the equation for potential is solved using the updated ionic concentration.
6. The process is repeated until getting desired accuracy. The convergence criteria can be represented as

$$\max_{j,k}|\Theta^{n+1}_{j,k} - \Theta^n_{j,k}| < \Delta,$$

where $\Theta = (u, v, n_1, n_2, \phi)$, $\Delta = 10^{-6}$. Here n denotes the iteration level and (j, k) stands for cell index.

In case of eluted species mixing (C), the discretized form of Eq. 1.41 is solved using Tridiagonal Matrix Algorithm (Appendix B) with same tolerance (Δ).

1.10 Organization of the Thesis

This thesis consists of seven chapters including the introductory chapter. We have also included three appendices related to numerical schemes. In the introductory chapter, the governing equations for fluid flow, ion transport, electric field and the transport of uncharged eluted species are described. The basic principles of electrokinetic phenomena and their importance in micro/nano fluidic systems are provided. In this chapter, we have introduced the basic characteristics of the electrokinetic flow, the electric double layer and the mathematical modeling of electrokinetic flows. The theoretical analysis of the electroosmotic flow (EOF) based on the Debye- Huckel approximation and its limitations are explained. At the end of this chapter, the computational methods for solving the governing set of coupled nonlinear partial differential equations for fluid flow, ions transport and electric potential have been discussed.

In Chapter 2, the electroosmotic flow and mixing of uncharged species of two different concentration are studied in a nano-fluidic system. The channel is modulated with a non-conducting block, embedded on the lower wall of the channel with surface potential heterogeneity. The results are presented in terms of electric field lines, streamlines, mixing efficiency and concentration contours by solving a coupled set of non-linear set of pde's involving Maxwell's equation for electric potential, Nernst-Planck equation for ion transport, Navier-Stokes equation for momentum transport and advection-diffusion equation for uncharged mixing species transport. A finite volume based numerical approach with QUICK [89] scheme is adopted for solving the governing system of equations. The simulated results show that the increment of block height with higher over-potential patch strength increases the retention time and effective contact ares between flow streams which in turn increases the effective diffusion flux to achieve an improved mixing. On the other hand, it is concluded that higher external electric field strength increases the average flow rate which is a cause of reduced mixing efficiency. At the last section of this chapter it is shown that, maximum mixing efficiency at the downstream of the channel can be achieved when the block is placed closer to inlet.

In Chapter 3, a comparative study on flow mixing and charge transport is conducted based on Poisson-Nernst-Planck model. In this chapter two different configurations are considered to create geometric and surface modulation. In the first configuration (Case I), a non conducting block with overpotential patch is embedded on the lower wall of the channel and two overpotential patches are placed on the upper wall asymmetrically. In Case II, two blocks with potential heterogeneity are placed on the lower wall and two overpotential patches are attached on the

upper wall symmetrically at the same axial locations. An analytical estimation for pressure and velocity is made far away from heterogenous region. The simulated results concluded that a larger pressure drop is developed in Case II as a consequence of higher effective circulation strength due to the presence of block-patch. As a result, the fluid streams experience more stretched and folded paths in Case-II which causes better downstream mixing as compared to earlier case.

In Chapter 4, a numerical investigation of flow mixing and flow reversal is carried out in a symmetric modulated microchannel. The side walls of this micromixer is composed of two sinusoidal wave functions. In the first section of this paper, a parametric estimation for flow reversal is discussed in terms of wave amplitude, ratio of EDL thickness to channel height and external electric field. This flow reversal diagram revels that the critical wave amplitude for flow reversal is increased with the increment of external electric field and solution strength. In the last section, the criterion for mixing enhancement is discussed for a wide range of above discussed parameters. An improved mixing is found for the increment of wave amplitude and for the decrement of external electric field and solution strength.

In Chapter 5, a numerical study of electrokinetic mixing and pressure drop is presented in a wavy patterned microchannel with different phase shift. The rheological behaviour of the electrolyte is described by power-law model. In this chapter, the wall zeta potential is assumed to vary sinusoidally with same wave length that of wall structures. In the first section of this chapter, a parametric study is made to choose the best choice of phase shift for achieving a good mixing with minimum pressure drop for Newtonian fluid. In the successive section the discussions for pseudoplastic (shear thinning) and dilatant (shear thickening) fluids are made using the best chosen phase shift ($\pi/2$). The results depict that the mixing efficiency is remarkably increased for the increment of wavy nature of the wall with higher power-law index, but the pressure drop is also increased accordingly. Thus to achieve an effective and controllable mixing, mixing performance factor (ratio of mixing efficiency and pressure drop) is studied here along with mixing efficiency. It is found that, higher values of power-law index is not always beneficial in term of mixing enhancement factor. Mixing performance factor is decreased after a certain value of power law index (here $n = 1.3$) due to the dominance of pressure drop over mixing efficiency.

In Chapter 6, a comparative numerical study on non-Newtonian (power-law) mixing is

performed in a cylindrical channel with sudden constriction / expansion with surface potential heterogeneity. In this chapter, overpotential patches are placed in the region of constriction / expansion zones. The simulated results are presented in terms of mixing enhancement and pressure drop. The results show that the mixing efficiency is increased with the increment of power-law index and wave amplitude for both the cases. It is important to mention that, for the same set of flow controlling parameters, constricted structure gives better mixing as compared to expanded one. But the reverse characteristic is followed for mixing enhancement factor due to the higher pressure drop in case of constricted channel. Thus it is concluded that, for mixing purpose, constricted structure is quiet better, but for overall performance, i.e. for effective mixing with minimum pressure drop, expanded structure is better.

Finally, we draw some conclusions of the above chapters and discuss future problems in this direction in **Chapter 7**.

Chapter 2

Mixing and Charge Transfer in a Nanofluidic System Due to a Patterned Surface

2.1 Introduction

Micro / nano fluidic systems have a wide range of biological and chemical applications such as drug delivery and control, separation and mixing in small channels, DNA manipulation and sequencing [70, 83, 84]. Electroosmotic flow is a very useful transport phenomenon in industrial applications such as heating and cooling of microchips in electronics, the separation of biological components in microfluidics system based on a lab-on-a-chip concept. To generate a flow field in channels of micro/nano scale, a mechanism called electroosmosis is adopted in which fluid flow occurs due to the interaction between two electric fields namely (i) induced electric field which is developed near the charged wall and (ii) external electric field which is applied along streamwise direction in general. A charged layer, called electric double layer (EDL) [146, 147] is induced in the vicinity of the channel walls.

The electroosmotic flow strongly depends on the surface charge density or zeta-potential, which varies with solution pH, ionic strength, dielectric constant and absorption of solute molecules on the walls [263]. The enhancement of mixing in microfluidics have been demonstrated by several authors through surface potential modulation. A non-uniform surface potential may arise due to surface defects or the absorption of organic material on the walls. In case of a positive over potential patch located on a negatively charged wall, a surplus of negative ions

are attracted by the patch while a surplus of positive ions are attracted by the negative charged wall. Due to the external electric field acting parallel to the wall, the flow near the patch will be in opposite direction to that of bulk flow, which may lead to a recirculation region [90]. The effects of non-uniform surface charge distribution on electrokinetic flows have been studied by several researchers. Electroosmotic flow between two parallel plates with periodic surface modulation has been studied by Ajdari [3,4] analytically. Many numerical and experimental works have been carried out by several authors on mixing in small channels. Erickson and Li [84] investigated the problem in micro channels with non-uniform charge for mixing applications. The Boltzmann distribution and the slip boundary conditions have been used in their model. Their results showed that mixing of two species can be enhanced by the localized circulation in the bulk flow field which is generated by the non-uniformity of the surface charge distribution. Wang et al. [266] numerically investigated flow mixing in micro channels with patterned grooves using a poincaré map. Their simulation showed that patterned grooves cause rotation of fluid streams to induce more passive mixing. Micro/nano scale mixing can be enhanced by chaotic advection that can be simulated using Lagrangian particle tracking methods, box counting and finite time Lyapunov exponents [130,232,251] in which the contact area between fluid elements are stretched and folded. A detailed mathematical description on stretching and folding of interfacial area to create significant enhancement in mixing has been discussed by Ottino [203]. Biddis et al. [31] visualized the effect of heterogenous charge arrangement along the channel walls experimentally for micro-channels. They concluded that patterning arrangement of surface charge heterogeneities develops flow recirculation and thus, introduces an additional advective component of mixing. Wang et al. [267] studied the flow pattern in micro-channels using the Lattice Boltzmann method and concluded that mixing efficiency can be enhanced by induced transversed velocity. Chang and Yang [43] numerically investigated the flow pattern and mixing performance in a rectangular micro-channel with patterned blocks. Their model is based on the Boltzmann distribution and the Debye-H*ü*ckel approximation. They have observed recirculating vortices over the blocks. Stroock et al. also observe this flow pattern experimentally [250]. Chen and Cho [50] numerically investigated the flow pattern in wavy surfaces and observed that a wavy surface expands the interfacial contact area between two streams, and hence, provides improved mixing. Wu and Li [276] numerically demonstrated a technique to increase the diffusive flux by considering fluid streams through a converging-diverging region, formed by a pair of conducting triangular hurdles. Wang et al. [264] demonstrated the effect of number, size and displacements of blocks in a rectangular channel with patterned blocks to determine the optimal choice to get significant mixing efficiency. Tang et al. [253] reported the

mixing efficiency enhancement in a channel with asymmetric zeta potential distribution using Lattice Boltzmann (LB) method. Transverse and longitudinal flow through a plane channel with a periodic arrangement of slipping and non-slipping strips has been investigated by Ng and Chu [195] using a semi-analytical method. Enhancement of mixing in micro-channels has been reported by Song and Bennett [246] due to a transverse flow generated by introducing two layers of electrodes face-to-face placed on the top and bottom of the channel. They noticed that an optimum effect can be obtained by a squarewave pattern of electrodes placed on both top and bottom of the channel. Ghosh and Chakraborty [94] studied electrokinetic mixing in a long micro-channel with non-homogeneous charge distribution on the walls. Cho et al. [66] numerically studied the mixing enhancement for power-law fluids. This study showed that shear-thinning fluids consist of a higher volumetric flow rate than shear-thickening fluids, and therefore resulting in poor mixing efficiency. Jain and Nandakumar [117] designed an optimal non-homogeneous charged pattern along the channel to get an effective mixing efficiency enhancement along the channel. Sezavar and Miri [233] designed two different geometries by placing triangular and rectangular hurdles respectively in a periodic manner on both of the walls of a micro-channel. Their result shows that rectangular obstacles give more homogenous mixing than triangular ones. It can also observed that for both types of obstacles, the height of the barrier is more important than their number for mixing enhancement.

A major limitation of the above studies is that most of the authors have used the Poisson-Boltzmann model with the Debye-H*ü*ckel approximation to analyze the flow mixing in small channels. The Boltzmann distribution is based on the condition that the electrochemical potential must be constant everywhere at equilibrium and there is no imposed electric field and no bulk flow. In the Poisson-Boltzmann model, it is typically assumed that electric potential is zero away from the channel wall and ionic concentration of the liquid away from charged surface is equal to the bulk ionic concentration. But these assumptions are not applicable for overlapped EDL cases, when the channel walls are sufficiently close to each other. Also, for heterogeneous surface potential with solution $pH > 8$, the surface potential may exceed $26mV$ which violates the applicability of the Debye-H*ü*ckel approximation [73]. To avoid these limitations, the Poisson-Nernst-Planck model has been used by many authors in which the convection and electric migration effects are also included. Conlisk and Mc Ferren [72] used the Nernst-Planck equation in their simulation instead of the Boltzmann's model to describe the distribution of ionic species in a channel. Bhattacharyya and Nayak [27] demonstrated enhancement in mixing in a micro-channel based on the Nernst-Planck model. They introduced non-homogeneity

in electric potential along the channel walls and showed that a transverse velocity is induced over the potential non-homogeneity which significantly modifies the flow field. It is found that the Nernst-Planck (NP) model and the Poisson-Boltzmann (PB) model show significant differences for higher value of external electric field and large overpotential patch strength. A non-linear distribution of velocity and potential has been studied by Chen and Conlisk [54] using the Nernst-Planck model. They concluded that the velocity and potential distribution show a significant difference from the results based on the PB-model when the flow field is strongly influenced by convection effects with a strong electric field. Nayak [189] showed that convection effects can not be neglected near a step jump in the zeta potential. It has also been concluded that a strong convection effect is observed close to channel walls when patches have high electric potential, close to the channel walls. An asymmetric arrangement of patch potential along the channel walls give an enhanced mixing efficiency downstream of the channel as compared to a symmetric arrangement. Bera and Bhattacharyya [22] studied the combined effect of a non-uniform electric double layer and surface roughness due to the presence of conducting obstacle mounted on the wall by using a free slip model combined with pressure gradient. Recently, Nayak et al. [191] studied mixing efficiency enhancement for a binary fluid in a circular channel with surface potential modulation of channel walls. They showed results for strong as well as for weak electrolyte solutions and obtained a significant mixing enhancement due to heterogeneity in surface charge distribution.

Mixing during flow in micro/nano scale channels can be enhanced by heterogeneous surface potential and/or non- uniform surface geometry. Chang and Yang [43] numerically investigated the combination of these two features in a study of mixing enhancement in electroosmotic flow with rectangular blocks on the channel walls, but they used the PB approach rather than the more appropriate NernstPlanck equations. The current chapter re-examines electroosmotic mixing in the presence of a rectangular block on the channel wall, and patterned surface potential, using the NernstPlanck equations. The authors believe that this has not yet been investigated.

A two dimensional numerical study is conducted for mixing analysis of the steady electroosmotic flow in nano-channels. A non conducting block is mounted on the lower wall of the channel to create heterogeneity inside the domain. To investigate the mixing enhancement, a variation of patterned potential is considered along the upper face of the block. The improvement of mixing efficiency is also studied by considering periodic potential instead of constant potential

in the patterned surface. A mixing-time analysis is performed with the variation of Peclet number for different patterning of the heterogeneous surface. There are thus two objectives of this chapter: (1) to investigate the effect of the imposed electric field and convection on the EOF and (2) to investigate mixing efficiency and mixing time with the variation of block position and patterning of heterogeneous surface on the upper face of the rectangular block.

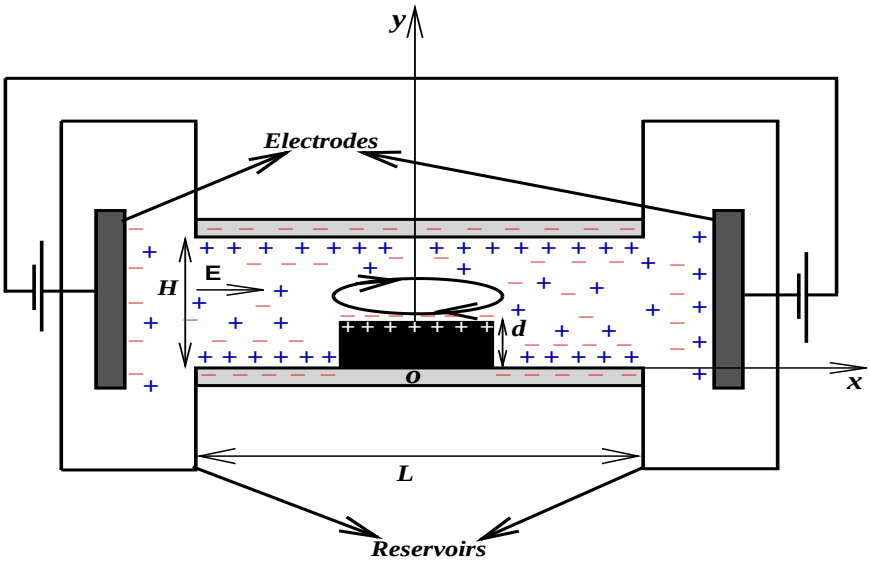

Figure 2.1: Schematic diagram of the flow geometry.

2.2 Physical Configuration

Based on the literature survey, it is predicted that flow mixing can be enhanced by creating a modulation in the channel geometry. In this chapter, our motivation is to study the enhancement of mixing efficiency of two streams of different concentrations in a long channel with a non-conducting block placed on the bottom wall [Fig. 2.1]. Our study is restricted near the block with an extra potential placed in the upper face and the remaining part of the block faces and channel wall possesses an uniform zeta potential. The channel is filled with Newtonian incompressible electrolyte. The configuration is such that the width of the channel is much smaller as compare to its length so that the flow field can be considered as two dimensional. Inside the channel, flow is generated due to the interaction between the electric double layer and the external electric field. The length of the block is taken same as of the height of the channel such that the aspect ratio becomes 1. In the present study the height of the channel is

considered as 20 nm and the height of the block varies between 0.2 to 0.5 times of its height. The uniform external electric field is assumed to vary from 10^4 V/m to 10^6 V/m.

2.3 Mathematical Model

Let us consider a cross section of a rectangular channel of height H and length L filled with an electrolyte solution of uniform permittivity ϵ_e and viscosity μ where an obstacle with length H and height d is placed along the bottom wall of the channel. The imposed electrodes are assumed to be placed at the inlet and outlet of the channel. To formulate the model mathematically, the following assumptions are made:

1. The electrolyte is considered as Newtonian and incompressible fluid.
2. It is assumed that charged species concentrations are so dilute that they do not interact and the diffusion coefficient for both the ions (counter ion and co-ion) are same.
3. Effect of Joule heating is negligible and the species do not interact chemically.
4. The effect of buoyancy and gravity are ignored.

The dimensional electric potential Φ^* is taken as

$$\Phi^*(x^*, y^*) = \phi^*(x^*, y^*) + \psi^*(x^*, y^*), \tag{2.1}$$

where ϕ^* and ψ^* are the induced and external potential respectively. The dimensional electric field $\mathbf{E}^*$ satisfies Maxwell's equation

$$\nabla \times \mathbf{E}^* = \mathbf{0} \tag{2.2}$$

along with the Poisson's equation

$$\nabla \cdot (\epsilon_e \mathbf{E}^*) = -\nabla \cdot \nabla \Phi^* = \rho_e, \tag{2.3}$$

where $\mathbf{E}^* = \left(E_x^*, E_y^*\right)$. Here ϵ_e is the permittivity of the medium and ρ_e is the charge density per unit volume. Permittivity of the medium is defined as, $\epsilon_e = \epsilon_0 \epsilon_r$, where ϵ_0 is the dielectric constant of the solution and ϵ_r is the permittivity of the vacuum.
The charge density is defined by

$$\rho_e = F \Sigma z_i c_i = F c \Sigma z_i X_i, \tag{2.4}$$

where c_i, z_i and X_i are the molar concentration, the valence and the mole fraction of the i^{th} species and c is the total molar concentration; F is the Faraday's constant.
For symmetric monovalent electrolyte solution one has

$$\Sigma_i z_i X_i = (n_1 - n_2). \tag{2.5}$$

Thus, the dimensionless induced potential equation of a symmetric monovalent electrolyte in two dimensions can be written as

$$\epsilon_1^2 \frac{\partial^2 \phi}{\partial x^2} + \frac{\partial^2 \phi}{\partial y^2} = -\frac{\beta}{\epsilon^2}(n_1 - n_2). \tag{2.6}$$

The induced potential is scaled by $\phi_0 = \frac{RT}{F} = 25.6\ mV$. Coordinates (x^*, y^*) are non dimensionalized by (L, H) and ϕ^* by ϕ_0. i.e. $x = \frac{x^*}{L}$, $y = \frac{y^*}{H}$ and $\phi = \frac{\phi^*}{\phi_0}$. $\beta = \frac{c}{I}$ is the ratio of total concentration and the ionic strength (I) of the solution where I is defined as $I = \Sigma_i z_i^2 c_i$. $\epsilon (= \frac{\lambda}{H})$ is the aspect ratio where λ is the Debye length which is defined as $\lambda = \sqrt{\frac{\epsilon_e RT}{IF^2}}$; R is the gas constant and T is the absolute room temperature which is taken here to be 300 K.

The external electric field is created by introducing electrodes in the upstream and downstream locations of the channel. The distribution of the external electric field is obtained by solving the Laplace equation

$$\nabla^2 \psi = 0. \tag{2.7}$$

It is assumed that all walls of the channel and the block are electrically insulated, i.e.$\nabla\psi \cdot \mathbf{n} = 0$, where $\mathbf{n}$ is the unit outward normal to the surface. Far away from the block, i.e. upstream and downstream of the channel, ψ is a linear function of x i.e. $\psi = -\Lambda x$. where $\Lambda = \frac{HE_0}{\phi_0}$ is the dimensionless imposed electric field strength.

The mass transport equation for the i^{th} ionic species for a dilute mixture in vector form is given by

$$\frac{\partial c_i}{\partial t} + \nabla \cdot \mathbf{N}_i^* = 0, \tag{2.8}$$

where $\mathbf{N}_i^*$ is the molar flux which consists of convective, diffusive flux and the flux due to electro-migration effect are related as [33]

$$\mathbf{N}_i^* = -D_i \nabla c_i + c_i \omega_i z_i F \mathbf{E}^* + c_i \mathbf{q}^*, \tag{2.9}$$

where $\mathbf{E} = (E_x, E_y)$ and $\mathbf{q}^*$ is the velocity of the fluid. D_i is the diffusivity and w_i $(= \frac{D_i}{RT})$ is the mobility of the i^{th} species. z_i is the valence of species i (1 for cation and -1 for anion).
Thus, the transport equation for i^{th} species for a steady EOF is written as

$$\nabla \cdot \mathbf{N}_i^* = 0. \tag{2.10}$$

For species i, the non-dimensional ionic transport equation in two dimensional form based on Nernst-Planck approach can be written as

$$\frac{\partial^2 X_i}{\partial y^2} + \epsilon_1^2 \frac{\partial^2 X_i}{\partial x^2} = Pe\left(\epsilon_1 u \frac{\partial X_i}{\partial x} + v\frac{\partial X_i}{\partial y}\right) + \left(\epsilon_1 z_i \frac{\partial (X_i E_x)}{\partial x} + z_i \frac{\partial (X_i E_y)}{\partial y}\right), \tag{2.11}$$

where E_x, E_y are the non-dimensional electric field in x and y direction respectively which can be written as

$$E_x = -\left(\epsilon_1 \frac{\partial \phi}{\partial x} + \epsilon_1 \frac{\partial \psi}{\partial x}\right), \tag{2.12}$$

$$E_y = -\left(\frac{\partial \phi}{\partial y} + \frac{\partial \psi}{\partial y}\right). \tag{2.13}$$

The velocity is scaled by the Helmholtz-Smoluchowski velocity U_{HS}, where $U_{HS} = \frac{\epsilon_e E_0 \Phi_0}{\mu}$. The non-dimensional parameters for EOF are Re (Reynolds number), Sc (Schmidt number), Pe (Peclet number) which are defined as $Re = U_{HS}H/\nu$, $Sc = \frac{\nu}{D_i}$ and $Pe = ReSc$.
The momentum equations in dimensional form for an incompressible Newtonian fluid are given by

$$\rho\left(\frac{\partial \mathbf{q}^*}{\partial t} + (\mathbf{q}^* \cdot \nabla)\mathbf{q}^*\right) = -\nabla p^* + \mu \nabla^2 \mathbf{q}^* + \rho_e \mathbf{E}^*, \tag{2.14}$$

where $\mathbf{q}^* = (u^*, v^*)$. The electrodes are placed at the inlet and outlet of the channel & the width of the channel is considered is of the order of its length. Thus all gradients with respect to z is neglected and the flow is taken as two dimensional.

The non-dimensional forms for the equation of motion of the ionized particles in steady state along with the equation for the induced perturbed potential and the equations for the ion transport for a binary symmetric electrolyte are

$$\epsilon_1 \frac{\partial u}{\partial x} + \frac{\partial v}{\partial y} = 0 \tag{2.15}$$

$$Re\left(\epsilon_1 u \frac{\partial u}{\partial x} + v\frac{\partial u}{\partial y}\right) = -\epsilon_1 \frac{\partial p}{\partial x} + \nabla^2 u - \frac{\beta}{\epsilon^2}\frac{\epsilon_1}{\Lambda}(n_1 - n_2)\left(\frac{\partial \phi}{\partial x} + \frac{\partial \psi}{\partial x}\right) \tag{2.16}$$

$$Re\left(\epsilon_1 u \frac{\partial v}{\partial x} + v\frac{\partial v}{\partial y}\right) = -\frac{\partial p}{\partial y} + \nabla^2 v - \frac{\beta}{\epsilon^2}\frac{1}{\Lambda}(n_1 - n_2)\left(\frac{\partial \phi}{\partial y} + \frac{\partial \psi}{\partial y}\right) \tag{2.17}$$

$$\epsilon_1^2 \frac{\partial^2 \phi}{\partial x^2} + \frac{\partial^2 \phi}{\partial y^2} = -\frac{\beta}{\epsilon^2}(n_1 - n_2) \tag{2.18}$$

$$\left(\epsilon_1^2\frac{\partial^2 n_1}{\partial x^2}+\frac{\partial^2 n_1}{\partial y^2}\right)=\frac{\beta}{\epsilon^2}n_1(n_1-n_2)-\left(\epsilon_1^2\frac{\partial\phi}{\partial x}\frac{\partial n_1}{\partial x}+\frac{\partial\phi}{\partial y}\frac{\partial n_1}{\partial y}\right)-\left(\epsilon_1^2\frac{\partial\psi}{\partial x}\frac{\partial n_1}{\partial x}+\frac{\partial\psi}{\partial y}\frac{\partial n_1}{\partial y}\right)+Pe\left(\epsilon_1 u\frac{\partial n_1}{\partial x}+v\frac{\partial n_1}{\partial y}\right) \tag{2.19}$$

$$\left(\epsilon_1^2\frac{\partial^2 n_2}{\partial x^2}+\frac{\partial^2 n_2}{\partial y^2}\right)=-\frac{\beta}{\epsilon^2}n_2(n_1-n_2)+\left(\epsilon_1^2\frac{\partial\phi}{\partial x}\frac{\partial n_2}{\partial x}+\frac{\partial\phi}{\partial y}\frac{\partial n_2}{\partial y}\right)+\left(\epsilon_1^2\frac{\partial\psi}{\partial x}\frac{\partial n_2}{\partial x}+\frac{\partial\psi}{\partial y}\frac{\partial n_2}{\partial y}\right)+Pe\left(\epsilon_1 u\frac{\partial n_2}{\partial x}+v\frac{\partial n_2}{\partial y}\right) \tag{2.20}$$

Here $p=\frac{p^*}{\mu U_{HS}/H}$ is dimensionless pressure and $\nabla^2=\epsilon_1^2\frac{\partial^2}{\partial x^2}+\frac{\partial^2}{\partial y^2}$. n_1 and n_2 are mole fractions for cation and anion species respectively. The velocity field is coupled with the mass transfer and the induced potential equations.

The flow is assumed to be fully developed at far away from the block. Along the solid walls no slip conditions are used for the velocity components. We can either specify the ion concentrations or the flux at the surface walls for mole fractions. The fixed wall mole fractions are obtained under the assumption that the average electrochemical potential in the channel is the same as that in the reservoir. Zheng et al. [292] described the procedure to obtain wall mole fractions from the electrochemical equilibrium requirements. The boundary conditions are given by [189]:

At far upstream (x=-L/2) of the channel is taken as

$$u=u^{\text{in}};\quad v=0;\quad \phi=\phi^{\text{in}};\quad n_1=n_1^{\text{in}};\quad n_2=n_2^{\text{in}};\quad \frac{\partial p}{\partial x}=0. \tag{2.21}$$

At far downstream (x=L/2) we consider Neumann's conditions as

$$\frac{\partial u}{\partial x}=0;\quad \frac{\partial v}{\partial x}=0;\quad \frac{\partial\phi}{\partial x}=0;\quad \frac{\partial n_1}{\partial x}=0;\quad \frac{\partial n_2}{\partial x}=0;\quad \frac{\partial p}{\partial x}=0. \tag{2.22}$$

The boundary condition along the channel walls (y=0 and y=1) can be taken as

$$u=v=0;\quad \phi=0;\quad n_1=n_1^0;\quad n_2=n_2^0. \tag{2.23}$$

Along the upper face of the block ($-0.5\le \text{x}\le 0.5$, $y=d/H$) the boundary condition is

$$u=v=0;\quad \phi=\phi_p;\quad n_1=n_{1_p};\quad n_2=n_{2_p}. \tag{2.24}$$

The values for u^{in}, ϕ^{in}, n_1^{in}, n_2^{in} are due to the fully developed EOF.

The non-dimensional patch potential along the upper face of the obstacle is denoted by ϕ_p. On the upper portion of the obstacle the potential & mole-fractions are assumed to be $\phi=\phi_p$, $n_{1_p}=n_1^0e^{\phi_p}$ and $n_{2_p}=n_2^0e^{-\phi_p}$ which satisfies the electrochemical equilibrium condition of the potential.

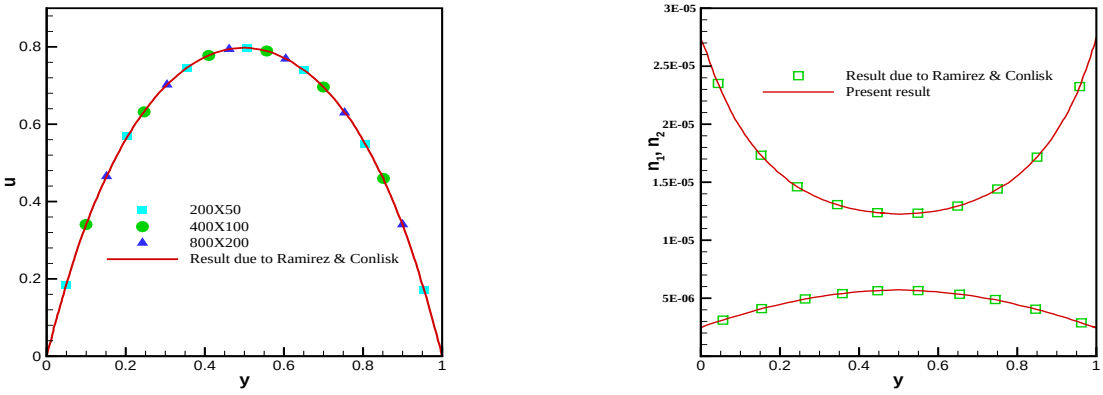

(a) (b)

Figure 2.2: Comparison of (a) Streamwise velocity component in fully developed region for various grid sizes from 200×50 to 800×200, (b) Mole fractions distribution due to Ramirez and Conlisk [220]. Here $n_1^0 = 0.154\ M$, $n_2^0 = 0.0141\ M$, $H = 50\ nm$ and $E_0 = 1.7143\ V/m$.

2.3.1 Mass Transport Equation

The transport of an uncharged species has been considered to analyze the mixing efficiency. The non-dimensional species transport equation due to the combined effect of convective and diffusive flux is

$$\frac{\partial C}{\partial t} + (\mathbf{q} \cdot \nabla)C = \frac{1}{Pe_s}\nabla^2 C, \tag{2.25}$$

where C is the dimensionless species concentration scaled by reference concentration C_{ref}. Non-dimensional time t is scaled by diffusion time scale $\frac{H^2}{D_s}$. For species transport, a constant species concentration is considered along the inlet and no flux condition along walls (channel walls and walls of the block) are assumed. Thus the boundary conditions for species transport are:
along upstream:

$$C = C_{in} \tag{2.26}$$

along downstream:

$$\frac{\partial C}{\partial x} = 0 \tag{2.27}$$

along walls:

$$\nabla C \cdot \mathbf{n} = 0 \tag{2.28}$$

where $\mathbf{n}$ is the unit outward normal along the surface. Here $C_{in} = 1$ on lower half of the channel inlet ($x = -L/2, \quad 0 \leq \mathrm{y} \leq 0.5$) and $C_{in} = 0$ on the upper half of the inlet ($x = -L/2, \ 0.5 \leq \mathrm{y} \leq 1$).

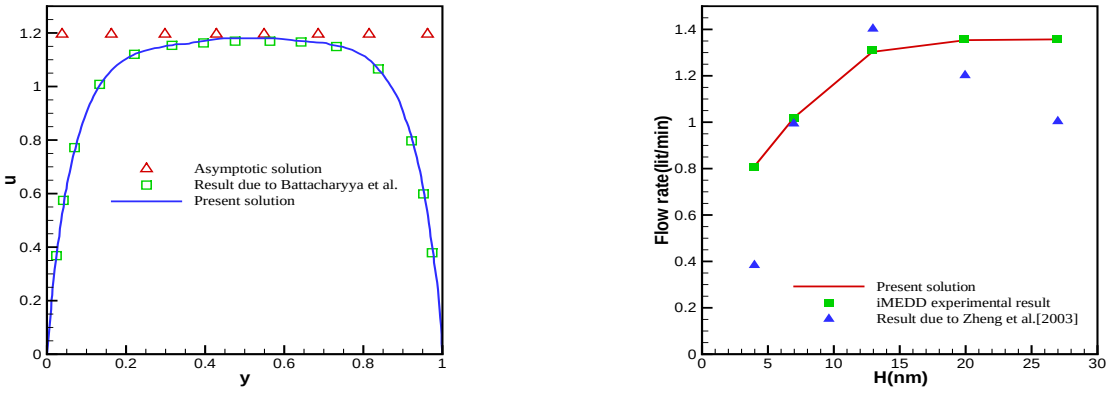

(a) (b)

Figure 2.3: Comparison of (a) present solution with the asymptotic solution and the solution due to Bhattacharyya et al. [26] in the fully developed region when $n_1^0 = 0.154\ M$, $n_2^0 = 0.0141\ M$, $H = 20\ nm$ and $E_0 = 1.7143\ V/m$. (b) Effective volume flow rate for different channel heights with the result due to Zheng et al. [292].

2.4 Numerical Method

The coupled nonlinear system of equations for mass transfer, fluid flow and potential distribution has been solved through finite volume approach using staggered grids. On a staggered grid, the scalar variables are stored in the cell centers and velocity & momentum variables are located at the cell faces. Equations are discretised by integrating the governing equations over different control volumes for scalers and vector quantities. A first order implicit scheme is used to discretise the time derivatives. To cope with the nonlinear terms in the governing equations, Newton's linearization technique is used. Numerical method adopted here is similar to the method described in Chapter 1 (Section 1.8). In contrast to the previous algorithm, here we have used an upwind discretization for the convection and electro-migration terms in momentum and ion transport equations. This upwind discretization imparts stability to the numerical scheme when the electro-migration and convection terms in the ion transport equations are significant. This makes the solver second order accurate in space variables. The discretized equations are solved through the pressure-correction based iterative SIMPLE (Semi Implicit Method for Pressure Linked Equation) algorithm. In every time step of the cyclic procedure Poisson's equation for pressure correction is solved through the SOR (Successive Over Relaxation) technique. The pressure field is corrected to justify the validation of velocity correction in the continuity equation. This cyclic procedure is repeated until the residuals are less than a certain tolerance, $max_{i,j}\ |\Theta_{i,j}^{n+1} - \Theta_{i,j}^{n}| < \Delta$, where $\Theta = (u, v, n_1, n_2, \phi)$, $\Delta = 10^{-6}$, n represents the iteration level and i, j denotes the computational grid points.

2.4.1 Code Validation

The results for axial velocity and mole-fractions are compared with the existing literature to validate our numerical algorithm. A grid independent test is performed for the velocity by taking different grids (200×50, 400×100, 800×200) and compare our result with the result of Ramirez and Conlisk [220]. Fig. 2.2(a) shows the grid independent co-relations where the optimum grid size is obtained at 400×100 and the error of approximation for the grid sizes is found to be 0.5%. To validate our numerical scheme, we have compared our result for streamwise velocity with the numerical solution obtained by Bhattacharyya et al. (Fig. 2.3(a)). The computed numerical solution for the streamwise velocity far away from the obstacle agrees well with the asymptotic solution $\frac{1}{2}\ln\left(\frac{n_1^0}{n_2^0}\right)$ obtained by Bhattacharyya et al. [26]. The comparison of the mole fractions with the result of Ramirez and Conlisk [220] is presented in Fig. 2.2(b). The present result agrees with the existing result very well with an error less than 0.05%. The axial flow rate of EOF is computed in a plane channel for different channel height (Fig. 2.3(b)) and validated with the results obtained by Zheng et al. [292]. The result for flow rate obtained from this model agrees 99% with the experimental observation by Zheng et al. [292].

2.5 Results and Discussions

In this section, simulated results are presented to investigate the combined effect of external electric field, block height and strength of patch potential on flow characteristics within a nano-channel. Since the Reynolds number is very low for such a small channel, the mixing between two species is dominated by diffusion and very poor mixing is allowed in small length unless a mixing enhancement technique is applied. The aim of the present study is to investigate how mixing performance can be enhanced within a nano-channel of fixed length by introducing a nonconducting block in the lower wall with non-homogeneous surface potential. The influence of an external electric field for improving the mixing efficiency under the surface potential heterogeneity is an another aspect of the present study.

In this chapter, concentrated mixture of solute NaCl and solvent water is taken as electrolyte solution. The wall concentration is considered to be $[Na^+] = 0.105\ M$, $[Cl^-] = 0.095\ M$ and water of 55.6 M which corresponds to an EDL thickness of 1 nm. For a channel height of 20 nm the value of Knudsen number [184] which is the ratio between molecular diameter and characteristic length is 0.06 [26] which ensures the applicability of continuum mechanics. We restrict our study on putting a single overpotential patch attached along the upper surface of the block. The wall concentration distribution on the upper face of the block is obtained by the

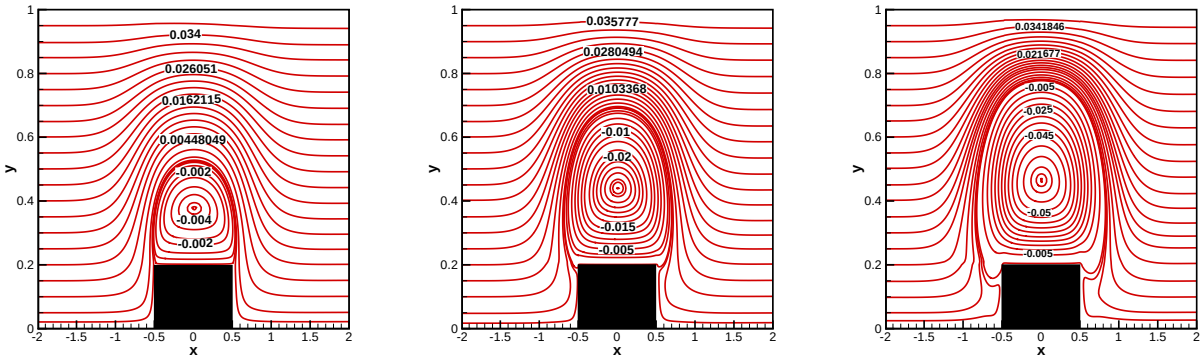

(a) (b) (c)

Figure 2.4: Streamlines for different strength of the patch potential (a)$\phi_p = 0.2$, (b)$\phi_p = 0.5$, (c)$\phi_p = 1.0$ with $d = 0.2$, $n_1^0 = 0.105\ M$, $n_2^0 = 0.095\ M$ and $\epsilon = 0.05$.

relations $n_{1_p} = n_1^0 e^{\phi_p}$ and $n_{2_p} = n_2^0 e^{\phi_p}$, where ϕ_p is the strength of the patch potential. Other key parameters used in the computations are: dielectric constant of the medium is 78.54, viscosity $\mu = 10^{-3}$ kg/(ms), density $\rho = 1000\ kg/m^3$, temperature as 300 K. The external electric field is varying between $10^4\ V/m$ to $10^6\ V/m$ with the overpotential patch ranges from 0.2 to 1.0. Diffusivity (D) of the cation and anion species is taken as $10^{-9}\ m^2/s$. The characteristic velocity (U_{HS}) for electroosmotic flow is obtained from the Helmholtz-Smoluchowski velocity condition as, $U_{HS} = \frac{\epsilon_e \phi_0 E_0}{\mu}$ which corresponds to 0.018 m/s for an electric field $10^6\ V/m$. The corresponding Reynolds number ($Re = \frac{\rho U_{HS} H}{\mu}$) and non dimensional electric field ($\Lambda = \frac{E_0 H}{\phi_0}$) are $Re = 0.00036$ and $\Lambda = 0.77$ respectively for a channel height of 20 nm. The Peclet number (Pe) for cation and anion species is 0.36. The reference potential ϕ_0 ($= \frac{RT}{F}$) is assumed to be 25.6 mV. The diffusivity of the eluted species (D_s) is considered as $0.5 \times 10^{-10}\ m^2/s$ which corresponds to the Peclet number (Pe_s) 7.2. The concentration contours are plotted in time, when the eluted species reaches the outlet, travelling from the inlet completing the total mixing time i.e. $t = 30$ (30,000 iterations $\times 0.001(\Delta t)$) in non-dimensional form for $\phi_p = 0.2$. In this case for H=20 nm, the diffusion time scale is $H^2/D_s = 8 \times 10^{-6} s$.

2.5.1 Dynamic Field

We present the streamline pattern to describe the flow field along the channel for different patch potential strengths 0.2, 0.5 and 1.0 in Fig. 2.4. It is observed from the streamline pattern that far away from the obstacles the flow is fully developed and the streamlines follow horizontal parallel lines. Above the block, the flow lines form a recirculation zone due to nonhomogeneous surface potential distribution. The size of the vortex above the block expands in size as the

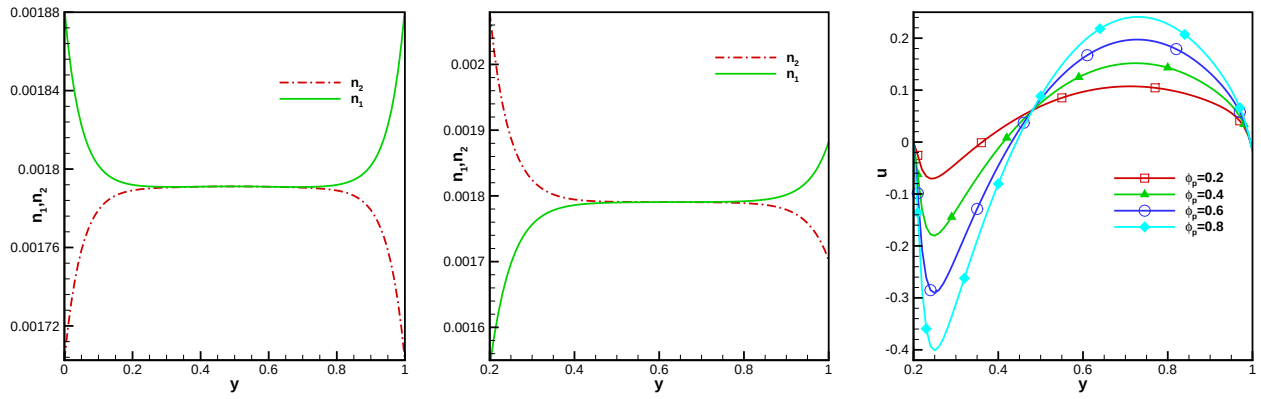

(a) (b) (c)

Figure 2.5: Mole fraction distributions (a) far away from the block, (b) above the block for a fixed $\phi_p = 0.2$ and (c) u-velocity distribution above the block for different values of ϕ_p. Here $n_1^0 = 0.105\ M$, $n_2^0 = 0.095\ M$, $d = 0.2$ and $\epsilon = 0.05$.

patch potential strength increases and thus the bulk flow follows more tortuous pattern while passing the block for higher value of ϕ_p. The height of the vortex center over the block is observed to be increased by 14%, when the patch strength is increased from 0.2 to 1.0 (Fig. 2.4 (c)). Distribution of mole fractions at far upstream and downstream and above the block are presented in Fig. 2.5 (a) and (b) respectively. It is clear from Fig. 2.5(a) that far away from the region of the surface non-homogeneity, the mole fraction distributions follows the Poisson-Boltzmann's distribution with symmetrical distribution of ions. When the bulk flow comes near the patch, embedded on the block, the bulk region shows a flow variation and is no longer symmetric (Fig. 2.5 (b)) which follows the Gouy-Chapman model. Fig. 2.5(c) shows the velocity distribution above the block for various patch strength. It can be seen that above the block, a negative velocity is developed which varies proportionally with the patch potential strength. The centerline distributions of pressure, streamwise velocity and transverse velocity are presented in Fig. 2.6 (a), (b), (c) respectively. It it observed that the pressure gradient increases with increasing ϕ_p and thus u and v-velocity also increase accordingly. For a particular channel height, it is observed that the pressure variation is very high at the outlet region when the strength of the patch potential is varied from 0.2 to 0.8 (Fig. 2.6 (a)). All the earlier studies show that pressure variation is very small with the variation of channel height of surface mounted heterogeneities. In this study the significant difference in pressure is observed due to the geometric modulation along with the surface heterogeneity. Fig. 2.6 (b) presents the axial velocity variation and found to be maximum for $\phi_p = 0.8$ above the heterogenous region. This velocity variation is achieved due to the pressure gradient which is created by the influence of

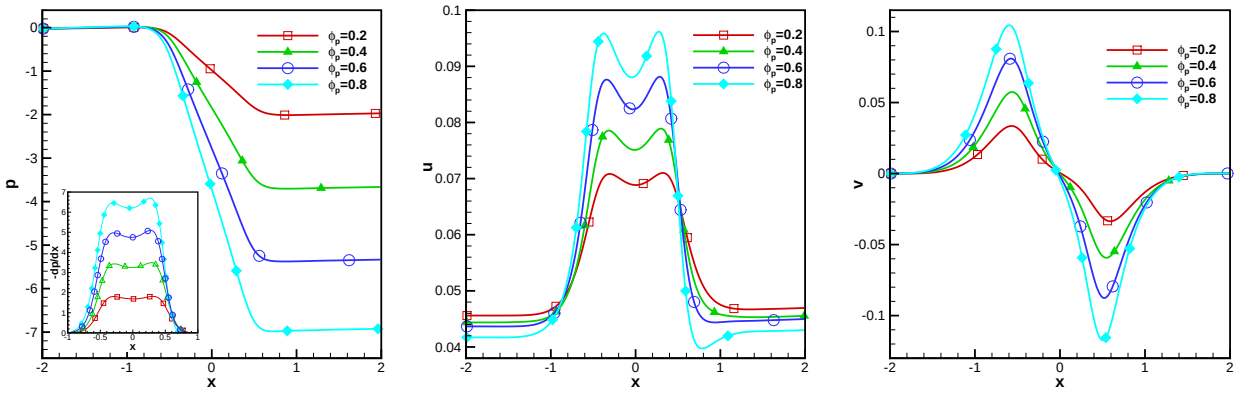

(a) (b) (c)

Figure 2.6: Centerline distribution of (a) pressure and pressure gradient, (b) u-velocity and (c) v-velocity for variation of patch potential with $d = 0.2$, $\Lambda = 0.77$, $n_1^0 = 0.105\ M$, $n_2^0 = 0.095\ M$, and $\epsilon = 0.05$.

block embedded patch potential. The transverse velocity shows a Lamb vortex profile when the flow passes over the block (Fig. 2.6 (c)). Usually, the convective effect is found to be negligible in case of low Reynolds number flows. But the v-velocity variation proves a steady convection generated effect which may be a major contributing factor for mixing.

The momentum in fluid is enhanced by the movement of ions due to external electric field and viscous effects. The driving effects in the mass transfer equation in dimensional form along the x-direction can be represented as

$$\frac{\rho_i \overrightarrow{u_i}}{c} = -D_i \nabla X_i + \frac{D_i}{RT} z_i F X_i E_x + X_i \mathbf{q}. \tag{2.29}$$

Using the non-dimensional variables, the velocity components for the i^{th} species take the form

$$u_i = -\frac{1}{PeX_i}\frac{\partial X_i}{\partial x}\epsilon_1 + \frac{1}{Pe} z_i \left(\Lambda - \epsilon_1 \frac{\partial \phi}{\partial x}\right) + u, \tag{2.30}$$

$$v_i = -\frac{1}{PeX_i}\frac{\partial X_i}{\partial y} - \frac{1}{Pe} z_i \frac{\partial \phi}{\partial y} + v, \tag{2.31}$$

where i stands for cation or anion. For a channel height of 20 nm, the values of the parameters Λ and Pe correspond to 0.77 and 0.36 respectively. The EDL's are thin corresponding to the electrolyte taken here and thus the dimensionless bulk velocity reaches the asymptotic solution which corresponds to 0.050. Hence, in the bulk region the streamwise velocity of the cations is constant and $u_{\text{cation}} = 2.16$. This indicates that the cations move in the same direction of the bulk flow with much higher velocity. The dimensionless streamwise velocity of anions is

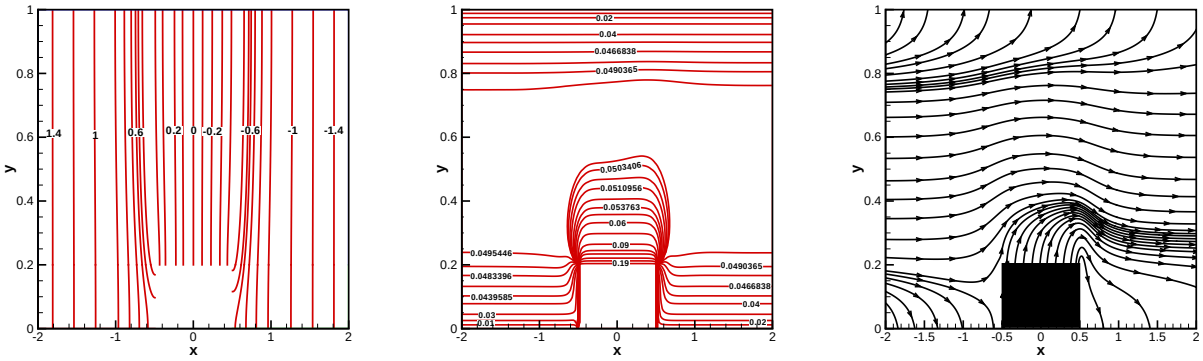

(a) (b) (c)

Figure 2.7: Distribution of (a) external electric potential, (b) induced potential and (c) total electric field lines for $\phi_p = 0.2$, $d = 0.2$, $n_1^0 = 0.105\ M$, $n_2^0 = 0.095\ M$, $\Lambda = 0.77$ and $\epsilon = 0.05$.

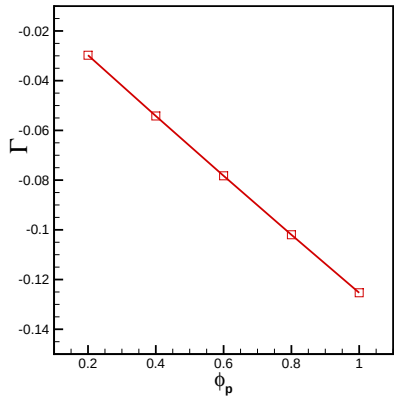

Figure 2.8: circulation strength variation with different patch potentials for $d = 0.2$, $n_1^0 = 0.105\ M$, $n_2^0 = 0.095\ M$, and $\epsilon = 0.05$.

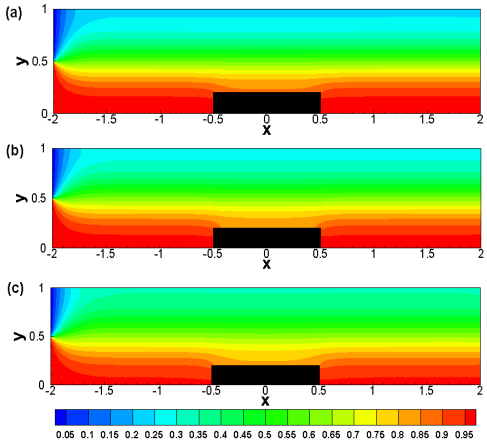

Figure 2.9: Concentration contour for different patch potentials (a)$\phi_p = 0.2$, (b)$\phi_p = 0.5$ and (c)$\phi_p = 1.0$. Here $d = 0.2$, $n_1^0 = 0.105\ M$, $n_2^0 = 0.095\ M$, and $\epsilon = 0.05$.

$u_{\text{anion}} = -2.16$ in the bulk, so the anions move in the opposite direction to the cations and the bulk flow.

Fig. 2.7 (a) and (b) show the electric potential distribution for external applied electric field and induced electric potential respectively inside the channel. From Fig. 2.7 (a) it is observed that the applied electric potential distribution possesses a classical profile as discussed by several authors [27,43]. Due to the Neumann's boundary conditions, ψ achieves a transversed component near the block which shows expansion and contraction in potential lines. The total electric field lines are obtained by the combined contribution of applied potential and induced

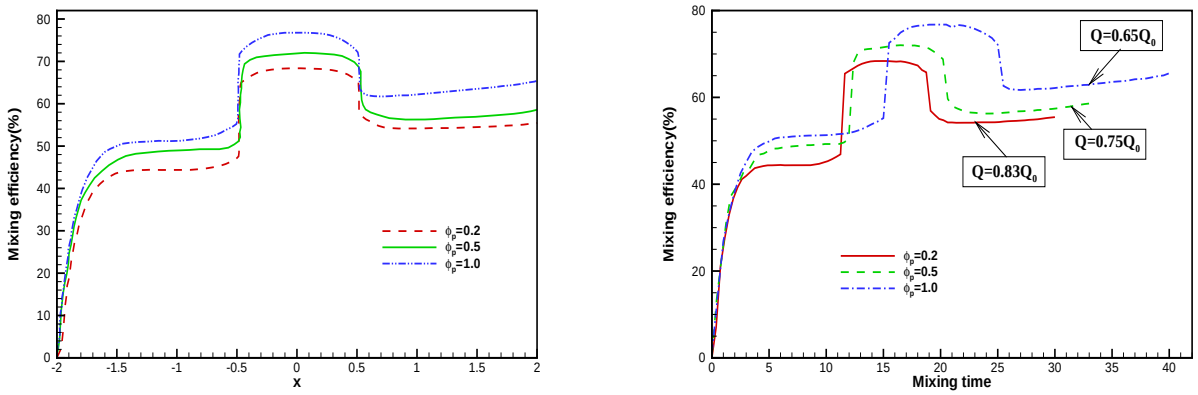

(a) (b)

Figure 2.10: Effect of patch potential on species mixing. (a) Mixing efficiency variation along channel length, (b) Variation of mixing efficiency with mixing time, where Q and Q_0 represent the average flow rate for present configuration and for plane channel with a unpolarized block with uniform zeta potential along the channel walls, where $d = 0.2$, $n_1^0 = 0.105\ M$, $n_2^0 = 0.095\ M$, and $\epsilon = 0.05$.

potential. The total electric field lines are obtained by the solution of

$$\frac{dy}{dx} = \frac{E_y}{E_x}. \tag{2.32}$$

The induced electric field lines are directed from the patch to the walls and the external field lines are from the upstream to the downstream of the channel. The combined effect of these two electric fields is observed from Fig. 2.7 (c).

2.5.2 Effect of Patch Potential Strength

In this section, the mixing enhancement is included by creating potential non homogeneity on the upper face of the embedded block of fixed height. Under the action of electric field, the fluid in the heterogeneous region moves in the opposite direction to that of the rest of the channel. Thus a recirculating zone above the block is created due to this opposite movement of streams. The mixing efficiency is mostly enhanced due to two integrating factors: (a) improved dispersive flux, (b) less volume flow rate i.e. prolonged mixing time. To establish the relationship between patch strength with the flow variables, the vortex strength is measured. The recirculation vortex strength is measured by the circulation (Γ), which is defined as

$$\Gamma = \int\int \omega dx dy \tag{2.33}$$

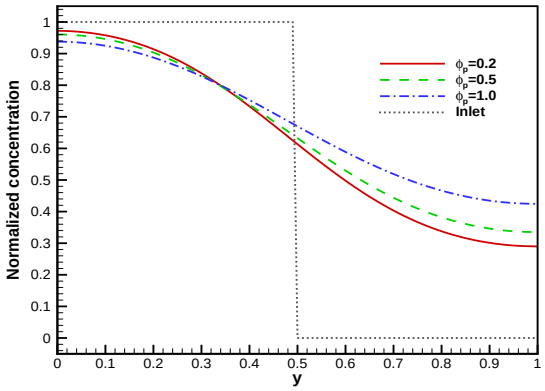

Figure 2.11: Species concentration distribution in the inlet and outlet regions for different patch potentials.

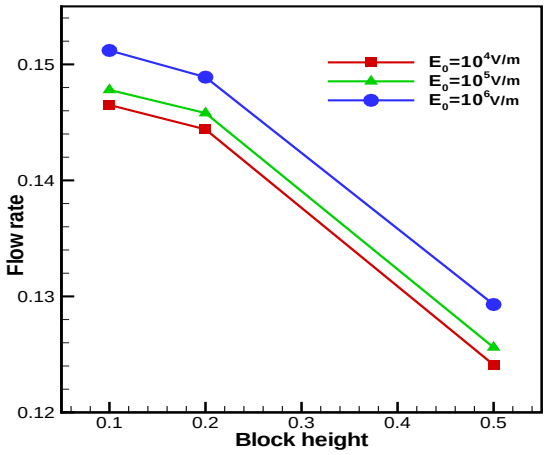

Figure 2.12: Flow rate distribution as a function of block height and E_0 when $\phi_p = 0.2$, $n_1^0 = 0.105M$, $n_2^0 = 0.095M$ and $\epsilon = 0.05$.

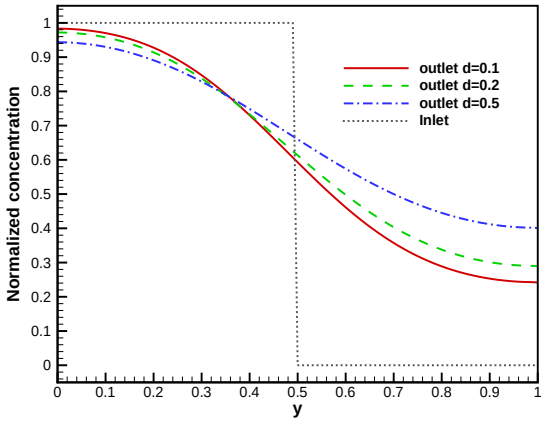

Figure 2.13: Downstream concentration profile for different block heights with $\phi_p = 0.2$, $n_1^0 = 0.105\ M$, $n_2^0 = 0.095\ M$ and $\epsilon = 0.05$.

where $\omega = \epsilon_1 \frac{\partial v}{\partial x} - \frac{\partial u}{\partial y}$ is the dimensional vorticity which is scaled by $\omega_0 = \frac{\epsilon_e RTE_0}{\mu FH}$. Circulation strength increases as vorticity increases. Fig. 2.8 shows that the dimensionless circulation increases linearly with the strength of the patch potential. As the vortex size expands in size, more circulation strength is caused for larger values of non-dimensional patch potential strength. When samples flow through the block embedded channel, the contact area between two streams increases and this contact area is getting enhanced with larger eddy size over the block. In addition, the average flow rate is observed to be decreased as the magnitude of patch potential increases. Thus by increasing the patch strength, the contact area between flow streams is stretched to get a better diffusive flux and a longer diffusive time (i.e. less volume flow rate) to enhance the mixing efficiency along the downstream.

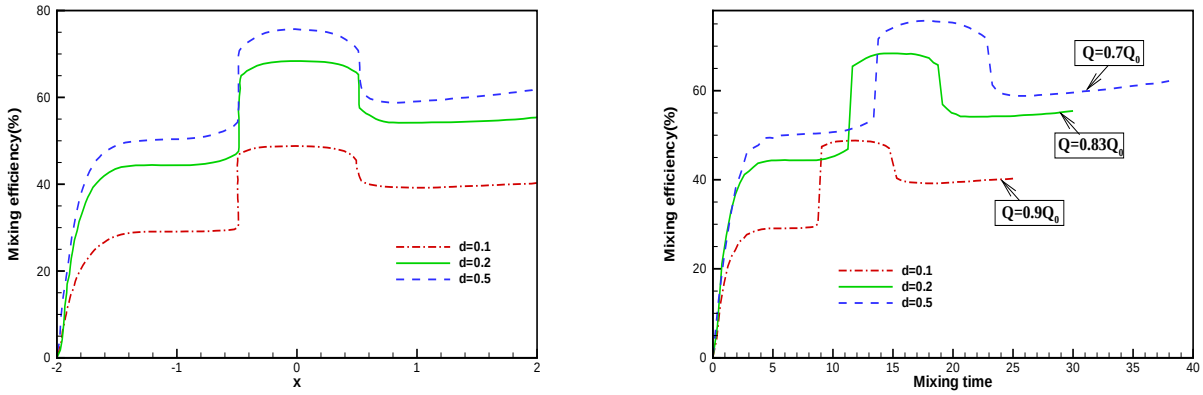

(a) (b)

Figure 2.14: Effect of block height on species mixing. (a)Mixing efficiency variation with channel length (b)Mixing efficiency vs mixing time. Q and Q_0 represent the average flow rate for present configuration and for plane channel with a unpolarized block with uniform zeta potential along the channel walls, where $\phi_p = 0.2$, $n_1^0 = 0.105\ M$, $n_2^0 = 0.095\ M$, and $\epsilon = 0.05$.

To quantify the mixing in a channel, the parameter mixing efficiency (σ) is defined as [84],

$$\sigma = \left[1 - \frac{\int_{lower\ surface}^{upper\ surface} |C - C_\infty| dy}{\int_{lower\ surface}^{upper\ surface} |C_0 - C_\infty| dy}\right] \times 100\% \tag{2.34}$$

where C is the species concentration across the channel. C_0 and C_∞ are the species concentrations in the completely unmixed and completely mixed states respectively. Thus a fully mixed state would have 100% mixing efficiency, while the completely unmixed state would have 0% mixing efficiency. Fig. 2.10 (a) represents the mixing efficiency variation with the increment of patch strength. It is observed that two streams of different concentrations are totally unmixed in the upstream region which leads to 0% mixing and mixing performance is improved in very low rate due to Fick's diffusion. Above the block, the bulk flow is forced to flow through a narrow passage which leads to higher diffusive flux and thus mixing is improved in this region. Due to the expansion of concentration gradient, mixing efficiency drops immediate next to the block, where there exists a comparatively less mixed samples. When the sample stream goes to the outlet region the mixing efficiency curve achieves a little increment due to further diffusion.

Mixing time plays a vital role for enhancement of mixing, when different streams of samples passed through mico/nano channels and mixing efficiency is quantified in terms of volume flow rate [18, 253]. Literature suggests that perfect design of EOF mixture relies on mixing time which can be expressed against the average flow rate. In the present study mixing time, $t(x)$ is considered as a function of distance (x) travelled by the species from the inlet to outlet of the

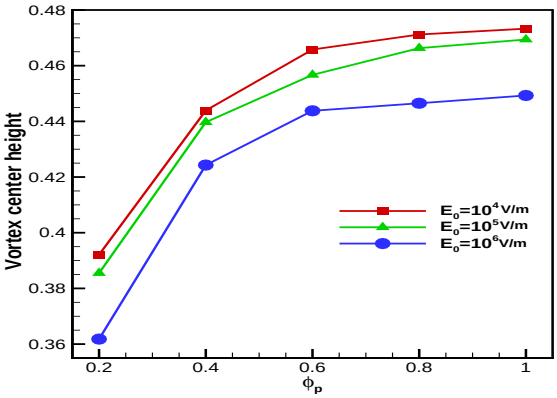

Figure 2.15: Distribution of vortex center height for different block heights and various external external electric field when $d = 0.2$, $n_1^0 = 0.105\ M$, $n_2^0 = 0.095\ M$ and $\epsilon = 0.05$.

channel. Therefore, the total mixing time of a species is the required time to cross the entire channel (from inlet to outlet). Fig. 2.10 (b) presents mixing efficiency variation with mixing time. To obtain perfect mixing of two different samples from the poor mixing, it is observed that the total mixing time is prolonged, since the flow rate is decreasing and requires more time to diffuse in the downstream. It is observed that the downstream species concentration curve gets closer to 0.5 with the increment of ϕ_p to signify homogeneous downstream concentration to achieve better mixing. The mixing efficiency at the downstream of the channel reaches 66% by improving the patch strength up to $\phi_p = 1.0$ (Fig. 2.10 (a, b)). It is observed that quantitative analysis of mixing efficiency with respect to patch potential strength suggest that micro mixtures achieve maximum efficiency with decrease in volume flow rate.

2.5.3 Effect of Block Height

In the previous sections, it is found that increasing patch potential strength enhances circulation strength over the block. The volumetric flow rate is defined as $Q = VA$, where V is the velocity of the flow field and A is the cross section vector area. The total flow rate is obtained by the surface integral

$$Q = \int \int_A V.dA. \tag{2.35}$$

Fig. 2.12 presents the simulated result of flow rate variation for different block heights. It is observed that flow rate is decreasing with the increase of block height for a fixed patch potential and a external electric field. It can be observed that for a fixed electric field strength ($10^6\ V/m$), volume flow rate is decreased by 17% by increasing the block height from 0.1 to 0.5. Decrement of flow rate signifies that the species get more time to diffuse causing more diffusion flux. By

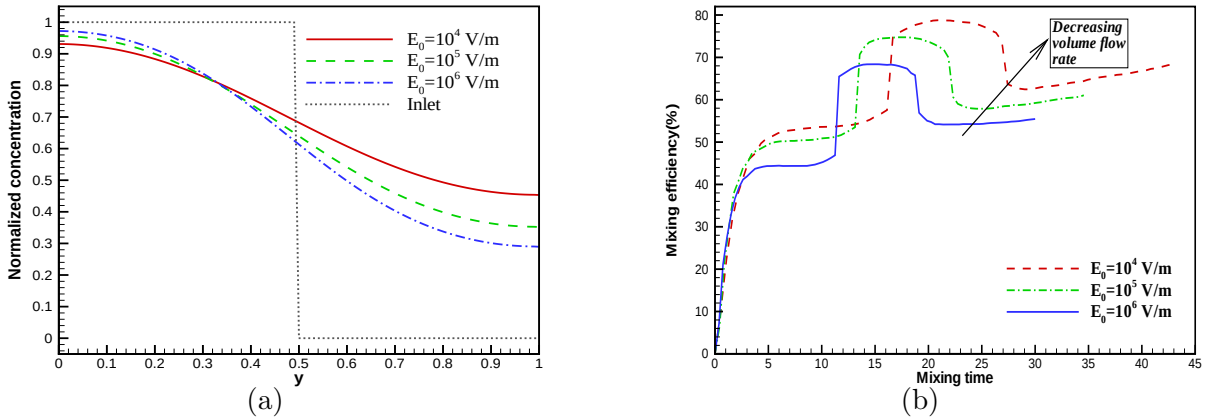

Figure 2.16: (a)Species concentration profile in the inlet and outlet regions and (b) Variation of mixing efficiency with mixing time for different external external electric field. Here $d = 0.2$, $\phi_p = 0.2$, $n_1^0 = 0.105\ M$, $n_2^0 = 0.095\ M$ and $\epsilon = 0.05$.

increasing the height of the block, the total mixing area (A) increases, whereas the passing zone over the barrier reduces which forces the fluid to flow through a comparatively narrow passage which increases the species concentration gradient (∇C) and therefore the product A.∇C is increased i.e. diffusion flux is enhanced significantly which leads to a better mixing. The concentration profiles (Fig. 2.13) along the downstream of the channel signifies that the narrower passage over the block i.e. higher block height leads to more homogeneous species distribution at downstream. Fig. 2.14 (a, b) illustrates the influence of block height variation on mixing efficiency. It is clearly observed that mixing efficiency can be enhanced from 40.1% to 55.45%, with the increase of block height from 0.1 to 0.2. The mixing efficiency can further be improved up to 62.17% by raising the height of the obstacle to 0.5.

2.5.4 Effect of External Electric Field

Fig. 2.12 represents the variation of flow rate with block heights for different electric field strength. The externally applied electric field forces the liquid to flow through the narrow channel. With the increment of external electric field, the flow is less reversed above the patch which results in less vorticity. Thus, for a higher imposed electric field, the size of the vortex over the obstacle is diminished in size and thus corresponds to less circulation. Fig. 2.15 presents that the height of the vortex center is reduced with increasing external field strength for a fixed potential patch. It is clearly observed from Fig. 2.12 that volume flow rate is increasing when the external electric field strength increases. By the variation of electric field strength from $10^4\ V/m$ to $10^6\ V/m$, the volume flow rate is increased up to 4% for a fixed block height

($d = 0.2$). The result shows that, with the decrement of external electric field strength the total mixing time prolongs due to reduced flow rate. The downstream species concentration profile for different external field is presented in Fig. 2.16 (a). It can be observed that as the external electric field strength is increased the downstream concentration profile goes away from the value 0.5, which signifies less homogeneous mixing. The mixing efficiency variation with respect to mixing time for various external electric field strength is represented in Fig. 2.16 (b). It is noticed that mixing efficiency at the downstream of the channel can be improved from 55.45% to 61.05% by reducing the external electric field from 10^6 V/m to 10^5 V/m due to longer retention time. This improvement in mixing can reach 68.4% by further decrement of flow rate by decreasing the electric field to 10^4 V/m.

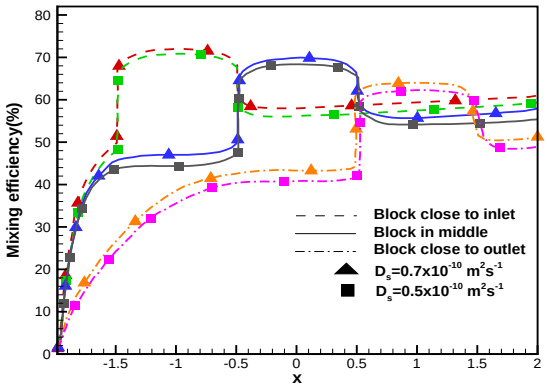

Figure 2.17: Variation of Mixing efficiency with different positioning of the block. The parameters used in the computation are $n_1^0 = 0.105$ M, $n_2^0 = 0.095$ M, $\epsilon = 0.05$ and E_0= 10^6 V/m

2.5.5 Effect of Block Position

Generally, the convection effects are lesser compared to ion diffusion effects for small Peclet number ($Pe < 1$), while convection effects dominate diffusion effect for large Peclet number ($Pe > 1$). Mostly in EOF, hydrodynamic convection is smaller than that of molecular diffusion as typical Re is on the order of 10^{-2} and Sc is smaller than 10^2 and, hence $ReSc$ is smaller than 1. To visualize the convection effects in a clear form we have considered low diffusion coefficient for eluted sample species (suppose DNA, $D_s = 0.5 \times 10^{-10}$ m^2/s), for which the advection time scale ($\tau_a = \frac{H}{U_{HS}}$), diffusion time scale ($\tau_D = \frac{H^2}{D_s}$) and the Peclet number ($\frac{\tau_D}{\tau_a}$) correspond to 1.11×10^{-6} s, 8×10^{-6} s and 7.2 respectively. The species transport is dominated by convection and mainly transport with the flow.

In this section three different positions (near inlet, middle of the channel and near outlet of the channel) of the wall embedded block is considered to make a comparative study of mixing

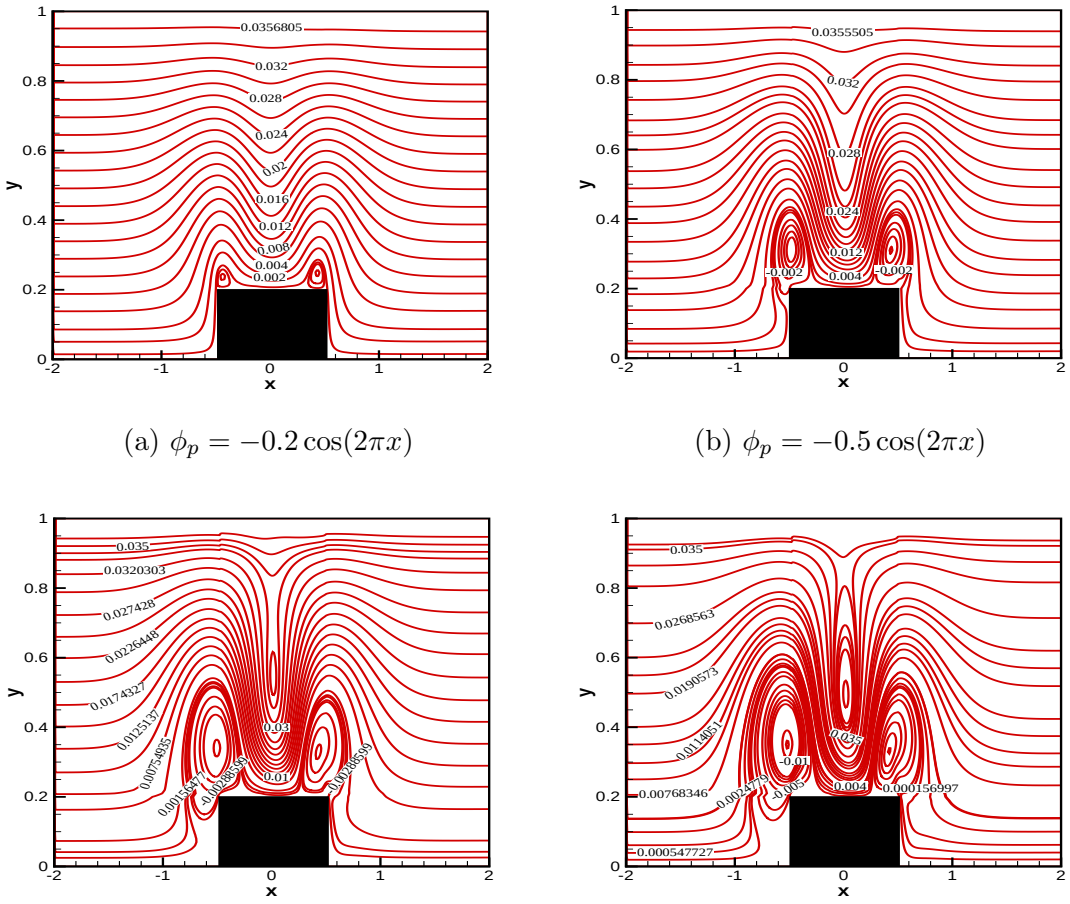

(a) $\phi_p = -0.2\cos(2\pi x)$ (b) $\phi_p = -0.5\cos(2\pi x)$

(c) $\phi_p = -0.8\cos(2\pi x)$ (d) $\phi_p = -1.0\cos(2\pi x)$

Figure 2.18: Streamlines with periodic potential patches for channel height $H = 20\ nm$ when $d = 0.2$, $E_0 = 10^6\ V/m$, $n_1^0 = 0.105\ M$, $n_2^0 = 0.095\ M$, $\epsilon = 0.05$.

enhancement for EOF in a channel of height 20nm. The simulation shows that as a result of the coupling of convection effect due to wall embedded block with overpotential patch, the pressure gradient and the electric body force term, the EOF provides the minimum volume flow rate when the block is placed close to the inlet shown in Fig. 2.17. Moreover, the volume flow rate increases with the distanced positioning of the block from the inlet source i.e. less mixing time is available for complete mixing of the species (Fig. 2.17). Consequently, mixing efficiency in the downstream of the channel is better for the positioning of the block nearer to the channel inlet and there is more time available for species to be mixed. Moreover increasing the diffusive coefficient (D_s) leads to decrease in the diffusion time scale to get smaller Peclet number. In all the above discussions the diffusive coefficient $D_s = 0.5 \times 10^{-10}\ m^2/s$ is considered. In this context, we observed that the mixing efficiency of an eluted species for two different diffusive coefficients $D_s = 0.5 \times 10^{-10}\ m^2/s$ & $D_s = 0.7 \times 10^{-10}\ m^2/s$, the Peclet numbers correspond

to 7.2 and 5.14 respectively. The mixing efficiencies along the downstream of the channel are observed to be 59%, 55.45% and 49% respectively, for tree different locations (close to inlet, middle and close to outlet) of the block for $D_s = 0.5 \times 10^{-10}\ m^2/s$ (i.e.$\tau_D = 8 \times 10^{-6} s$). It is observed from the Fig. 2.17 that, with the decrement of diffusion time scale (keeping the advection time scale fixed) the mixing efficiency increases for each of the three different positioning of the block. For $\tau_D = 5.71 \times 10^{-6}$ i.e. for $D_s = 0.7 \times 10^{-10}\ m^2/s$, the mixing efficiency at the outlet of the channel reach upto 51.25% and 58.95% for block locations close to outlet and middle respectively. In this case the downstream mixing efficiency is observed to be improved upto 61.1% for the configuration in which block is located close to inlet.

2.5.6 Effect of Periodic Patch Potential

In this case the patch potential strength over the block is assumed to have the following form [53]

$$\phi_p = -\phi_a \cos(n\pi x). \tag{2.36}$$

For different values of n and ϕ_a different vortex structures are observed. Streamlines for n=2 and ϕ_a= 0.2, 0.5, 0.8 and 1.0 are shown in Fig. 2.18. Two small negative vortices (clockwise circulation) are found over the block for ϕ_a=0.2 (Fig. 2.18 (a)) and these vortices are increased in size with increasing ϕ_a (Fig. 2.18(b)). For ϕ_a=0.8 a positive vortex is formed between two negative circulations (Fig. 2.18(c)). This positive circulation zone expands in size with further increment of ϕ_a (Fig. 2.18(d)). The sum of the magnitude of the circulation strength is Γ=0.0308 for ϕ_a=0.2, Γ=0.1041 for ϕ_a=0.5, Γ=0.2175 for ϕ_a=0.8 and Γ=0.2947 for ϕ_a=1.0. Thus net circulation over the block is increased with increasing ϕ_a and the increment in circulation enhances the species mixing efficiency. The different flow circulation regions formed above the block can be a further research for mixing enhancement.

2.6 Conclusions

Efficient mixing of species in low Reynolds number regime remains a challenging task in micro/nano fluidic systems. Overcoming these challenges numerous endeavorers intent on introducing supplementary mechanism such as advection to the lengthy diffusion based process. This chapter describes the mixing enhancement due to the presence of a non-conducting block with charged surface mounted on the lower wall of the channel where both convection and diffusion with reduction of mixing time analysis is considered. The external electric field acts as an efficient mixing reagent, since it forces the fluid to pass through a narrow region where convection

effect is maximum, genertates a higher mixing rate along the downstream region. It is also observed that increasing block height together with patch potential strength increases mixing efficiency. However, it is also found that mixing efficiency increases with the use of a periodic potential instead of a constant potential patch, since periodic potential generates stronger vortices. The convection effect is significant for higher Peclet number irrespective of the channel length. It is also noticed that mixing time plays a vital role for enhancement of mixing when two different streams of samples pass through wall modulated block and shows a maximum mixing level, when the block is placed close to inlet.

Chapter 3

Induced Mixing Electrokinetics in a Charged Corrugated Nano-Channel: Towards a Controlled Ionic Transport

3.1 Introduction

Fluid flow and mixing in small channels is an important area of research due to its potential applications ranging from pharmacy, DNA hybridization to cytometric analysis and biochemistry for effective novel mixing processes [175] in passive electrokinetic micromixer. Flow mixing highlights the importance of smooth functioning of highly explosive or exothermic chemical reactions in the fabrication of micro reaction machineries [165]. Experimentally, it is possible to construct fluid systems with feature sizes as small as few microns by using microfabrication technology for application in the 'Lab-on-a-Chip' concept which involves the miniaturization of many chemical processes onto a single silicon chip [221]. These micro systems allow one to manipulate single cells and even single macro molecules and hence microfludic systems are used for analytic tests in biotechnology [38]. Most of the biological applications, such as immunoassay and DNA hybridization [218, 280], require a rapid mixing of reagents but these substances have low diffusion coefficients. Hence, to study the fundamental behavior of fluids in thin channels a rapid process of mixing is required which is a challenge.

Mixing schemes used for rapid mixing in micro and nano channels are classified as; passive mixer and active mixer [255] and the mixer is said to be active when an external source of energy like applied pressure, imposed electric or magnetic field etc. are utilized to drive the flow

and enhance the mixing efficiency. But, the active mixers require some moving parts within channels or due the application of AC-electric field causes additional frictions. Passive mixers use the same energy source but complex geometries (i.e. irregular or asymmetric) to set up secondary flow structures in the fluids to achieve better mixing due to chaotic advection within a short transport distance [25, 27, 120, 137]. However, the major difficulty in passive mixers are found in the design and optimization of manufacture complexity in micro-scale level. In many applications, however above mentioned manufacturability and procedures take advantage for mixing time, they may do not rely on the strain in getting united into microfluidic systems [277].

Mostly, electrokinetic mixing is used in microfluidic devices for concentrated solutions. Fluid motion develope inside micro/nano-channels due to an imposed electric field in EDL which forcees the charged ions to move in the diffused part of the electric double layer (EDL) [225, 260], leads to a EOF [189]. This is an important transport process to pump biological and chemical reagents in micro/nano-channels because the ease with which fluid can be controlled and the flow velocity shows plug like profile with no mechanical driven activities [212]. Moreover, electroosmotic flow mixing is small to low Reynolds number ensures a weak transport of charged ions.

Many passive mixers have been developed in recent years using different types of channel geometry (usually T- or Y-Mixer) generate chaotic advection and increase the interfacial area for circulation [41, 150]. The mixing of different liquids in electroosmotic flows are heavily relied on the channel shape and surface chemistry [205]. It is observed that electrically driven flows and mixing characteristics are mostly effected by the surface potential (ζ-potential), dielectric constant, pH of the solution, ionic strength, and solute molecules close to the walls [77]. However, in many cases, solid surfaces inevitably exhibit certain non-uniform ζ-potential as a result of defects in designs or the absorption of organic materials to the surfaces during fabrication.

If the heterogeneous part of the surface is positively charged, then surplus of negative ions will occur over it and the remained positive ions will move towards the negatively charged wall. The driving force due to imposed electric field along the axial direction provokes a reverse flow close to the non-uniform surface potential/ charge density regions [84, 141, 157, 217]. Erickson and Li [84] numerically observed that the recirculation vortex is stronger when $\zeta-$potential pertains the same value along the heterogeneous surface and negative to that along homogeneous surface. It has also been observed that a sudden change (step jump) of $\zeta-$potential close

to the channel wall creates a change in gradient of pressure and velocity [90]. Some analytical and numerical studies have been preformed for slowly varying micro channel to observe the effect of fluid flow and heat transfer [179, 237–239, 243]. Using lubrication approximation theory, Arcos [12] performed a theoretical study on EOF for a viscoelastic symmetrical $(z:z)$ electrolyte in a microchannel with varying $\zeta-$potential. All of these studies deal with the Poisson-Boltzmann model for the flow analysis and mass transfer phenomena using the Debye-Hückel approximation. Small regions of non-uniform wall potential create a reversed flow above the patch along with a favorable pressure gradient in the electroosmotic flow [54]. Chen and Conlisk [54] used a nonuniform potential patch with different ζ-potential embedded along the lower wall of the channel. They used the Poisson-Nernst-Planck model which can be valid for overlapping EDL fields and core non-neutrality without using the Debye-Hückel approximation. In addition, higher values of external electric field predicts a deviation in electric potential and ion concentration in case of Boltzmann model, and also predicts a weak convection effect.

The interaction of surface roughness and heterogeneity during the electroosmotic flow produces a strong convection effect [45, 116]. The modulation of channel wall can be possible due to the adsorption of other species like micro molecules create an induced pressure gradient. In such cases electroosmotic flow is strongly affected due to the presence of roughness in the surfaces which may change the surface wetted and the flow passage area. Fluid mixing in micro- and nano fluidic devices (μ-TAS) & Bio-MEMS are frequently required in the context of effective mixing capability and cannot be achieved effectively due to low Reynolds number. Campo et al. [40] fabricated the patterned surfaces with pillars in controlled $3D$ tip geometry mimicking bio-attachment devices. The fabrication strategy exploits a filling mechanism of $2D$ lithographic templates, combined with inking and printing steps using elastomeric precursors with various viscosities and cross linking kinetics. Also, Matteucci et al. [173] developed a method for fabrication of multi-level all-polymer chips by means of silicon dry etching, electroplating and injection molding. This method can be used for successful fabrication of microfluidic chips for applications in the fields of electrochemistry, cell trapping and DNA elongation. These chips incorporate channel depths in the range between 100 nm and 100μm and depth to width aspect ratios between 1/200 and 2. Several other fabrication techniques including traditional nano-lithography [82], etching-and-deposition [279], DLP [127], sequentially patterning oxides [61] and packing of different nano-particles [144] have been used to integrate (fabricate) complicated nano-fluidic devices with gradually changing geometry & non-homogenous surface charge polarity.

Up to now, many numerical and experimental studies were conducted based on modulated surfaces with non-uniform surface potential for microfluidic mixing. IN some of our earlier studies [25, 27] we used oscillating electric field, surface mounted block and overpotential regions for mixing enhancement in micro- and nano-channels. The performance of micro fluidic mixing in heterogeneous channels due to overpotential regions depends on the strength of the vortices [189] and the flow velocity effectively increases with the increase of the wall ζ-potential and the external electric field.

An experimental study carried out by Sadr et al. [230], stated that the average EOF velocity is linearly proportional to the driving electric field and the uniform distribution of flow can be possible up to the channel wall and the EDL thickness is much less for a fully developed EOF in a nano-channel. Singh et al. [242] performed an experimental study on EOF to investigate the effect of nano channel diameter and surface charge density on current-voltage characteristics in a nanofluidic transistor. An experimental study for surface roughness in electroosmosis in micro- and nano-channels, carried out by Koga et al. [135] to study EOF mobility which is effected by surface roughness and surface chemistry. The surface roughness of micro and nanofluidic channels were varied from Angstroms (12.2A to 17A) to micrometers (5 μm) and EOF velocity had a intense correlation with the surface roughness, especially when the arithmetic mean of surface roughness was in the order of the thickness of the electric double layer. Experimentally it has been also shown that a geometric modulation can increase the cross sectional region for the liquids to be mixed, used to achieve a faster laminar mixing [44,220,278].

EOF effects due to surface roughness height and cavitations in micro-channels was carried out by Liu and Yang [154] using a FEM simulation for ions distribution based on Boltzmann distribution (PB model) and were unable to predict any flow recirculation. Moreover, it has been found that small block height reduces the flow velocity but regular placement of blocks with the interval length as channel height maximizes the flow velocity. Validation of PB model on EOF was made by Wang et al. [270] both for micro and nano channel.

Mixing enhancement in micro fluidic channels with constrictions under periodic electroosmotic flow was experimentally carried out by Lim et al. [149]. Four types of T-type micro mixer with constrictions were fabricated to study the mixing effects with different amplitude and frequency of the alternating current (AC) electric field. The experimental result suggests

that mixing efficiency can be enhanced by increasing the constriction length. The analysis of ion transport mechanism of a KCl concentrated solution in a gated nanofluidic channel has been modelled by Fuest et al. [91] based on electromigration, considering the local accumulation and depletion of ions and subsequent changes in species concentrations. The fabricated nanochannel enables the similar effect to biological systems while providing throughput and benefits in 1-D analysis. The fabricated device presents the demonstration of current switching in a nanofluidic field effect configuration, with tunable control over both the magnitude and direction of current. The gate electrodes have been patterned and placed asymmetrically to allow investigation of the effect of electrode location on the field effect control and suggested that ionic flux driven by the axial potential through the nanochannel along with high electric fields prevent the formation of an EDL in the electrolyte region immediately below the gate electrode, leaving the gate electrode partially descreened. Xu et al. [281] extended the work of Lim et al. [149] by considering a particular T-type micro mixer for the mixing performance. They developed a mathematical model to evaluate mixing performance by considering one particular dependent variable (frequency) and several independent variables (constriction length, phase difference, direct current (DC) bias). Their results concluded that best mixing performance can be obtained in practical applications when the constriction length is maximum and DC is minimum.

Mixing process in T-type mixers also requires higher channel length as well as lay time depending on the diffusion. Optimal patterning of heterogeneous surface potential can be utilized to furnish vortices or localized circulations to obtain complete mixing [117]. Effect of ionic concentration on EOF and EOF mixing were investigated by Peng and Li [212] through a straight micro-channel. They considered mixing of electrolyte solutions of two streams with dissimilar ionic concentrations inside the channel and found that maximum mixing is observed when a non-uniform electric field and a high velocity gradient is considered.

Effects of surface roughness and electrokinetic heterogeneity on EOF in a micro-channel have been carried out by Masilamani et al. [168]. They investigated the effects of surface heterogeneity on the EOF for different roughness heights, width, roughness interval spacing. Simulated results indicate that induced flow vortices are responsible for the flow and mixing within the micro-channel. A combined pressure driven EOF was performed by Bhattacharyya and Bera [30] to study mixing effects due to surface mounted block and effective pressure gradient. It has been demonstrated that rapid mixing can be achieved by surface modulation and heterogeneity and the performance can be quantified through dispersion of solute.

In most of the micro and nano scale flows thickness of EDL is assumed to be smaller than the channel dimension by employing Boltzmann distribution of ions, which generates Poisson-Boltzmann equation (PB model) for potential. Also, from the previous studies it is observed that the ionic transport depends on the shape of the roughness such as amplitude and length of the walls, since the flow rate decreases. The numerical computation of exact NP model can succeed the difficulties arises in case of PB-model, where core neutrality is required. Since, PB model is questionable when the core of the channel is non-neutral and convection effect is considered with the external electric field.

In all of the previous studies, EOF due to convection diffusion effects have been presented by using the NP model and the PB model. The effect of fluid inertia due to the presence of nonuniform surface potential on EOF in micro- and nano-channels are discussed. It is found that in all of the ongoing works, quantitative analysis of vortex strength and vortical flow dependent parameters are impaired. To the best knowledge of the authors, the mixing effects due to the variation of channel height, ion concentrations, surface potential and wall heterogeneity due to the NP model has not yet been dealt with in literature. The primary goal of the present work is to obtain the flow attributes due to wall heterogeneity using NP model. The wall heterogeneity is created by mounted blocks or blocks with patches and patches along the lower and upper wall of the channel, where the patch and block lengths are on the order of the height of the channel. In the present analysis, to clarify the effects of EOF mixing parameters like, electric field strength, non-uniform charge strength, EDL thickness and ionic concentrations are addressed. The composite solutions such as mixture of multivalent ions can also be easily handled through this model.

The validity of the NP-model with PB-model for a steady EOF is made, where NP-model considers the flexibility about the center line symmetry and low potential restriction. Micro and nanoscale mixing is analyzed through the heterogenous patches and charged blocks in the corrugated channel wall, some are symmetric and some are asymmetric. Since, the EOF velocity and mixing are enhanced when the channel height is increased [126, 188, 241], the channel heights are assumed to vary between 10 nm to 100 nm. The flow is fully developed far away from the heterogeneities and along the axial direction. The study focuses on the flow patterns and electroosmotic effects on the formation of vortical flow in corrugated micro/nano channels in the vicinity of a heterogeneous surfaces. The heterogeneity in corrugated surfaces are created

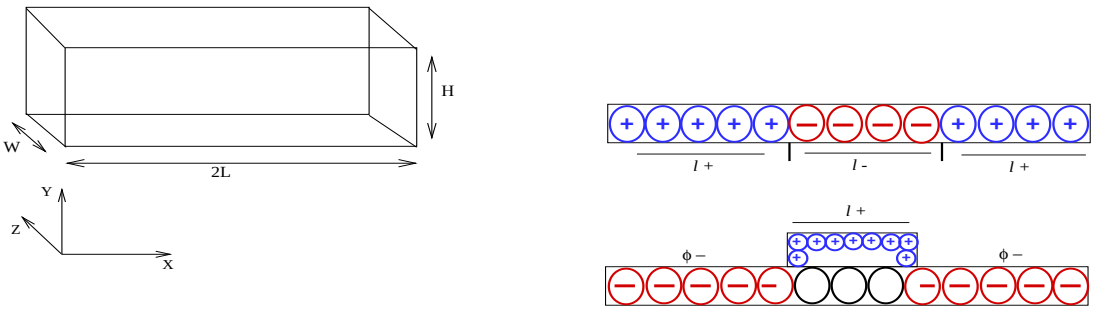

Figure 3.1: Schematic diagram of the nano-channel and computational domain. In the figure the corrugated surfaces along the channel are obtained due to the placement of blocks and patches of length l_+ and l_- ($\sim$ O(H)) along the channel surfaces.

by the geometrical modulation and heterogeneous surface potentials, where potentials can vary both in axial and lateral directions, collectively represents the characteristic equations for fluid flow, induced potential and ion distributions. The flow patterns for corrugated micro/nano-channel are obtained both analytically and numerically using the coupled equation of Poisson, Nernst-Planck, and the Navier-Stokes simultaneously. This provides an opportunity to visualize the complex flow characteristics on micro/nano scale species transport for flow control in microfluidics.

In the continuation of this work further studies will be carried out for increment of micro mixing enhancement incase of weak and strong electrolytes for different physical quantities. With these approaches, in the first phase, governing equations based on Fick's law of diffusion with NP approach coupled with Poisson equation is developed. Both analytical and numerical aspects of the solution algorithm is developed and stability analysis is made and compared with PB-model solutions. A description of the channel height, ionic strength, induced streaming potential and surface heterogeneity on micro mixing are made successively.

3.2 Electroosmotic Nano-Channel System and Governing Equations

For the mathematical modelling, the steady laminar electroosmotic fluid flow of an incompressible Newtonian electrolyte circulating through a long flat parallel plates channel of length $2L$,

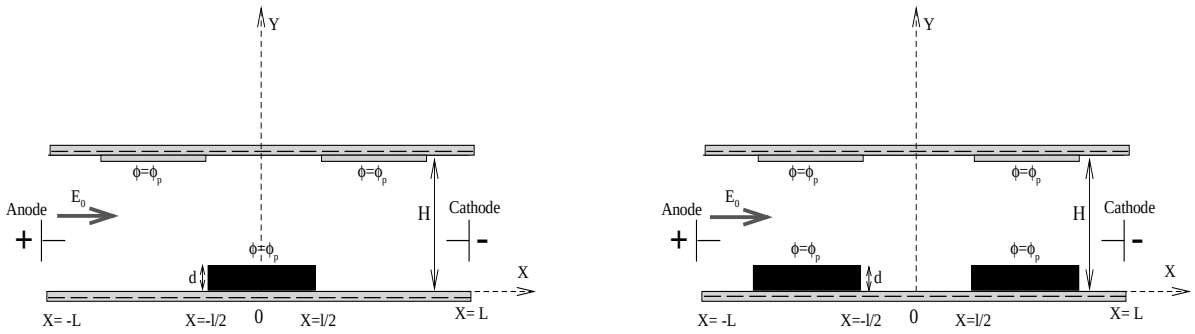

(a) Case(I) (b) Case(II)

Figure 3.2: Schematic of the computational domain due to corrugated surfaces. Case (I) adaptation of blocks, Case (II) setting of block with patches.

width W and height H is considered. The channel height H is comparable with the electric double layer (EDL) thickness with $H \ll L, W$. The system is filled with a fluid composed of a mixture of water and an electrolyte buffer with n-species with permittivity ϵ_e and viscosity μ respectively. The length, height and width are in the x-, y- and z-directions and electrodes are placed at inlet and outlet of the channel, where external electric field is applied along the x-axis of the channel (see Fig. 3.1).

We have already discussed that species concentration distribution will not follow Boltzmann distribution in the edges of the patch and the surface modification can be effected by an initial reaction with a coupling reagent that will modify the surface potential [54]. The surface heterogeneity has been created by putting blocks of height d and length l, block with patch and stepwise surface potential of length l on to the channel walls, shown in Fig. 3.2.

3.2.1 Electric Potential Distribution

The imposed dimensional electric field [189], $\mathbf{E}^* = (E_x^*, E_y^*, E_z^*)$ satisfying the Maxwell's equations, $\mathbf{E}^* = -\nabla\Phi^*$ is governed by the following relation:

$$\nabla \cdot (\epsilon_e \mathbf{E}^*) = \rho_e. \tag{3.1}$$

Here, ρ_e is the charge density per unit volume which is defined as, $\rho_e = F\sum_i z_i c_i = Fc\sum_i z_i X_i$. The electric potential, total molar concentration and molarity of ionic species i are defined by Φ^* , c and c_i, respectively. z_i and $X_i = c_i/c$ are the valency and mole fraction of species i,

where F is Faraday's constant. The dimensional potential Φ^* can be written as $\Phi^*(x,y,z)= \psi^*(x,y,z) + \phi^*(x,y,z)$, where ϕ^* and ψ^* are the induced and external potential respectively. Non-dimensional induced potential equation, for the Eq. (3.1) is

$$\frac{\partial^2\phi}{\partial y^2} + \epsilon_1^2\frac{\partial^2\phi}{\partial x^2} + \epsilon_2^2\frac{\partial^2\phi}{\partial z^2} = -\frac{\beta}{A^2}\sum_i z_i X_i. \tag{3.2}$$

The potential is scaled as, $\phi = \phi^*/\phi_0$ and ϕ_0 is defined as $RT/F(= K_BT/e)$. R is the gas constant, T is a reference temperature of the solution (taken as 300K), K_B is the Boltzmann constant, e is the elementary electric charge. The coordinates are scaled by (L, H, W), i.e. $x = \frac{x^*}{L}, y = \frac{y^*}{H}, z = \frac{z^*}{W}$. Here $\epsilon_1 = H/L$, $\epsilon_2 = H/W$, $A = \lambda/H$ and $\beta = c/I$.

For a symmetric monovalent electrolyte, $z_i = \pm 1$, and hence, $\sum_i z_i X_i = n_1 - n_2$. Thus the final representation of induced potential is of the form:

$$\frac{\partial^2\phi}{\partial y^2} + \epsilon_1^2\frac{\partial\phi}{\partial x^2} + \epsilon_2^2\frac{\partial^2\phi}{\partial z^2} = -\frac{\beta}{A^2}(n_1 - n_2). \tag{3.3}$$

3.2.2 Mass Transfer for Ions

Let us consider a species transport equation for water mixed with multivalent ions and the flow is governed by the movement of ions. Then, mostly the ion transport will be influenced by the molecular diffusion, external electric field and electric body force term due to bulk motion of charges [54]. The molar flux of species i oriented perpendicular to the flow direction (without any wall chemical reaction or absorption of species) in vector form can be obtained as [219]

$$\mathbf{N}_i^* = -D_i\nabla c_i + c_i\omega_i z_i F\mathbf{E}^* + c_i\mathbf{q}^*, \tag{3.4}$$

where D_i is the diffusion coefficient, ω_i is the mobility defined as $\omega_i = D_i/RT$ of the species i and $\mathbf{q}^*$ is the fluid velocity.

The mass transport equation for species i in steady EOF is governed by

$$\nabla\cdot\mathbf{N}_i^* = 0. \tag{3.5}$$

Using Eq. (3.4) and Eq. (3.5), non-dimensional molar flux equation can be written as

$$\begin{aligned}&\frac{\partial^2 X_i}{\partial y^2} + \epsilon_1^2\frac{\partial^2 X_i}{\partial x^2} + \epsilon_2^2\frac{\partial^2 X_i}{\partial z^2}\\ &= Pe\left(\epsilon_1 u\frac{\partial X_i}{\partial x} + v\frac{\partial X_i}{\partial y} + \epsilon_2 w\frac{\partial X_i}{\partial z}\right) + \left(\epsilon_1 z_i\frac{\partial X_i E_x}{\partial x} + z_i\frac{\partial X_i E_y}{\partial y} + \epsilon_2 z_i\frac{\partial X_i E_z}{\partial z}\right).\end{aligned} \tag{3.6}$$

Thus, the non-dimensional electric field $\mathbf{E}$ in (x, y, z) directions are of the form: $E_x = -\left(\epsilon_1\frac{\partial\phi}{\partial x} + \epsilon_1\frac{\partial\psi}{\partial x}\right)$, $E_y = -\left(\frac{\partial\phi}{\partial y} + \frac{\partial\psi}{\partial y}\right)$, $E_z = -\left(\epsilon_2\frac{\partial\phi}{\partial z} + \epsilon_2\frac{\partial\psi}{\partial z}\right)$. Here Pe=$ReSc$ is the Peclet

number. The Reynolds number Re is $U_{HS}H/\nu$ and the Schmidt number $Sc = \nu/D_i$. The scaled factor for fluid velocity is defined as U_{HS} and ν is the kinematic viscosity of the fluid.

The EDL thickness or Debye length λ, is estimated as $\sqrt{\epsilon_e RT}/FI^{1/2}$, which is the characteristic thickness of the electrical double layer and the ionic strength $I = \sum_i z_i^2 c_i$. The reduced non-dimensional ionized equation for divalent ions can be written as

$$\left(\epsilon_1^2\frac{\partial^2 n_1}{\partial x^2} + \frac{\partial^2 n_1}{\partial y^2} + \epsilon_2^2\frac{\partial^2 n_1}{\partial z^2}\right) = \frac{\beta}{A^2}n_1(n_1 - n_2) - \left(\epsilon_1^2\frac{\partial\phi}{\partial x}\frac{\partial n_1}{\partial x} + \frac{\partial\phi}{\partial y}\frac{\partial n_1}{\partial y} + \epsilon_2^2\frac{\partial\phi}{\partial z}\frac{\partial n_1}{\partial z}\right)$$
$$- \left(\epsilon_1^2\frac{\partial\psi}{\partial x}\frac{\partial n_1}{\partial x} + \frac{\partial\psi}{\partial y}\frac{\partial n_1}{\partial y} + \epsilon_2^2\frac{\partial\psi}{\partial z}\frac{\partial n_1}{\partial z}\right) + Pe\left(\epsilon_1 u\frac{\partial n_1}{\partial x} + v\frac{\partial n_1}{\partial y} + \epsilon_2 w\frac{\partial n_1}{\partial z}\right) \tag{3.7}$$

$$\left(\epsilon_1^2\frac{\partial^2 n_2}{\partial x^2} + \frac{\partial^2 n_2}{\partial y^2} + \epsilon_2^2\frac{\partial^2 n_2}{\partial z^2}\right) = -\frac{\beta}{A^2}n_2(n_1 - n_2) + \left(\epsilon_1^2\frac{\partial\phi}{\partial x}\frac{\partial n_2}{\partial x} + \frac{\partial\phi}{\partial y}\frac{\partial n_2}{\partial y} + \epsilon_2^2\frac{\partial\phi}{\partial z}\frac{\partial n_2}{\partial z}\right)$$
$$+ \left(\epsilon_1^2\frac{\partial\psi}{\partial x}\frac{\partial n_2}{\partial x} + \frac{\partial\psi}{\partial y}\frac{\partial n_2}{\partial y} + \epsilon_2^2\frac{\partial\psi}{\partial z}\frac{\partial n_2}{\partial z}\right) + Pe\left(\epsilon_1 u\frac{\partial n_2}{\partial x} + v\frac{\partial n_2}{\partial y} + \epsilon_2 w\frac{\partial n_2}{\partial z}\right). \tag{3.8}$$

3.2.3 Governing Fluid Flow Equations

The corresponding momentum equation for an ionized fluid with electroosmotic body forces in dimensional form is written as

$$\rho\left(\frac{\partial \mathbf{q}^*}{\partial t^*} + (\mathbf{q}^*\cdot\nabla)\mathbf{q}^*\right) = -\nabla p^* + \mu\nabla^2\mathbf{q}^* + \rho_e\mathbf{E}^* \tag{3.9}$$

where $\mathbf{q}^* = (u^*,\ v^*,\ w^*)$, satisfies the equation of continuity, $\nabla\cdot\mathbf{q}^* = 0$.

We have already defined the scaling factor for the fluid velocity as U_{HS}, which is the Helmoholtz-Smoluchosky velocity and $U_{HS} = \epsilon_e E_0\phi_0/\mu$. Time t^* is scaled by H/U_{HS}. Here Peclet number establishes the relation between the height of the channel to the strength of the applied electric field and the pressure is nondimensionalized as $p = \frac{p^*}{\mu U_{HS}/H}$. The velocity field is coupled to the mass transfer equations and the equation for the potential. The governing flow equations for an incompressible, steady ionic fluid in dimensionless form are:

$$\epsilon_1\frac{\partial u}{\partial x} + \frac{\partial v}{\partial y} + \epsilon_2\frac{\partial w}{\partial z} = 0 \tag{3.10}$$

$$Re\left(\epsilon_1 u\frac{\partial u}{\partial x} + v\frac{\partial u}{\partial y} + \epsilon_2 w\frac{\partial u}{\partial z}\right) = -\epsilon_1\frac{\partial p}{\partial x} - \frac{\beta}{A^2}\frac{\epsilon_1}{\Lambda}(n_1 - n_2)\left(\frac{\partial\phi}{\partial x} + \frac{\partial\psi}{\partial x}\right) + \nabla^2 u \tag{3.11}$$

$$Re\left(\epsilon_1 u\frac{\partial v}{\partial x} + v\frac{\partial v}{\partial y} + \epsilon_2 w\frac{\partial v}{\partial z}\right) = -\frac{\partial p}{\partial y} - \frac{\beta}{A^2}\frac{1}{\Lambda}(n_1 - n_2)\left(\frac{\partial\phi}{\partial y} + \frac{\partial\psi}{\partial y}\right) + \nabla^2 v \tag{3.12}$$

$$Re\left(\epsilon_1 u\frac{\partial w}{\partial x} + v\frac{\partial w}{\partial y} + \epsilon_2 w\frac{\partial w}{\partial z}\right) = -\epsilon_2\frac{\partial p}{\partial z} - \frac{\beta}{A^2}\frac{\epsilon_2}{\Lambda}(n_1 - n_2)\left(\frac{\partial\phi}{\partial z} + \frac{\partial\psi}{\partial z}\right) + \nabla^2 w, \tag{3.13}$$

where $\Lambda = HE_0/\phi_0$ is the dimensionless electric field.

The above mentioned PDE's are accompanied with extremely nonlinear terms. In the present approach, spanwise width (W) is considered to be very large compared to the height of the channel and hence ϵ_2 is very small [26, 54] i.e. the important gradients occur in the main flow direction (x) and in the normal direction (y) parallel to the channel height. In this case the problem can be treated as two-dimensional and the terms containing variable z can be omitted. Now, the problem will be reduced to the EOF within a channel of width H and height $W \gg H$, as the gravitational and buoyancy effects are neglected [30].

3.2.4 Computational Domain and Boundary Conditions

In general, to recapitulate the electrolyte solution for two different samples, we will have 4+2 (species) equations with 6 variables. In order to obtain the solution for velocity, anions, cations, potential and pressure of the samples, four dimensionless flow parameters are governing the problem i.e. Re, Pe, Λ and A.

The channel is considered to have long upstream and downstream from the corrugated surfaces i.e. fully developed flow can be assumed at far upstream and downstream region. Most often in nano-channel systems fluids are injected and collected at the inlet and outlet respectively through reservoirs. The computational domain and the channel surfaces used for the simulation process are represented in Fig. 3.2. The corrugated surfaces are heterogeneous in nature due to the placement of blocks of lengths l_+ and $l_-(\sim O(H))$ with constant height d, along with the patches of finite lengths l_+ and l_-, which is mounted along upper and lower wall of the channel.

When modeling EOF within the micro- and nano-channel, a number of assumptions are made in this study. For example, zeta potential (ζ) is much less compare to applied external potential, no-slip conditions along the channel walls and constant wall potential. The potential gradient appears in the governing flow equations involves the potential term, which can be evaluated from the wall potential by deducting the wall $\zeta-$potential [189]. In the present analysis different $\zeta-$potentials (i.e. ζ_p) are attached along the heterogeneous portion. The overpotential along the patch and block tips can be defined as, $\phi_p = \zeta_p - \zeta$. The ion concentrations or molar flux along the solid walls and the inlet reservoir are assumed to be at one atmosphere of pressure. Here EOF can be predicted by the given $\zeta-$potential and vice versa [135] and λ, H needs to be specified to obtain parameters like Λ and Re. The boundary conditions for mole fractions along the channel

walls are obtained by considering same electrochemical potential at the reservoirs and arbitrary cross-section of the channel, which leads the Nernst equation as, $\nabla\psi = \frac{RT}{z_i F} ln \frac{c_{iR}}{c_{ic}}$ [26]. Here, c_{iR} and c_{ic} represents the average value of the concentration of species i in the reservoir and the fully developed region. The simulation is performed for a binary electrolyte NaCl buffer and the mole fractions for cation is n_1 (Na^+) and anion is n_2 (Cl^-).

Hence the simulation follows the boundary conditions (B.C.'s) as

Walls: along the channel walls (y=0 and y=1) B.C.'s can be expressed as

$$u = v = 0; \quad \phi = 0; \quad n_1 = n_1^0; \quad n_2 = n_2^0. \tag{3.14}$$

When the solution ($H_2O + NaCl$) is in contact with the solid surface, the concentration of OH^- ions will decrease due to the adsorption on the solid surface. In order to reach the equilibrium condition, a certain amount of water molecules will dissociate into H_3O^+ and OH^- ions. Experimentally [42], it is also observed that $\zeta-$potential and diameter of oxide systems can act as functions of concentration, solution of pH and ionic strength of the solutions.

The heterogeneous regions are created by placing some finite overpotential regions by supplying extra potential or fabricating with different materials. This region is specified by ϕ_p, whose length is comparable with channel height and block lengths i.e. $L = H$ and it can be assumed that $\epsilon_1 = 1$.

Switching flow: The boundary condition along the patches and along the surface of blocks are,

$$u = v = 0; \quad \phi = \phi_p; \quad n_1 = n_1^p; \quad n_2 = n_2^p. \tag{3.15}$$

Note that the Debye- Hückel approximation is based on the Poisson-Boltzmann model and it is only strictly valid for $\phi \ll 25.5\ mV$. The Boltzmann distribution of mole fraction of species is $X_i = X_i^0 e^{-z_i\phi}$. The wall mole fractions along the upper surface of the block and patches are $n_1^p = n_1^0 e^{\phi_p}$ and $n_2^p = n_2^0 e^{-\phi_p}$ (for binary, monovalent ions), which justifies the equilibrium condition for electrochemical potential at y=0 and y=1 [72].

It is assumed that, channel is longer and widened where corrugated walls are formed by the attachment of blocks and patches along the walls and are places at too far up- and down stream regions where convection effect is not negligible. At far up- and down stream regions, it is assumed that the flow is fully developed.

Inlet flow: Upstream region of the heterogeneities, (x=-L)

$$v = 0; \quad u = u^{\text{in}}; \quad \phi = \phi^{\text{in}}; \quad n_1 = n_1^{\text{in}}; \quad n_2 = n_2^{\text{in}}; \quad \frac{\partial p}{\partial x} = 0. \tag{3.16}$$

Parallel flow: Far down stream of the heterogeneities (x=L), a symmetrical condition is used, i.e.

$$\frac{\partial u}{\partial x} = 0; \quad \frac{\partial v}{\partial x} = 0; \quad \frac{\partial \phi}{\partial x} = 0; \quad \frac{\partial n_1}{\partial x} = 0; \quad \frac{\partial n_2}{\partial x} = 0; \quad \frac{\partial p}{\partial x} = 0. \tag{3.17}$$

The values of u^{in}, ϕ^{in}, n_1^{in}, n_2^{in} are obtained due to the fully developed EOF effects of potential. Detailed analysis of fully developed EOF equations and the corresponding boundary conditions is completely discussed by Nayak [189]. For the present discussion the electrolyte is considered to be consists of monovalent cation and monovalent anion such as $NaCl$, the mole fractions sum is 1 along the homogeneous boundary regions far from the blocks and patches.

3.3 Analytical Estimation of Electric Potential ($\lambda \ll H$ and $\lambda \sim O(H)$)

Generally, the time variation in EOF inside the EDL are of the order of 10^{-8} to 10^{-7} s [111]. This time scale is very less compare to the time scale evolved on the EOF in the core region which are of order 10^{-3} to 10^{-5} s. Therefore, according to the theory of elasticity the net charge density is governed by Poisson equation which is independent of time, that is

$$\epsilon_1^2 \frac{\partial^2 \phi}{\partial x^2} + \frac{\partial^2 \phi}{\partial y^2} = -\frac{H^2}{\phi_0} \frac{\rho_e}{\epsilon_r \epsilon_0} = -\frac{H^2}{\phi_0} \frac{\sum_i z_i e n_i^*}{\epsilon_r \epsilon_0}, \tag{3.18}$$

where ϵ_r and ϵ_0 are the dielectric constant of the mixture and permittivity of the free space respectively, n_i^* can be expressed as, $n_i^0 e^{-z_i \phi}$. n_i^0 is called number density of an ionic species at the boundary. Since the number density of an ion species is directly proportional to the molar concentration of that ion species, we can write $n_i = N_A c_i$, $X_i = c_i/c$. N_A is the Avagadro's number.

The reduced form of the equation can be re-written as

$$\epsilon_1^2 \frac{\partial^2 \phi}{\partial x^2} + \frac{\partial^2 \phi}{\partial y^2} = -\frac{ch^2 F^2}{\epsilon_r \epsilon_0 RT} \sum_i z_i X_i = -\frac{c}{IA^2} \sum_i z_i X_i, \tag{3.19}$$

where $k = \sqrt{\frac{\sum_i z_i^2 n_i^0 e^2}{\epsilon_e KT}} = \frac{1}{\lambda}$. Since, we are considering the potential difference due to the imposed electric field in the flow direction and wall potentials are axially invariant which is also low enough $|\zeta| \ll 25.6mV$. To simplify the analysis we use the Debye-Hückel approximation which is valid, when $\lambda \ll H$ and dimensionless potential $\phi \ll 1$. For symmetrical distribution of ions the Boltzmann distribution for ions for species i is, $X_i = X_i^0 e^{-z_i \phi}$. In expanded form we can write this as, $X_i = X_i^0(1 - z_i \phi)$, since $\phi \ll 1$. Substituting in Eq.(3.19)

$$\epsilon_1^2\frac{\partial^2\phi}{\partial x^2}+\frac{\partial^2\phi}{\partial y^2}=-\frac{c}{A^2\sum_i z_i^2X_i^0c}\sum_i(z_iX_i^0-z_i^2X_i^0\phi)=-\frac{1}{A^2\sum_i z_i^2X_i^0}\sum_i z_i^2X_i^0\left(\frac{z_iX_i^0}{z_i^2X_i^0}-\phi\right). \quad (3.20)$$

The reduced form of Eq. 3.20 can be written as,

$$\epsilon_1^2\frac{\partial^2\phi}{\partial x^2}+\frac{\partial^2\phi}{\partial y^2}=\frac{1}{A^2}\left(\phi-\frac{\sum_i z_iX_i^0}{\sum_i z_i^2X_i^0}\right). \quad (3.21)$$

In the present chapter the potential developed across the channel consists of two parts. The potential (ϕ_{FD}) developed at far upstream and downstream from the heterogeneous region and the potential developed across the heterogeneities (ϕ_H). Hence, it is reasonable to assume that the total change in potential is given by the linear superposition of ϕ_{FD} and ϕ_H which is valid for long channel. Hence,

$$\phi(x,y)=\phi_H(x,y)+\phi_{FD}(y). \quad (3.22)$$

Since the flow is one dimensional (1D) at far upstream and downstream [54], the equation for ϕ_{FD} can be rewritten as,

$$\frac{\partial^2\phi_{FD}}{\partial y^2}=\frac{1}{A^2}\left(\phi_{FD}-\frac{\sum_i z_iX_i^0}{\sum_i z_i^2X_i^0}\right). \quad (3.23)$$

Here ϕ_{FD} is an unknown. If $\lambda\sim O(H)$ the BC's are $\phi=0$ at $y=0$ and $\frac{\partial\phi}{\partial y}=0$ at $y=1/2$ (centerline symmetry) for $\lambda\sim O(H)$ and $\phi=0$ at $y=0$ and $\phi=\phi_0$ at $y=y_\infty$ for $\lambda\ll O(H)$. The solution follows as described by Conlisk et al. [72], as $\phi=ae^{-y}+be^{y}+\frac{\sum_i z_iX_i^0}{A^2\sum_i z_i^2X_i^0}$.

For $\lambda\ll O(H)$, the solution is, $\phi=\frac{\sum_i z_iX_i^0}{A^2\sum_i z_i^2X_i^0}\left(1-e^{-y}\right)$.

For $\lambda\sim O(H)$, the solution is, $\phi=\frac{\sum_i z_iX_i^0}{A^2\sum_i z_i^2X_i^0}\left(1-\frac{\cosh(y-1/2)}{\cosh(1/2)}\right)$.

The equation for ϕ_H can be written as

$$\epsilon_1^2\frac{\partial^2\phi_H}{\partial x^2}+\frac{\partial^2\phi_H}{\partial y^2}=\frac{1}{A^2}\phi_H. \quad (3.24)$$

This is the perturbed potential in the heterogeneous region due to the external electric field in the x direction and the over potential patch. The boundary conditions for this equation are, $\phi_H=\phi_p$ for $\mid x\mid\leq 0.5$ and at $y=d$ and $\phi_H=0$ for $|x|>0.5$ at $y=0$ and $y=1$ (in the case of a single block attached along the lower channel wall).

Due to a suddenly applied constant wall voltage, the electrolyte gets accelerated and moves fast due to electroosmosis. The solution is obtained by using separation of variables and introducing the new variables as follows:

$$\phi_H(x,y) = X(x)Y(y). \tag{3.25}$$

Putting the far upstream and downstream boundary conditions i.e. $\phi_H = 0$ at $x = \pm L$ gives, $X(x) = a_n \sin(\frac{n\pi}{2L}(x+L))$, where a_n is an undetermined coefficient for the solution. This is a solution for a periodic array of patches. Similarly $\phi_H = 0$ at $y = 1$. This gives $Y(y) = 0$. Then the solution of equation (3.25) is

$$Y(y) = b_n \sinh\left(\sqrt{\left(\frac{n\pi}{2L}\right)^2 + \frac{1}{A^2}(1-y)}\right). \tag{3.26}$$

The complete solution for $\phi_H(x,y)$ is given by

$$\phi_H(x,y) = X(x)Y(y) = a_n b_n \sin\left(\frac{n\pi}{2L}(x+L)\right) \sinh\left(\sqrt{\left(\frac{n\pi}{2L}\right)^2 + \frac{1}{A^2}(1-y)}\right). \tag{3.27}$$

On the lower side of the wall at $y = d$, $\phi_H = \phi_p$. Hence, $\phi_H(x,y)$ will be reduced to

$$\phi_H(x,y) = X(x)Y(y) = a_n b_n \sin\left(\frac{n\pi}{2L}(x+L)\right) \sinh\left(\sqrt{\left(\frac{n\pi}{2L}\right)^2 + \frac{1}{A^2}(1-d)}\right) = c_n \sin\left(\frac{n\pi}{2L}(x+L)\right) \tag{3.28}$$

where $c_n = a_n b_n \sinh\left(\sqrt{\left(\frac{n\pi}{2L}\right)^2 + \frac{1}{A^2}(1-d)}\right)$ need to be determined for the boundary condition $\phi_H(x,y) = \phi_p$ for $\mid x \mid \leq 0.5$ and at $y = d$ and $\phi_H(x,y) = 0$ for $|x| > 0.5$ at $y = 0$ and $y = 1$.

$$\phi_H(x,y) = \sum_{i=1}^{\infty} \frac{2\phi_p \sin(\frac{n\pi}{2}) \sin(\frac{n\pi}{4L}) \sin(\lambda_n(x+L)) \sinh((1-y)\sqrt{\varepsilon})}{\frac{n\pi}{2} \sinh\left(\sqrt{\frac{1}{A^2}(1-d) + (\frac{n\pi}{2L})^2}\right)}. \tag{3.29}$$

where $\varepsilon = \left(\frac{1}{A^2} + (\frac{n\pi}{2L})^2\right)$.

3.4 Analytical Estimation of Pressure and Velocity Far Away from the Potential Non-Homogeneity ($\lambda \ll H$ and $\lambda \sim O(H)$)

Using the PB model the charge distribution of binary symmetric ions is governed by

$$n_1 = e^{-\phi}, \; n_2 = e^{\phi}. \tag{3.30}$$

Using Eq. (3.30), the induced potential and momentum equations take the form:

$$\epsilon_1^2 \frac{\partial^2 \phi}{\partial x^2} + \frac{\partial^2 \phi}{\partial y^2} = \frac{2\beta}{A^2} \sinh(\phi) \tag{3.31}$$

$$Re\left(\epsilon_1 u \frac{\partial u}{\partial x} + v \frac{\partial u}{\partial y}\right) = -\epsilon_1 \frac{\partial p}{\partial x} + \nabla^2 u + \frac{2\beta}{A^2} \frac{\epsilon_1}{\Lambda} \sinh(\phi) \left(\frac{\partial \phi}{\partial x} + \frac{\partial \psi}{\partial x}\right) \tag{3.32}$$

$$Re\left(\epsilon_1 u \frac{\partial v}{\partial x} + v \frac{\partial v}{\partial y}\right) = -\frac{\partial p}{\partial y} + \nabla^2 v + \frac{2\beta}{A^2} \frac{1}{\Lambda} \sinh(\phi) \left(\frac{\partial \phi}{\partial y} + \frac{\partial \psi}{\partial y}\right) \tag{3.33}$$

Taking the curl of the momentum Eq. (3.32) and (3.33), the vorticity transport equation takes the form:

$$Re\left(\epsilon_1 u \frac{\partial \omega}{\partial x} + v \frac{\partial \omega}{\partial y}\right) = \nabla^2 \omega + \frac{2\beta}{A^2} \frac{\epsilon_1}{\Lambda} \cosh(\phi) \left(\frac{\partial \phi}{\partial x} \frac{\partial \psi}{\partial y} - \frac{\partial \phi}{\partial y} \frac{\partial \psi}{\partial x}\right) \tag{3.34}$$

Using the Debye-Hückel approximation and taking a translation of coordinates by $Y = y - \frac{1}{2}$ for a two-dimensional, fully developed EOF, the induced potential and vorticity equations are reduced to

$$\frac{\partial^2 \phi}{\partial Y^2} = (k_1 H)^2 \phi \tag{3.35}$$

$$\frac{\partial^2 \omega}{\partial Y^2} = -\frac{2\beta\epsilon_1}{A^2} \cosh(\phi) \frac{\partial \phi}{\partial Y} \tag{3.36}$$

where $k_1 = \left(\frac{2\beta}{\lambda^2}\right)^{\frac{1}{2}}$. Solving above equations with the boundary conditions: $\phi = -1$ at $Y = \pm 1/2$; $\omega = 0$ and $\frac{d\omega}{dY} = 0$ at $Y = 0$, we can get

$$\phi(Y) = -\frac{\cosh(k_1 HY)}{\cosh(k_1 H/2)} \tag{3.37}$$

$$\omega(Y) = -\frac{2\beta\epsilon_1}{A^2}\frac{\sinh(k_1 HY)}{(k_1 H)\cosh(k_1 H/2)}. \tag{3.38}$$

For a fully developed flow, the relation between vorticity and velocity is

$$\omega(Y) = -\frac{du}{dY} \tag{3.39}$$

Integration of Eq. (3.39) with no-slip boundary condition, yields the expression for velocity as

$$u(Y) = -\frac{2\beta\epsilon_1}{A^2}\frac{1}{(k_1 H)^2}\Big[\phi(Y) + 1\Big]. \tag{3.40}$$

Simplifying Eq. (3.32) and (3.33) under the fully developed condition, the equations for the pressure gradients can be expressed in the form:

$$\frac{\partial p}{\partial x} = \frac{\partial^2 u}{\partial Y^2} - 2\beta\frac{\epsilon_1}{A^2}\phi \tag{3.41}$$

$$\frac{\partial p}{\partial Y} = \frac{2\beta}{\Lambda}\frac{1}{A^2}\phi\frac{\partial \phi}{\partial Y} \tag{3.42}$$

Substituting Eq. (3.37) and (3.40) into Eq. (3.41) it is observed that the axial pressure gradient is zero far away from potential heterogeneity where the flow is fully developed. The pressure distribution in the transverse direction is given by

$$p(Y) = \frac{\beta}{2(k_1 H)^2}\frac{1}{\Lambda\epsilon^2}\frac{\cosh(2k_1 HY)}{\cosh^2(k_1 H/2)} + c, \tag{3.43}$$

where c is a constant. From, Eq. (3.43), it can be clearly observed that a pressure gradient is existing normal to the surface in the fully developed region but vanishes along the axial direction.

3.5 Sample Concentration Equation (C) for Flow

To understand the sample flow distribution in a nano-channel, it is essential to obtain the solution for sample diffusion equation by numerical simulation. Distribution of the sample species is obtained by solving the non-dimensional steady convection-diffusion equation as

$$\mathbf{q}\cdot\nabla C = \frac{1}{Pe_s}\nabla^2 C, \tag{3.44}$$

where C represents the non-dimensional species concentraion, scaled by reference concentration C_{ref} and $\mathbf{q}$ is the dimensionless velocity, defined as, $\mathbf{q} = \mathbf{q}^*/U_{HS}$. Here Pe_s stands for the Peclet number of the eluted species, defined by $Pe_s = \frac{U_{HS}H}{D_s}$, where D_s is the diffusivity of the sample species. The boundary conditions for the species transport are:
Upstream boundary condition:

$$C = C_{in} \tag{3.45}$$

Downstream boundary condition:

$$\frac{\partial C}{\partial x} = 0 \tag{3.46}$$

Boundary conditions on the walls:

$$\nabla C \cdot \mathbf{n} = 0 \tag{3.47}$$

where $\mathbf{n}$ is the unit outward normal to the corresponding surface. Here $C_{in} = 0$ on lower half of channel inlet ($x = -L$, $0 \leq$ y ≤ 0.5) and $C_{in} = 1$ on the upper half of the inlet ($x = -L$, $0.5 \leq$ y ≤ 1).

3.6 Time Scale Analysis

It is important to generalize the discussion of EOF in full time scale analysis for flow characteristics inside the channel. Since different time scale can be used to non dimensionalize the flow governing equations, such as viscous time scale i.e. $t_\nu = H^2/\nu$, axial diffusive time scale i.e. $t_d = H^2/D_i$ and the convective time scale i.e. $t_c = H/U_{HS}$. In the present analysis the electroosmotic flow is considered within a nano channel under the influence of external electric field . The corresponding momentum balance equation for an ionized fluid in vector form can be represented as

$$\rho\left(\frac{\partial \mathbf{q}^*}{\partial t^*} + (\mathbf{q}^* \cdot \nabla)\mathbf{q}^*\right) = -\nabla p^* + \mu\nabla^2\mathbf{q}^* + \rho_e\mathbf{E}^* \tag{3.48}$$

and the corresponding mass conservation equation is

$$\nabla \cdot \mathbf{q}^* = 0. \tag{3.49}$$

The scaling factor for the fluid velocities is U_{HS} known as the HelmholtzSmoluchowski velocity and is defined as, $U_{HS} = \epsilon_e E_0 \phi_0/\mu$, pressure scaled by $p = \frac{p^*}{\mu U_{HS}/H}$. If the time is scaled by convective time scale t_c or diffusion time scale t_d or viscous time scale t_ν, the dimensionless governing equation is

$$B\frac{\partial \mathbf{q}}{\partial t} + Re\Big((\mathbf{q}\cdot\nabla)\mathbf{q}\Big) = -\nabla p + \nabla^2\mathbf{q} - \frac{\beta}{\Lambda A^2}(n_1 - n_2)\nabla\phi, \tag{3.50}$$

where B is non dimensional parameter which may be Re or $1/Sc$ or unity depends on the time scaled variable.

If the EOF is considered as an unsteady unidirectional flow with uniform zeta potential ζ along the channel walls, then the potential flows for Boltzmann distribution and the flow governing equation reduces to

$$B\frac{\partial u}{\partial t} = \frac{\partial^2 u}{\partial y^2} - \frac{\partial^2 \phi_\zeta}{\partial y^2}. \tag{3.51}$$

and the induced potential equation is

$$\frac{d^2\phi_\zeta}{dy^2} = \frac{\phi_\zeta}{A^2}. \tag{3.52}$$

The electric field generated due to the wall zeta potential (Eq. 3.52) along with the boundary conditions $\phi_\zeta = \zeta$ at $y = 0$ and $y = 1$, subject to the applied external electric potential can be written as

$$\phi = \phi_E + \phi_\zeta = -x + \zeta[\cosh(y/A) + a\sinh(y/A)]. \tag{3.53}$$

To study the transient behavior of the EOF represented in Eq. 3.51 we have assumed that the flow is both steady and unsteady in nature along with no slip boundary condition. Therefore the steady state solution is obtained as

$$u_s(y) = \zeta\Big[\cosh(y/A) + a\sinh(y/A) - 1\Big]. \tag{3.54}$$

To obtain the solution of the unsteady problem, the initial and boundary conditions are used as

$$u(y,t)|_{t=0} = u(y) \tag{3.55}$$

$$u(0,t) = 0 = u(1,t). \tag{3.56}$$

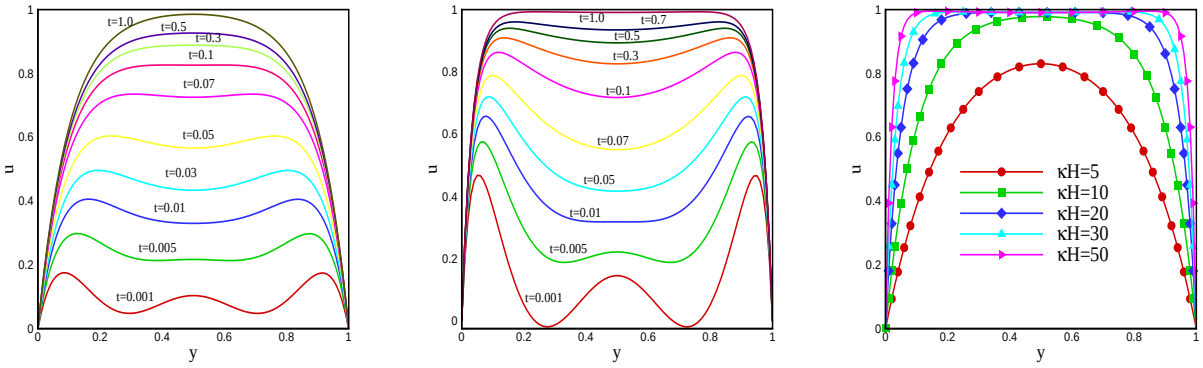

(a) (b) (c)

Figure 3.3: (a) $\kappa H = 1/A = 10$ (b) $\kappa H = 1/A = 30$ are the velocity distribution for different times and (c) velocity distribution at different $\kappa H = 1/A$ at $t = 0.001$.

The solution is obtained by the method of separation in which the dependent function is defined as the product of the two independent functions as $u(y,t) = Y(y)T(t)$. Using the above boundary condition the unsteady state solution can be written as

$$u_{us}(y,t) = \sum_{n=1}^{\infty} E_n \exp(-n^2\pi^2 t/B)\sin(n\pi y) \tag{3.57}$$

where constant E_n can be determined by the initial condition and the orthogonality properties as

$$E_n = 2\zeta\left[\frac{1}{n\pi} - \frac{n\pi}{1/A^2 + n^2\pi^2}\right]\left(1 - (-1)^n\right) \tag{3.58}$$

Thus the expression for time dependent velocity is

$$u(y,t) = \zeta\left[\frac{\sinh((1-y)/A) + \sinh(y/A)}{\sinh(1/A)} - 1\right] + 2\zeta\sum_{n=1}^{\infty}\left[\frac{1}{n\pi} - \frac{n\pi}{1/A^2 + n^2\pi^2}\right]\left(1 - (-1)^n\right)\exp(-n^2\pi^2 t/B)\sin(n\pi y). \tag{3.59}$$

The parameter B plays an important role in the flow distribution. From the closed form of analytic solution it is observed that the solution has been reached at the steady state if $B > 1$ which is clearly visualized from the Fig. 3.3. Since $Sc = \nu/D_i = 5.0\times10^2$ or 10^3 if $D_i = 2.0\times10^{-9}$ or 1.0×10^{-9} is the diffusivity coefficient of the species. Similarly $Re = Pe/Sc < 1$ and $B = 1/Re > 1$. Thus in diffusion time scale or convective time scale, the transfer of species from one end of the channel to other end the velocity is essentially steady.

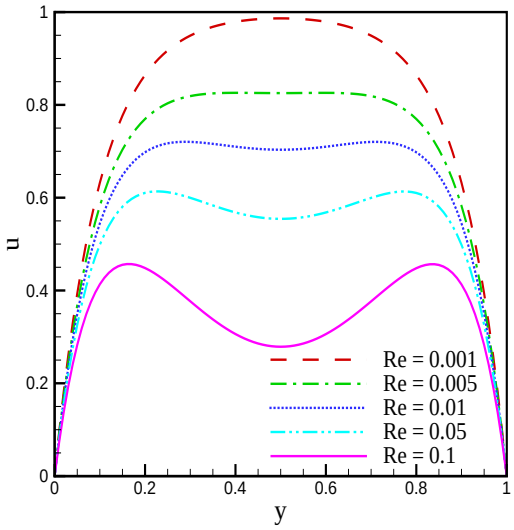

Figure 3.4: Velocity characteristic for different values of Reynolds number in the base-state solution at fixed time step.

3.6.1 Discussion of Linear Stability

The flow conventions in our formulation ensure that the direction of EOF is from left to right as shown in Fig. 3.4 by the base-state velocity profiles at a fixed time for different values of Reynolds number. Where as a Poiseulle-type flow is observed with a parabolic profile for low Reynolds number. Thus a flow reversal is observed in core region for higher values of Reynolds number. Therefore an instability nature of flow characteristics may occur in EOF in a small channel.

Now a linear stability of the unidirectional EOF can be studied by imposing small perturbation to the base-state solution profiles, $u = \bar{u} + u'$, $v = v'$, $p = \bar{p} + p'$ and $\phi = \bar{\phi} + \phi'$ [172, 185], where $-$ denote the mean variables and $'$ denote the perturbed variables. Thus the resulting perturbed equations are

$$\frac{\partial u'}{\partial x} + \frac{\partial v'}{\partial y} = 0 \tag{3.60}$$

$$Re\left[\frac{\partial u'}{\partial t} + \bar{u}\frac{\partial u'}{\partial x} + v'\frac{\partial \bar{u}}{\partial y}\right] = -\frac{\partial p'}{\partial x} + \frac{\partial^2 u'}{\partial x^2} + \frac{\partial^2 u'}{\partial y^2} - \frac{1}{\Lambda}\left(\frac{\partial^2 \phi'}{\partial x^2} + \frac{\partial^2 \phi'}{\partial y^2} - \frac{\partial \phi'}{\partial x}\frac{\partial^2 \bar{\phi}}{\partial y^2}\right) \tag{3.61}$$

$$Re\left[\frac{\partial v'}{\partial t} + \bar{u}\frac{\partial v'}{\partial x}\right] = -\frac{\partial p'}{\partial y} + \frac{\partial^2 v'}{\partial x^2} + \frac{\partial^2 v'}{\partial y^2} + \frac{1}{\Lambda}\left(\frac{\partial^2 \phi'}{\partial x^2}\frac{\partial \bar{\phi}}{\partial y} + \frac{\partial^2 \phi'}{\partial y^2}\frac{\partial \bar{\phi}}{\partial y} + \frac{\partial \phi'}{\partial y}\frac{\partial^2 \bar{\phi}}{\partial y^2}\right) \tag{3.62}$$

Eliminating pressure terms from the above equations and normalized the linearized equation by $u' = \delta[\tilde{u}(y)e^{ik(x-ct)}]$, $v' = \delta[\tilde{v}(y)e^{ik(x-ct)}]$, $p' = \delta[\tilde{p}(y)e^{ik(x-ct)}]$ and $\phi' = \delta[\tilde{\phi}(y)e^{ik(x-ct)}]$, where $\delta(<< 1)$, k and $c(= c_r + ic_i)$ are amplitude, wavenumber and phase speed of the infinitesimal perturbation respectively, resulting in an eigenvalue problem analogous to the Orr-Sommerfeld equation:

$$(D^2 - k^2)^2\tilde{v} = ik\left[Re(\bar{u} - c)(D^2 - k^2)\tilde{v} - Re\tilde{v}\frac{d^2\bar{u}}{dy^2} - \frac{\zeta}{\Lambda A}(1/A^2 - k^2)\sinh(y/A)\right] + \frac{k^4\zeta^2}{\Lambda A}\left[\frac{1}{2}\sinh(2y/A) + B\cosh^2(y/A)\right], \tag{3.63}$$

$$\tilde{u} = -\frac{1}{ik}\frac{d\tilde{v}}{dy}, \tag{3.64}$$

where the notation D denotes the ordinary differentiation $\frac{d}{dy}$ and the boundary condition is $\tilde{v} = \tilde{v}_y = 0$.

The above set of equations form an eigenvalue problem, which is solved numerically by using spectral collocation method. The linear growth coefficient (kc_i) and the corresponding wave number (k) thus obtained are the time and length scales of the instabilities. The dominant growth coefficient $(kc_i)_m$ is found by determining the global maxima of kc_i and the neutral stability plots are obtained by identifying the conditions under which $kc_i = 0$.

3.7 Numerical Scheme

The coupled set of governing non-linear equations for potential, ionic concentrations and fluid flow are solved through a finite volume method [89,123] with their associated boundary conditions. Numerical method adopted here is similar to the method described in Chapter 1 (Section 1.8) in the context of electroosmosis in a charged corrugated nano-channel. A Newtonian linearization technique is used to linearize the nonlinear terms in this process, and the equation is then solved using the SIMPLE method with staggered grid system. Individual control volumes are used to integrate all the equations, since edge effects close to the heterogeneous surface undergo a sharp change. In order to control the sharp variation in the variables, a higher order upwind scheme QUICK is used to discretize the convective and elctroosmotic migration terms.

The pressure Poisson equation is formulated to establish the relationship between continuity and momentum equation. In every time step of the cyclic procedure, this pressure correction is solved through the SOR (Successive Over Relaxation) method to achieve an updated flow field. This cyclic procedure is repeated until getting a desired accuracy, max $|\Theta_{i,j}^{n+1} - \Theta_{i,j}^{n}| < \Delta$, where $\Theta = (n_1, n_2, \phi, u, v)$, $\Delta = 10^{-6}$, n denotes the iteration level and i, j stand for computational

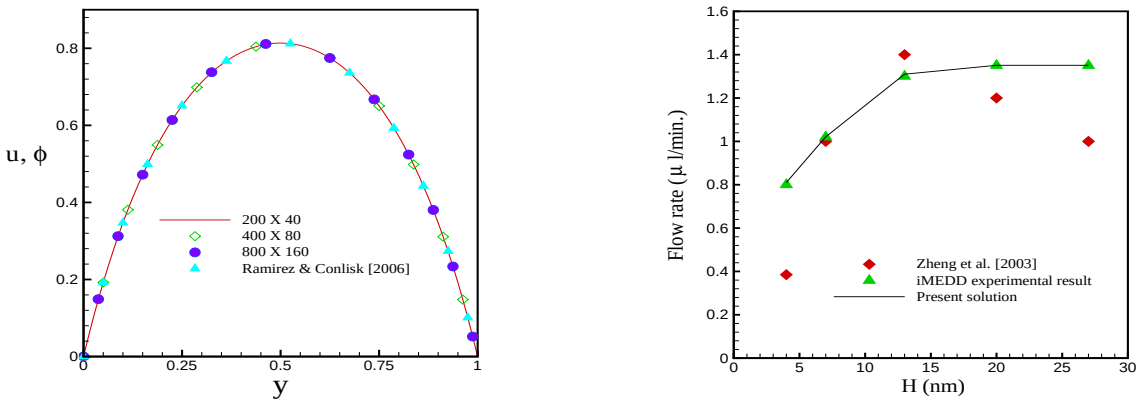

(a) (b)

Figure 3.5: (a) Comparison of velocity and potential with Ramirez and Conlisk [220] along the axial direction in a fully developed EOF region for H=50 nm, $n_1^0 = 2.77 \times 10^{-5}$, $n_2^0 = 2.54 \times 10^{-6}$ and $E_0 = 1.7143\ V/\mu m$. Grid independency is also represented in the figure. (b) Comparison of flow rate variation due to Zheng et al. [292] for various channel heights.

grid points.

3.7.1 Code Validation

Several test runs are made to obtain the upstream and downstream region where the variables become independent and obtains fully developed EOF at a distance $2l$ from the center of the block. This distance is obtained when two side-by-side blocks are considered and considered to be larger. To obtain optimal grid size, grid-independent tests are conducted by changing the grid size between 400×80 and 800×160 and is shown in Fig. 3.5 (a). The grids are found to be optimal at 400×80. The computed results are verified with the existing results to check the accuracy.

A valid comparison is made with the results obtained by Ramirez and Conlisk [220] and found that present simulated results agree well. The comparisons for u and ϕ are presented in Fig. 3.5 (a), when H=50 nm and the wall mole fractions correspond to $[Na^+] = 0.00154M$ and $[Cl^-] = 0.000141M$, with the external electric field $10^6\ V/m$ for a fully developed EOF. The velocity profiles are parabolic in nature in case of thick EDL and flow rate increases with the increase of imposed electric field and ζ-potential [292]. The comparison of experimental results for axial flow rate due to Zheng et al. [292] is made with the present simulated result for various channel heights in case of a plane EOF and presented in Fig. 3.5 (b). It is found that simulated results agree well with the experimented results.

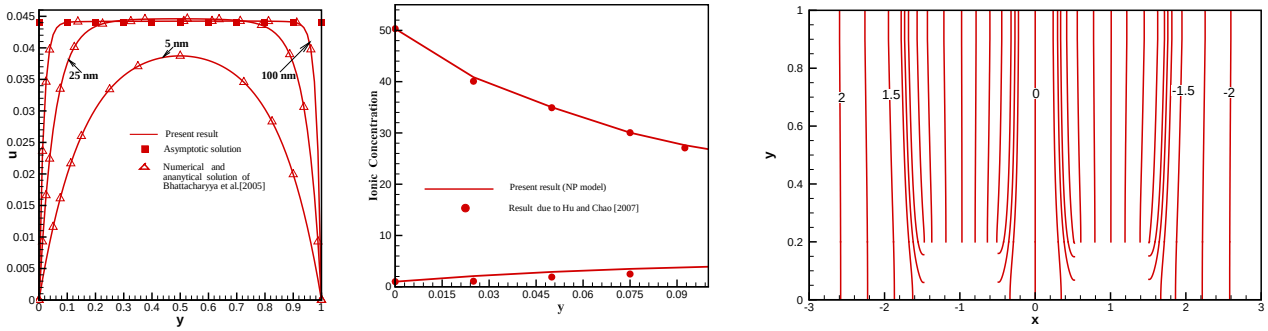

(a) (b) (c)

Figure 3.6: (a) Comparison of axial velocity distribution at the far upstream region with the result due to Bhattacharyya et al. [26] for different channel heights $H = 5\ nm,\ 25\ nm,\ 100\ nm$, where $[Na^+]$, $[Cl^-]$ corresponds to 0.154 M and 0.141 M respectively with the external electric field strength $3.5 \times 6\ V/\mu m$, (b) Comparison of ion distribution with the result due to Hu and Chao [112], (c) Electric potential distribution of external electric field case (II) with $E_0 = 10^6\ V/m$, $H = 20\ nm$, $\phi_p = 0.2$ and $\epsilon = 0.05$.

3.8 Results and Discussions

Most of the simulations are performed for a strong electrolyte NaCl (solute) solution with solvent as water. The wall concentrations for this strong NaCl electrolyte solution is assumed as, $[Na^+] = 0.154M$, $[Cl^-] = 0.141M$. The water molarity is considered as, $55.6M$ $((1000g)/(18gM^{-1})) = 55.6$ moles) leads to an EDL thickness of $0.8nm$. The concentration distribution along the asymmetric part of the surface is obtained by the relations $n_{1_p} = n_1^0 e^{-\phi_p}$ and $n_{2_p} = n_2^0 e^{\phi_p}$, where ϕ_p is the patch potential strength. The diffusivity of the eluted species (D_s) is considered as $1.0 \times 10^{-11}\ m^2/s$ which corresponds to the Peclet number (Pe_s) 14.4.

3.8.1 Electric Field Spectrum

The potential distribution of the external electric field around the wall mounted rectangular blocks, whose heights are a fraction of the channel height and the length is on the order of the channel height, combined with over potential regions are presented in Fig. 3.6(c). The external electric potential is obtained by solving the Laplace equation $\bigtriangledown^2\psi = 0$ by assuming that all walls of the channel and the block are electrically insulated, *i.e.* $\nabla\psi.\mathbf{n} = 0$, where $\mathbf{n}$ is the unit outward normal to the surface. Far away from the block, i.e. upstream and downstream of the channel, ψ is a linear function of x i.e. $\psi = -\Lambda x$. The non-dimensional external field strength is designated as Λ and is defined by $\Lambda = \frac{HE_0}{\phi_0}$, where the electric field strength E_0 is varies from $10^4\ V/m$ to $10^6\ V/m$. Mostly the electric field is predominantly along x-axis

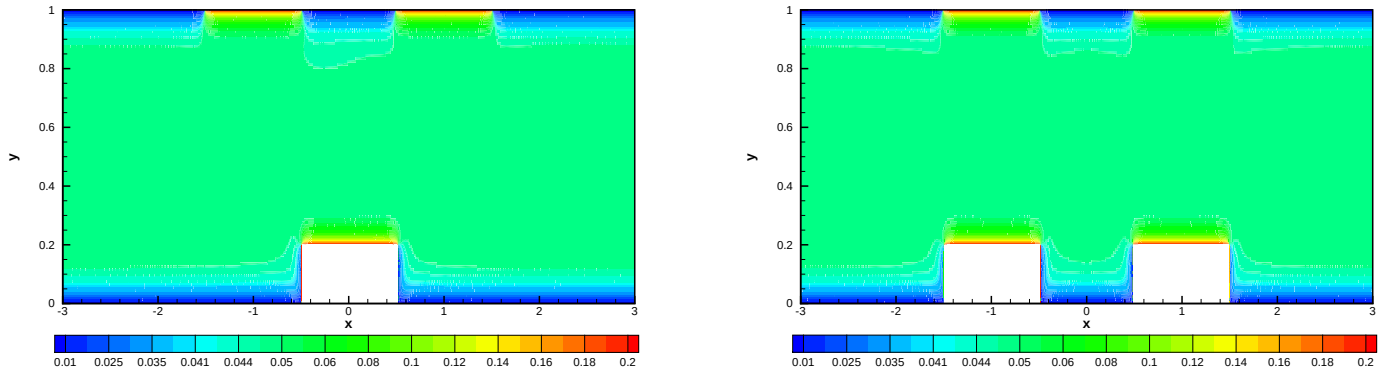

(a) (b)

Figure 3.7: EDL-potential contours for (a) case (I) and (b) case (II), when $[Na^+] = 0.154\ M$, $[Cl^-] = 0.141\ M$, $H = 20\ nm$, $\epsilon = 0.05$ and $\phi_p = 0.2$.

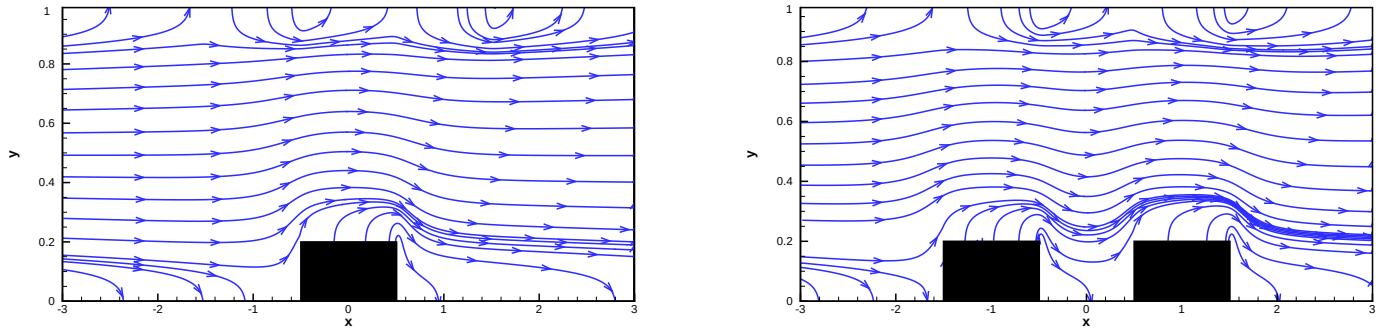

(a) (b)

Figure 3.8: Total electric field lines (combination of external and induced electric field) for (a) case (I), (b) case (II), when $[Na^+] = 0.154\ M$, $[Cl^-] = 0.141\ M$, $H = 20\ nm$, $\epsilon = 0.05$ and $\phi_p = 0.2$.

except in the region near the block, where a y-component of the electric field exists i.e. $\frac{\partial \psi}{\partial y}$ and has a maximum magnitude about 8% of Λ due to blocks (Fig. 3.6(c)). The strength of the electric field is enhanced in the downstream side and above the charged block due to the external electric field acting along the x-direction. Fig. 3.6(a) represents a velocity comparison at different channel heights with Bhattacharyya et al. [26]. The comparison is made with a strong electrolyte solution of $[Na^+] = 0.154\ M$, $[Cl^-] = 0.141\ M$ and water 55.6 M with an external electric field strength 6V applied over a channel of length $3.5\mu\ m$. These parameters of concentration correspond to EDL thickness of 0.8 nm. The analytical and numerical comparison for $H = 5\ nm$, $25\ nm$ and $100\ nm$ shows 1% variation of the numerical solution along the far upstream velocity profiles. The parabolic and top hat nature follows according to the EDL

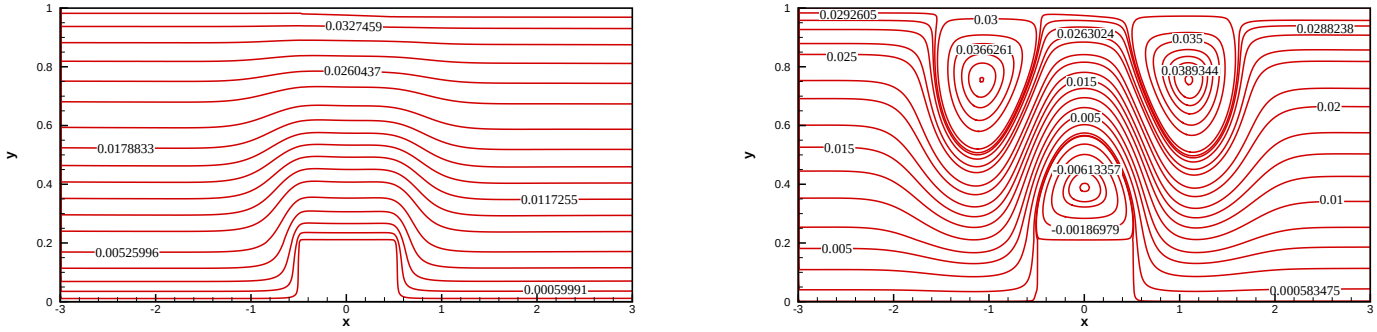

(a) (b)

Figure 3.9: Streamlines for case (I) with (a) $\phi_p = 0$ and (b) $\phi_p = 0.2$, when $[Na^+] = 0.154\ M$, $[Cl^-] = 0.141\ M$, $H = 20\ nm$, $\epsilon = 0.05$.

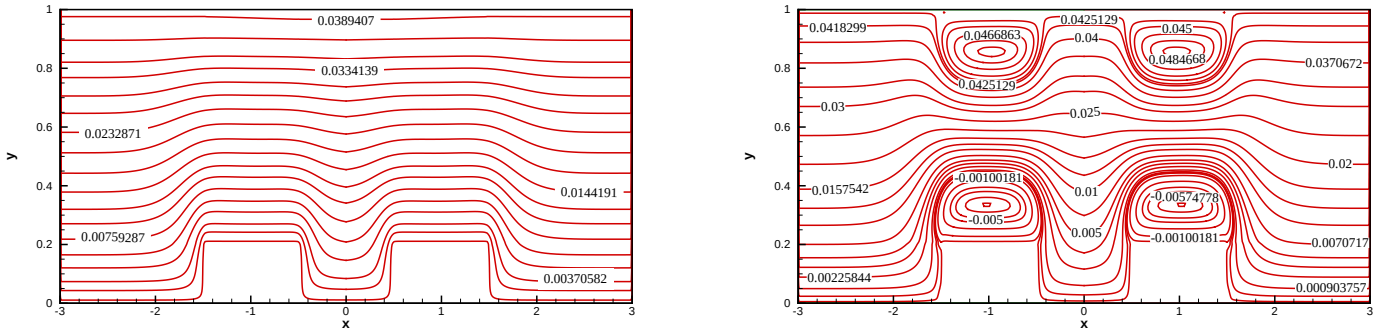

(a) (b)

Figure 3.10: Streamlines for case (II) with (a) $\phi_p = 0$ and (b) $\phi_p = 0.2$, when $[Na^+] = 0.154\ M$, $[Cl^-] = 0.141\ M$, $H = 20\ nm$, $\epsilon = 0.05$.

overlapping and non-overlapping behavior depending on the channel height and molarity of the solutions. The analytical solution, discussed in Sec. 3, differs by 3.4% from the result of Bhattacharyya et al. [26], but closely agree with the present numerical results for larger channel heights *i.e.* above 25 nm. Fig. 3.6(b) presents the distribution for ionic concentration in a parallel plane channel and shows a good agreement with the result due to Hu and Chao [112] for channel height of 0.2 μm and $E_0 = 10^5\ V/m$.

Fig. 3.7 presents the distribution of induced potentials for both the configurations, developed in the flow domain due to non-homogenous ζ- potential arrangement. The combined influence of the externally applied electric field and the induced electric field created by the over potential patch along with the block is presented in Fig. 3.8. The electric field lines composed of both

the externally applied electric field and the induced field by the patch and the block top. The direction of the applied electric field is in x-direction, from left to right in all cases and the direction of the induced field is from the patch to the opposite channel walls. The density of electric field lines are increased in case of multiple blocks as observed from Fig. 3.8 (b).

3.8.2 Growth of Flow Profile and Flow Spectrum

Above the patch and the block, the asymmetry of these electric field lines causes the asymmetry of the velocity and concentration distribution of charged ions as shown in Fig. 3.9, Fig. 3.10 and Fig. 3.11. The streamlines for both configurations suggest that no flow separation takes place in the channel in absence of overpotential patch (*i.e.* $\phi_p = 0$) and the reverse flow regions arise for non-zero (positive) strength of potential patch due to surface potential heterogeneity. The size of the vortex is balanced by the electrical force and the favorable pressure gradient. The overpotential regions attract more anions to the region near the patch and thus generate more reversed flow. The flow velocity increases if parallelly two obstacles with two overpotential patches are placed (Fig. 3.10 (b)) compared to a single obstacle with two overpotential regions (Fig. 3.9 (b)). The flow streamlines are increased up to 20% for a nanochannel of height 20nm with external electric field of 10^6 V/m and the overpotential strength is considered to $\phi_p = 0.2$. Electroosmotic circulation created by ducts is increased up to 11% incase of a overpotential region. The mole fraction distribution shows large variation when the flow past over two polarized blocks compared to a single polarized block with fixed overpotential patches along the upper wall. The plug-like velocity profile and core neutrality of mole fractions no longer exist close to the upstream and downstream of the overpotential regions (Fig. 3.11 (a) (b)).

3.8.3 Effect of E_x and Overpotential on the Pressure Distribution Due to Block Height

In Fig. 3.2, it is assumed that the channel is connected to large baths of upstream and downstream reservoirs where the filled fluid is initially at rest. The fluid starts movement within channel when the external electric field is applied. It is already predicted by several authors *e.g.* Wu et al. [277] and Peng et al. [212], that there was no axial pressure gradient in the fully developed EOF region. But there is a pressure effect when the flow is passing above the heterogeneous surface in fully developed regions means pressure is not zero in that level. Fig. 3.12 shows an example when the ratio of block height to channel height is considered to 0.2,

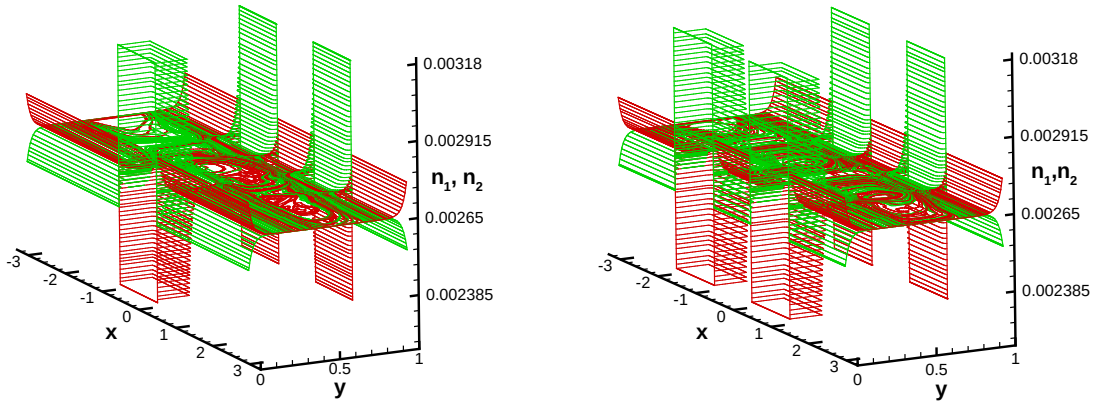

(a) (b)

Figure 3.11: Mole fraction distributions (a) case (I), (b) case (II), when $[Na^+] = 0.154\ M$, $[Cl^-] = 0.141\ M$, $H = 20\ nm$, $\epsilon = 0.05$ and $\phi_p = 0.2$.

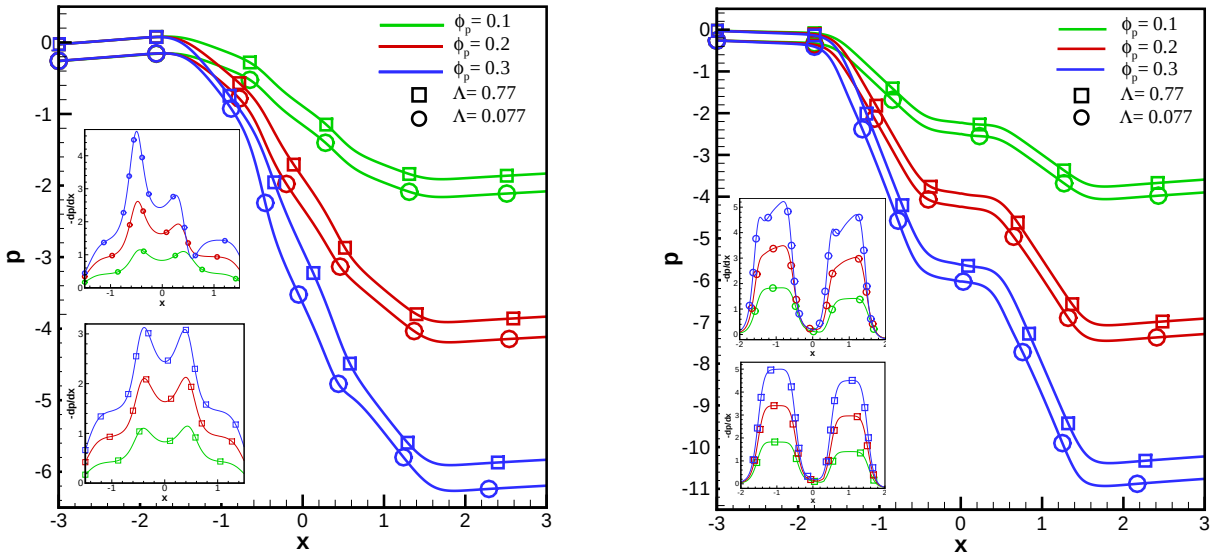

(a) (b)

Figure 3.12: Pressure distribution for different overpotential patch and external electric field strength for (a) case (I), (b) case (II), when $[Na^+] = 0.154\ M$, $[Cl^-] = 0.141\ M$, $H = 20\ nm$, $\epsilon = 0.05$.

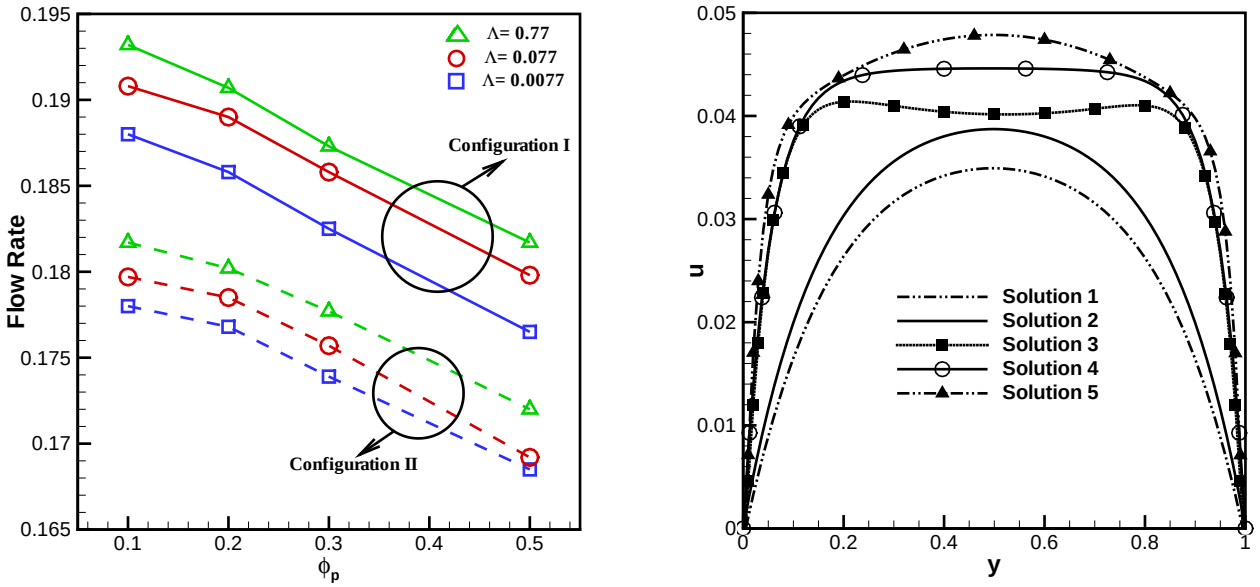

(a) (b)

Figure 3.13: (a) Volume flow rate for asymmetrically arranged nonuniform surface potential, for H=20 nm, $\epsilon = 0.05$. $n_1^0 = 0.00276$ $([Na^+] = 0.154\ M)$, $n_2^0 = 0.00252$ $([Cl^-] = 0.141\ M)$ with the variation of overpotential patch strength ϕ_p for different electric field strength. (b) Axial velocity at far upstream for different solution strength, Solution 1 (0.00105, 0.00095), Solution 2 (0.00154, 0.00141), Solution 3 (0.105, 0.095), Solution 4 (0.154, 0.141) and Solution 5 (0.308, 0.141).

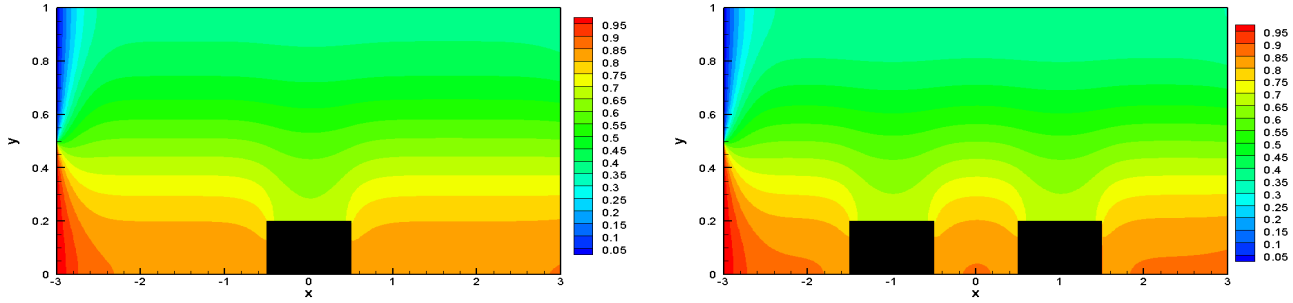

(a) (b)

Figure 3.14: Concentration levels for (a) case (I), (b) case (II), when $[Na^+] = 0.154\ M$, $[Cl^-] = 0.141\ M$, $H = 20\ nm$ and $\phi_p = 0.2$.

$E_x = 10^5\ V/m$ and surface potential is assumed to be 0. In this chapter we tried to clarify the existence of pressure variation in nano-channels by means of an analytical analysis in case of a fully developed EOF. Mostly, the analytical pressure values along the transverse directions provide a negative distribution for all the channel heights varying from H=20 nm to 100 nm. Close to the channel walls the pressure distribution provides a positive variation for all channel heights and as the distance increases from the wall, the values increase negatively reaching maximum variation along y=0.5. For H=20 nm the analytical pressure along the channel centerline is 0.18 where as the numerically computed value is about 0.2. The axial pressure distribution for different over potential strengths and the external electric field for case (I) are shown in Fig. 3.12(a). The inlet values of pressure differ due to the constant value appeared in the analytical solution for different electric fields. In the present observations we can expect the inlet fluid observes a different pressure for different external electric fields even if the solution and overpotential remains the same. The comparison between Fig. 3.12(a) and Fig. 3.12(b) provides a big difference if we can consider the gradient variation close to the obstacle. In the upstream edge of the patch a positive pressure gradient is found but the electric body force term present in the momentum equation generates a negative force due to the factor $(n_1 - n_2) < 0$, resulting an inflection point, i.e., $\frac{d^2u}{dy^2} > 0$ and leads to a flow separation. In both the cases it is observed that an increment in electric field strength and block height shows a large difference in pressure variation. For case (I) if the electric field strength is increasing from $10^5\ V/m$ to $10^6\ V/m$ for $\phi_p = 0.2$ the pressure is increasing up to 17% negatively but in case (II) it is showing variations up to 10% for a channel height of 20 nm. The increment in overpotential strength creates a pressure difference conversely compare to the earlier case. The variation is maximum in case (II) compared to case (I) if the overpotential strength is varying from 0.1 to 0.3. The variation of pressure in case (II) is 63% where as for case (I) it is observed to be 65%. But the variation of pressure in case (II) is larger compared to case (I). Since for a particular channel height and fixed overpotential patch and electric filed strength (0.1 and $10^5\ V/m$), the pressure is increased up to 45%.

3.8.4 Effect of External and Local Electric Field on Volume Flow Rate for a Given Block Height

The volume flow rate for a different external electric field strength $10^4\ V/m$, $10^5\ V/m$ and $10^6\ V/m$ with the variation of ϕ_p is presented in Fig. 3.13(a). If the channel dimension reduces, the reciprocal importance of surface to volume forces grow up which create an advantage for faster mixing of the entities with confined stream lines dominating the diffusion effect without

axial dispersion. From this figure, we can see that the volume flow rate drops significantly with the decrement of electric filed strength as well as with the increase of overpotential strength along the channel walls. It is already shown in Fig. 3.5(a) that both numerical and experimental observation predict the flow rate enhancement due to an increase in channel height. It is clearly observed from Fig. 3.13(a) that volume flow rate is increasing when the electric field increases. By the variation of electric field strength from $10^4\ V/m$ to $10^6\ V/m$ the volume flow rate is increased up to 4% for a fixed block height ($d = 0.2$). It can be observed that for a fixed electric field strength ($10^6\ V/m$), volume flow rate is decreased by 17% for increasing the overpotential strength from 0.1 to 0.5. This signifies that increased strength of the external electric field allows the species less time to diffuse. Thus, increasing the electric field strength results in a decrease of diffusive flux which corresponds less mixing.

The effective flow variation in terms of velocities for different ionic strength solutions both in dilute and strong cases in terms of cations and anions are considered as Solution 1 $(0.00105,\ 0.00095)$, Solution 2 $(0.00154,\ 0.00141)$, Solution 3 $(0.105,\ 0.095)$, Solution 4 $(0.154,\ 0.141)$ and Solution 5 $(0.308,\ 0.141)$ are presented in Fig. 3.13(b). The flow variation is plotted for $H = 20\ nm$ along the upstream region where one dimensional nature of the flow variation is predicted. The flow nature is shifted from parabolic nature to top hat profiles as the molarity is getting stronger.

3.8.5 Mixing Efficiency on the Effect of Overpotential Patch Strength

Mixing of different streams in microfluidics is a challenging task due to low inertial effects. The flow Reynolds number in such systems are too small due to the small characteristic length for which it is not possible to get the advantage of turbulence to stir the fluid streams to mix. Thus, the mass transfer in micro/nano-channels is mainly dominated by Fick's diffusion which is a very slow mechanism. Thus a long channel length is required to get a homogeneous mixture in the outlet when two streams of different concentrations are injected at the inlet. It is experimentally observed that the diffusion flux is proportional to the concentration gradient and the mixing interface area. In this chapter two fabricated channel geometry are proposed to get a significant mixing enhancement in a small channel length. The configurations are chosen in such a way that the concentration gradient can be improved sufficiently by creating surface heterogeneity through fabrication technique along the channel walls and simultaneously the mixing interface area can be made larger by placing blocks on the channel wall to maximize the overall diffusion flux to achieve a good mixing efficiency in the downstream of the channel.

To quantify the mixing enhancement along the streamwise direction of the channel, a parameter

named mixing efficiency (σ) is defined as [84],

$$\sigma = \left[1 - \frac{\int_{lower\ surface}^{upper\ surface} |C - C_\infty| dy}{\int_{lower\ surface}^{upper\ surface} |C_0 - C_\infty| dy}\right] \times 100\%, \tag{3.65}$$

where C represents the species concentration across the width of the channel. C_0 and C_∞ are the species concentrations in the completely unmixed ($C_0 = 0$ or 1) and fully mixed ($C_\infty = 0.5$) states respectively. Thus a fully mixed state would have 100% mixing efficiency, while the completely unmixed state would have 0% mixing efficiency. Fig. 3.14 shows the concentration contours for both configurations for $\phi_p = 0.2$ with $E_0 = 10^6\ V/m$. The corresponding species concentration profiles in the downstream is presented in Fig. 3.15 for both the configurations with various ϕ_p. It can be observed from Fig. 3.15 that for both configurations the downstream concentration profile approaches to fully mixed profile ($C = 0.5$) with increasing ϕ_p. It can also be noticed that for Case-II the downstream concentration profile is closer to 0.5 compared to Case-I for a fixed ϕ_p. The mixing efficiency for both the cases along the streamwise direction is presented in Fig. 3.16 (a) and (b). The mixing efficiency for $\phi_p = 0.1$, $\phi_p = 0.2$ and $\phi_p = 0.3$ at the downstream of the channel for Case-I are found to be 51.9%, 56.8% and 61.5% respectively. The decrement in total flow rate with increasing dimensionless overpotential patch (Fig. 3.13(a)) suggests that the fluid is allowed more time to diffuse in the channel which gives more mixing efficiency along the channel downstream. The mixing efficiency is improved for Case-II for each ϕ_p due to the presence of an extra block with potential heterogeneity which enhances the diffusive flux to give more homogeneous mixing. Compared to the earlier configuration the mixing efficiency is improved highly in Case-II, since the mixing efficiency reaches 54.1%, 61% and 65.15% for $\phi_p = 0.1$, $\phi_p = 0.2$ and $\phi_p = 0.3$ respectively.

The above discussions (theoretical and numerical) suggest that, Case- II is one of the most suitable technique for choosing a passive mixing method of the specific need and also advocate the novelty by using the standard fabrication techniques like nano-lithography [40, 82, 173], etching-and-deposition [279], DLP [127], sequentially patterned oxides [61], packing of different nano-particles [144] etc.

3.9 Conclusions

In this chapter, both numerical and analytical approaches are used to probe the effects of EOF in nano-channels. The change of pressure in case of a fully developed flow is computed analytically, where all of the previous studies directly assumed that axial pressure gradient is zero. The fully developed regions along the inlet upstream and outlet downstream regions are found by doing

several test runs and observe that a very small change of pressure gradient is occurring at the entry and exit locations. The steep variation of axial pressure gradient above the heterogeneous regions due to convection effect and body force terms in the momentum equation reflect a sharp variation of velocity components. The variation of electric field produces a induced positive pressure gradient along the axial direction and convective effects become stronger which produces a higher Lamb-vortex profile for v-velocity. In case of multiple blocks and overpotential regions the EOF produces a convective force dominating diffusion and axial dispersion process compared to a single block and obtains fully developed nature at far distances from the blocks. To optimize the mixing performance, augmented mixing efficiencies are created by formation of localized flow recirculation regions due to corrugated surfaces with overpotential regions which is important for design of lab-on-a-chip devices to avoid the lengthy diffusion based process. One more important factor is to specify the channel length to avoid the tip wall effects, as induced pressure gradient increases the dispersion of sample species which reduces the performance of the system [212]. The analytical proof suggests that velocity and pressure gradient are induced maximum above the corrugated region due to advective component but negligible if the flow approaches to fully developed nature.

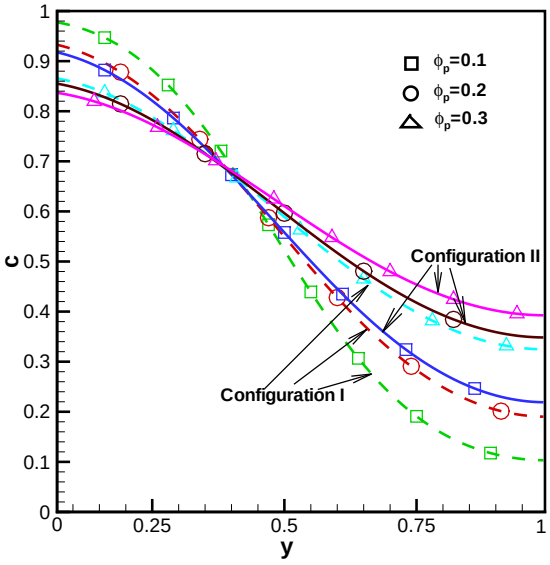

Figure 3.15: Concentration profile at the downstream of the channel for different ϕ_p, where $[Na^+] = 0.154\ M$, $[Cl^-] = 0.141\ M$, $\epsilon = 0.05$, channel height of 20 nm.

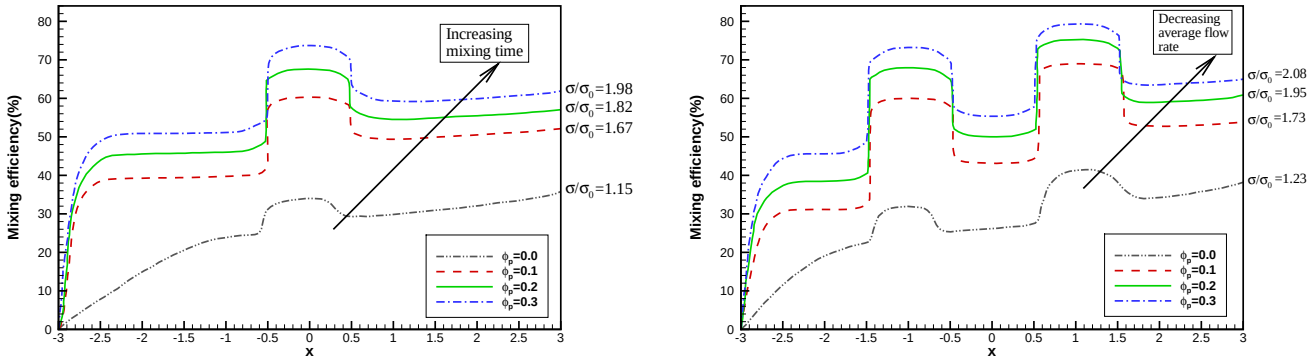

(a) (b)

Figure 3.16: Mixing efficiency for (a) case (I), (b) case (II) where $[Na^+] = 0.154\ M$, $[Cl^-] = 0.141\ M$, $H = 20\ nm$, $d = 0.2$, $E_0 = 10^6\ V/m$, $\epsilon = 0.05$. Here σ and σ_0 represent mixing efficiency for present configuration and plane channel with uniform zeta potential respectively.

Chapter 4

Enhanced Mixing and Flow Reversal in a Modulated Micro-Channel

4.1 Introduction

The transport mechanism in micro/nano-fluidic systems has evolved into a research field of fundamental curiosity due to its wide range of applications in electronics, medical sciences and biology [249, 288]. Recently, transport of biofluids through micro & nano channels has received much attention, as EOF with micro pumping method is used in many systems, such as familiar micro-electrical mechanical systems (MEMS) [152], intervenous drug delivery systems, Lab-on-a-Chip (LOC) [85], micromixers [262] etc. Traditionally, flow in channels with large characteristic scale is often driven by pressure gradient, supplied by mechanical pumping, but this technique becomes increasingly difficult when the characteristic scale comes down to micro-nano level due to fatigue, mechanical failure and fabrication difficulty. To overcome such drawbacks, electrokinetic force driven flow is generally adopted in micro/nano-fluidics in which the driving momentum is achieved through the influence of external electric field and EDL. The electrokinetic interaction of electrolyte solution with the charged channel wall forms the EDL. Also, this interaction creates an electromotive force close to the channel walls and provokes fluid motion (electroosmosis) [219, 269] which is gradually transmitted to the adjacent layers through the viscous drag [219].

Rapid mixing in microfluidic systems is essential due to its applications in biomedical analysis, nucleic acid synthesis, targeted drug delivery, chemical synthesis, DNA hybridization etc. [55, 56, 70, 114]. However rapid mixing in such small scales is very challenging as it is

not possible to take advantage of turbulence in weak Reynolds number (Re) system. Thus, the transport mechanism is dominated by the diffusion effect to mix miscible fluid layers in laminar flow regime. Consequently, it is challenging to execute a desirable mixing within a reasonable time in a limited channel length as diffusion dominated mixing takes place very slowly [120,204]. This mechanism is obviously incompatible with the general trend towards device miniaturization, and thus it becomes an important issue to the researchers for the fabrication of micro/nano channels to get the optimum flow mixing.

Micromixers, depending on the strategy of mixing as reported in the literature can be separated into two major categories: active and passive mixers [52]. In active mixing scheme, sample streams are mixed through induced periodic or aperiodic perturbation forces, e.g. pressure perturbations [143,199], thermal perturbations [7,131,268], magnetic perturbations [107,200], electrical stirring perturbations [138,174,201] or a combined perturbation due to magnetic and electric fields [21]. The structure of active mixers are often comparatively simple, easy to control, but the requirement of energy sources makes them difficult to integrate [39] & moreover, the manufacturing cost is relatively expansive [153]. In contrast, passive micromixers rely on chaotic advection or diffusion which reduces the complexity of integration, fabrication and power consumption. Therefore, passive micromixers, fabricated by geometric and surface modulation are widely used as compared to the active micromixers. Such micromixers are designed to provide more contact surface area between the fluid layers to increase the diffusion flux. In order to achieve a desirable mixing in passive micromixers, geometric modulation can be created in addition to surface heterogeneity to fold and stretch the fluid streams through specified designs, e.g. patterned block structures [20,30,66,202], conducting barriers [14,276], convergent-divergent geometry [2], sharp corner structure [87], grooved structures [6,266], zig-zag geometry [57,59], sinusoidal wavy structured walls [37,50,65] etc. Subsequently, efforts are made for quantitative improvement of mixing in both design as well as fluid control. In this regard surface modulation provides large surface area to volume ratio for saturated concentrations. In addition to geometric modulation, peristaltic channels geometry may be effective in transporting reagents in miniature Lab-On-a-Chip systems for mixing purposes [19,222]. In the recent past, a number of analytic and numerical studies have been carried out by several authors on wavy surfaces and peristaltic motions in micro and macro devices [180–183,257].

The fluid advection effect in the heterogeneous region plays an important role for ion transport [17,27,28]. The available literature on mixing mostly follows the Poisson-Bolzmann distribution along with surface heterogeneity due to surface modulation and extra potential, without

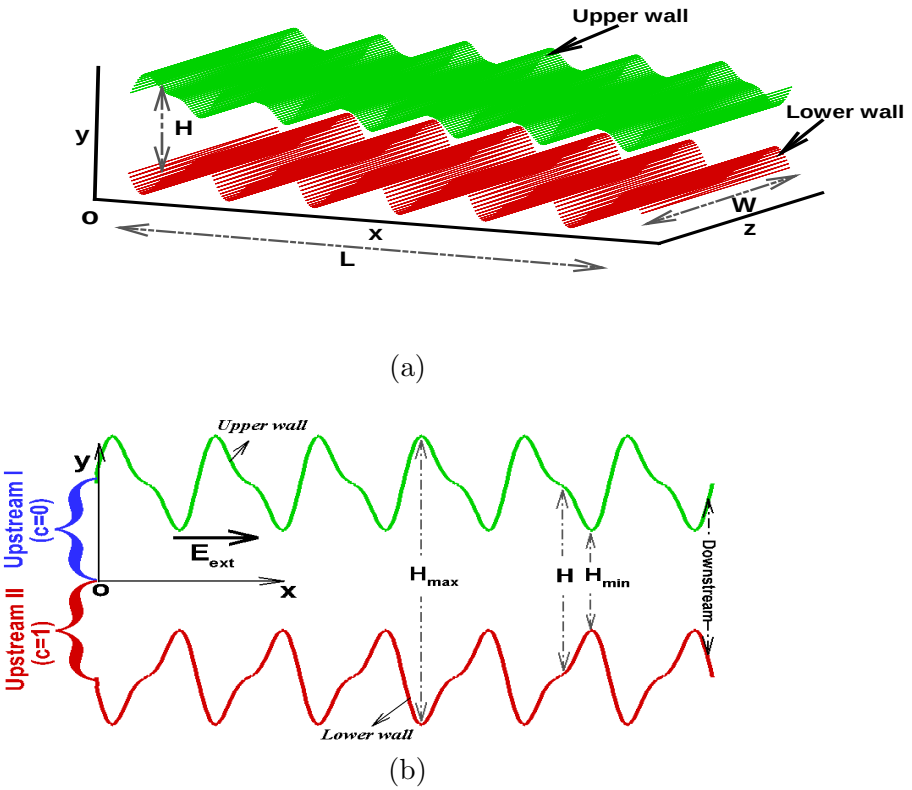

Figure 4.1: (a) Physical geometry (3D) (b) Computational domain (2D).

considering the effect of well built advection and ionic electromigration terms. However, an advective component of ion transport may be introduced into the flow field and concentration distributions through nonuniform surface charge (ζ - potential) and geometric barriers [23, 190]. In this chapter, following the recent developments on micro scale mixing, we propose a modulated micromixer design based on geometric modulation by incorporating two sinusoidal wave functions into channel walls symmetrically in the framework of Poisson-Nernst-Planck model. Park et al. [208] performed an analytical study to estimate the relationship between flow governing factors for formation of eddies (perimeter eddy and central eddy) in a constricted cylindrical domain. A phase diagram for both types of eddy formation has been presented as a function of Debye length, aspect ratio and wave amplitude. Following this idea, the critical modulation factor (scaled wave amplitude) for the appearance of recirculating eddies (primary and secondary eddy) near the channel walls are investigated numerically in this chapter for a large range of

flow governing parameters (external electric field and solution's molar strength). In section 2, the geometric configuration of the problem, mathematical modelling and dimensionless parameters are described. In section 3, the numerical schemes with the discretization technique is presented. In the following section, the key issue of this study, enhancing mixing efficiency as well as determining critical wave amplitude for a wide range of wave amplitude, electric field strength and Debye-H*ü*ckel parameter are described to optimize the mixing enhancement with respect to the controlling parameters.

4.2 Mathematical Formulation

This chapter focuses on the ion transport mechanism of an aqueous electrolyte in a long channel with corrugated side walls of length L, width W and average height H as shown in Figure 4.1. The width of the channel is assumed to be in the order of its length and the flow field is considered as two dimensional. The side walls are symmetric and comprised of two superimposed sinusoidal wave structured surface which forms converging-diverging flow domain. The fluid flow is driven through an external electric field along the channel & the fluid is assumed to be incompressible and Newtonian. The surface potential (ζ-potential) is assumed to be distributed uniformly along the surface walls with constant magnitude and the externally applied electric field is considered to be acted along the streamwise direction. The wall corrugation is considered to be a superposition of two sinusoidal waves as

$$\left.\begin{aligned} y^*(x^*) &= \pm\mathcal{F}^*(x^*) \\ &= \pm 0.5H \pm [\alpha_1^* sin(2\pi x^*/H) + \alpha_2^* sin(4\pi x^*/H)] \end{aligned}\right\} \tag{4.1}$$

where "$\pm$" signs represent upper $(+)$ and lower $(-)$ wavy walls respectively. Here α_1^* and α_2^* denote the wave amplitudes of two superimposed sinusoidal waves. By scaling the coordinates by H (i.e. $x = x^*/H$ and $y = y^*/H$), the scaled amplitudes α_1 and α_2 are defined as $\alpha_1 = \alpha_1^*/H$ and $\alpha_2 = \alpha_2^*/H$ respectively. The geometry of the corrugated surfaces are characterized by the parameter R_α $(= \alpha_1/\alpha_2)$, called amplitude ratio.

The physical domain with wavy side walls is transformed into rectangular geometry with a suitable coordinate transformation as

$$\xi = x, \qquad \eta = \frac{y}{\mathcal{F}(x)},$$

where $\mathcal{F}(x) = \frac{1}{H}\mathcal{F}^*(x^*)$. In the framework of continuum hypothesis, the governing equations

for the transport of incompressible, ionized, isothermal, Newtonian fluid is governed by Navier-Stokes equations, which can be expressed in dimensionless form as [169]

$$\nabla \cdot \mathbf{q} = 0 \tag{4.2}$$

$$Re(\mathbf{q} \cdot \nabla)\mathbf{q} + \nabla p - \nabla^2 \mathbf{q} + \frac{(\kappa H)^2}{2\Lambda} \rho_e \nabla(\phi + \psi) = 0 \tag{4.3}$$

where

$$\nabla \equiv \left(\frac{\partial}{\partial \xi} - \eta \frac{\mathcal{F}'}{\mathcal{F}} \frac{\partial}{\partial \eta}, \frac{1}{\mathcal{F}} \frac{\partial}{\partial \eta} \right)$$

and

$$\nabla^2 \equiv \frac{\partial^2}{\partial \xi^2} - 2\eta \frac{\mathcal{F}'}{\mathcal{F}} \frac{\partial^2}{\partial \xi \partial \eta} + \left[\eta^2 \left(\frac{\mathcal{F}'}{\mathcal{F}} \right)^2 + \frac{1}{\mathcal{F}^2} \right] \frac{\partial^2}{\partial \eta^2} + \eta \left[2 \left(\frac{\mathcal{F}'}{\mathcal{F}} \right)^2 - \frac{\mathcal{F}''}{\mathcal{F}} \right] \frac{\partial}{\partial \eta}.$$

Here $\mathbf{q}$=(u, v) is the dimensionless velocity vector scaled by the Helmholtz-Smoluchowski velocity ($U_{HS} = \epsilon_e \phi_0 E_0/\mu$) and $\rho_e = (n_1 - n_2)$ is the non-dimensional net charge density scaled by $n_0 e$ where n_i is the concentration of i^{th} ionic species with valance z_i. We scale other dimensional variables as follows: the spatial coordinates by the average height of the channel (H), $\mu U_{HS}/H$ is the pressure scale, $\phi_0 = k_B T/e$ is the scale for electric potentials and the bulk number concentration (n_0) is the number concentration scale [7,30]. The non-dimensional number Λ ($= E_0 H/\phi_0$) and Re ($= \rho U_{HS} H/\mu$) denote dimensional electric potential and Reynolds number respectively. Here μ, ρ, E_0, e, k_B and T stand for fluid visocity, fluid density, dimensional externally applied electric field, elementary charge, Boltzmann's constant and absolute temperature respectively. The inverse EDL thickness is defined as κ ($= \lambda^{-1}$) $= \sqrt{2en_0/\varepsilon_e \phi_0}$. Here ϕ and ψ are respectively denoted the induced potential due to the formation of EDL and the external potential due to applied electric field.

The induced potential due to wall charge density is described by the Poisson's equation

$$\nabla^2 \phi = -\frac{(\kappa H)^2}{2} \rho_e. \tag{4.4}$$

The electric potential due to external electric field is obtained by the solution of Laplace equation $\nabla^2 \psi = 0$ with electrically insulated boundary condition, i.e. $\nabla \psi \cdot \mathbf{n} = 0$, where $\mathbf{n}$ represents the unit normal to the corresponding surface pointing towards the domain.

The non-dimensional form of the Nernst-Planck equation governing the transport of i^{th} species is [33]

$$Pe(\mathbf{q} \cdot \nabla n_i) = \nabla^2 n_i + z_i \nabla n_i \cdot \nabla(\phi + \psi) - \frac{(\kappa H)^2}{2} z_i n_i \rho_e \tag{4.5}$$

The present model (Poisson-Nernst-Planck) has the flexibility to handle multivalent ions. For simplicity we consider simple $1:1$ electrolyte (e.g. $NaCl + H_2O$) with $z_i = \pm 1$ for $i = 1, 2$ respectively and the diffusivity of both the species are considered to be equal i.e. $D_1 = D_2 = D$. Here Pe is the Peclet number which measures the ratio of advective to diffusive transport of ions & is defined as $Pe = HU_{HS}/D$.

The fluid is assumed to maintain no-slip condition for velocity and no-ion penetration condition for species along the boundary walls. Along the channel walls some prescribed zeta potential (or surface charge density) is assumed. Thus the wall boundary conditions are as follows:

$$\mathbf{q} = \mathbf{0};\ (\nabla n_i + z_i n_i \nabla \phi) \cdot \mathbf{n} = 0;\ \phi = \zeta,$$

where $\mathbf{n}$ represents the unit normal vector along the channel walls indicating towards the fluid and ζ is the surface potential. A periodic boundary condition is considered for all the flow variables along the upstream and downstream of the main flow domain.

4.2.1 Transportation of Eluted Species

Transportation of the uncharged eluted species is defined by the combined species convection-diffusion equation. In the absence of species absorption and chemical reaction, the dimensionless species transport equation is of the form

$$(\mathbf{q} \cdot \nabla) C - \frac{1}{Pe_S} \nabla^2 C = 0, \tag{4.6}$$

where C is the non-dimensional species concentration scaled by C_{ref} and $Pe_s (= U_{HS} H/D_s)$ represents the Peclet number for eluted mixing species. Here D_s symbolizes the diffusion coefficient of the mixing species. To obtain mixing efficiency at different cross sections of the channel, no mass flux ($\nabla C \cdot \mathbf{n} = 0$) is assumed at walls ($y = \pm \mathcal{F}(x)$) and $\frac{\partial C}{\partial x} = 0$ is considered along the outlet boundary. At the inlet of the channel ($x = 0$) a step-like concentration distribution is assumed, i.e. $C = 1$ in the lower half ($-\mathcal{F}(x) \leq y \leq 0$) and $C = 0$ in the upper half ($0 < y \leq \mathcal{F}(x)$).

A measure of species mixing at different levels of the channel is defined by a (mixing efficiency) parameter, σ, as [84, 190]

$$\sigma = \left[1 - \frac{\int_{-\mathcal{F}(x)}^{\mathcal{F}(x)} |C - C_\infty| dy}{\int_{-\mathcal{F}(x)}^{\mathcal{F}(x)} |C_0 - C_\infty| dy} \right] \times 100\%.$$

Here C_∞ and C_0 represent the concentrations at the mixed ($C_\infty = 0.5$) and unmixed ($C_0 = 0$ *or* 1) states, respectively. Mixing efficiency is 100% when the two species are in fully mixed condition and a completely unmixed mode signifies 0% mixing efficiency.

The non-dimensional parameters governing the electrokinetic flow of ionized species with uncharged eluted species through the wavy channel are defined by Re, Pe, Pe_s, α_1, Λ and the Debye-Hückel parameter κH.

4.3 Numerical Method

In the simulations, a staggered grid based finite volume method (FVM) is used to solve the coupled set of non-linear equations [4.2-4.6] [89, 227, 245, 286]. In integrating the coupled equations over the control volumes, a fully implicit scheme is used for unsteady terms, whereas QUICK [145] scheme is used for convective terms in the mass transfer and momentum equations. To cope with the non-linearity, Newton's linearization technique is adopted in the above set of equations. The discretized set of equations are solved through SIMPLE [210] algorithm which is based on a cyclic prediction-correction operations. Velocity field is coupled with pressure field to justify the conservation laws of mass and generate the pressure Poisson equation. We have implemented successive over relaxation (SOR) iterative scheme to obtain the solution of pressure upto a desired accuracy.

The detailed analysis of the numerical scheme used in this chapter are mentioned below. On integrating the $u-$ and $v-$ momentum equations at the $(n+1)^{th}$ time step over the $(j,k)^{th}$ control volumes for u and v (Fig. 4.2) respectively, yield

$$\left.\begin{aligned} a_j^u u_{j-1,k}^{n+1} + b_j^u u_{j,k}^{n+1} + c_j^u u_{j+1,k}^{n+1} &= d_j^u - \left(p_{j+1,k}^{n+1} - p_{j,k}^{n+1}\right)\Delta\eta_k + \tfrac{1}{8}\eta_k\left(\frac{\mathcal{F}'}{\mathcal{F}}\right)_j \\ &\quad \times\left(p_{j,k+1}^{n+1} + p_{j+1,k+1}^{n+1} - p_{j,k-1}^{n+1} - p_{j+1,k-1}^{n+1}\right)(\Delta\xi_j + \Delta\xi_{j+1}) \\ a_j^v v_{j-1,k}^{n+1} + b_j^v v_{j,k}^{n+1} + c_j^v v_{j+1,k}^{n+1} &= d_j^v - \left(\tfrac{1}{\mathcal{F}}\right)_j\left(p_{j,k+1}^{n+1} - p_{j,k}^{n+1}\right)\Delta\xi_j \end{aligned}\right\} \quad (4.7)$$

The mole-fraction equations for the species (counter ion and co-ion) at the $(n+1)^{th}$ time step over the $(j,k)^{th}$ scalar control volume gives

$$\left.\begin{aligned} a_j^{n_1} n_{1_{j-1,k}}^{n+1} + b_j^{n_1} n_{1_{j,k}}^{n+1} + c_j^{n_1} n_{1_{j+1,k}}^{n+1} &= d_j^{n_1} \\ a_j^{n_2} n_{2_{j-1,k}}^{n+1} + b_j^{n_2} n_{2_{j,k}}^{n+1} + c_j^{n_2} n_{2_{j+1,k}}^{n+1} &= d_j^{n_2} \end{aligned}\right\} \quad (4.8)$$

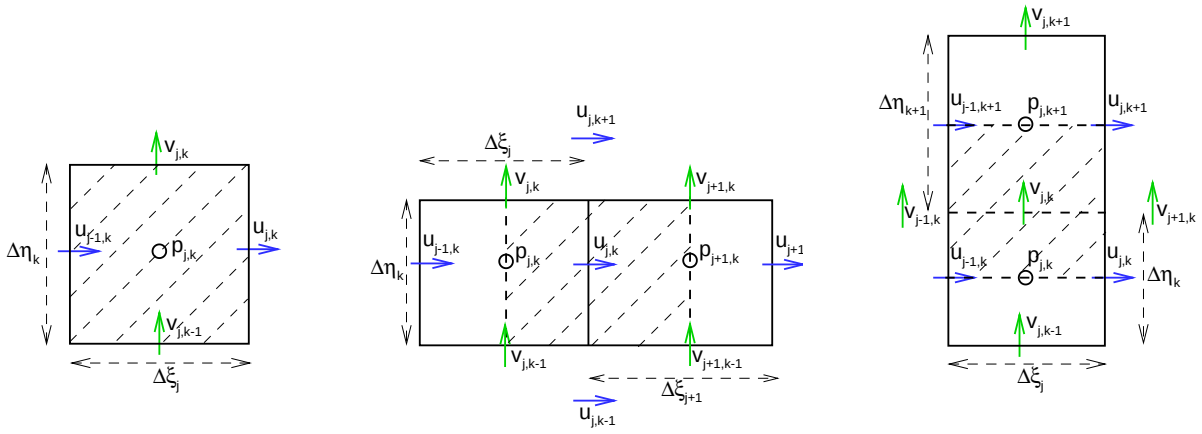

(a) Scalar control volume

(b) u- control volume

(c) v- control volume

Figure 4.2: Schamatic of different control volumes.

Here n_1 and n_2 stand for mole-fraction for counter and co-ions respectively. Thus for a fixed value of k, the system of equations can be expressed in a matrix form as

$$A_j X_{j-1}^{n+1} + B_j X_j^{n+1} + C_j X_{j+1}^{n+1} = D_j, \tag{4.9}$$

where the coefficient matrices (A_j, B_j, C_j), the known vector (D_j) and the vector of unknown variables (X_j) are given by

$$A_j = \begin{bmatrix} a_j^u & 0 & 0 & 0 \\ 0 & a_j^v & 0 & 0 \\ 0 & 0 & a_j^{n_1} & 0 \\ 0 & 0 & 0 & a_j^{n_2} \end{bmatrix}; \; B_j = \begin{bmatrix} b_j^u & 0 & 0 & 0 \\ 0 & b_j^v & 0 & 0 \\ 0 & 0 & b_j^{n_1} & 0 \\ 0 & 0 & 0 & b_j^{n_2} \end{bmatrix}; \; C_j = \begin{bmatrix} c_j^u & 0 & 0 & 0 \\ 0 & c_j^v & 0 & 0 \\ 0 & 0 & c_j^{n_1} & 0 \\ 0 & 0 & 0 & c_j^{n_2} \end{bmatrix};$$

$$X_j = \begin{bmatrix} u_{j,k}^{n+1} \\ v_{j,k}^{n+1} \\ n_{1_{j,k}}^{n+1} \\ n_{2_{j,k}}^{n+1} \end{bmatrix}; \; D_j = \begin{bmatrix} d_j^u - \left(p_{j+1,k}^{n+1} - p_{j,k}^{n+1}\right)\Delta\eta_k + \frac{1}{8}\eta_k \left(\frac{\mathcal{F}'}{\mathcal{F}}\right)_j \left(p_{j,k+1}^{n+1} + p_{j+1,k+1}^{n+1} - p_{j,k-1}^{n+1} \right. \\ \left. - p_{j+1,k-1}^{n+1}\right)(\Delta\xi_j + \Delta\xi_{j+1}) \\ d_j^v - \left(\frac{1}{\mathcal{F}}\right)_j \left(p_{j,k+1}^{n+1} - p_{j,k}^{n+1}\right)\Delta\xi_j \\ d_j^{n_1} \\ d_j^{n_2} \end{bmatrix}.$$

Thus the system of equation can be written in a matrix from as

$$\mathbf{AX} = \mathbf{D}, \tag{4.10}$$

where A represents a block tridiagonal matrix, each element of which is a square matrix of order four. Here X, D stands for the vector of unknown variables and the vector of known quantities respectively. The matrix equation is solved using block elimination Varga's Algorithm (Appendix).

On integrating the continuity equation over $(j,k)^{th}$ scalar control volume, we have

$$\left(u_{j,k}^{n+1}-u_{j-1,k}^{n+1}\right)\Delta\eta_k-\frac{\eta_k}{4}\left(\frac{\mathcal{F}'}{\mathcal{F}}\right)_j\left(u_{j-1,k+1}^{n+1}+u_{j,k+1}^{n+1}-u_{j-1,k-1}^{n+1}-u_{j,k-1}^{n+1}\right)\Delta\xi_j + \left(\frac{1}{\mathcal{F}}\right)_j\left(v_{j,k}^{n+1}-v_{j,k-1}^{n+1}\right)\Delta\xi_j=0. \tag{4.11}$$

The pressure link between the continuity and momentum equations are accomplished by transforming the discretized continuity equation into a Poisson's equation for pressure correction. This pressure correction equation implements a divergence free velocity field.

At initial stage, pressure $p_{j,k}$ is unknown at each cell. To get a solution for equation 4.10, we guess a pressure field $p_{j,k}^c$. Corresponding to this guessed pressure field $p_{j,k}^*$, the velocity field $(u_{j,k}^*, v_{j,k}^*)$ is determined form equation 4.7. Since $u_{j,k}^*, v_{j,k}^*$ satisfy equation 4.7, then

$$\left.\begin{aligned} a_j^u u_{j-1,k}^* + b_j^u u_{j,k}^* + c_j^u u_{j+1,k}^* &= d_j^u - \left(p_{j+1,k}^*-p_{j,k}^*\right)\Delta\eta_k + \tfrac{1}{8}\eta_k\left(\tfrac{\mathcal{F}'}{\mathcal{F}}\right)_j \\ &\quad\times\left(p_{j,k+1}^*+p_{j+1,k+1}^*-p_{j,k-1}^*-p_{j+1,k-1}^*\right)(\Delta\xi_j+\Delta\xi_{j+1}) \\ a_j^v v_{j-1,k}^* + b_j^v v_{j,k}^* + c_j^v v_{j+1,k}^* &= d_j^v - \left(\tfrac{1}{\mathcal{F}}\right)_j (p_{j,k+1}^*-p_{j,k}^*)\Delta\xi_j \end{aligned}\right\} \tag{4.12}$$

Since the velocity field $(u_{j,k}^*, v_{j,k}^*)$, corresponding to the guessed pressure $p_{j,k}^*$ may not satisfy the continuity equation (Eq. 4.11), a correction of velocity field is needed. The correction of the velocity field can be made through a pressure correction. The pressure link between the momentum and continuity equations is accomplished by transforming the continuity equation (Eq. 4.11) into a pressure Poisson equation. Let $p_{j,k}^c$ be the pressure correction at $(j,k)^{th}$ cell and $(u_{j,k}^c, v_{j,k}^c)$ be the corresponding correction in velocity field. Thus the updated pressure and velocity field can be expressed as

$$\left.\begin{aligned} p_{j,k}^{n+1} &= p_{j,k}^* + p_{j,k}^c \\ u_{j,k}^{n+1} &= u_{j,k}^* + u_{j,k}^c \\ v_{j,k}^{n+1} &= v_{j,k}^* + v_{j,k}^c \end{aligned}\right\}. \tag{4.13}$$

Substituting equation 4.12 from equation 4.7, we get a relation between pressure correction and

velocity correction as

$$\left.\begin{aligned} a_j^u u_{j-1,k}^c + b_j^u u_{j,k}^c + c_j^u u_{j+1,k}^c &= -\left(p_{j+1,k}^c - p_{j,k}^c\right)\Delta\eta_k + \tfrac{1}{8}\eta_k\left(\tfrac{\mathcal{F}'}{\mathcal{F}}\right)_j\left(p_{j,k+1}^c + \right. \\ &\qquad \left. p_{j+1,k+1}^c - p_{j,k-1}^c - p_{j+1,k-1}^c\right)(\Delta\xi_j + \Delta\xi_{j+1}) \\ a_j^v v_{j-1,k}^c + b_j^v v_{j,k}^c + c_j^v v_{j+1,k}^c &= -\left(\tfrac{1}{\mathcal{F}}\right)_j\left(p_{j,k+1}^c - p_{j,k}^c\right)\Delta\xi_j \end{aligned}\right\} \tag{4.14}$$

Ignoring, the neighboring small correction components as

$$\left.\begin{aligned} u_{j,k}^c &= -\tfrac{\Delta t}{0.5(\Delta\xi_j+\Delta\xi_{j+1})}\left(p_{j+1,k}^c - p_{j,k}^c\right) \\ &\quad +\tfrac{1}{4}\eta_k\left(\tfrac{\mathcal{F}'}{\mathcal{F}}\right)_j\tfrac{\Delta t}{\Delta\eta_k}\left(p_{j,k+1}^c + p_{j+1,k+1}^c - p_{j,k-1}^c - p_{j+1,k-1}^c\right) \\ v_{j,k}^c &= -\tfrac{\Delta t}{0.5(\Delta\eta_k+\Delta\eta_{k+1})}\left(\tfrac{1}{\mathcal{F}}\right)_j\left(p_{j,k+1}^c - p_{j,k}^c\right) \end{aligned}\right\} \tag{4.15}$$

Substituting the corrected velocity field $(u_{j,k}, v_{j,k})$ into the continuity equation, the following Poisson's equation for pressure corection is obtained.

$$\begin{aligned} &p_{j-1,k}^c\left[-\alpha_u\frac{\Delta t\Delta\eta_k}{0.5(\Delta\xi_j+\Delta\xi_{j+1})} + \frac{1}{8}\alpha_u\left\{\eta_k\left(\frac{\mathcal{F}'}{\mathcal{F}}\right)_j\right\}^2\frac{\Delta t\Delta\xi_j}{\Delta\eta_k}\right] \\ &+p_{j,k}^c\left[2\alpha_u\frac{\Delta t\Delta\eta_k}{0.5(\Delta\xi_j+\Delta\xi_{j+1})} + 2\alpha_v\left\{\left(\frac{1}{\mathcal{F}}\right)_j\right\}^2\frac{\Delta t\Delta\xi_j}{0.5(\Delta\eta_k+\Delta\eta_{k+1})} + \frac{1}{4}\alpha_u\left\{\eta_k\left(\frac{\mathcal{F}'}{\mathcal{F}}\right)_j\right\}^2\frac{\Delta t\Delta\xi_j}{\Delta\eta_k}\right] \\ &+p_{j+1,k}^c\left[-\alpha_u\frac{\Delta t\Delta\eta_k}{0.5(\Delta\xi_j+\Delta\xi_{j+1})} + \frac{1}{8}\alpha_u\left\{\eta_k\left(\frac{\mathcal{F}'}{\mathcal{F}}\right)_j\right\}^2\frac{\Delta t\Delta\xi_j}{\Delta\eta_k}\right] \\ &\quad = -div^* - \frac{1}{4}\alpha_u\eta_k\left(\frac{\mathcal{F}'}{\mathcal{F}}\right)_j\Delta t\left(p_{j+1,k+1}^c + p_{j-1,k-1}^c - p_{j+1,k-1}^c - p_{j-1,k+1}^c\right) \\ &\qquad -\frac{1}{4}\alpha_u\eta_k\left(\frac{\mathcal{F}'}{\mathcal{F}}\right)_j\frac{\Delta t\Delta\xi_j}{0.5(\Delta\xi_j+\Delta\xi_{j+1})}\left(p_{j+1,k+1}^c + p_{j-1,k-1}^c - p_{j+1,k-1}^c - p_{j-1,k+1}^c\right) \\ &\qquad +\frac{1}{16}\alpha_u\left\{\eta_k\left(\frac{\mathcal{F}'}{\mathcal{F}}\right)_j\right\}^2\frac{\Delta t\Delta\xi_j}{\Delta\eta_k}\left(p_{j-1,k+2}^c + p_{j-1,k-2}^c + 2p_{j,k+2}^c + 2p_{j,k-2}^c \right. \\ &\qquad\qquad \left. +p_{j+1,k+2}^c + p_{j+1,k-2}^c\right) \\ &\qquad +\alpha_v\left\{\left(\frac{1}{\mathcal{F}}\right)_j\right\}^2\frac{\Delta t\Delta\xi_j}{0.5(\Delta\eta_k+\Delta\eta_{k+1})}\left(p_{j,k+1}^c + p_{j,k-1}^c\right), \end{aligned} \tag{4.16}$$

where

$$\begin{aligned} div^* = &\left(u_{j,k}^* - u_{j-1,k}^*\right)\Delta\eta_k - \frac{\eta_k}{4}\left(\frac{\mathcal{F}'}{\mathcal{F}}\right)_j\left(u_{j-1,k+1}^* + u_{j,k+1}^* - u_{j-1,k-1}^* - u_{j,k-1}^*\right)\Delta\xi_j \\ &+\left(\frac{1}{\mathcal{F}}\right)_j\left(v_{j,k}^* - v_{j,k-1}^*\right)\Delta\xi_j. \end{aligned} \tag{4.17}$$

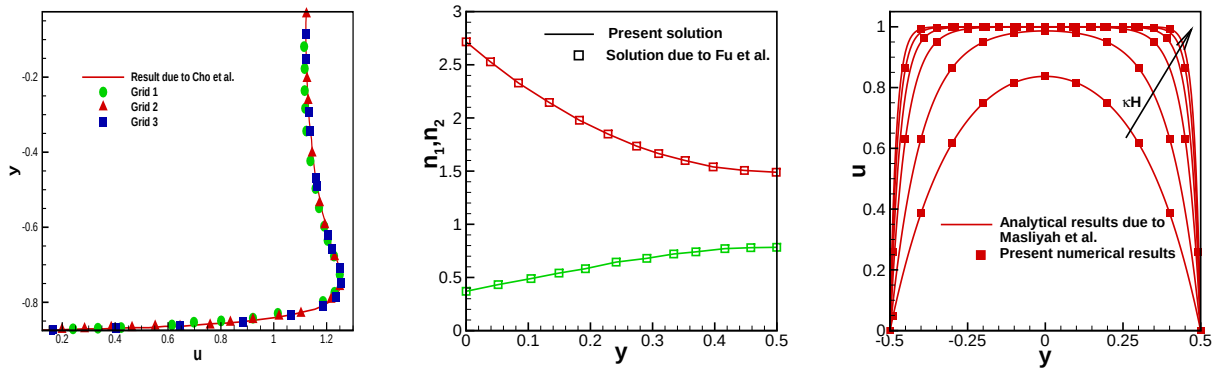

(a) (b) (c)

Figure 4.3: (a) Comparison for streamwise velocity at wavy crest with Cho et al. [63] for a symmetric wavy channel of the form $y = \pm\{0.5 + \alpha_1 sin(2\pi x) + \alpha_2 sin(4\pi x)\}$. Here $\alpha_1 = 0.05$, $\alpha_2 = 0.02$, $\kappa H = 50$ and $E_0 = 100\ V\ cm^{-1}$. (b) Mole-fractions comparison with Fu et al. [90] for a plane channel when the concentration of the bulk electrolyte is $10^{-4}\ mol\ m^{-3}$, external electric field $E_0 = 10^4\ Vm^{-1}$ and channel height $H = 0.1\ \mu m$. Here n_1 and n_2 stand for counter-ion and co-ion respectively. (c) Axial velocity comparison for plane channel with the analytic solutions due to Masliyah et al. [169] for $\kappa H = 5, 10, 20, 30, 40, 50$.

Here α_u and α_v are relaxation factors corresponding to axial and transverse velocity corrections respectively. The Eq. 4.16 is solved using a Gauss-Seidel iterative method to achieve the pressure correction $(p^c_{j,k})$ at each cell of the flow domain. For rapid convergence, the pressure field is under-relaxed as

$$p^{n+1}_{j,k} = p^*_{j,k} + \alpha_p p^c_{j,k}, \tag{4.18}$$

where α_p is the under-relaxation factor. The relaxation factor is taken between 0 and 1, so that guessed pressure field is added in a fraction of the corrected pressure field p^c, in order to improve iteration process to carry forward. Similarly, the velocity components $u^{n+1}_{j,k}$ and $v^{n+1}_{j,k}$ are under-relaxed in the following manner:

$$\left.\begin{aligned} u^{n+1}_{j,k} &= u^*_{j,k} + \alpha_u u^c_{j,k} \\ v^{n+1}_{j,k} &= v^*_{j,k} + \alpha_v v^c_{j,k} \end{aligned}\right\}. \tag{4.19}$$

A rapid convergence is found in this chapter for $\alpha_p = 0.5$ and $\alpha_u = 2/3 = \alpha_v$. Thus any time step of this algorithm consists of sequential steps, discussed in Chapter 1 (Section 1.8).

4.3.1 Code Validation

In order to validate the numerical algorithm, results for velocity and mole-fractions distribution of the present scheme are compared with several existing results. The numerical simulations are performed with the non-uniform grid arrangement to capture the gradients of all

the flow variables for which dense grids are chosen close to the wavy walls with $\delta t = 0.001$. A grid independence test is performed with three different grid sizes with $Grid\ 1 : 200 \times 200$ ($\Delta\xi_j = 0.01, \Delta\eta_k = 0.01$), $Grid\ 2 : 200 \times 480$ ($\Delta\xi_j = 0.01, 0.0025 \leq \Delta\eta_k \leq 0.005$), $Grid\ 3 : 400 \times 480$ ($\Delta\xi_j = 0.005, 0.0025 \leq \Delta\eta_k \leq 0.005$) for a single periodic transformed domain and compared with the result by Cho et al. [63]. Fig. 4.3 (a) suggests that our results are in a good agreement for $Grid\ 2$ and $Grid\ 3$ with the result of streamwise velocity at wave crest as of Cho et al. [63]. All the computations are performed for the simulated results with the optimum meshing $Grid\ 2$. The computed results for mole-fraction distributions for $\mathcal{F}(x) = 1$ agrees well with the result by Fu et al. [90] (Fig. 4.3 (b)). The results for u-velocity is compared with the analytic solution of Masliyah and Bhattacharjee [169] for a non-wavy channel ($\alpha_1 = 0$) with different κH, shown in Fig. 4.3 (c) and are found to be an excellent agreement.

4.4 Results and Discussions

The typical height of the channel is assumed to be 5 μm with the channel length of 50 μm. In addition, it is assumed that the wall potential is uniformly distributed with magnitude $\zeta = -1$ ($\zeta^* = -25.6\ mV$) and the externally applied electric field is considered to be applied along the primary flow direction which is assumed to vary from $\Lambda = 1.5$ ($E_0 = 7.7\times10^3\ V\ m^{-1}$) to $\Lambda = 3.0$ ($E_0 = 15.4\times10^3\ V\ m^{-1}$) for which Reynolds number (Re) varies from 6.8×10^{-4} to 13.6×10^{-4}. The non-dimensional amplitude ratio of the wavy surface, defined as $R_\alpha = \alpha_1/\alpha_2$ and is set as $R_\alpha = 2.5$ [67]. The diffusion coefficients of the ionic species is set as $D = 1 \times 10^{-9}\ m^2\ s^{-1}$. The other physical properties are specified as follows: fluid viscosity, $\mu = 10^{-3}\ kg\ m^{-1}\ s^{-1}$; fluid density, $\rho = 10^3\ kg\ m^{-3}$; Faraday's constant, $F = 96485\ C\ mol^{-1}$; permittivity of the medium, $\epsilon_e = 695.4 \times 10^{-12}\ C\ V^{-1}\ m^{-1}$; universal gas constant, $R = 8.3\ J\ mol^{-1}\ K^{-1}$; Boltzmann's constant, $k_B = 1.38 \times 10^{-23}\ m^2\ kg\ s^{-2}\ K^{-1}$; absolute temperature, $T = 300\ K$ and elementary charge, $e = 1.6 \times 10^{-19}\ C$. The diffusion coefficient for the uncharged eluted species is considered as $D_s = 1 \times 10^{-11}\ m^2\ s^{-1}$ [44] for which the corresponding Peclet number (Pe_S) varies from 68 (for $\Lambda = 1.5$) to 136 (for $\Lambda = 3$). In addition, the Debye-Hückel parameter (κH) is considered to vary from 10 ($\lambda = 0.5\ \mu m$) to 40 ($\lambda = 0.125\ \mu m$) when the ionic strength of the electrolyte concentration varies from $3.7\times10^{-7}\ M$ ($n_0 = 2.22\times10^{20}\ ions/m^3$) to $5.9\times10^{-6}\ M$ ($n_0 = 3.55 \times 10^{21}\ ions/m^3$) which satisfies the range for solution's strength used in previous literatures [30, 177].

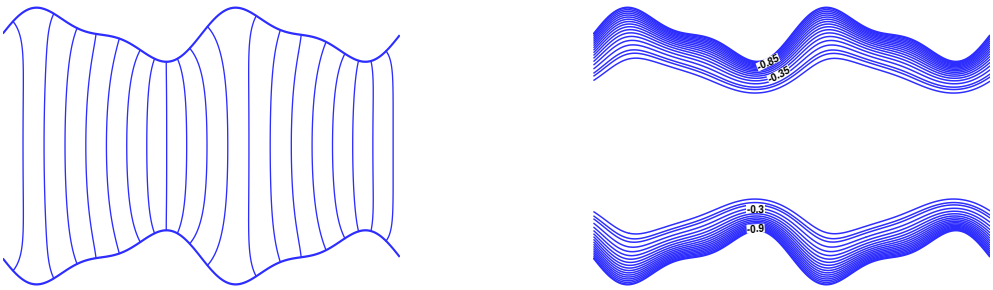

(a) (b)

Figure 4.4: Distribution of equipotential lines for (a) applied electric field and (b) induced electric field, for $\alpha_1 = 0.11$, $\kappa H = 10$, $\Lambda = 2$.

4.4.1 Influence of Physical Parameters on Flow Reversal

In this section, we depict the influence of wave amplitude, Debye-H*ü*ckel parameter and external electric field strength on flow separation inside the channel with wavy side walls. Fig. 4.4 (a) and (b) shows the distributions of EDL potential and external electric potential respectively. It can be observed that the equipotential lines for induced potential are uniformly distributed whereas distorted distribution of equipotential lines is seen for external electric field. A denser arrangement of externally applied equipotential lines is obtained near wave crest and a sparser equipotential line distribution is followed near wave trough which implies that electric field strength increases in the crest region of the wavy surface but decreases along the wave trough region. This trend of non-uniform potential distribution is more evident by increasing the wave amplitude. The electric field actively influence the ions in the EDL, causes a body force in the fluid which is present close to the channel walls of the entire mixer, since the external electric field is acting in the flow direction. Present study deals with the wavy surface walls, where the fluid encounters a reverse path i.e. rotation is created near wavy walls and the fluid streams are dragged by the electric body force.

The influence of wave amplitude and Debye-H*ü*ckel parameter (for fixed Λ) on flow pattern can be visualized from Fig. 4.5. It is clearly observed from Fig. 4.5 (left column) that, for a fixed value of κH (say $\kappa H = 10$), the streamlines follow the curvature of the wavy walls and no back flow comes into picture upto $\alpha_1 = 0.10$. As the wave amplitude takes higher values, flow pattern starts to deviate and flow reversal zone occurs near wavy walls. The streamline pattern for $\alpha_1 = 0.12$ confirms the occurrence of back flow region between two consecutive wave trough and crest in each periodic length of the channel. The fluid experiences less momentum

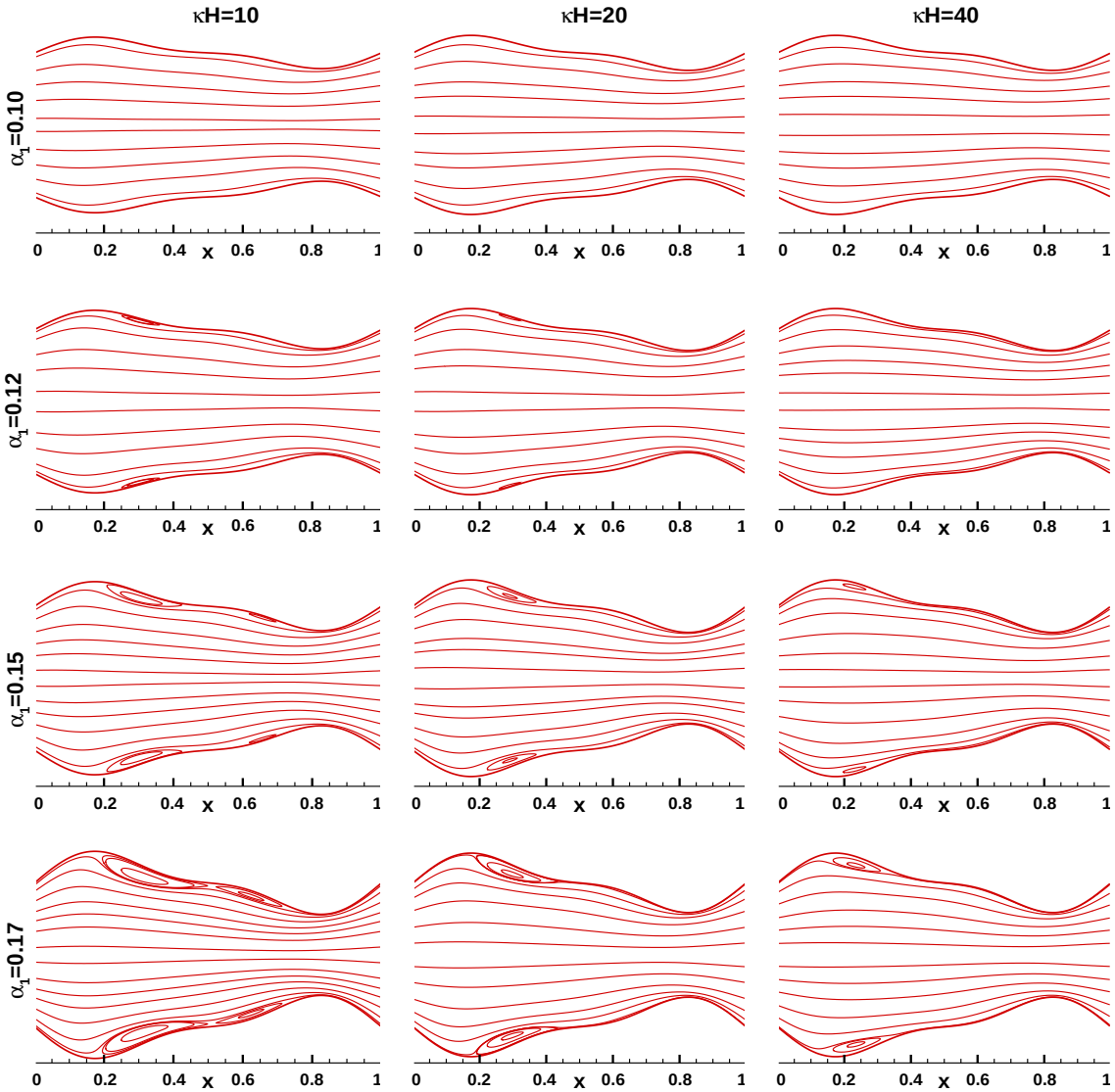

Figure 4.5: Streamlines for the variation of α_1 and κH with $\Lambda = 2$.

in the wavy region and does not posses a smooth path to justify the conservation laws. A small primary eddy is observed in this region, say, at $x \in (0.2, 0.4)$ in a single period, say, in [0, 1]. As the scaled wave amplitude increases (say for $\alpha_1 = 0.15$), the size of the primary eddy enlarges and a secondary eddy starts to take place at $x \in (0.6, 0.7)$. For further increment of α_1, both primary and secondary eddies expand in size. Same flow line pattern is followed for higher values of κH.

The occurrence of flow separation and re-attachment points for higher values of scaled wave amplitude (for $\Lambda = 2$ and $\kappa H = 10$) can be interpreted in terms of wall shear stress and axial velocity distribution. Fig. 4.6 (a) presents the wall shear stress distribution for different values of α_1. It can be noticed that wall shear stress keeps same sign throughout the domain upto

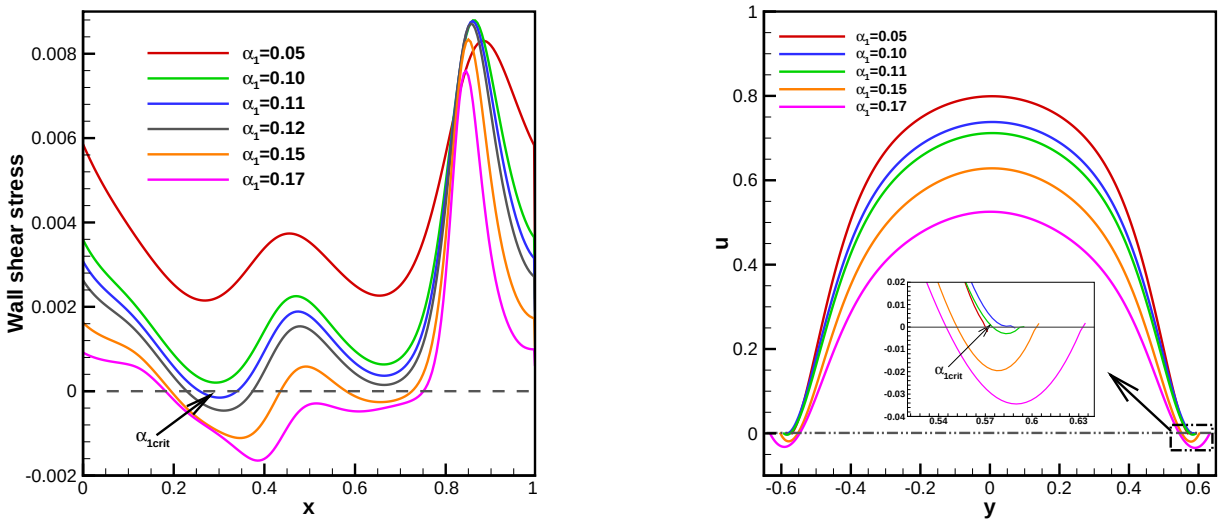

(a) (b)

Figure 4.6: Distribution of (a) wall shear stress and (b) axial velocity distribution for different wave amplitudes with $\kappa H = 10$, $\Lambda = 2$.

$\alpha_1 = 0.10$. As α_1 takes the value 0.11, wall shear stress starts to change its sign in $x \in (0.2, 0.4)$ signifying flow separation beyond $\alpha_1 = 0.11$. The formation of net effect looks to be a twisted parabolic shear stress distribution, since the driving force operates within the EDL only to succeed in dealing with the frictional force along the walls. It can also be observed that at $\alpha_1 = 0.15$, wall shear stress changes its sign twice in a single periodic domain, expectedly, at $x \in (0.2, 0.4)$ and $x \in (0.6, 0.7)$ clarifying the occurrence of secondary eddy. Flow reversal phenomena can be verified by axial velocity distribution at a flow separation point (say $x = 0.33$) for various values of α. It can be observed that axial flow velocity does not change its sign for $\alpha_1 = 0.05$, $\alpha_1 = 0.07$ and $\alpha_1 = 0.10$. When α_1 reaches its value 0.11, axial velocity curve changes sign from $+ve$ to $-ve$ which ensures flow reversal. In addition, it can be concluded from Fig. 4.5 and Fig. 4.6 that the threshold value (or critical value) of scaled wave amplitude (α_1) for which the flow reversal starts to take place, is approximately 0.11, *i.e.* $\alpha_{1_{crit}} \sim 0.11$ for $\kappa H = 10$, $\Lambda = 2$.

Above discussions suggest that, keeping κH and Λ fixed, increment in α promotes flow reversal. It is also be observed from Fig. 4.5 that flow reversal can also controlled by an another dimensionless parameter κH. For a fixed α_1 (say 0.12), small eddies can be observed near channel walls for low solution strength (say $\kappa H = 10$), and these eddies are shrinked in size and disappear for higher solution strength and the streamlines follow same pattern as electric field lines. Same trend is followed for $\alpha_1 = 0.15$ and $\alpha_1 = 0.17$. Fig. 4.7 presents the distribution

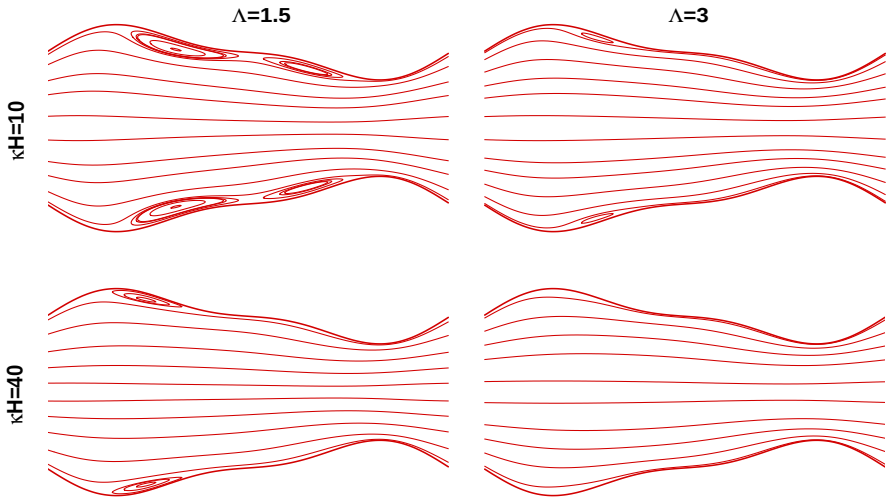

Figure 4.7: Streamlines with the variation of κH and Λ for a fixed $\alpha_1 = 0.15$.

of flow lines as a function of κH and Λ (for $\alpha_1 = 0.15$) which concludes that flow recirculation zone is wiped out for sufficient increment of electric field strength and solution's molarity.

It is observed from Fig. 4.5 - Fig. 4.7, that flow separation strongly depends on the dimensionless parameters Λ, κH and α_1. Increment of α_1 promotes flow reversal, whereas a reverse characteristic is noticed for Λ and κH. A parametric relationship (recirculation diagram) is established between the critical wave amplitude with (i) external electric field strength and (ii) solution's ionic strength, represented in Fig. 4.8 estimates a barrier between circulation zone and circulation free zone. This type of estimatin was prectided by Park et al. [208] to differentiate the circulation zone and eddy-free zone in a constricted circular channel. From Fig. 4.8, it is observed that for a fixed κH (say $\kappa H = 30$), whole region is splitted into two zones: a recirculation zone on and above the curve and a recirculation free zone below of it. The growth in electric field strength enhances the average fluid velocity to prevent the fluid streams to allow for a back flow. As a result, for higher external field strength, the scaled threshold wave amplitude is increased. It is also observed that in case of higher ionic strength, recirculation free zone is expanded, whereas reverse characteristic is followed for lower ionic strength as the electric body force becomes higher to generate larger flow rate for higher κH.

4.4.2 Influence of Physical Parameters on Mixing

Microfluidic mixing is a challenging task, when the flow is governed by low Reynolds number since flow mixing occurs due to slow diffusion process followed by Fick's law. Thus to get a desirable mixed species along the downstream, a long channel length and longer retention time

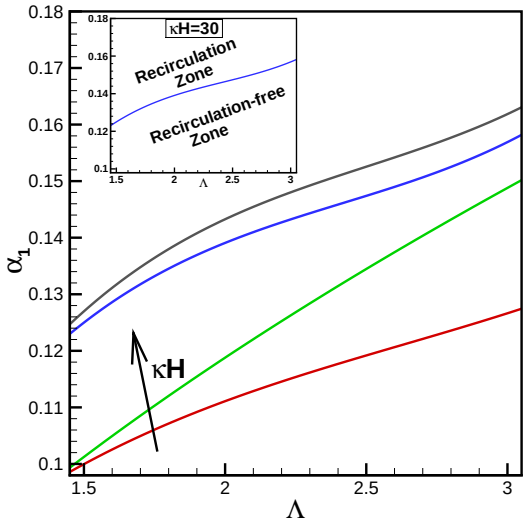

Figure 4.8: Flow recirculation diagram as a function of wave amplitudes (α_1) and non-dimensional electric field strengths (Λ) with various values of κH (=10, 20, 30, 40).

is required. Literature survey suggests that mixing performance can be enhanced remarkably through the surface patterned heterogeneity. Thus to achieve a good mixing within a shorter channel length, diffusion effects should be improved by moduling the channel geometry and selecting the best fit of flow regulating parameters. In this chapter, the relationships between flow governing parameters are established to achieve the flow separating zones. The occurrence of flow reversal provides an effective factor for mixing efficiency enhancement as the overall diffusion flux is increased due to the induced recirculations.

This section focuses on mixing efficiency improvement by introducing reverse flow regions combined with the stretched and folded paths. Fig. 4.9 shows the variation of volume flow rate with the scaled wave amplitude as a function of dimensionless electric field strength and Debye-H*ü*ckel parameter. As the scaled wave amplitude increases (for a fixed Λ and κH), fluid streams follow longer effective path to achieve a reduced flow rate (Fig. 4.9). This phenomenon can be interpreted in terms of mixing efficiency enhancement. As the fluid streams flow through microchannel with wavy side walls, the sample streams are stretched and folded as it passes through constricted and expanded regions enhancing the interfacial contact area between two streams which increases with the increment of scaled wave amplitude. Thus, both diffusion mixing time and effective interfacial contact area is increased with the increment of wave amplitude (α_1). When α_1 crosses the critical amplitude (for flow reversal), diffusion effect becomes more effective for the appearance of eddies near channel walls. As a result, mixing efficiency is

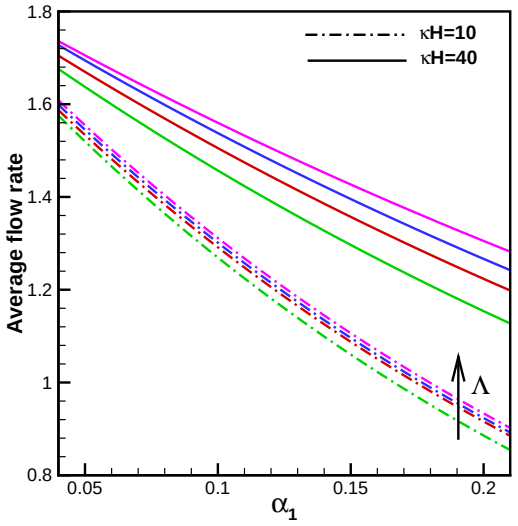

Figure 4.9: Average flow rate as a function of α_1, κH for different values of Λ (=1.5, 2, 2.5, 3).

improved with increment of wave amplitude (α_1). Furthermore, on the electric field increment, the volume flow rate is increased irrespective of α_1 values. For steady flow under a constant external electric field, the volume flow rate is reduced due to the effect of viscosity. If the EDL effect is not negligible then the flow rate equation is changed to classical Poiseuille flow rate equation. This effect is clearly visible from Fig. 4.9, that the volume flow rate is higher in case of higher concentration (high κH) where the thickness of EDL is small. In case of diluted solutions the EDL thickness is more, resulting low volume flow rate irrespective of α_1. Fig. 4.10 (a) represents the variation of mixing efficiency along the primary flow direction and Fig. 4.10 (b) represents the concentration profile at the downstream along vertical direction of the channel respectively as a function of scaled wave amplitude (α_1). Generally the fabrication pattern of micro channels in micromixers is designed in such a fashion that it can reduce the mixing path with the augmentation of contact area. We report a new strategy for efficient mixing which involves two sinusoidal functions for structured walls. The mixing process in micromixers is acquired by injecting two sample streams of different concentration species to be assorted along the interfacial contact area. This mixing mechanism solely depends on molecular diffusion. The dimensionless species distribution is presented in Fig. 4.11 for various values of scaled wave amplitudes along the flow direction keeping all other flow parameters fixed.

It can be observed that, flow streams are stated by blue colour (concentration $C = 0$) infiltrate the corrugated channel through upper half of the inflow region, while specified red coloured streams (with concentration $C = 1.0$) enter the channel from lower half inlet. The ideal mixed concentration (with concentration $C = 0.5$) is demonstrated by green colour. It is observed

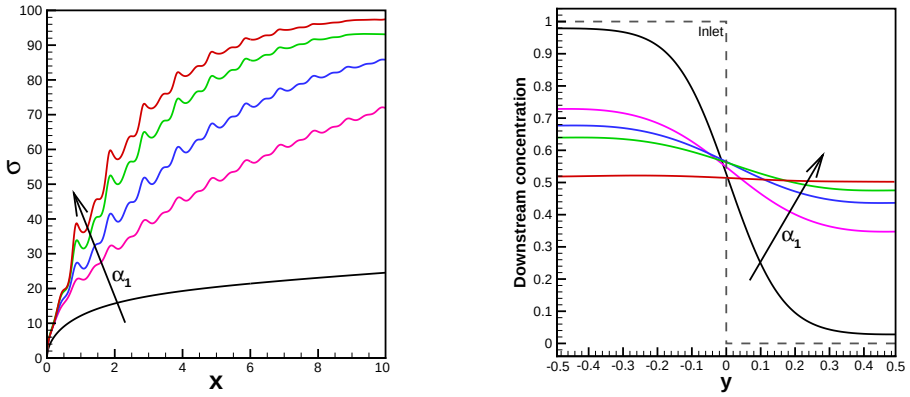

(a) (b)

Figure 4.10: (a) Variation of mixing efficiency along the channel length and (b) normalized downstream concentration profile for different $\alpha_1(= 0, 0.05, 0.10, 0.15, 0.20)$. Here $\kappa H = 10$, $\Lambda = 2$.

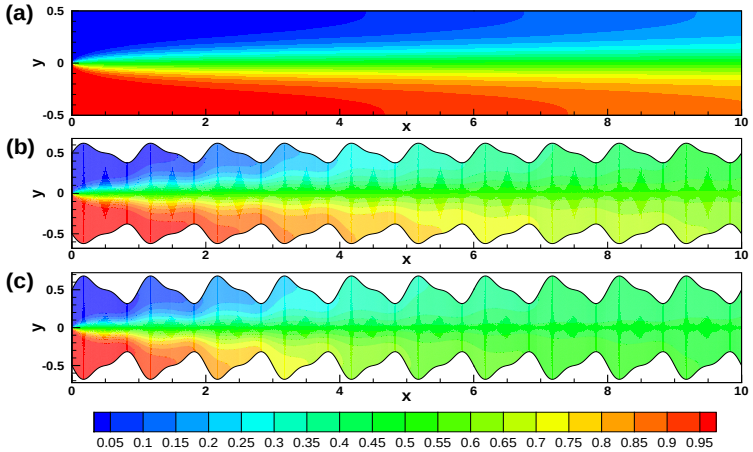

Figure 4.11: Concentration contours for different scaled wave amplitudes (a) $\alpha_1 = 0.0$, (b) $\alpha_1 = 0.10$, (c) $\alpha_1 = 0.15$ with $\kappa H = 10$, $\Lambda = 2$.

from concentration contour (Fig. 4.11) that, the flows of distinctive species are totally unmixed in the inlet region showing 0% mixing efficiency and the same is enhanced along the channel length due to improved diffusion flux. From Fig. 4.10(b) it can be noticed that normalized downstream concentration profile keeps close to 0.5 with the augmentation of α_1 which confirms more uniform downstream concentration distribution. The mixing efficiency for $\alpha_1 = 0.10$ and $\alpha_1 = 0.15$ are found to be 85% and 93% at the outlet of the channel (figure 4.9(a)) and it is further improved up to 97% (which is four times compared to plane channel ($\alpha_1 = 0$)) for $\alpha_1 = 0.20$. In this case mixing is increased by circulation strength which develops a transverse velocity between two consecutive trough and crest region of the wavy surfaces.

Fig. 4.12(a) and (b) illustrate the mixing efficiency at the channel downstream as a function

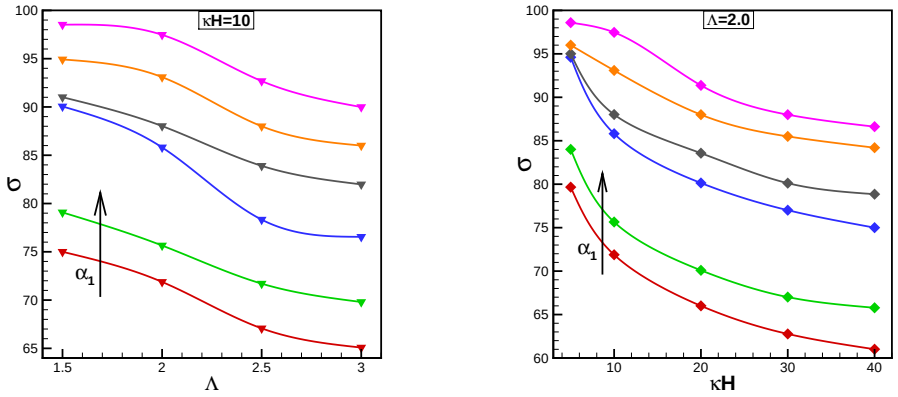

(a) (b)

Figure 4.12: Mixing efficiency at the downstream of the channel for different α_1 (=0.05, 0.07, 0.10, 0.12, 0.15, 0.20) with the variation of (a) scaled electric field strength (Λ) and (b) κH.

of Λ and κH respectively for a wide range of α_1. As the scaled electric field strength increases, the fluid streams pass more rapidly through the channel to have a higher value of average flow rate (shown in Fig. 4.9). As a result, recirculating eddies diminish in size and consequently mixing efficiency is reduced with the increment of external electric field strength. In the contrary, when the external electric field strength is decreased, an advancement in mixing is found along the downstream of the channel which is shown in the Fig. 4.12(a).

Fig. 4.12(b) shows the effect of Debye-H*ü*ckel parameter (κH) on mixing efficiency. For a smaller κH, the EDL occupies a relatively larger proportion of the flow domain causing a relatively lower average flow rate (shown in Fig. 4.9). Thus, the diffusion mixing time is increased for lower values of Debye-H*ü*ckel parameter (κH). As a result, mixing efficiency at the downstream of the channel is improved for the decrement of κH.

4.5 Conclusions

This chapter deals with new mathematical model which concludes the flow reversal and mixing analysis in a corrugated micro-channel within the framework of Poisson-Nernst-Planck flow governed equations. The predicted results depict a concurrent relevance with an ever increasing desire to mimic the microfluidic structures in terms of mixing. The results demonstrates that mixing length may be significantly reduced by introducing a wavy structure in the flow geometry. Furthermore, it is concluded that after crossing the threshold amplitude, recirculating eddies take place to preserve a constant mass flow rate at each cross section and the size of the

eddies expand with higher wave amplitude to enhance effective diffusive flux to achieve a higher mixing at channel downstream. In addition to this, at higher electric field strength with the increment of Debye-H*ü*ckel parameter, fluid streams are forced to pass through the wavy channel to get an enhanced flow rate which in turn increases the threshold wave amplitude. As a result, irrespective of the values of wave amplitude, mixing efficiency along the downstream is enhanced with the decrement in electric field strength and Debye-H*ü*ckel parameter. Thus, we can conclude that a desired mixing can be achieved within a shorter channel length by regulating the key parameters: such as ionic strength, geometric parameter and applied electric field. These results can be useful for the design of efficient passive micromixers by maintaining a balance between average flow rate and mixing efficiency.

Chapter 5

Influence of Varying Zeta Potential on non-Newtonian Flow Mixing and Pressure Drop in a Wavy Patterned Micro-Channel

5.1 Introduction

In last two decades, the rapid advancement of micro-electro-mechanical systems (MEMS) facilitated it to integrate the multi-functional microfluidic devices on a single chip (Lab-on-a-chip) [13, 273] to accomplish micro-total analysis system (μ-TAS) for biomedical, chemical, biological applications. The performance of these devices relies on efficient and controllable mixing which are indispensable in DNA sequencing, targeted drug delivery, chemical synthesis etc. Fluid mixing in microsystems is an integral operation in many of the procedures performed using the microchips. Hence, an efficient procedure is required in order to achieve a rapid mixing effect to improve the performance of these devices. In small characteristic scales, fluid flow and solute transport is constrained to low Reynolds number regime. As a consequence, flow is laminar, and the mixing of different miscible streams is dominated by molecular diffusion which is inherently a slow process. Thus, to achieve a homogenized solution, a large channel length and a longer mixing time is required which is incompatible with the general trend towards device miniaturization and high throughput. Thus, control of mixing and mixing efficiency enhancement in micro/ nano domain possesses a great challenge for researcher now a days. Many studies have been performed on micro scale mixing, aims of which is to get an efficient and

effective mixing.

As proposed in literature, the micromixing strategies (depending on the manner in which they are mixed) can be classified into active and passive categories [120, 142]. Active mixing strategies are developed in such a way that, external pulsating forces create chaotic flow pattern in the flow field to achieve a better mixing. In this regard, external forces can be supplied by generating pressure fields [95], in which an accelerating pulsatory injection method is applied in the channel inlet to alter the flow rate periodically; electric fields [138,174], in which alternating electric field is applied to promote mixing; temperature fields [7, 131, 268], where flow reversal zones are induced due to temperature gradient; magneto-hydrodynamic fields [21], where the flow perturbations are created by the induction of Lorentz forces in electrolyte solutions; hydrodynamic fields [178], in which flow disturbance is created by imposing different electrical properties in the hydrodynamic fields; ultrasonic fields [284], where the flow perturbations are created due to acoustic stirring by ultrasonic waves. In contrast, passive micromixers relies on geometric and surface modulation by stirring the fluid streams to reduce the diffusion length and by maximizing the contact area between the miscible fluid streams [143]. Different passive mixing schemes, based on geometric modulation and non-homogeneity in wall fabrication have been studied in literature, such as channels with surface heterogeneity [84,189], staggered herringbone microchannels [122,128], three dimensional serpentine mixers [11,207], patterned block channels [190,253], zig-zag channel geometry [57], wave-form microchannels [37], channels with conducting barriers [22,276] etc. these channel geometries can be easily fabricated by using the standard fabrication techniques like nano-lithography [40,82,173], etching-and-deposition [279], DLP [127], sequentially patterned oxides [61], packing of different nano-particles [144] etc. Out of these two types of micromixing strategies, passive one is widely used, since it is easy to handle and it does not require any external stirring agents, easy to integrate with other devices and has a greater reliability due to lack of moving parts.

Most of the studies on electrokinetic flow and micromixing mentioned above dealt with Newtonian fluids with constant viscosity. But, in reality micromixing strategies are frequently involved in biofluids (e.g. DNA, blood, protein, saliva etc.), polymers, colloids etc., where Newtonian model fails to describe the physical rheology of the system. The characterization of flow rheology of such systems rely on general Cauchy momentum equation in which the viscosity of the fluid is considered to be varied with the rate of hydrodynamic shear, rather than Navier-Stokes equation [289]. To characterize the non-Newtonian flow behavior in such systems, a number of models have been used in literature like Bingham [32], Casson [158, 196, 234, 235],

Power-law [16,125,192], Phan-Thien-Tanner [167], Eringen [223], Herschel-Bulkley [106], Carreau [294], CarreauYasuda [132], Maxwell model [148,185] etc. Based on the above mentioned models, power-law model has received much attention because of it's simple usage and suitable to fit with a wide range of non-Newtonian fluids [289]. One of the earlier studies on electrokinetic flow of power-law fluid has been preformed by Das and Chakraborty [76] in a micro-domain by using a semi-analytical approach. Subsequently, Zhao et al. [287] provided an analytical solution using the Debye-H*ü*ckel approximation under a low zeta-potential assumption for velocity distribution in a slit micro-channel filled with power-law fluid. Several studies, based on Poisson-Boltzmann with Debye-H*ü*ckel approximation were later performed for both cartesian and cylindrical micro/ nano channels [16,229,288,290]. Vasu and De [258] analytically studied the EOF characteristics based on power-law model for high surface potentials. Babaie et al. [15] further extended this work for combined electroosmotic-pressure driven flow. Based on lattice Boltzmann simulation, Tang et al. [254] introduced electroviscous effect for pressure assisted EOF in a slit microchannel. EOF of power-law fluid in microchannels with non-uniform cross section has been presented by Ng and Qi [197].

Most of the above mentioned studies on power-law fluids dealt with analytic and semi-analytic solutions with simple geometry and uniform surface potential. However, potential non-homogeneity and non-uniform channel geometry creates flow perturbation inside the flow domain which stir the flow streams of different concentrations to get a homogenized solution. Electrokinetic flow and mixing enhancement for power-law fluids for the case of potential heterogeneity has been numerically studied by Hadigol [100,101]. Cho et al. [63–66] presented the flow mixing of power-law fluids with different non-uniform geometry and wall roughness. Recently Bag and Bhattacharyya [17] analyzed numerically the non-Newtonian flow mixing inside a slit channel with heterogenous surface properties. The above mentioned results [17,63–66] showed that the flow behavior index influenced largely the mixing performance along the flow domain. It can also be observed that a higher flow rate (for pseudoplastic fluids) is not beneficial for mixing enhancement, whereas a reduced average flow rate (for dilatant fluids) promotes higher mixing efficiency.

As mentioned above, designing of micromixer for efficient mixing is a very challenging task, since design specification must be different from conventional mixers. In this aspect, the motivation of this chapter is to investigate the flow mixing in a patterned micromixer with fluid trapped

surfaces, where the pressure drop along the channel length can be acted as an effective parameter for a controllable mixing efficiency, as high pressure drop may cause a less performance of the system [35, 68]. Literature survey reveals that geometric and surface non-homogeneity promotes higher pressure drop along the channel length [23, 120, 209]. Also, with the increment of power-law index, the pressure drop is increased accordingly [17]. Following the recent literature, mixing performance factor [23, 151] (which is the ratio of mixing efficiency at downstream of the channel and average pressure drop along the channel) is taken into account to predict the best set of flow governing parameters to achieve a good mixing along with minimum pressure drop. The problem is formulated by considering the Maxwell's equation for electric potential field, Nernst-Planck equation for ionic concentration field, modified Cauchy momentum equation for flow field and advection-diffusion equation for uncharged eluted species distribution. The velocity, ionic concentration, potential and eluted species distributions are obtained by an iterative numerical solution of coupled set of governing equations. However, to the best knowledge of the authors, the study of electrokinetic micro-mixing together with pressure drop of a non-Newtonian fluid in a wavy-structured micro channel with sinusoidal zeta potential on the framework of Poisson-Nernst-Planck theory has not yet been studied in literature. This chapter is organized as follows: Section 2 presents the detailed of problem formulation and mathematical model based on power-law rheology. A suitable coordinate transformation is made in this section to map the corrugated domain into a simpler rectangular one. Section 3 contains the numerical algorithm and validation of our scheme with previously published results for a wide range of power-law index. In Section 4, we present the mixing efficiency and pressure drop for Newtonian, pseudoplastic and dilatant fluids for a suitable range of wave amplitudes and ionic strength of the electrolyte solution. In the first part of this section a parametric study is presented to choose the best choice of phase shift in terms of mixing and pressure drop which is the main motivation of the present study. Choosing the best geometric configuration (phase difference between two wavy walls), numerical simulations are performed with the variation of power-law index, solution's ionic strength and wave amplitude. Important conclusions are appeared in the last section of this chapter.

5.2 Problem Formulation

An incompressible, steady, isothermal power-law fluid is considered to be passed through a microchannel, surrounded by two sinusoidal plates with different phase shifts where the wall zeta potential is distributed periodically as presented in Fig. 5.1 (a). As shown in the figure,

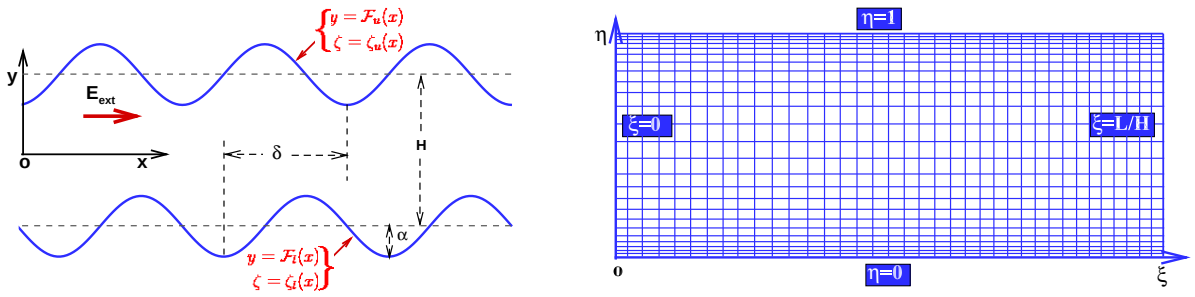

(a) (b)

Figure 5.1: (a) Physical geometry and (b) Computational domain of the problem.

the microchannel is maintained with an average height H, width W and length L. The width of the channel is supposed to be of the order of its length and the flow field is considered as two dimensional. The wall shapes are defined as

$$\begin{aligned} \mathcal{F}_l^*(x^*) &= -0.5H - \alpha^* sin\left\{2\pi x^*/H\right\}, \\ \mathcal{F}_u^*(x^*) &= 0.5H - \alpha^* sin\left\{2\pi x^*/H + \delta^*/H\right\}, \end{aligned}$$

where $\mathcal{F}_l^*(x^*)$ and $\mathcal{F}_u^*(x^*)$ respectively denote the lower and upper wall shapes. Here α^* and δ^* represent the wave amplitude and phase shift respectively. By scaling the coordinates by H $(i.e.\ x = x^*/H\ and\ y = y^*/H)$, the scaled wave amplitude and scaled phase shift are defined as $\alpha = \alpha^*/H$ and $\delta = \delta^*/H$. A constant electric field is imposed externally along the primary flow direction whereas the zeta potential is applied periodically according to the walls shape with the same wave length that of walls & are defined as

$$\begin{aligned} \zeta_l(x) &= -\zeta_0 sin(2\pi x), \\ \zeta_u(x) &= \zeta_0 sin(2\pi x + \delta), \end{aligned}$$

where ζ_l and ζ_u stands for the scaled wall zeta potential (scaling factor is $\phi_0 = 25.6\ mV$) for lower and upper wall respectively. In this chapter, the rheological behavior of the non-Newtonian electrolyte is characterized by Power-law model. The constitutive relationship between the shear stress and shear strain can be expressed as [101]

$$\boldsymbol{\tau}^* = 2\mu_a^*(\dot{\gamma}^*)\dot{\boldsymbol{\gamma}}^*,$$

where $\dot{\gamma}^* = \sqrt{\frac{1}{2}(\dot{\boldsymbol{\gamma}}^* : \dot{\boldsymbol{\gamma}}^*)}$ and $\mu_a^*(\dot{\gamma}^*) = m(\dot{\gamma}^*)^{n-1}$. Here $\boldsymbol{\tau}^*$ and $\boldsymbol{\gamma}^*$ denote the stress tensor and the strain rate tensor respectively. Here μ_a^* is the apparent viscosity, m is the flow consistency

index and n is the flow behavior index according to which Power-law fluid is categorized as shear-thinning (pseudoplastic) or shear thickening (dilatant) for $n < 1$ or $n > 1$ respectively, whereas for $n = 1$ it shows Newtonian behavior. The relationship between shear stress and shear strain rate can be expressed as

$$\tau_{ij}^* = \mu_a^* \left(\frac{\partial u_i^*}{\partial x_j^*} + \frac{\partial u_j^*}{\partial x_i^*} \right).$$

In two dimensions, the apparent viscosity, μ_a^* takes the form

$$\mu_a^* = m \left[2 \left(\frac{\partial u^*}{\partial x^*} \right)^2 + 2 \left(\frac{\partial v^*}{\partial y^*} \right)^2 + \left(\frac{\partial u^*}{\partial y^*} + \frac{\partial v^*}{\partial x^*} \right)^2 \right]^{\frac{n-1}{2}}.$$

A suitable transformation is introduced to convert the deflected geometry to a simple rectangular (Fig. 5.1 (b)) one as

$$\xi = x, \qquad \eta = \frac{y - \mathcal{F}_l(x)}{\mathcal{F}_u(x) - \mathcal{F}_l(x)},$$

where $\mathcal{F}_l(x) = \frac{1}{H}\mathcal{F}_l^*(x^*)$ & $\mathcal{F}_u(x) = \frac{1}{H}\mathcal{F}_u^*(x^*)$. Using the above transformation, the flow field, governed by Cauchy momentum equation and equation of Continuity can be expressed as

$$Re \left[\frac{\partial \mathbf{q}}{\partial t} + (\mathbf{q} \cdot \nabla)\mathbf{q} \right] = -\nabla p + \nabla \cdot \boldsymbol{\tau} + \frac{(\kappa H)^{n+1}}{2\Lambda \zeta n^n} \rho_e \nabla \Phi, \tag{5.1}$$

$$\nabla \cdot \mathbf{q} = 0. \tag{5.2}$$

Here time is scaled by H/U_S and $\mathbf{q}$ is the dimensionless velocity vector scaled by generalized Helmholtz-Smoluchowski velocity U_S, where $U_S = n\kappa^{\frac{1-n}{n}} \left(-\frac{\varepsilon_e E_0 \phi_0 \zeta_0}{m} \right)^{1/n}$ [17]. The other dimensional variables are scaled as follows: the spatial coordinates by the average channel height (H) & the pressure scale is mU_s^n/H^{n+1}. The electrolyte solution is considered to be binary and symmetric (e.g. $NaCl + H_2O$) with z_i $(i = 1, 2) = \pm 1$. Here $\rho_e = (n_1 - n_2)$ is the dimensionless charge density scaled by $n_0 e$, where e is the elementary charge and n_0 is the bulk number concentration. Here z_i $(i = 1, 2)$ denotes the valance and n_i $(i = 1, 2)$ denotes the non-dimensional number concentration of i^{th} ionic species scaled by the bulk number concentration (n_0). $\boldsymbol{\tau}$ is the dimensionless stress tensor scaled by $m(U_S/H)^n$. Here Φ, scaled by ϕ_0 $(= RT/F)$ denotes the total electric potential which is a linear superposition of applied potential (ψ) due to external electric field and induced potential (ϕ) due to EDL formation. The dimensionless parameters namely Λ $(= E_0 H/\phi_0)$ and Re $(= U_S^{2-n} H^n/m)$ denote the scaled electric strength and Reynolds number respectively. The inverse of the Debye layer thickness is defined as $\kappa = \sqrt{2en_0/\varepsilon_e \phi_0}$, where ε_e denotes the permittivity of the

medium. Here the operators ∇ and ∇^2 stand for the gradient and Laplacian in the transformed domain ($\xi-\eta$ domain) which are defined as $\nabla \equiv \left(\frac{\partial}{\partial\xi} - \left(\eta\frac{\mathcal{F}_0'}{\mathcal{F}_0} + \frac{\mathcal{F}_l'}{\mathcal{F}_0}\right)\frac{\partial}{\partial\eta}, \frac{1}{\mathcal{F}_0}\frac{\partial}{\partial\eta}\right)$ and $\nabla^2 \equiv \frac{\partial^2}{\partial\xi^2} - 2\left\{\eta\frac{\mathcal{F}_0'}{\mathcal{F}_0} + \frac{\mathcal{F}_l'}{\mathcal{F}_0}\right\}\frac{\partial^2}{\partial\xi\partial\eta} + \left\{\left(\eta\frac{\mathcal{F}_0'}{\mathcal{F}_0} + \frac{\mathcal{F}_l'}{\mathcal{F}_0}\right)^2 + \frac{1}{\mathcal{F}_0^2}\right\}\frac{\partial^2}{\partial\eta^2} + \left\{2\eta\left(\frac{\mathcal{F}_0'}{\mathcal{F}_0}\right)^2 - \eta\frac{\mathcal{F}_0''}{\mathcal{F}_0} - \frac{\mathcal{F}_l''}{\mathcal{F}_0} + 2\frac{\mathcal{F}_0'\mathcal{F}_l'}{\mathcal{F}_0^2}\right\}\frac{\partial}{\partial\eta}$ respectively, where $\mathcal{F}_0(x) = \mathcal{F}_u(x) - \mathcal{F}_l(x)$. Here $'$ and $''$ stand for the first and second order derivatives of the corresponding functions.

The expression for non-dimensional apparent viscosity, scaled by $m(U_s/H)^{n-1}$ in $\xi-\eta$ domain takes the form

$$\mu_a = \left[2\left\{\frac{\partial u}{\partial\xi} - \left(\frac{\eta\mathcal{F}_0'}{\mathcal{F}_0} + \frac{\mathcal{F}_l'}{\mathcal{F}_0}\right)\frac{\partial u}{\partial\eta}\right\}^2 + \frac{2}{\mathcal{F}_0^2}\left\{\frac{\partial v}{\partial\eta}\right\}^2 + \left\{\frac{1}{\mathcal{F}_0}\frac{\partial u}{\partial\eta} + \frac{\partial v}{\partial\xi} - \left(\frac{\eta\mathcal{F}_0'}{\mathcal{F}_0} + \frac{\mathcal{F}_l'}{\mathcal{F}_0}\right)\frac{\partial v}{\partial\eta}\right\}^2\right]^{\frac{n-1}{2}},$$

and the components of the shear-stress tensor in the transformed domain are of the form

$$\begin{aligned}
\tau_{\xi\xi} &= 2\mu_a\left\{\frac{\partial u}{\partial\xi} - \left(\frac{\eta\mathcal{F}_0'}{\mathcal{F}_0} + \frac{\mathcal{F}_l'}{\mathcal{F}_0}\right)\frac{\partial u}{\partial\eta}\right\} \\
\tau_{\xi\eta} &= \tau_{\eta\xi} = \mu_a\left\{\frac{\partial v}{\partial\xi} - \left(\frac{\eta\mathcal{F}_0'}{\mathcal{F}_0} + \frac{\mathcal{F}_l'}{\mathcal{F}_0}\right)\frac{\partial v}{\partial\eta} + \frac{1}{\mathcal{F}_0}\frac{\partial u}{\partial\eta}\right\} \\
\tau_{\eta\eta} &= 2\mu_a\left\{\frac{1}{\mathcal{F}_0}\frac{\partial v}{\partial\eta}\right\}
\end{aligned} \tag{5.3}$$

The dimensionless form of the equation for induced potential (due to EDL) is represented by Poisson's equation as

$$\nabla^2\phi = -\frac{(\kappa H)^2}{2}\rho_e. \tag{5.4}$$

The electric potential distribution due to externally applied voltage is followed by the solution of $\nabla^2\psi = 0$ with insulated wall boundary condition i.e. $\nabla\psi\cdot\mathbf{n} = 0$, where $\mathbf{n}$ represents the unit normal to the corresponding surface pointing towards the liquid. Based on convection, diffusion and electro-migration transport mechanism, the equations for ionic species transport can be represented in non-dimensional form as [33]

$$Pe(\mathbf{q}\cdot\nabla n_i) = \nabla^2 n_i + z_i\nabla n_i\cdot\nabla\Phi - \frac{(\kappa H)^2}{2}z_i n_i\rho_e. \tag{5.5}$$

This model (Poisson-Nernst-Planck model) has the flexibility to handle multivalent ionic species. As mentioned above, for simplicity, we consider a $1:1$ electrolyte with z_i $(i=1,2) = \pm 1$. The diffusivity for both the ionic species (cation and anion) is considered to be same, i.e. D_i $(i=1,2) = D$. The non-dimensional number Pe (Peclet number for charged species) measures the ratio of advective to diffusive transport and is defined as $Pe = HU_S/D$.

A fully developed boundary condition is considered along the upstream and downstream of the channel. A sinusoidally distributed zeta potential ($\zeta(x)$) is assumed along the walls and the walls are treated as ion impenetrable, i.e. the molar flux of the ionic species is assumed to be zero along the boundary walls. In addition, a no-slip condition is assumed to maintain the velocity components along the channel walls. Thus the wall boundary conditions can be represented as

$$\mathbf{q} = \mathbf{0};\ (\nabla n_i + z_i n_i \nabla\phi) \cdot \mathbf{n} = 0;\ \phi = \zeta(x),$$

where $\mathbf{n}$ represents the unit normal vector along the channel walls indicating towards the liquid and $\zeta(x)$ is the surface potential which depends on longitudinal coordinate axis.

5.2.1 Transport of Uncharged Mixing Species

Transportation of the uncharged eluted species is defined by the combined species convection-diffusion equation. In the absence of species absorption and chemical reaction, the dimensionless species transport equation are of the form

$$(\mathbf{q} \cdot \nabla)C - \frac{1}{Pe_S}\nabla^2 C = 0, \tag{5.6}$$

where C is the dimensionless species concentration scaled by C_{ref} and Pe_S ($= HU_S/D_S$) represents the Peclet number for eluted mixing species. Here D_S stands for the diffusion coefficient of the mixing species. To obtain mixing efficiency at different levels of the channel, no mass flux ($\nabla C \cdot \mathbf{n} = 0$) is assumed along the walls ($y = \mathcal{F}_l(x)$ and $y = \mathcal{F}_u(x)$) and $\frac{\partial C}{\partial x} = 0$ is set as the outlet boundary condition. At the inlet of the channel i.e. at $x = 0$, a step-like concentration distribution is assumed, i.e. $C = 1$ in the lower half ($\mathcal{F}_l(x) \leq y \leq 0$) and $C = 0$ in the upper half ($0 < y \leq \mathcal{F}_u(x)$).

A measure of species mixing at different levels of the channel is defined by a (mixing efficiency) parameter, σ, as [84, 190]

$$\sigma = \left[1 - \frac{\int_{\mathcal{F}_l}^{\mathcal{F}_u} |C - C_\infty| dy}{\int_{\mathcal{F}_l}^{\mathcal{F}_u} |C_0 - C_\infty| dy}\right] \times 100\%.$$

Here C_∞ and C_0 represent the concentrations in the mixed ($C_\infty = 0.5$) and unmixed ($C_0 = 0$ *or* 1) states, respectively. Mixing efficiency is 100% when the two species are in fully mixed condition and a completely unmixed mode signifies 0% mixing efficiency.

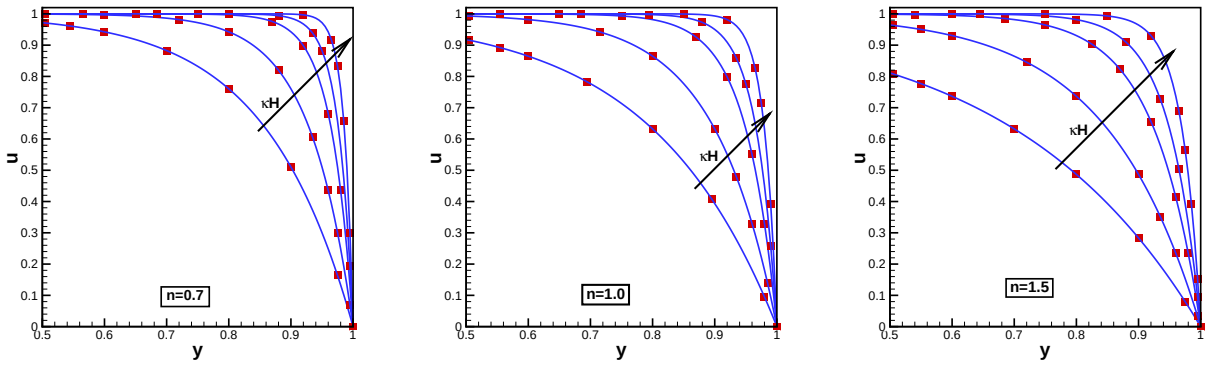

(a) (b) (c)

Figure 5.2: Comparison of axial velocity in the present study for uniform zeta potential in a slit micro-channel with the analytic results obtained by Zhao et al. [287] for various values of flow behavior index (a) $n = 0.7$, (b) $n = 1.0$, (c) $n = 1.5$ when $\zeta = -1$, $H = 10\ \mu m$ and $kH = 5, 10, 20, 30, 50$.

5.3 Numerical Method

In performing the simulations, a staggered grid based finite volume method (FVM) [47, 89, 98, 231] is employed to solve the coupled non-linear set of equations [5.2-5.6]. On integrating the coupled set of equations over different control volumes, a fully implicit scheme is adopted for the transient terms, whereas a QUICK scheme [145] is used for convective terms in the mass transfer and momentum equations in order to achieve sharp gradients for fluid velocity, ion concentration, electrostatic potential near channel walls. A time marching numerical methodology is achieved by advancing the fluid variables through a sequence of shorter time steps of duration 0.001. For the range of parameter values considered here, the flow field achieves a steady state after a transient state and this steady state is independent of the initial conditions prescribed. To cope with the non-linearity, Newton's linearization technique is adopted. The governing discretized equations are solved through a cyclic pressure correction based SIMPLE algorithm [210]. The pressure link between the momentum and continuity equations are accomplished by transforming the discretized continuity equation into a Poisson equation for pressure correction which is solved iteratively using a SOR (Successive over relaxation) scheme until getting a desired accuracy. The convergence criterion is defined as, $\max_{i,j} \ |\Theta_{i,j}^{k+1} - \Theta_{i,j}^{k}| < \Delta$, where $\Theta = (n_1, n_2, \phi, u, v)$, $\Delta = 10^{-6}$, k denotes the iteration level and i, j stand for computational grid points. A non-uniform grid spacing is taken in η direction to capture the Debye layer effect on velocity, concentration and potential field, whereas an uniform spacing is considered in ξ direction. The grid spacing in η direction is varied from 0.005 to 0.01. Moreover, an

under-relaxation scheme is introduced for apparent viscosity to avoid the divergence as [101]

$$\mu_a = \alpha_n \mu_a^{new} + (1-\alpha_n)\mu_a^{old}; \qquad 0.2 < \alpha_n < 0.5. \tag{5.7}$$

A detailed study on numerical methods have been presented in the previous chapter (Chapter 4). The pressure correction equation and the corresponding velocity corrections are included as follows. Using the same steps discussed in the previous chapter, the Poisson equation for pressure correction takes the form

$$\begin{aligned}
&p^c_{j-1,k}\left[-\alpha_u\frac{\Delta t\Delta\eta_k}{0.5(\Delta\xi_j+\Delta\xi_{j+1})}+\frac{1}{8}\alpha_u\left\{\eta_k\left(\frac{\mathcal{F}_0'}{\mathcal{F}_0}\right)_j+\left(\frac{\mathcal{F}_l'}{\mathcal{F}_0}\right)_j\right\}^2\frac{\Delta t\Delta\xi_j}{\Delta\eta_k}\right]\\
&+p^c_{j,k}\left[2\alpha_u\frac{\Delta t\Delta\eta_k}{0.5(\Delta\xi_j+\Delta\xi_{j+1})}+2\alpha_v\left\{\left(\frac{1}{\mathcal{F}_0}\right)_j\right\}^2\frac{\Delta t\Delta\xi_j}{0.5(\Delta\eta_k+\Delta\eta_{k+1})}\right.\\
&\qquad\left.+\frac{1}{4}\alpha_u\left\{\eta_k\left(\frac{\mathcal{F}_0'}{\mathcal{F}_0}\right)_j+\left(\frac{\mathcal{F}_l'}{\mathcal{F}_0}\right)_j\right\}^2\frac{\Delta t\Delta\xi_j}{\Delta\eta_k}\right]\\
&+p^c_{j+1,k}\left[-\alpha_u\frac{\Delta t\Delta\eta_k}{0.5(\Delta\xi_j+\Delta\xi_{j+1})}+\frac{1}{8}\alpha_u\left\{\eta_k\left(\frac{\mathcal{F}_0'}{\mathcal{F}_0}\right)_j+\left(\frac{\mathcal{F}_l'}{\mathcal{F}_0}\right)_j\right\}^2\frac{\Delta t\Delta\xi_j}{\Delta\eta_k}\right]\\
&=-div^*-\frac{1}{4}\alpha_u\eta_k\left(\frac{\mathcal{F}_0'}{\mathcal{F}_0}\right)_j\Delta t\left(p^c_{j+1,k+1}+p^c_{j-1,k-1}-p^c_{j+1,k-1}-p^c_{j-1,k+1}\right)\\
&\quad-\frac{1}{4}\alpha_u\left\{\eta_k\left(\frac{\mathcal{F}_0'}{\mathcal{F}_0}\right)_j+\left(\frac{\mathcal{F}_l'}{\mathcal{F}_0}\right)_j\right\}\frac{\Delta t\Delta\xi_j}{0.5(\Delta\xi_j+\Delta\xi_{j+1})}\left(p^c_{j+1,k+1}\right.\\
&\qquad\left.+p^c_{j-1,k-1}-p^c_{j+1,k-1}-p^c_{j-1,k+1}\right)\\
&\quad+\frac{1}{16}\alpha_u\left\{\eta_k\left(\frac{\mathcal{F}_0'}{\mathcal{F}_0}\right)_j+\left(\frac{\mathcal{F}_l'}{\mathcal{F}_0}\right)_j\right\}^2\frac{\Delta t\Delta\xi_j}{\Delta\eta_k}\left(p^c_{j-1,k+2}+p^c_{j-1,k-2}\right.\\
&\qquad\left.+2p^c_{j,k+2}+2p^c_{j,k-2}+p^c_{j+1,k+2}+p^c_{j+1,k-2}\right)\\
&\quad+\alpha_v\left\{\left(\frac{1}{\mathcal{F}_0}\right)_j\right\}^2\frac{\Delta t\Delta\xi_j}{0.5(\Delta\eta_k+\Delta\eta_{k+1})}\left(p^c_{j,k+1}+p^c_{j,k-1}\right),
\end{aligned}\tag{5.8}$$

where

$$\begin{aligned}
div^* = &\left(u^*_{j,k}-u^*_{j-1,k}\right)\Delta\eta_k-\frac{\eta_k}{4}\left\{\eta_k\left(\frac{\mathcal{F}_0'}{\mathcal{F}_0}\right)_j+\left(\frac{\mathcal{F}_l'}{\mathcal{F}_0}\right)_j\right\}\left(u^*_{j-1,k+1}+u^*_{j,k+1}-u^*_{j-1,k-1}-u^{n+1}_{j,k-1}\right)\Delta\xi_j\\
&+\left(\frac{1}{\mathcal{F}_0}\right)_j\left(v^*_{j,k}-v^*_{j,k-1}\right)\Delta\xi_j.
\end{aligned}\tag{5.9}$$

The equation 5.8 is solved using Gauss Seidel method for every iteration to achieve pressure correction in each of the control volumes. The corrections for velocity components associated

to the pressure correction are as

$$\left.\begin{aligned} u^c_{j,k} &= -\frac{\Delta t}{0.5(\Delta\xi_j+\Delta\xi_{j+1})}\left(p^c_{j+1,k}-p^c_{j,k}\right) \\ &\quad +\frac{1}{4}\eta_k\left\{\eta_k\left(\frac{\mathcal{F}_0'}{\mathcal{F}_0}\right)_j+\left(\frac{\mathcal{F}_l'}{\mathcal{F}_0}\right)_j\right\}\frac{\Delta t}{\Delta\eta_k}\left(p^c_{j,k+1}+p^c_{j+1,k+1}-p^c_{j,k-1}-p^c_{j+1,k-1}\right) \\ v^c_{j,k} &= -\frac{\Delta t}{0.5(\Delta\eta_k+\Delta\eta_{k+1})}\left(\frac{1}{\mathcal{F}_0}\right)_j\left(p^c_{j,k+1}-p^c_{j,k}\right). \end{aligned}\right\} \tag{5.10}$$

To get a steady state solution of (u, v, n_1, n_2, ϕ) upto a desired accuracy, sequential steps are followed as discussed in the previous chapter (Chapter 4).

5.3.1 Code Validation

A grid independence test is performed to make a balance between numerical cost and numerical convergence. In order to validate our numerical scheme for power law model, we have considered the case of a slit micro channel with uniform zeta potential distribution and compared the analytic solution for axial velocity profile by Zhao et al. [287] with our results for different power law indices ($n = 0.7, 1, 1.5$) with uniform $\zeta-$ potential, presented in Fig. 5.2 which shows an excellent agreement with our results for $kH = 5, 10, 20, 30, 40, 50$. Fig. 5.3 presents the comparison for axial velocity with the numerical results provided by Cho et al. [63] for $n = 0.6, 1, 1.4$ along the wave crest for a symmetric wavy channel geometry of the form $\mathcal{F}_l(x) = -0.5-\{\alpha_1 sin(2\pi x)+\alpha_2 sin(4\pi x)\}$ and $\mathcal{F}_u(x) = 0.5+\{\alpha_1 sin(2\pi x)+\alpha_2 sin(4\pi x)\}$. The comparison shows a good agreement with our results.

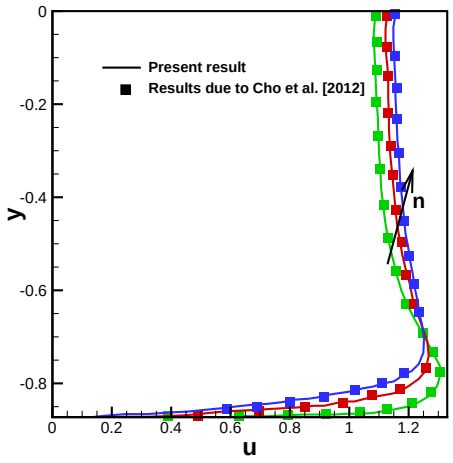

Figure 5.3: Comparison for streamwise velocity at wave crest with Cho et al. [63] for different power law indices (n=0.6, 1, 1.4) for a symmetric wavy channel of the form $y = \pm\{0.5 + \alpha_1 sin(2\pi x) + \alpha_2 sin(4\pi x)\}$. Here $\alpha_1 = 0.05$, $\alpha_2 = 0.02$, $\kappa H = 50$ and $E_0 = 100\ V/cm$.

5.4 Results and Discussions

In this section, the effect of patterned geometry with periodic surface charge distribution is presented for Newtonian and power law electrolytes. For simulation purpose, the channel of average height $H = 10\ \mu m$ is considered with length $L = 6H$. The thermal potential and the externally applied electric field are considered as 25.6 mV and $10^4\ V\ m^{-1}$. In addition, the magnitude of the maximum dimensional zeta potential is considered as 25.6 mV with $\zeta_0 = -1$. For the sake of simplicity, the diffusion coefficients for the cation and anion species are assumed to be same as $D = 1 \times 10^{-9}\ m^2\ s^{-1}$. The other physical properties are specified as follows: flow consistency index, $m = 10^{-3}\ Pa\ s^n$; fluid density, $\rho = 10^3\ kg\ m^{-3}$; Faraday's constant, $F = 96485\ C\ mol^{-1}$; universal gas constant, $R = 8.314\ J\ mol^{-1}\ K^{-1}$; Boltzmann's constant, $k_B = 1.38 \times 10^{-23}\ m^2\ kg\ s^{-2}K^{-1}$; permittivity of the medium, $\epsilon_e = 695.4 \times 10^{-12}\ C\ V^{-1}\ m^{-1}$; absolute temperature, $T = 300\ K$ and elementary charge, $e = 1.602 \times 10^{-19}\ C$. Additionally, the range of the Debye-Hückel parameter (κH) is considered between 10 ($\lambda = 1\ \mu m$) and 50 ($\lambda = 200\ nm$) by varying the ionic strength of the electrolyte concentration from $9.22 \times 10^{-8}\ M$ ($n_0 = 5.55 \times 10^{19}\ ions/m^3$) to $2.3 \times 10^{-6}\ M$ ($n_0 = 1.39 \times 10^{21}\ ions/m^3$). This range of ionic concentration is consistent with the solutions used in the available literatures [17, 177]. The dimensionless parameters namely Reynolds number, Peclet number (for ionic species) and the scaled external electric field strength take the value $Re = 1.78 \times 10^{-3}$, $Pe = 1.78$ and $\Lambda = 3.9$ respectively thought this chapter. Furthermore, The diffusion coefficient for the uncharged mixing species is considered as $D_s = 1 \times 10^{-11}\ m^2\ s^{-1}$ [44, 113].

5.4.1 Mixing and Pressure Drop for Newtonian Fluid with Different Phase Shifts

The streamline pattern for different phase shifts in case of Newtonian fluid are presented in Fig. 5.4. The depicted figure shows the flow line distributions for the sinusoidal patterned microchannel with the variation of phase shifts. It is observed that recirculating vortices take place near the channel walls in the crest region due to sinusoidally varying ζ-potential. The fluids near the regions of wave trough flows in the direction of external electric field due to negative ζ-potential distribution. Due to the positive surface potential (i.e. opposite to wave trough), the fluid streams in the crest region experiences an opposite momentum which drive a reverse flow resulting flow reversal zones near the crest regions. The appearance of flow reversal zones is beneficial to have an improved mixing in the microfluidics. Fig. 5.5 presents the downstream mixing efficiency for fixed κH and α respectively for different phase shifts. The

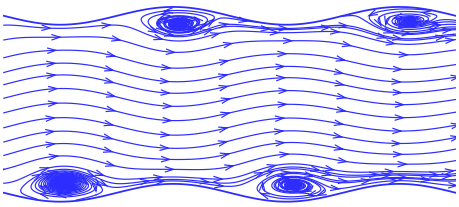

(a) $\delta = 0$

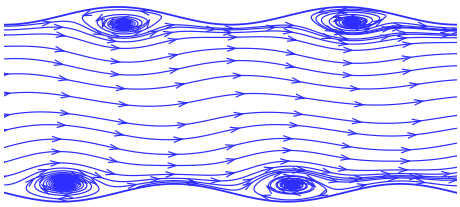

(b) $\delta = \pi/2$

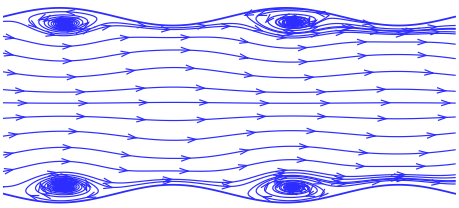

(c) $\delta = \pi$

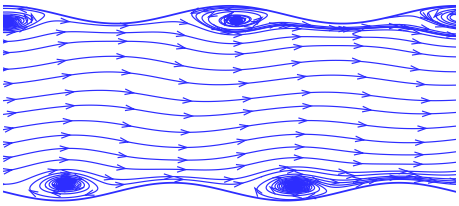

(d) $\delta = 3\pi/2$

Figure 5.4: Streamline patterns for Newtonian case ($n = 1$) with different phase shifts ($\delta = 0, \pi/2, \pi, 3\pi/2$) when $\kappa H = 10$, $H = 10\mu m$ and $E_0 = 10^4\ Vm^{-1}$.

results shows that the phase shift $\delta = \pi/2$ gives highest mixing efficiency at the downstream of the channel, whereas for $\delta = 3\pi/2$ the mixing efficiency is lowest (Fig. 5.5 (a)). The mixing efficiency preserved its maximum value at $\delta = \pi/2$ and minimum at $\delta = 3\pi/2$ with the variation of wave amplitude from 0 to 0.12 (Fig. 5.5 (b)). Fig. 5.6 presents the variation of pressure drop (Δp) along the channel length as a function of phase shift for various values of wave amplitudes and EDL thickness. Here the pressure drop is defined as $\Delta p = p_{avg}^{inlet} - p_{avg}^{outlet}$ [17], where p_{avg}^{inlet} and p_{avg}^{outlet} denote the average pressure at upstream and downstream of the channel respectively. It can be observed that the pressure drop is highest for $\delta = 3\pi/2$ and lowest for $\delta = \pi/2$. To measure the mixing enhancement together with pressure drop, mixing enhancement factor (χ) [23], the ratio of downstream mixing efficiency to average pressure drop is presented in Fig. 5.7 for different phase shifts. It is concluded from Fig. 5.7 that both the mixing efficiency and mixing enhancement factor are highest for $\delta = \pi/2$ irrespective of the Debye layer thickness and wave amplitude. Consequently, the numerical simulations are presented in the successive sections using the phase shift $\delta = \pi/2$.

5.4.2 Mixing and Pressure Drop for Power-Law Fluid

In this section, the influence of power law index, EDL thickness and wave amplitude on flow mixing and pressure drop for the phase shift $\delta = \pi/2$ are analyzed. Fig. 5.8 shows the flow

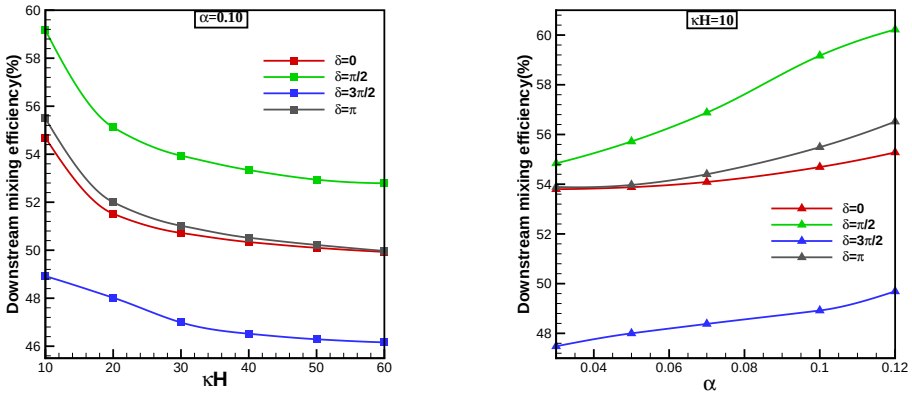

(a) (b)

Figure 5.5: Mixing efficiency at the downstream of the channel for Newtonian case ($n = 1$) with the variation of (a) Debye-Hückel parameter (κH) and (b) wave amplitude (α) when $H = 10\ \mu m$, $\zeta_0 = -1$, $E_0 = 10^4\ Vm^{-1}$.

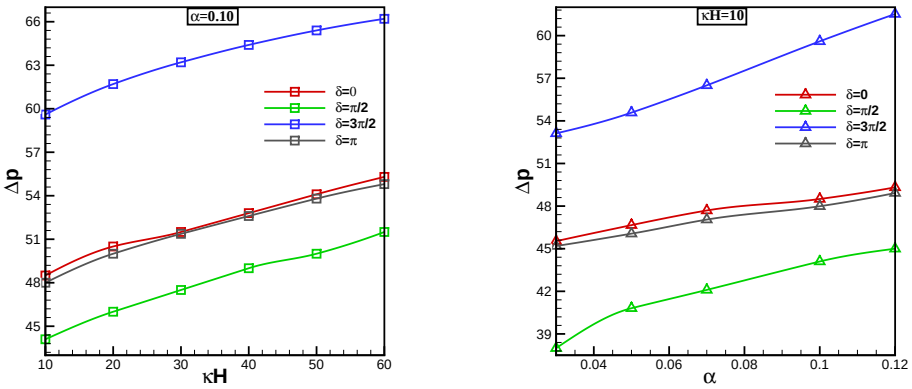

(a) (b)

Figure 5.6: Average pressure drop for Newtonian case ($n = 1$) with the variation of (a) Debye-Hückel parameter (κH) and (b) wave amplitude (α) when $H = 10\ \mu m$, $\zeta_0 = -1$, $E_0 = 10^4\ Vm^{-1}$.

streamlines for different power-law indices for a fixed wave amplitude. In EOF, the driving force acts in the EDL and the bulk flow is not driven directly, but it is dragged through momentum coupling effect. It is observed from Fig. 5.8 that, for $n = 1$, recirculating eddies appear in the wave trough due to the coupled effect of heterogenous surface charge and curvature of the wavy designed geometry. It can also be noticed that, for a higher value of n (under same flow condition), say for $n = 1.5$, the recirculating eddies expanded in size, whereas with the decrement in power-law index i.e. for $n = 1.0$ the eddies diminish and disappear for $n = 0.7$. This phenomena can be described in view of effective viscosity of power-law fluids. For pseudoplastic fluids, the viscosity is lower than Newtonian and dilatant fluids. Thus, with the decremented values of the power-law index, the average velocity is enhanced due to less friction force and consequently

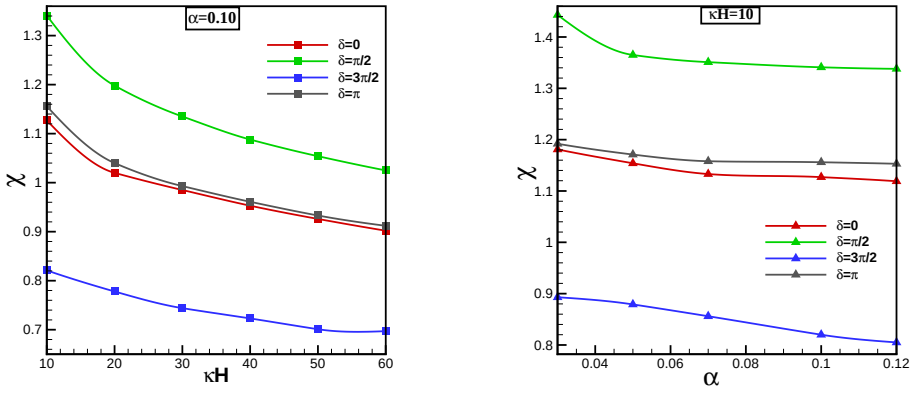

(a) (b)

Figure 5.7: Mixing performance factor for Newtonian case ($n = 1$) with the variation of (a) Debye-Hückel parameter (κH) and (b) wave amplitude (α) when $H = 10\ \mu m$, $\zeta_0 = -1$, $E_0 = 10^4\ Vm^{-1}$.

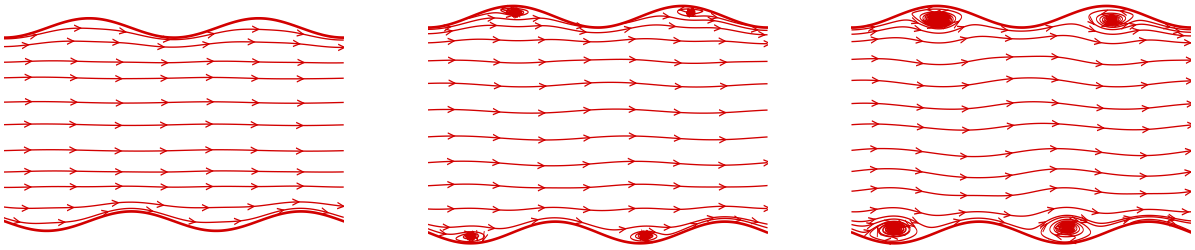

(a) n=0.7 (b) n=1.0 (c) n=1.5

Figure 5.8: Distribution of flow streamlines for (a) $n = 0.7$, (b) $n = 1.0$ and (c) $n = 1.5$. Here $\alpha = 0.05$, $\zeta_0 = -1$, $\kappa H = 10$, $E_0 = 10^4\ Vm^{-1}$, $H = 10\ \mu m$.

flow separating zones are sinked and disappear. In otherwords, it can be concluded that, with the increment of power-law index, fluid streams experience more tortious path when passing through the corrugated domain due to high shear force which produces a weak flow rate and consequently the retention time is increased. Fig. 5.9 presents the effect of wave amplitude on streamlines distribution. It can be observed that, the reverse flow zones expanded in size as the wave amplitude is increased, i.e. flow streams follow more stretched and folded paths when the flow past through the wavy domain with high wave amplitude.

It is evident from the above discussion that, the increment of power-law index increases the effective fluid viscosity which in turn produces a lower flow rate. Fig. 5.10 shows a parametric

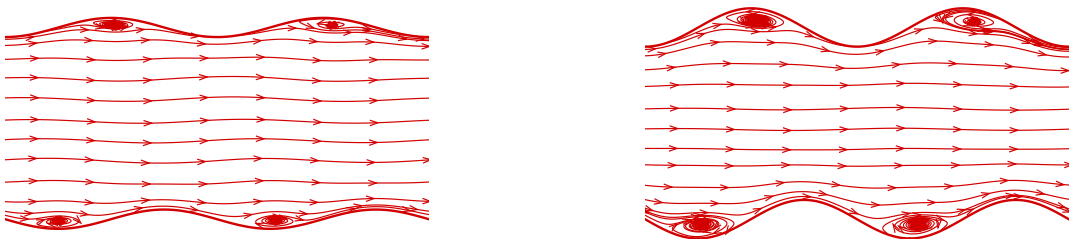

(a) $\alpha = 0.05$ (b) $\alpha = 0.10$

Figure 5.9: Streamlines for different wave amplitude (a) $\alpha = 0.05$ and (b) $\alpha = 0.10$ with $n = 1.2$, $\kappa H = 10$ $\zeta_0 = -1$, $E_0 = 10^4$ Vm^{-1}, $H = 10$ μm.

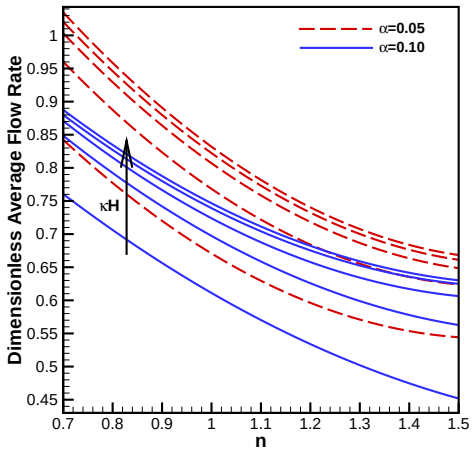

Figure 5.10: Variation of average flow rate with power-law index (n) and wave amplitude (α) for $kH = 10, 20, 30, 40, 50$. Here $\zeta_0 = -1$, $E_0 = 10^4$ V/m, $H = 10$ μm.

relationship between average flow rate, power-law index and EDL thickness. It can also be observed that the flow rate is decreased with higher wave amplitude as a consequence of stronger reverse flow. Also, Fig. 5.10 shows that for a fixed power-law index and wave amplitude, average flow rate is enhanced for higher values of κH (i.e. for thinner EDL), as thicker EDL produces a less momentum to drive the flow streams. A larger flow rate is beneficial in increasing sample throughput but leads to a weak mixing. The occurrence of attending a reduced flow rate is compatible with mixing efficiency enhancement in microfluidics.

From the above discussions, it is observed that flow streams for pseudoplastic fluids produce higher flow rate as compared to dilatant fluids. In other words, it can be concluded that flow streams of pseudoplastic fluids pass much faster through the corrugated channel compared to dilatant fluids which follows a reverse characteristic. Thus, with the increment of power-law index, not only the contact area between different flow streams are increased but the retention

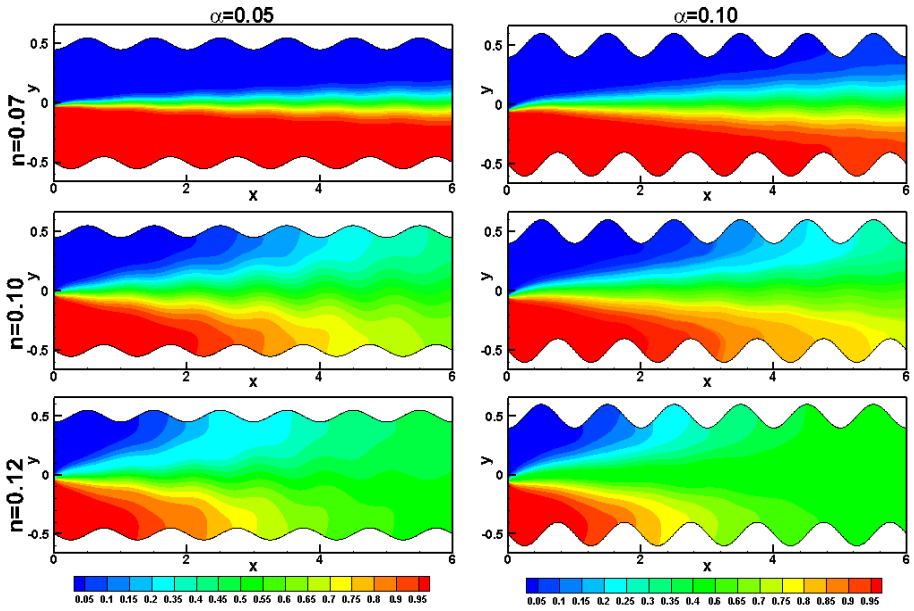

Figure 5.11: Distribution of concentration contours for different power-law index (n) and wave amplitude (α) when $\zeta_0 = -1$, $\kappa H = 10$, $E_0 = 10^4\ Vm^{-1}$, $H = 10\ \mu m$.

time is also increased. As a result diffusion flux in increased for higher values of n to achieve an improved mixing along different levels of the channel. Also, with the increment of wave amplitude (irrespective of n), the effective interfacial contact area is increased and consequently mixing efficiency is increased. Fig. 5.11 illustrates the non-dimensional concentration contour along the channel length as a function of power-law index and wall's wave amplitude. It is seen that, stream specified by blue color (with concentration $C = 0$) enters the corrugated channel through lower half of the inlet, while specified red color streams (with concentration $C = 1.0$) enter the channel from the upper half inlet. The ideal mixed concentration (with concentration $C = 0.5$) is demonstrated by green color. It is observed from concentration contour (Fig. 5.11) that, the streams of different concentrations are totally unmixed in the upstream, showing 0% mixing efficiency and the same is getting enhanced along flow direction due to the improvement of diffusion flux with the increment in power-law index with higher wave amplitude. Fig. 5.12 (a) & Fig. 5.12 (b) present the mixing efficiency along the channel length and the concentration profile at the channel downstream respectively. It is observed from Fig. 5.12 (b) that the downstream concentration profiles approaches the saturated value ($C = 0.5$) when the value of the power-law index is increased. It can also be concluded that the downstream concentration profile becomes more closer to the saturated value when the wave amplitude is increased. This phenomena verifies that the flow mixing at the downstream of the channel is increased with the power-law index and wave amplitude. The mixing efficiency at the downstream of the channel is improved from 18% to 96% with the increment of power-law index from 0.7 to 1.5 for

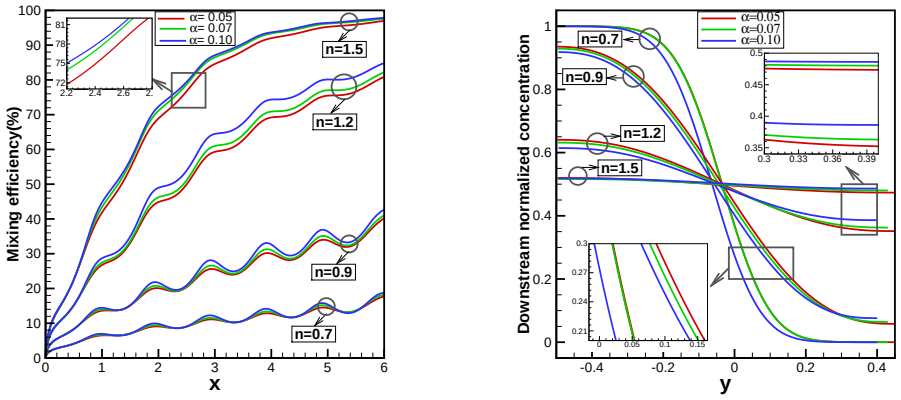

(a) (b)

Figure 5.12: (a) Mixing efficiency along the channel length and (b) downstream concentration profile for different power-law index (n) and wave amplitude (α). Here $\zeta_0 = -1$, $\kappa H = 10$, $E_0 = 10^4\ Vm^{-1}$, $H = 10\ \mu m$.

a fixed wave amplitude ($\alpha = 0.05$). It is also observed that mixing can be further improved along the downstream by increasing the wave amplitude. Fig. 5.13 represents the downstream mixing efficiency variation as a function of Debye-H$\ddot{u}$ckel parameter (κH) & power-law index with different wave amplitudes. For higher values of κH (i.e. for thin EDL), the retention time is decreased as a consequence of higher flow rate (Figute 5.10), and thus the overall mixing efficiency at the downstream of the channel is decreased (irrespective of n and α) which can be observed from Fig. 5.13.

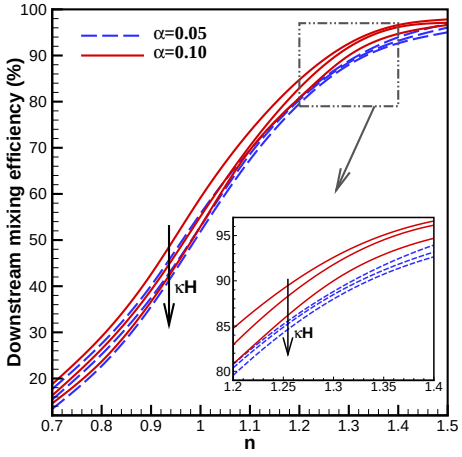

Figure 5.13: Mixing efficiency at the downstream of the channel for the variation of power-law index (n), Debye-H$\ddot{u}$ckel parameter (κH) and wave amplitude (α). Here $\zeta_0 = -1$, $E_0 = 10^4\ Vm^{-1}$, $H = 10\ \mu m$.

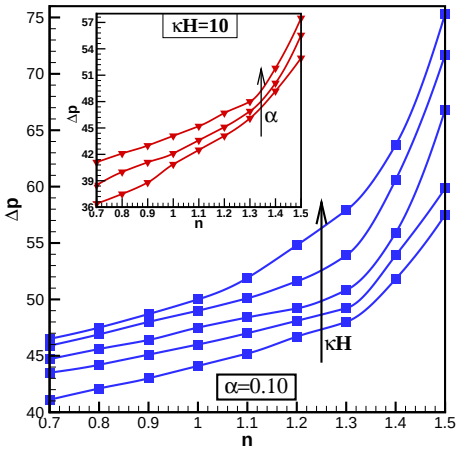

Figure 5.14: Variation of pressure drop with the variation of power-law index (n) and Debye-Hückel parameter ($\kappa H = 10, 20, 30, 40, 50$) for a fixed value of wave amplitude ($\alpha = 0.10$). Here $\zeta_0 = -1$, $E_0 = 10^4\ Vm^{-1}$, $H = 10\ \mu m$. The inset presents the variation of pressure drop as a function of n and α $(0.05, 0.07, 0.10)$ for $\kappa H = 10$.

For designing an efficient and effective mixer, the understanding of pressure drop is necessary, as high pressure drop may reduce the overall efficiency of the system. Fig. 5.14 demonstrates the variation of dimensionless pressure drop with the increment of power-law index for different κH and α. It is clearly observed that pressure drop is lower for pseudoplastic fluid ($n < 1$) as compared to dilatant fluid ($n > 1$) as the average velocity is increased with the increment of power-law index. One may conclude that the pressure drop establishes a proportional relationship with the wave amplitude, whereas the variation shows an inversely proportional relationship with the EDL thickness. In order to model a novel micromixer (based on power-law rheology), taking the average pressure drop into account with mixing efficiency, mixing enhancement factor is presented in Fig. 5.15. One may observe from Fig. 5.15 (a) that, for fixed wave amplitude and power-law index, mixing enhancement factor is reduced with the increment of κH as a consequence of lower mixing efficiency and higher pressure drop. On the other hand, a close look of Fig. 5.15 (b) revels that, with the increase of the wave amplitudes (for fixed n and κH), the enhancement factor is reduced slightly as the increment in pressure drop dominates the mixing efficiency enhancement. One may find the most important observations of this study from Fig. 5.15 (a) and Fig. 5.15 (b) as follows: the mixing enhancement factor is increased with the increment of power-law index (irrespective of κH and α) upto $n = 1.3$ and then it is decreased due to high pressure drop. The above observations signify that the increment of wave amplitude and power-law index may improve the mixing efficiency but not always be beneficial in terms of the enhancement factor. Hence, to propose and demonstrate the design of a novel

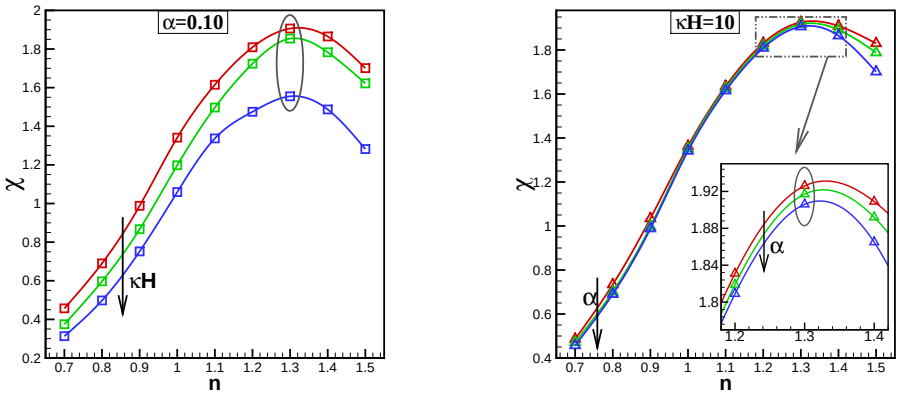

(a) (b)

Figure 5.15: Variation of mixing performance factor ($\chi = \sigma/\Delta p$) with different power-law index (n) for different (a) Debye-Hückel parameter ($\kappa H = 10, 20, 50$) and (b) wave amplitude ($\alpha = 0.05, 0.07, 0.10$). Here $\zeta_0 = -1$, $E_0 = 10^4\ Vm^{-1}$, $H = 10\ \mu m$.

micromixing structure, it is essential to consider the pressure drop which is one of the key issues for industrial usage to get optimum output (maximum mixing efficiency with minimum pressure drop).

5.5 Conclusions

A two-dimensional numerical study in electrokinetically driven flow is demonstrated to model micro mixing structure through a micro-channel based on Poisson-Nernst-Planck model to investigate the mixing efficiency and pressure drop with periodic variation of surface potential and sinusoidal wavy surface. Electroosmotic mixing is purely diffusive in case of straight microchannel. The current simulation results depict that the vortices formed due to wavy surfaces as a result of increment in the interfacial contact area between two streams which can improve the diffusion flux, and the vortex size is expanded with the increment of flow behavior index which causes a reduction in the flow rate to achieve a desirable mixing. Although, mixing efficiency is increased remarkably for higher values of flow behavior and higher wave amplitudes, it causes a large pressure drop which is not compatible with the system performance. Thus a parametric relationship is estimated to achieve an efficient, effective and controllable mixing by a combined study of mixing efficiency and enhancement factor. The simulations have also considered the effect of heterogeneously charged surface which prompted the formation of circulation zones generating the perturbation which may be an enhancement factor for heat dissipation. The idea described in this study can be helpful to design a novel passive micromixer by maintaining

a suitable balance between mixing efficiency and average pressure drop.

Chapter 6

A Comparative Analysis of Mixing Performance of Power-Law Fluid in Cylindrical Micro-Channels with Sudden Contraction / Expansion

6.1 Introduction

In recent years, promising advancements in micro fluidics have been achieved in the application to the micro total analysis systems (μ TAS) and Lab-On-a-chip (LOC) which aims to integrate a variety of functions in a small platform [62, 86, 273]. As compare to macro-scale counterparts, these miniaturized devices offer significant advantages like higher performance, reduced reagent consumption, lower cost & excellent portability, and thus such devices have received significant attentions from different scientific and engineering applications, such as DNA extraction and synthesis [206, 275], bacteria and virus detection [75, 103, 139], detection and separation of proteins [51], mixing operations [142, 143] etc. Electrokinetic pumping (Electroosmosis) which have several advantages over the conventional pressure driven flow (discussed in Chapter-IV) serves as an efficient mechanism in micro / nano devices for driving and manipulating the sample fluids. To deal with such systems with small characteristic scale (of the order of micro and nano meter), micro-fluidic mixers play an effective role to stir the fluid streams at different levels in protein crystallization [121, 214], chemical reactions [133], biological assays [228], biomedical diagnostics [236] and so on.

Because of low Reynolds number regime, the fluid flow in micro fluidic devices is laminar and fluid mixing relies on slow molecular diffusion and thus to obtain an efficient mixing performance in such miniaturized devices is a great challenge to the researchers. As discussed in the literature, micromixers are categorized into active and passive [41] depending on whether mixing is assisted by external stirring agents or not. As discussed in previous chapters, active micromixers require external energy sources, such as acousticaiiy induced vibrations [24], pressure perturbation [95], ultrasound [283], electro-kinetic instabilities [201], incoming flow pulsing [49,95,174], electrothermal pumping [92], magneto-hydrodynamic interaction [272] etc. to stir the fluid streams in order to achieve enhanced mixing performance. On the other hand, passive micromixers do not require any external perturbing sources, but rely on geometric and surface structure manipulation to modify the flow field, so as to reduce the diffusion length and maximize the contact area between the fluids. Although active micromixers lead to better mixing but due to active moving parts and fabricating difficulties, integration of such mixers with other devices becomes a great challange. Because of such drawbacks, passive mixing strategies are becoming more effective and popular to microfluidic community in mixing purpose. Several numerical and experimental works have been done on passive mixing by many research groups to propose micromixer designs to get an optimum mixing. To achieve a desirable mixing in a shorter channel length, various methods have been developed in recent past [143]. Different approaches are used to create geometric modulation of the microchannels by using the various shapes of microchannels or by placing obstacles in the flow domain. Thus, designing the microchannel configuration is a notable concern for achieving effective and efficient mixing.

In recent past several numerical and experimental studies have been performed by various research groups around the world to improve passive mixing ability by manipulating the channel geometry [39, 134, 143]. In this regard different channel shapes have been introduced by the researchers like T/Y junctions [80, 110, 166], E shaped channels [60], H-shaped sub channels [198], placing of obstacle/ ribs within the channels [5, 36, 190, 276], patterned grooved structures [6, 265], convergent-divergent channel geometry [2], zig-zag channels [252], wavy and serpentine geometry [58, 59, 109] etc. In addition of geometric modulations, irregular distribution of surface charge density (or ζ potential), caused by manufacturing defects or by creating surface potential heterogeneity manually using standard fabrication techniques [144, 279], mixing efficiency can be notably enhanced [28, 84, 189]. Although, the passive mixing schemes mentioned above are capable to improve the mixing efficiency effectively, but all are restricted to Newtonian fluid model only. However, many of the chemical (e.g., colloidal suspensions and

polymer solutions) and biological (e.g., blood, saliva, and DNA solutions) fluids are actually complex, exhibiting non-Newtonian characteristics [78,156,289]. In this regard a number of non-Newtonian fluid models in mixing applications have been proposed, mentioned in the previous chapter [Chapter 5]. Compared to the other non-Newtonian models, power-law model is the most preferred and popular due to it's simplicity and ability to characterize a wide range of non-Newtonian fluids [289,290]. In last decade a number of analytical and numerical studies have been performed on rectangular and cylindrical micro channels based on Poisson-Boltzmann (PB) model [15,16,76,81,197,282,287,289–291,293]. Recently Nekoubin [193] performed a numerical study for a power-law fluid in a curved rectangular micro-channel with high zeta potential. The results have shown that the increment in channel aspect ratio leads to an significant enhancement in the circulation strength for shear thinning fluid flows. Several studies have been done on electrokinetic mixing analysis for power-law fluid in micro domains with surface heterogeneity [17,100,101] and wall modulation [63–66]. However, to the best knowledge of the authors, the non-Newtonian electrokinetic flow mixing in circular tubes with surface modulation (sudden expansion/ constriction of channel radius) and potential non-homogeneity has not been investigated in literature. In the present chapter, the most general Poisson-Nernst-Planck model is considered for comparative mixing analysis, rather than using Poisson-Boltzmann model which have some limitations [169]. In addition, average pressure drop is investigated together with mixing efficiency enhancement to find the optimum parameters to get a maximum possible mixing with minimum pressure drop. This chapter is organized as follows: Section 2 presents the formulation of the problem with two parallel configurations for comparative mixing analysis. Also the mathematical formulation based on power-law model is described. In Section 3, the numerical schemes associated with this chapter is presented. The validation of our numerical scheme with the previously published literatures is described in this section. Section 4 contains a detail discussion on flow mixing and pressure drop for both the configurations for a wide range of power-law index, wave amplitude of the deflected region and non-homogenous potential patch strength. At the last section of this chapter concluding remarks are made.

6.2 Problem Formulation

In this chapter, a steady comparative mixing in two axisymmetric cylindrical tubes with sudden (i) constriction and (ii) expansion are considered and presented in Fig. 6.1. The considered cylindrical channels are of diameter $2r_0$ and length L are filled with aqueous non-Newtonian (power-law) incompressible electrolyte in isothermal flow environment. The external electric

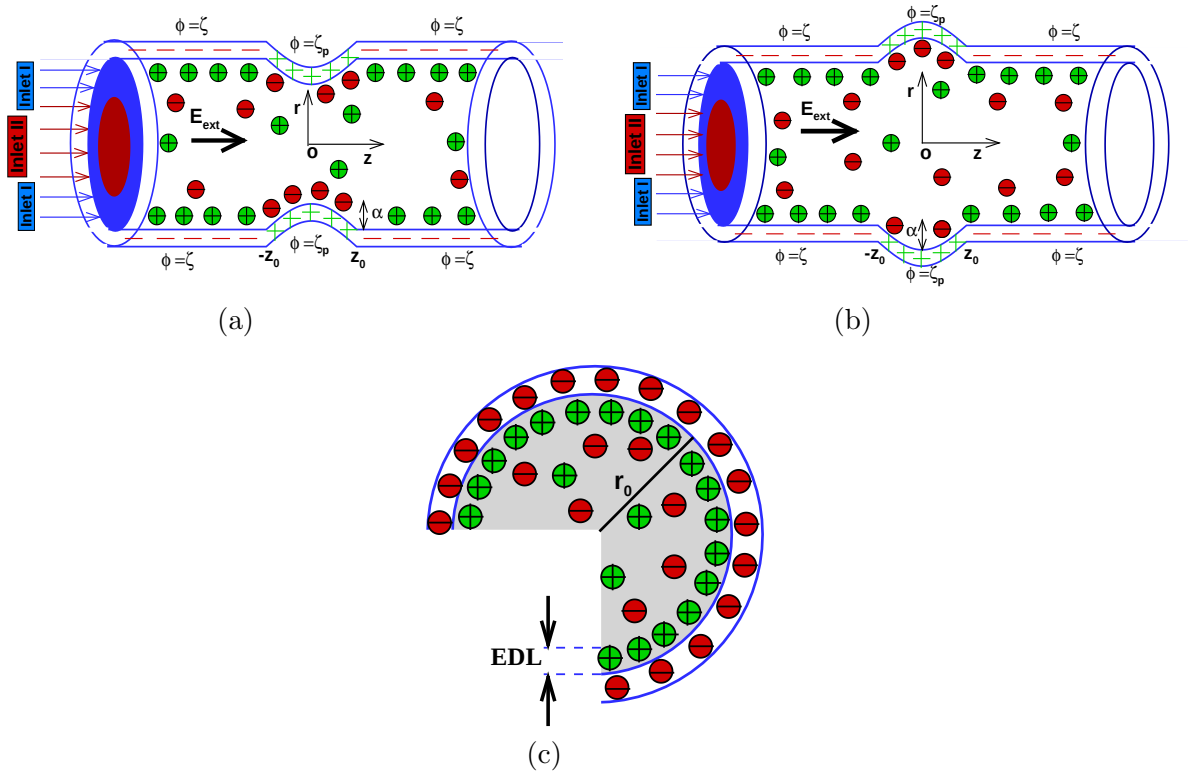

Figure 6.1: Schematic diagram of the flow geometry. Cylindrical channel with sudden (a) constriction and (b) expansion. (c) Arrangement of charges of EDL in the non-corrugated region.

field is considered to be acted along the streamwise direction, whereas the surface potential (ζ-potential) is assumed to be distributed uniformly with constant magnitude, except the deflected region (*i.e.* the region of constriction / expansion). It is also assumed that overpotential patches of strength ζ_p (with opposite sign of wall ζ- potential of homogenous part) are placed along the deflected regions to create surface heterogeneity. The geometry of the axisymmetric micro tubes with sudden constriction / expansion are defined as

$$r^*(z^*) = \mathcal{R}_0^*(z^*) = \begin{cases} r_0 \mp \alpha^* \left[1 + cos\left(\frac{2\pi z^*}{r_0}\right)\right] ; & -z_0^* \leq z^* \leq z_0^* \\ r_0 \ ; & \text{otherwise,} \end{cases}$$

where "$\mp$" signs stand for constricted ($-$) and expanded ($+$) channels respectively. Here r_0, α^*, z_0^* denote the radius of the tube (in non-deflected cross sections), the dimensional amplitude and the half length of the deflected regions respectively. In this chapter, z_0^* is considered to be $r_0/2$. By scaling the the coordinates with the radius r_0 (*i.e.* $z = z^*/r_0$, $r = r^*/r_0$), the expression of the constricted / expanded tube becomes

$$r(z) = \mathcal{R}_0(z) = \begin{cases} 1 \mp \alpha[1 + cos(2\pi z)] \ ; & -0.5 \leq z \leq 0.5 \\ 1 \ ; & \text{otherwise,} \end{cases}$$

where $\alpha = \frac{1}{r_0}\alpha^*$ and $\mathcal{R}_0(z) = \frac{1}{r_0}\mathcal{R}_0^*(z^*)$. In this chapter, the rheology of the aqueous solution, used to describe the fluid flow and mixing enhancement is characterized by non-Newtonian flow behavior and is considered to follow power-law model. Considering power-law model, the functional dependence between shear stress and rate-of-strain can be written as [17, 193]

$$\boldsymbol{\tau}^* = 2\mu_a^*(\dot{\gamma^*})\dot{\boldsymbol{\gamma}}^* \tag{6.1}$$

with

$$\dot{\gamma^*} = \sqrt{\frac{1}{2}(\dot{\boldsymbol{\gamma}}^* : \dot{\boldsymbol{\gamma}}^*)} \tag{6.2}$$

where $\boldsymbol{\tau}^*$ and $\dot{\boldsymbol{\gamma}}^*$ denote the shear stress tensor and the rate-of-strain tensor respectively. Here μ_a^* is the apparent viscosity, which can be expressed as [192, 193]

$$\mu_a^*(\dot{\gamma^*}) = m(\dot{\gamma^*})^{n-1} \tag{6.3}$$

where m is the flow consistency index and n is the flow behavior index. It is mentioned that $n < 1$ and $n > 1$ correspond to pseudoplastic (shear- thinning) and dilatant (shear-thickening) fluids respectively, whereas Newtonian rheology is followed for $n = 1$.

In this framework of power-law model, the dimensional apparent viscosity in cylindrical coordinates for axisymmetric flow takes the form [193]

$$\mu_a^* = m\left[2\left\{\left(\frac{\partial u_r^*}{\partial r^*}\right)^2 + \left(\frac{u_r^*}{r^*}\right)^2 + \left(\frac{\partial u_z^*}{\partial z^*}\right)^2\right\} + \left\{\frac{\partial u_r^*}{\partial z^*} + \frac{\partial u_z^*}{\partial r^*}\right\}^2\right]^{\frac{n-1}{2}} \tag{6.4}$$

where u_r^*, u_z^* are the velocity components in the radial and axial direction respectively. The equations for the transport of aqueous non-Newtonian electrolyte in axisymmetric flow field, governed by the equation of continuity and the Cauchy momentum equation can be expressed as [34, 97, 193]

- continuity:

$$\frac{1}{r^*}\frac{\partial}{\partial r^*}(r^* u_r^*) + \frac{\partial u_z^*}{\partial z^*} = 0 \tag{6.5}$$

- z momentum:

$$\rho\left(u_r^*\frac{\partial u_z^*}{\partial r^*}+u_z^*\frac{\partial u_z^*}{\partial z^*}\right)=-\frac{\partial p^*}{\partial z^*}-\left[\frac{1}{r^*}\frac{\partial}{\partial r^*}(r^*\tau_{rz}^*)+\frac{\partial}{\partial z^*}(\tau_{zz}^*)\right]-\rho_e^*\frac{\partial\Phi^*}{\partial z^*} \tag{6.6}$$

- r momentum:

$$\rho\left(u_r^*\frac{\partial u_r^*}{\partial r^*}+u_z^*\frac{\partial u_r^*}{\partial z^*}\right)=-\frac{\partial p^*}{\partial r^*}-\left[\frac{1}{r^*}\frac{\partial}{\partial r^*}(r^*\tau_{rr}^*)+\frac{\partial}{\partial z^*}(\tau_{zr}^*)-\frac{\tau_{\theta\theta}^*}{r^*}\right]-\rho_e^*\frac{\partial\Phi^*}{\partial r^*} \tag{6.7}$$

where $\tau_{rr}^*=-\mu_a^*\left(2\frac{\partial u_r^*}{\partial r^*}\right)$, $\tau_{\theta\theta}^*=-\mu_a^*\left(2\frac{u_r^*}{r^*}\right)$, $\tau_{zz}^*=-\mu_a^*\left(2\frac{\partial u_z^*}{\partial z^*}\right)$, $\tau_{zr}^*=\tau_{rz}^*=-\mu_a^*\left(\frac{\partial u_r^*}{\partial z^*}+\frac{\partial u_z^*}{\partial r^*}\right)$ are the components of the shear stress tensor $\boldsymbol{\tau^*}$. Although the flow is axisymmetric, the shear stress component $\tau_{\theta\theta}^*$ appears in the radial component of the momentum equation because of the appearance of u_r^*/z^* [97,193]. Here $\rho_e^*=\Sigma z_i e n_i^*$ is the net charge density, where e, z_i and n_i^* denote the elementary charge, valance and the number concentration of the i^{th} species. In this regard Φ^* is the total potential which is the linear superposition of external potential (ψ^*) and induced potential (ϕ^*).

The following parameters are used to non-dimensionalise the flow governing equations. $t=\frac{t^*}{(r_0/U_s)}$, $r=\frac{r^*}{r_0}$, $z=\frac{z^*}{r_0}$, $u_r=\frac{u_r^*}{U_s}$, $u_z=\frac{u_z^*}{U_s}$, $p=\frac{p^*}{(mU_s^n/r_0^{n+1})}$, $\boldsymbol{\tau}=\frac{\boldsymbol{\tau^*}}{m(U_s/r_0)^n}$, $n_i=\frac{n_i^*}{n_0}$, $\phi=\frac{\phi^*}{\phi_0}$, $\psi=\frac{\psi^*}{\phi_0}$. Here n_0 is the bulk ionic number concentration, U_s is the generalized Helmoholtz-Smoluchowski velocity which is defined as $U_S=n\kappa^{\frac{1-n}{n}}\left(-\frac{\varepsilon_e E_0\phi_0\zeta}{m}\right)^{1/n}$ [193]. The reciprocal of the Debye layer thickness is defined as $\kappa=\sqrt{2en_0/\varepsilon_e\phi_0}$, where ε_e denotes the permittivity of the medium, and ϕ_0 ($=RT/F$) is the thermal potential. Here R, T and F stand for universal gas constant, absolute temperature and Faraday's constant respectively.

A suitable coordinate transformation is used to map the physical domain with constriction / expansion zones into a simpler non-deflected geometry as

$$\xi=z,\qquad \eta=\frac{r}{\mathcal{R}_0(z)}.$$

Under the above mentioned transformation, the continuity and momentum equations can be expressed as

$$\frac{\partial u_z}{\partial\xi}-\eta\frac{\mathcal{R}_0}{\mathcal{R}_0'}\frac{\partial u_z}{\partial\eta}+\frac{1}{\mathcal{R}_0}\frac{\partial u_r}{\partial\eta}+\frac{1}{\mathcal{R}_0}\frac{u_r}{\eta}=0 \tag{6.8}$$

$$\begin{aligned}Re\left[\frac{\partial}{\partial\xi}(u_z^2)-\eta\frac{\mathcal{R}_0'}{\mathcal{R}_0}\frac{\partial}{\partial\eta}(u_z^2)+\frac{1}{\mathcal{R}_0}\frac{\partial}{\partial\eta}(u_zu_r)+\frac{1}{\mathcal{R}_0}\frac{u_zu_r}{\eta}\right]&=-\frac{\partial p}{\partial\xi}+\eta\frac{\mathcal{R}_0'}{\mathcal{R}_0}\frac{\partial p}{\partial\eta}-\left[\frac{1}{\mathcal{R}_0\eta}\frac{\partial}{\partial\eta}(\eta\tau_{\xi\eta})\right.\\&\left.+\left\{\frac{\partial}{\partial\xi}-\eta\frac{\mathcal{R}_0'}{\mathcal{R}_0}\frac{\partial}{\partial\eta}\right\}(\tau_{\xi\xi})\right]+\frac{(\kappa r_0)^{n+1}}{2\Lambda\zeta n^n}\rho_e\left[\left(\frac{\partial\phi}{\partial\xi}+\frac{\partial\psi}{\partial\xi}\right)-\eta\frac{\mathcal{R}_0'}{\mathcal{R}_0}\left(\frac{\partial\phi}{\partial\eta}+\frac{\partial\psi}{\partial\eta}\right)\right]\end{aligned} \tag{6.9}$$

$$Re\left[\frac{\partial}{\partial\xi}(u_r u_z) - \eta\frac{\mathcal{R}_0'}{\mathcal{R}_0}\frac{\partial}{\partial\eta}(u_r u_z) + \frac{1}{\mathcal{R}_0}\frac{\partial}{\partial\eta}(u_r^2) + \frac{1}{\mathcal{R}_0}\frac{u_r^2}{\eta}\right] = -\frac{1}{\mathcal{R}_0}\frac{\partial p}{\partial\eta} - \left[\frac{1}{\mathcal{R}_0\eta}\frac{\partial}{\partial\eta}(\eta\tau_{\eta\eta}) + \left\{\frac{\partial}{\partial\xi} - \eta\frac{\mathcal{R}_0'}{\mathcal{R}_0}\frac{\partial}{\partial\eta}\right\}(\tau_{\eta\xi}) + 2\frac{\mu_a}{{\mathcal{R}_0}^2}\frac{u_r^2}{\eta^2}\right] + \frac{(\kappa r_0)^{n+1}}{2\Lambda\zeta n^n}\rho_e\frac{1}{\mathcal{R}_0}\left(\frac{\partial\phi}{\partial\eta} + \frac{\partial\psi}{\partial\eta}\right) \quad (6.10)$$

where $\tau_{\xi\xi} = -2\mu_a\frac{1}{\mathcal{R}_0}\frac{\partial u_r}{\partial\eta}$, $\tau_{\eta\xi} = \tau_{\xi\eta} = -\mu_a\left\{\frac{\partial u_r}{\partial\xi} - \eta\frac{\mathcal{R}_0'}{\mathcal{R}_0} + \frac{1}{\mathcal{R}_0}\frac{\partial u_z}{\partial\eta}\right\}$ and $\tau_{\xi\xi} = -2\mu_a\left\{\frac{\partial u_r}{\partial\xi} - \eta\frac{\mathcal{R}_0'}{\mathcal{R}_0}\frac{\partial u_z}{\partial\eta}\right\}$ with

$$\mu_a = m\left[2\left\{\left(\frac{\partial u_z}{\partial\xi} - \eta\frac{\mathcal{R}_0'}{\mathcal{R}_0}\frac{\partial u_z}{\partial\eta}\right)^2 + \left(\frac{1}{\mathcal{R}_0}\frac{\partial u_r}{\partial\eta}\right)^2 + \left(\frac{1}{\mathcal{R}_0}\frac{u_r}{\eta}\right)^2\right\} + \left\{\frac{\partial u_r}{\partial\xi} - \eta\frac{\mathcal{R}_0'}{\mathcal{R}_0}\frac{\partial u_z}{\partial\eta}\right\}^2\right]^{\frac{n-1}{2}}.$$

For simplicity, in this chapter we consider a binary and symmetric electrolyte (e.g. $NaCl + H_2O$) with valance z_i $(i = 1, 2) = \pm 1$. Thus the non-dimensionless charge density becomes $\rho_e = (n_1 - n_2)$, scaled by en_0. The dimensionless parameters namely Reynolds number (Re), and dimensionless external field strength Λ are defined as $Re = U_S^{2-n}r_0^n/m$ and $\Lambda = E_0 r_0/\phi_0$ respectively.

The non-dimensional form of the Nernst-Planck equation governing the ion transport of the i^{th} ionic species in the transformed $(\xi - \eta)$ domain is given by [33]

$$Pe(\mathbf{q}\cdot\nabla n_i) = \nabla^2 n_i + z_i\nabla n_i\cdot\nabla\Phi - \frac{(\kappa r_0)^2}{2}z_i n_i\rho_e, \quad (6.11)$$

where

$$\nabla \equiv \left(\frac{\partial}{\partial\xi} - \eta\frac{\mathcal{R}_0'}{\mathcal{R}_0}\frac{\partial}{\partial\eta}, \frac{1}{\mathcal{R}_0}\frac{\partial}{\partial\eta}\right)$$

and

$$\nabla^2 \equiv \frac{\partial^2}{\partial\xi^2} - 2\eta\frac{\mathcal{R}_0'}{\mathcal{R}_0}\frac{\partial^2}{\partial\xi\partial\eta} + \left[\eta^2\left(\frac{\mathcal{R}_0'}{\mathcal{R}_0}\right)^2 + \frac{1}{\mathcal{R}_0^2}\right]\frac{\partial^2}{\partial\eta^2} + \left[2\eta\left(\frac{\mathcal{R}_0'}{\mathcal{R}_0}\right)^2 - \eta\frac{\mathcal{R}_0''}{\mathcal{R}_0} + \frac{1}{\eta\mathcal{R}_0^2}\right]\frac{\partial}{\partial\eta},$$

with $\mathcal{R}_0' = \frac{d\mathcal{R}_0}{dz}$ and $\mathcal{R}_0'' = \frac{d^2\mathcal{R}_0}{dz^2}$. This model (Poisson-Nernst-Planck model) has the flexibility to handle multivalent ionic species. In this chapter, for the sake of simplicity, the diffusivity for both the ionic species (cation and anion) is considered to be same, i.e. D_i $(i = 1, 2) = D$. The non-dimensional number Pe (Peclet number for charged species) measures the ratio of advective to diffusive transport and is defined as $Pe = r_0 U_S/D$.

The driving momentum in EOF is achieved due the linear interaction between local electric field (due to EDL) and applied electric field (due to external power sources). The equation for induced potential in dimensionless form is represented as

$$\nabla^2\phi = -\frac{(\kappa r_0)^2}{2}\rho_e. \quad (6.12)$$

The distribution of external electric potential described by the solution of $\nabla^2\psi = 0$ with insulated wall boundary condition i.e. $\nabla\psi \cdot \mathbf{n} = 0$, where $\mathbf{n}$ represents the unit normal to the corresponding surface pointing towards the liquid.

A fully developed boundary condition, i.e. gradients of flow variables $(u_r, u_z, \phi, n_1, n_2)$ with respect to z is zero is considered along the upstream and downstream of the channel. The zeta potential is assumed to be homogenous except the region of sudden constriction / expansion, where a constant surface potential of opposite sign (of homogeneous region) is placed, thus

$$\phi = \begin{cases} \zeta_p \ ; & -0.5 \leq z \leq 0.5 \\ \zeta \ ; & \text{otherwise,} \end{cases}$$

where ζ_p is the potential patch placed in the deflected part of the channel. In addition, no-slip and no-ion penetration condition is considered along the channel boundary ($r = \mathcal{R}_0$) for velocity and ion distribution respectively which can be expressed as

$$\mathbf{q} = \mathbf{0}; \ (\nabla n_i + z_i n_i \nabla\phi) \cdot \mathbf{n} = 0.$$

Along the centerline of the channel ($r = 0$) a symmetric boundary condition is considered i.e. $\frac{\partial\varphi}{\partial r} = 0$, where $\varphi = (u_r, u_z, \phi, n_1, n_2)$.

6.2.1 Transport of Uncharged Mixing Species

The transport of the uncharged eluted species in absence of chemical reaction and species absorption is governed by advection-diffusion equation which is represented in dimensionless form as

$$(\mathbf{q} \cdot \nabla)C - \frac{1}{Pe_S}\nabla^2 C = 0, \tag{6.13}$$

where C is the non-dimensional species concentration scaled by C_{ref} and Pe_S $(= r_0 U_S/D_S)$ represents the Peclet number for eluted species which measures the ratio of convective to diffusive transport of solutes. Here D_S stands for the diffusion coefficient of the solute. To obtain mixing efficiency at different levels of the channel, no mass flux ($\nabla C \cdot \mathbf{n} = 0$) is considered along the channel wall ($r = \mathcal{R}_0$) and a symmetric condition ($\frac{\partial C}{\partial r} = 0$) is considered along the centerline ($r = 0$) as boundary conditions. At the inlet of the channel a step-like concentration distribution is assumed, i.e. $C = 1$ in the lower half ($0 \leq r \leq r_0/2$) and $C = 0$ in the upper half ($r_0/2 < r \leq r_0$). In addition $\frac{\partial C}{\partial z} = 0$ is assumed along the downstream of the channel.

As like rectangular channels, a measure of species mixing at different levels of the deflceted circular tubes can be defined by a parameter σ, called mixing efficiency which is defined as [84,190]

$$\sigma(z) = \left[1 - \frac{\int_0^{\mathcal{R}_0} |C - C_\infty| dr}{\int_0^{\mathcal{R}_0} |C_0 - C_\infty| dr}\right] \times 100\%,$$

where C_∞ and C_0 indicate the concentrations in the fully mixed ($C_\infty = 0.5$) and totally unmixed ($C_0 = 0 \; or \; 1$) states, respectively. Therefore, $\sigma = 100\%$ represents fully mixing stage and $\sigma = 0\%$ for no mixing.

6.3 Numerical Method

The coupled set of non-linear equations [6.8-6.13] for fluid flow, ionic species, electric potential and uncharged eluted species are solved numerically using a control volume approach [89,159–163] based on staggered grid arrangement. The discretized form of the governing equations are obtained by integrating the respective control volumes. At each control volumes, the QUICK (Quadratic Upstream Interpolation for Convective Kinematics) scheme, proposed by Leonard [145], is used to discretize the convective terms in the mass transfer and momentum equations in order to achieve sharp gradients for fluid velocity, ion concentration, electrostatic potential near channel walls. In addition, a second order central difference scheme is considered to discretize the diffusion term, while an implicit first-order scheme is used for transient terms. The QUICK scheme uses a quadratic interpolation / extrapolation between three successive nodal values to estimate the flow variables at the interface of each control volume. A detailed description of QUICK scheme is presented in the introductory chapter (Chapter I). In performing the simulations Newton's linearization technique is adopted to cope with the non-linearity in the governing equations. In this chapter a time marching numerical methodology is adopted with time step $\Delta t = 0.001$. It is to be mentioned that the ionic concentration, electric potential, species concentration and velocity field achieves a steady state after a transient state and this steady state is independent of the initial conditions prescribed. The discretized equations are solved through SIMPLE algorithm [210], which is based on a cyclic guess-and-correct operation. The pressure link between the momentum and continuity equations are accomplished by transforming the discretized continuity equation into a Poisson equation for pressure correction which is solved iteratively using a SOR (Successive over relaxation) scheme until getting a desired accuracy.

The detailed structure of the numerical algorithm used in this chapter are as follows.

Different control volumes are used (see Fig. 6.2) to discretize the different equations. Integration of the $z-$ momentum equation (Eq. 6.9) at the $(n+1)^{th}$ time step over the $(j,k)^{th}$ control volumes for u_z yields

$$a_j^{u_z} u_{z_{j-1,k}}^{n+1} + b_j^{u_z} u_{z_{j,k}}^{n+1} + c_j^{u_z} u_{z_{j+1,k}}^{n+1} = d_j^{u_z} - \left(p_{j+1,k}^{n+1} - p_{j,k}^{n+1}\right)\Delta\eta_k + \frac{1}{8}\eta_k\left(\frac{\mathcal{R}_0{}'}{\mathcal{R}_0}\right)_j\Big(p_{j,k+1}^{n+1} + p_{j+1,k+1}^{n+1} - p_{j,k-1}^{n+1} - p_{j+1,k-1}^{n+1}\Big)(\Delta\xi_j + \Delta\xi_{j+1}) \quad (6.14)$$

Similarly on integrating the $r-$ momentum equation (Eq. 6.10) at the $(n+1)^{th}$ time step over the $(j,k)^{th}$ control volumes for u_z gives

$$a_j^{u_r} u_{r_{j-1,k}}^{n+1} + b_j^{u_r} u_{r_{j,k}}^{n+1} + c_j^{u_r} u_{r_{j+1,k}}^{n+1} = d_j^{u_r} - \left(\tfrac{1}{\mathcal{R}_0}\right)_j\left(p_{j,k+1}^{n+1} - p_{j,k}^{n+1}\right)\Delta\xi_j \quad (6.15)$$

The mole-fraction equations for the species (counter ion and co-ion) at the $(n+1)^{th}$ time step over the $(j,k)^{th}$ scalar control volume gives

$$\left.\begin{aligned} a_j^{n_1} n_{1_{j-1,k}}^{n+1} + b_j^{n_1} n_{1_{j,k}}^{n+1} + c_j^{n_1} n_{1_{j+1,k}}^{n+1} &= d_j^{n_1} \\ a_j^{n_2} n_{2_{j-1,k}}^{n+1} + b_j^{n_2} n_{2_{j,k}}^{n+1} + c_j^{n_2} n_{2_{j+1,k}}^{n+1} &= d_j^{n_2} \end{aligned}\right\} \quad (6.16)$$

Here n_1 and n_2 stand for mole-fraction of counter and co-ions respectively. For a fixed value of k, the system of equations can be expressed in a matrix form as

$$A_j X_{j-1}^{n+1} + B_j X_j^{n+1} + C_j X_{j+1}^{n+1} = D_j, \quad (6.17)$$

where the coefficient matrices (A_j, B_j, C_j) the known vector (D_j) and the vector of unknown variables (X_j) are given by

$$A_j = \begin{bmatrix} a_j^{u_z} & 0 & 0 & 0 \\ 0 & a_j^{u_r} & 0 & 0 \\ 0 & 0 & a_j^{n_1} & 0 \\ 0 & 0 & 0 & a_j^{n_2} \end{bmatrix};\ B_j = \begin{bmatrix} b_j^{u_z} & 0 & 0 & 0 \\ 0 & b_j^{u_r} & 0 & 0 \\ 0 & 0 & b_j^{n_1} & 0 \\ 0 & 0 & 0 & b_j^{n_2} \end{bmatrix};\ C_j = \begin{bmatrix} c_j^{u_z} & 0 & 0 & 0 \\ 0 & c_j^{u_r} & 0 & 0 \\ 0 & 0 & c_j^{n_1} & 0 \\ 0 & 0 & 0 & c_j^{n_2} \end{bmatrix};$$

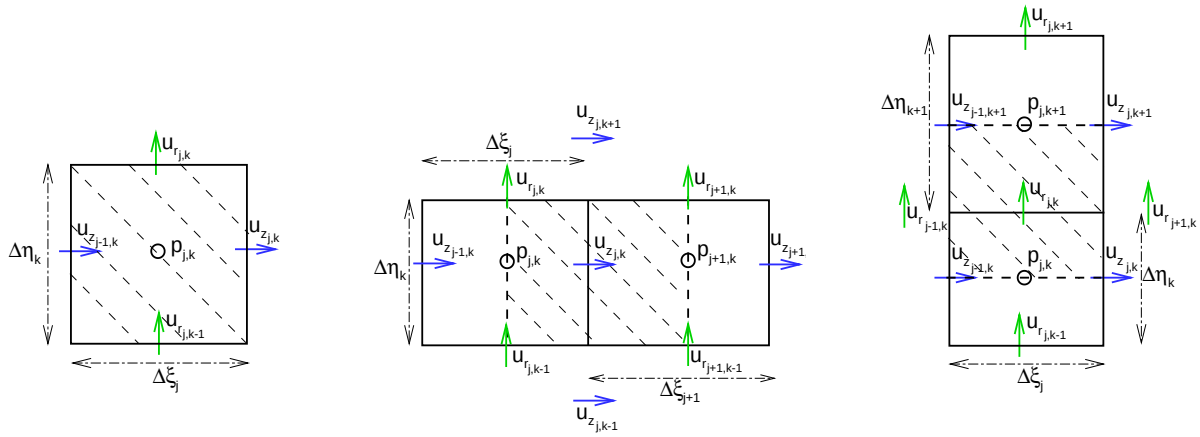

(a) (b) (c)

Figure 6.2: Schamatic of different control volumes. (a) Scalar control volume, (b) u_z control volume, (c) u_r control volume.

$$D_j = \begin{bmatrix} d_j^{u_z} - \left(p_{j+1,k}^{n+1} - p_{j,k}^{n+1}\right)\Delta\eta_k + \frac{1}{8}\eta_k\left(\frac{\mathcal{R}_0{}'}{\mathcal{R}_0}\right)_j\left(p_{j,k+1}^{n+1} + p_{j+1,k+1}^{n+1} \right. \\ \left. -p_{j,k-1}^{n+1} - p_{j+1,k-1}^{n+1}\right)(\Delta\xi_j + \Delta\xi_{j+1}) \\ d_j^{u_r} - \left(\frac{1}{\mathcal{R}_0}\right)_j\left(p_{j,k+1}^{n+1} - p_{j,k}^{n+1}\right)\Delta\xi_j \\ d_j^{n_1} \\ d_j^{n_2} \end{bmatrix}; \; X_j = \begin{bmatrix} u_{z_{j,k}}^{n+1} \\ u_{r_{j,k}}^{n+1} \\ n_{1_{j,k}}^{n+1} \\ n_{2_{j,k}}^{n+1} \end{bmatrix}.$$

Thus the system of equation can be written in a matrix from as

$$\mathbf{AX} = \mathbf{D}, \tag{6.18}$$

where A represents a block tridiagonal matrix, each element of which is a square matrix of order four. Here X, D stand for the vector of unknown variables and the vector of known quantities respectively. The matrix equation is solved using block elimination Varga's Algorithm (Appendix).

On integrating the continuity equation over $(j,k)^{th}$ scalar control volume, we have

$$\left(u_{z_{j,k}}^{n+1} - u_{z_{j-1,k}}^{n+1}\right)\eta_k\Delta\eta_k - \frac{\eta_k}{4}\left(\frac{\mathcal{R}_0{}'}{\mathcal{R}_0}\right)_j\left(u_{z_{j-1,k+1}}^{n+1} + u_{z_{j,k+1}}^{n+1} - u_{z_{j-1,k-1}}^{n+1} - u_{z_{j,k-1}}^{n+1}\right)\eta_k\Delta\xi_j$$
$$+ \left(\frac{1}{\mathcal{R}_0}\right)_j\left(u_{r_{j,k}}^{n+1} - u_{r_{j,k-1}}^{n+1}\right)\eta_k\Delta\xi_j + \left(\frac{1}{\mathcal{R}_0}\right)_j u_{r_{j,k}}^{n+1}\Delta\xi_j\Delta\eta_k = 0. \tag{6.19}$$

The pressure link between the continuity and momentum equations are accomplished by transforming the discretized continuity equation into a Poisson's equation for pressure correction. This pressure correction equation implements a divergence free velocity field.

At each control volume $p_{j,k}$ are unknown at initial stage. To get a solution for Eq. 6.18, a guessed pressure field $p^c_{j,k}$ is assumed. Corresponding to this guessed pressure field $p^*_{j,k}$, the velocity field $(u^*_{j,k}, v^*_{j,k})$ determined form Eq. 6.18 is denoted as $(u^*_{j,k}, v^*_{j,k})$. Since $u^*_{j,k}$ and $v^*_{j,k}$ satisfy Eq. 6.14 and Eq. 6.15, then

$$a_j^{u_z} u^*_{z_{j-1,k}} + b_j^{u_z} u^*_{z_{j,k}} + c_j^{u_z} u^*_{z_{j+1,k}} = d_j^{u_z} - \left(p^*_{j+1,k} - p^*_{j,k}\right)\Delta\eta_k + \frac{1}{8}\eta_k \left(\frac{\mathcal{R}_0{}'}{\mathcal{R}_0}\right)_j \Big(p^*_{j,k+1} + p^*_{j+1,k+1} - p^*_{j,k-1} - p^*_{j+1,k-1}\Big)(\Delta\xi_j + \Delta\xi_{j+1}) \tag{6.20}$$

$$a_j^{u_r} u^*_{r_{j-1,k}} + b_j^{u_r} u^*_{r_{j,k}} + c_j^{u_r} u^*_{r_{j+1,k}} = d_j^{u_r} - \left(\frac{1}{\mathcal{R}_0}\right)_j \left(p^*_{j,k+1} - p^*_{j,k}\right)\Delta\xi_j \tag{6.21}$$

Since the velocity field $(u^*_{z_{j,k}}, u^*_{r_{j,k}})$, corresponding to the guessed pressure $p^*_{j,k}$ may not satisfy the continuity equation (Eq. 6.19), a correction of velocity field is needed. The correction of the velocity field can be made through a pressure correction. The pressure link between the momentum and continuity equations is accomplished by transforming the continuity equation (Eq. 6.19) into a pressure Poisson equation. Let $p^c_{j,k}$ be the pressure correction at $(j,k)^{th}$ cell and $(u^c_{z_{j,k}}, u^c_{r_{j,k}})$ be the corresponding correction in velocity field. Thus the updated pressure and velocity field can be expressed as

$$\left.\begin{aligned} p^{n+1}_{j,k} &= p^*_{j,k} + p^c_{j,k} \\ u^{n+1}_{z_{j,k}} &= u^*_{z_{j,k}} + u^c_{z_{j,k}} \\ u^{n+1}_{r_{j,k}} &= u^*_{r_{j,k}} + u^c_{r_{j,k}} \end{aligned}\right\}. \tag{6.22}$$

Substituting Eq. 6.20 from Eq. 6.14 and Eq. 6.21 from Eq. 6.15, we get a relation between pressure correction and velocity correction as

$$\left.\begin{aligned} a_j^{u_z} u^c_{z_{j-1,k}} + b_j^{u_z} u^c_{z_{j,k}} + c_j^{u_z} u^c_{z_{j+1,k}} &= -\left(p^c_{j+1,k} - p^c_{j,k}\right)\Delta\eta_k + \tfrac{1}{8}\eta_k \left(\tfrac{\mathcal{R}_0{}'}{\mathcal{R}_0}\right)_j \Big(p^c_{j,k+1} + p^c_{j+1,k+1} - p^c_{j,k-1} - p^c_{j+1,k-1}\Big)(\Delta\xi_j + \Delta\xi_{j+1}) \\ a_j^{u_r} u^c_{r_{j-1,k}} + b_j^{u_r} u^c_{r_{j,k}} + c_j^{u_r} u^c_{r_{j+1,k}} &= -\left(\tfrac{1}{\mathcal{R}_0}\right)_j \left(p^c_{j,k+1} - p^c_{j,k}\right)\Delta\xi_j \end{aligned}\right\} \tag{6.23}$$

Ignoring, the neighboring small correction components as

$$\left.\begin{aligned} u^c_{z_{j,k}} &= -\tfrac{\Delta t}{0.5(\Delta\xi_j + \Delta\xi_{j+1})}\left(p^c_{j+1,k} - p^c_{j,k}\right) + \tfrac{1}{4}\eta_k \left(\tfrac{\mathcal{R}_0{}'}{\mathcal{R}_0}\right)_j \tfrac{\Delta t}{\Delta\eta_k}\left(p^c_{j,k+1} + p^c_{j+1,k+1} - p^c_{j,k-1} - p^c_{j+1,k-1}\right) \\ u^c_{r_{j,k}} &= -\tfrac{\Delta t}{0.5(\Delta\eta_k + \Delta\eta_{k+1})}\left(\tfrac{1}{\mathcal{R}_0}\right)_j \left(p^c_{j,k+1} - p^c_{j,k}\right) \end{aligned}\right\} \tag{6.24}$$

Substituting the corrected velocity field $(u_{z_{j,k}}, u_{r_{j,k}})$ into the continuity equation, the following Poisson's equation for pressure correction is obtained as

$$
\begin{aligned}
&p^c_{j-1,k}\left[-\alpha_{u_z}\eta_k\frac{\Delta t\Delta\eta_k}{0.5(\Delta\xi_j+\Delta\xi_{j+1})}+\frac{1}{8}\alpha_{u_z}\eta_k\left\{\eta_k\left(\frac{\mathcal{R}_0{}'}{\mathcal{R}_0}\right)_j\right\}^2\frac{\Delta t\Delta\xi_j}{\Delta\eta_k}\right]\\
&+p^c_{j,k}\left[2\alpha_{u_z}\eta_k\frac{\Delta t\Delta\eta_k}{0.5(\Delta\xi_j+\Delta\xi_{j+1})}+2\alpha_{u_r}\eta_k\left\{\left(\frac{1}{\mathcal{R}_0}\right)_j\right\}^2\frac{\Delta t\Delta\xi_j}{0.5(\Delta\eta_k+\Delta\eta_{k+1})}\right.\\
&\qquad\left.+\frac{1}{4}\alpha_{u_z}\eta_k\left\{\eta_k\left(\frac{\mathcal{R}_0{}'}{\mathcal{R}_0}\right)_j\right\}^2\frac{\Delta t\Delta\xi_j}{\Delta\eta_k}+\alpha_{u_r}\left\{\left(\frac{1}{\mathcal{R}_0}\right)_j\right\}^2\frac{\Delta t\Delta\xi_j\Delta\eta_k}{0.5(\Delta\eta_k+\Delta\eta_{k+1})}\right]\\
&+p^c_{j+1,k}\left[-\alpha_{u_z}\eta_k\frac{\Delta t\Delta\eta_k}{0.5(\Delta\xi_j+\Delta\xi_{j+1})}+\frac{1}{8}\alpha_{u_z}\eta_k\left\{\eta_k\left(\frac{\mathcal{R}_0{}'}{\mathcal{R}_0}\right)_j\right\}^2\frac{\Delta t\Delta\xi_j}{\Delta\eta_k}\right]\\
&\quad=-div^*-\frac{1}{4}\alpha_{u_z}\eta_k^2\left(\frac{\mathcal{R}_0{}'}{\mathcal{R}_0}\right)_j\Delta t\left(p^c_{j+1,k+1}+p^c_{j-1,k-1}-p^c_{j+1,k-1}-p^c_{j-1,k+1}\right)\\
&\qquad-\frac{1}{4}\alpha_{u_z}\eta_k^2\left(\frac{\mathcal{R}_0{}'}{\mathcal{R}_0}\right)_j\frac{\Delta t\Delta\xi_j}{0.5(\Delta\xi_j+\Delta\xi_{j+1})}\left(p^c_{j+1,k+1}+p^c_{j-1,k-1}-p^c_{j+1,k-1}-p^c_{j-1,k+1}\right)\\
&\qquad+\frac{1}{16}\alpha_{u_z}\eta_k\left\{\eta_k\left(\frac{\mathcal{R}_0{}'}{\mathcal{R}_0}\right)_j\right\}^2\frac{\Delta t\Delta\xi_j}{\Delta\eta_k}\left(p^c_{j-1,k+2}+p^c_{j-1,k-2}+2p^c_{j,k+2}+2p^c_{j,k-2}\right.\\
&\qquad\qquad\left.+p^c_{j+1,k+2}+p^c_{j+1,k-2}\right)\\
&\qquad+\alpha_{u_r}\eta_k\left\{\left(\frac{1}{\mathcal{R}_0}\right)_j\right\}^2\frac{\Delta t\Delta\xi_j}{0.5(\Delta\eta_k+\Delta\eta_{k+1})}\left(p^c_{j,k+1}+p^c_{j,k-1}\right)\\
&\qquad+\alpha_{u_r}\left\{\left(\frac{1}{\mathcal{R}_0}\right)_j\right\}^2\frac{\Delta t\Delta\xi_j}{0.5(\Delta\eta_k+\Delta\eta_{k+1})}\left(p^c_{j,k+1}+p^c_{j,k-1}\right).
\end{aligned}
\tag{6.25}
$$

where

$$
\begin{aligned}
div^*=\eta_k\left(u^*_{z_{j,k}}-u^*_{z_{j-1,k}}\right)\Delta\eta_k-\frac{\eta_k^2}{4}\left(\frac{\mathcal{R}_0{}'}{\mathcal{R}_0}\right)_j\left(u^*_{z_{j-1,k+1}}+u^*_{z_{j,k+1}}-u^*_{z_{j-1,k-1}}-u^*_{z_{j,k-1}}\right)\Delta\xi_j\\
+\eta_k\left(\frac{1}{\mathcal{R}_0}\right)_j\left(u^*_{r_{j,k}}-u^*_{r_{j,k-1}}\right)\Delta\xi_j+\left(\frac{1}{\mathcal{R}_0}\right)_j u^*_{r_{j,k}}\Delta\xi_j\Delta\eta_k.
\end{aligned}
\tag{6.26}
$$

Here α_u and α_v are relaxation factors corresponding to axial and transverse velocity corrections respectively. The Eq. 6.25 is solved using a Gauss-Seidel iterative method with successive over relaxation (SOR) technique (Appendix) to achieve the pressure correction $(p^c_{j,k})$ at each cell of the flow domain. For rapid convergence, the pressure field is under-relaxed as

$$
p^{n+1}_{j,k}=p^*_{j,k}+\alpha_p p^c_{j,k},
\tag{6.27}
$$

where α_p is the under-relaxation factor. The relaxation factor is taken between 0 and 1, so that guessed pressure field can be added in a fraction of the corrected pressure field p^c, in order to

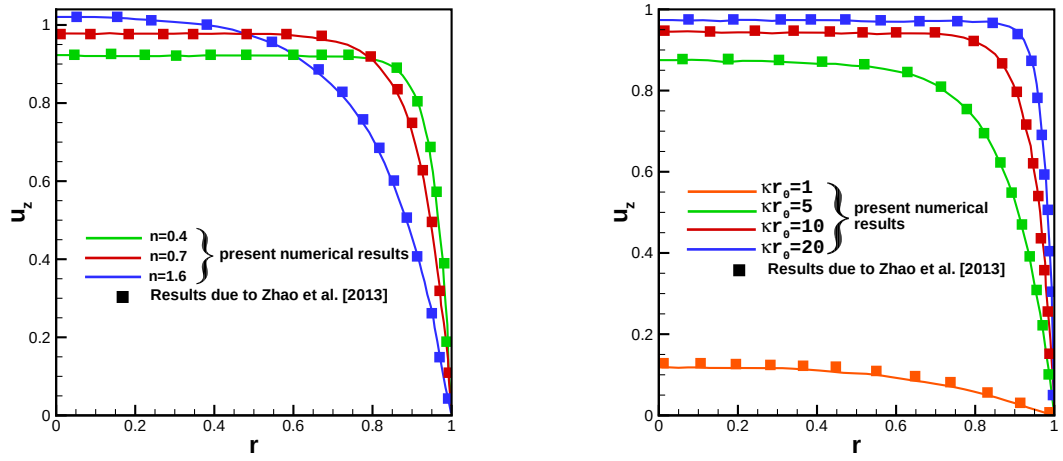

(a) (b)

Figure 6.3: Comparison of axial velocity in the present study for uniform zeta potential in a cylindrical micro-channel with the analytic results obtained by Zhao et al. [290] for (a) different power-law index ($n = 0.4, 0.7, 1.6$) with $\kappa r_0 = 10$ and (b) different EDL thickness ($\kappa r_0 = 1, 5, 10, 20$) with $n = 0.5$. Here $r_0 = 20\ \mu m$, $E_0 = 10^4\ V\ m^{-1}$, $\zeta = -1$.

improve iteration process to carry forward. Similarly, the velocity components $u^{n+1}_{z_{j,k}}$ and $u^{n+1}_{z_{j,k}}$ are under-relaxed in the following manner:

$$\left.\begin{aligned} u^{n+1}_{z_{j,k}} &= u^{*}_{z_{j,k}} + \alpha_{u_z} u^{c}_{z_{j,k}} \\ u^{n+1}_{r_{j,k}} &= u^{*}_{r_{j,k}} + \alpha_{u_r} u^{c}_{r_{j,k}} \end{aligned}\right\}. \tag{6.28}$$

In this chapter a rapid convergence is found for $\alpha_p = 0.6$ and $\alpha_{u_z} = 2/3 = \alpha_{u_r}$. Same sequential steps are adopted which have been discussed in Chapter 1 (Scetion 1.8)

6.3.1 Code Validation

We have developed an inhouse computer code based on the algorithm as outlined above. In order to validate our algorithm, we have compared our results with the existing results. To capture the sharp gradients near channel walls (mainly in the regions of surface modulation with potential non-homogeneity) a non-uniform grid spacing is taken in radial direction, whereas an uniform spacing is considered in axial direction. The grid spacing in η direction is varied from 0.005 to 0.01. Moreover, an under-relaxation scheme is introduced for apparent viscosity to avoid the divergence as [101]

$$\mu_a = \alpha_n \mu_a^{new} + (1 - \alpha_n)\mu_a^{old}; \qquad 0.2 < \alpha_n < 0.5. \tag{6.29}$$

A grid independence test is performed to make a balance between numerical cost and numerical convergence. In order to access the accuracy of our numerical scheme, we have compared our

results for axial velocity distribution with Zhao et al. [290] (Fig. 6.3). In Fig 6.3(a) we made a comparison of velocity distribution for wide range of power-law index ($n = 0.4, 0.7, 1.6$) in a cylindrical channel with uniform ζ- potential and shows an excellent agreement. In Fig. 6.3(b) a comparison for axial velocity is made for different EDL thickness with power-law index $n = 0.5$. We found a good matching of our computed axial velocity profiles with Zhao et al. [290] for the variation of power-law index and Debye length.

6.4 Results and Discussions

In this chapter, we discuss the effect of corrugation height, flow behavior index, overpotential patch strength in terms of mixing efficiency enhancement and pressure drop. For simulation purpose, the non-deflected radius of the cylindrical tube is considered as $r_0 = 20\ \mu m$ with length $L = 120\ \mu m$. In this chapter the externally applied field is set as $10^4\ V\ m^{-1}$ and the zeta potential in the homogenous part of the channel is considered to be $\zeta^* = -25.6\ mV$ (*i.e.* $\zeta = -1$). The zeta potential at the regions of potential heterogeneity is considered to vary from $12.8\ mV$ (*i.e.* $\zeta_p = 0.5$) to $64\ mV$ (*i.e.* $\zeta_p = 2.5$). We assume that the diffusion coefficients for both the ionic species (cation and anion) are same as $D_1 = D_2 = 1 \times 10^{-9}\ m^2\ s^{-1}$. The other physical properties are specified as follows: fluid density, $\rho = 10^3\ kg\ m^{-3}$; fluid viscosity, $\mu = 10^{-3}\ kg\ m^{-1}\ s^{-1}$; flow consistency index, $m = 10^{-3}\ Pa\ s^n$; Faraday's constant, $F = 96485\ C\ mol^{-1}$; universal gas constant, $R = 8.314\ J\ mol^{-1}\ K^{-1}$; Boltzmann's constant, $k_B = 1.38 \times 10^{-23}\ m^2\ kg\ s^{-2}\ K^{-1}$; absolute temperature, $T = 300\ K$ and elementary charge, $e = 1.602 \times 10^{-19}\ C$. In addition, the ionic strength of the electrolyte concentration is taken into consideration as $2.3 \times 10^{-5}\ mM$ ($n_0 = 1.38 \times 10^{19}\ ions/m^3$) which corresponds the Debye-Hückel parameter as $\kappa r_0 = 10$. Moreover, the diffusion coefficient for the uncharged eluted species is considered as $D_s = 1 \times 10^{-11}\ m^2\ s^{-1}$ [44, 92].

6.4.1 Effect of Flow Behavior Index

In this section we depict the effect of flow behavior index (n) on comparative mixing analysis between two cylindrical corrugated configurations. Fig. 6.4(a) and Fig. 6.4(b) present the streamlines pattern for constricted and expanded geometry respectively. It can be observed that, flow lines away from the geometric and potential non-homogeneity follows parallel pattern and no flow deviation takes place. It is also found that flow lines are started to follow a flow reversal near the wall corrugation due to the combined effect of wall constriction/ expansion and surface potential heterogeneity. Moreover from Fig. 6.4(a) we find that, irrespective of flow

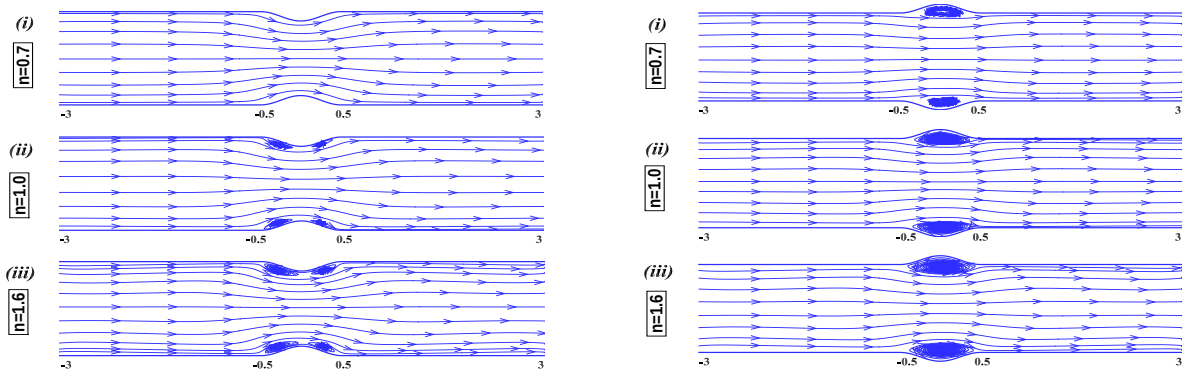

(a) (b)

Figure 6.4: Streamlines for (a) constricted, (b) expanded channel for different power-law index (n), when $r_0 = 20\ \mu m$, $\alpha = 0.1$, $\kappa r_0 = 10$, $\zeta = -1$, $\zeta_p = 1$, $E_0 = 10^4\ Vm^{-1}$.

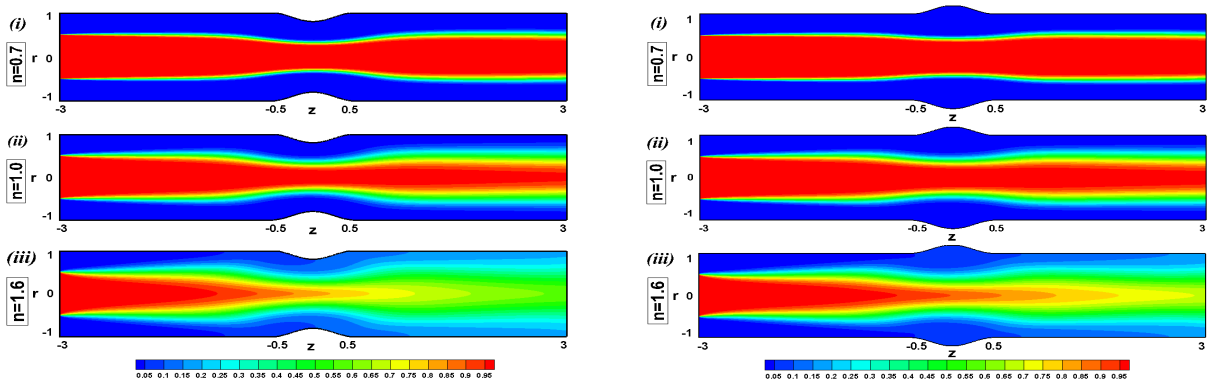

(a) (b)

Figure 6.5: Concentration contour for (a) constricted, (b) expanded channel for different power-law index (n), when $r_0 = 20\ \mu m$, $\kappa r_0 = 10$, $\alpha = 0.1$, $\zeta = -1$, $\zeta_p = 1$, $E_0 = 10^4\ Vm^{-1}$.

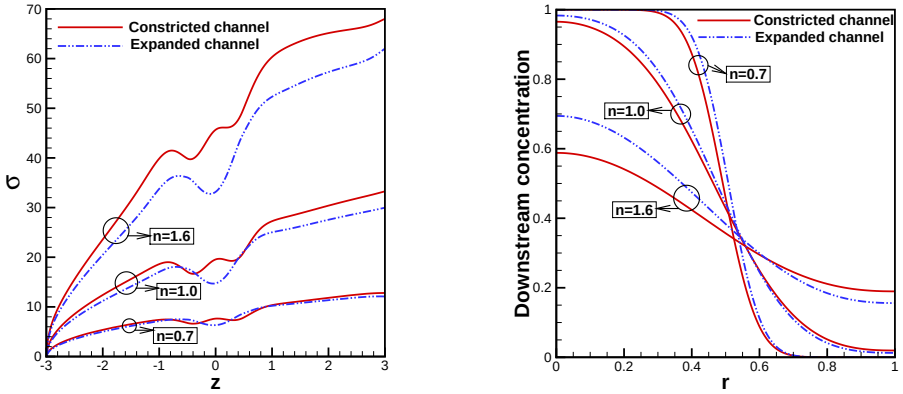

(a) (b)

Figure 6.6: Distribution of (a) mixing efficiency along the channel length and (b) downstream concentration profile for constricted and expanded circular channels as a function of power-law index (n), with $r_0 = 20\ \mu m$, $\kappa r_0 = 10$, $\alpha = 0.1$, $\zeta = -1$, $\zeta_p = 1$, $E_0 = 10^4\ Vm^{-1}$.

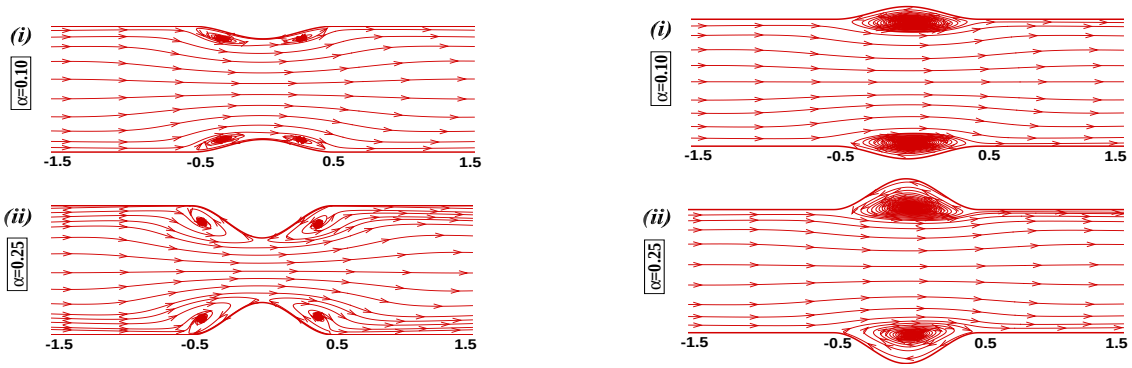

(a) (b)

Figure 6.7: Streamlines for (a) constricted and (b) expanded channel for different wave amplitude (α) with $n = 1.5$. Here $r_0 = 20\ \mu m$, $\kappa r_0 = 10$, $\zeta = -1$, $\zeta_p = 1$, $E_0 = 10^4\ Vm^{-1}$.

configurations, the vortical zone near the wall corrugation expands in size with the increment of flow behavior index (n). As n decreases, the effective viscosity near the wall decreases which in turn creates stronger electric body force near EDL to drive the flow. Thus by reducing the value of n, the flow reversal zones are reduced in size (for pseudoplastic fluids). On the otherhand, it can be concluded that with the increment of flow behavior index, the fluid streams experience more tortuous path when passing through the constricted/ expanded zones. In order to show the inter mixing of two fluid streams of different concentrations, concentration contours are shown in Fig. 6.5 for both the configurations with the variation of n. It is observed from Fig. 6.5 that the sample streams are totally unmixed in the channel inlet where two different concentrations $C = 0$ (represented by blue color) and $C = 1$ (takes red colour) are injected through the respective inlets. It is evident from the figure that the inlet streams approach to the saturated concentrated level ($C = 0.5$, represented by green color) towards the downstream irrespective of n and geometric configuration. For higher values of n (for dilatant fluids), the sample streams are allowed more folded paths due to stronger recirculating eddies which in turn causes improved diffusion flux due to longer retention (since for $n > 1$ mixing becomes diffusion dominated [17]) time which is the cause of better mixing along the channel downstream. Fig. 6.6(a) and Fig. 6.6(b) present the mixing efficiency along the channel length and downstream normalized concentration profile respectively as a function of flow behavior index and geometric configurations. It is evident from Fig. 6.6 that, for $n = 0.7$ the mixing efficiency at the downstream for both the configurations do not differ much, but for Newtonian and dilatant fluids, the constricted geometry shows much better mixing performance as compared to expanded one.

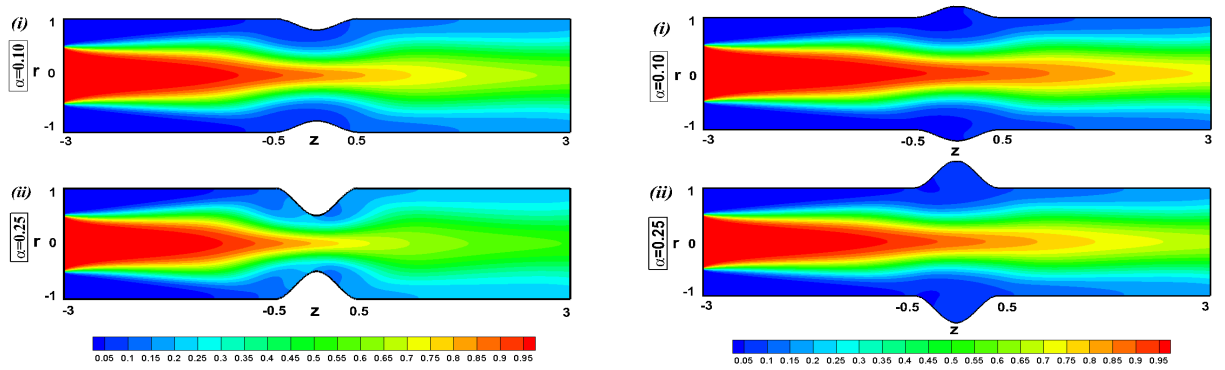

(a) (b)

Figure 6.8: Concentration contour for (a) constricted and (b) expanded channels for different wave amplitude (α) with $n = 1.5$. Here $r_0 = 20\ \mu m$, $\kappa r_0 = 10$, $\zeta = -1$, $\zeta_p = 1$, $E_0 = 10^4\ Vm^{-1}$.

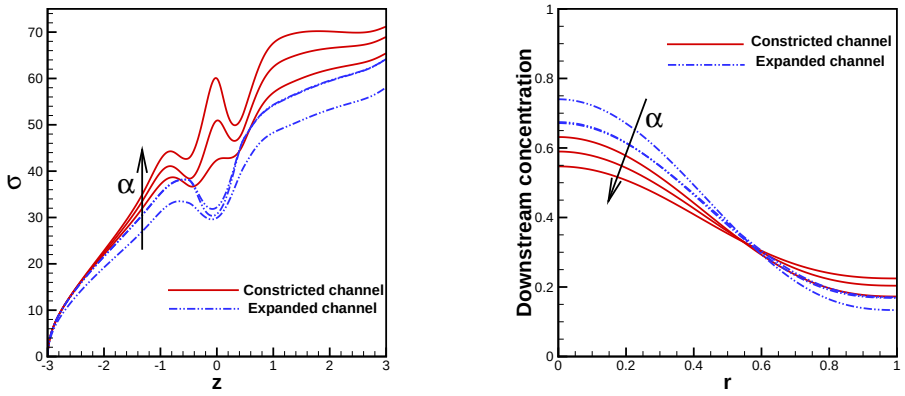

(a) (b)

Figure 6.9: Distribution of (a) mixing efficiency along the channel length and (b) downstream concentration profile for constricted expanded channels with different wave amplitude ($\alpha = 0.10,\ 0.20,\ 0.25$) with $n = 1.5$. Here $r_0 = 20\ \mu m$, $\kappa r_0 = 10$, $\zeta = -1$, $\zeta_p = 1$, $E_0 = 10^4\ Vm^{-1}$.

6.4.2 Effect of Wave Amplitude

The above discussions suggest that the mixing efficiency is higher for constricted channel irrespective of flow behavior index, and the mixing efficiency in the channel downstream is improved with the increment of flow behavior index for both the configurations due to the dominance of diffusive transport over convection. In this section we discuss the effect of the amplitude of deflected zones (for a fixed $n = 1.5$ and fixed $\phi_p = 1$). The streamline pattern and concentration contours are presented in Fig. 6.7 and Fig. 6.8 respectively both for constricted and expanded domains. It can be observed from the streamlines pattern (Fig. 6.7(a) and Fig. 6.7(b)) that higher value of wave amplitude causes more stronger flow reversal zones which enhances the

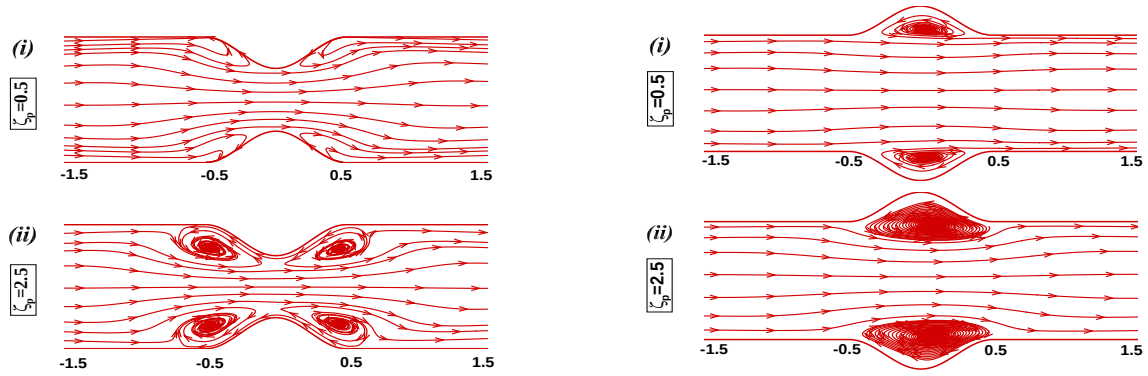

(a) (b)

Figure 6.10: Streamlines for (a) constricted and (b) expanded channels for different overpotential patch strength (ζ_p) with $n = 1.6$. Here $r_0 = 20\ \mu m$, $\kappa r_0 = 10$, $\alpha = 0.2$, $\zeta = -1$, $E_0 = 10^4\ Vm^{-1}$.

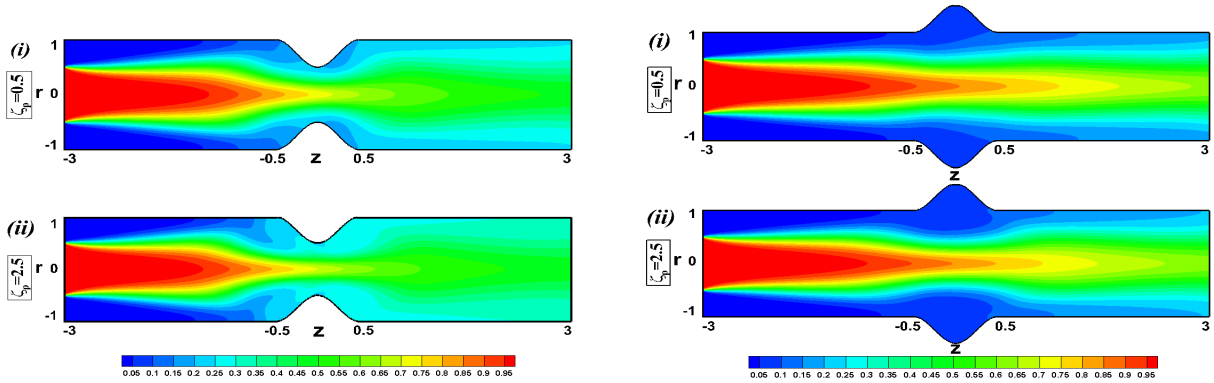

(a) (b)

Figure 6.11: Concentration contour for (a) constricted and (b) expanded channels for different overpotential patch strength (ζ_p) with $n = 1.6$. Here $r_0 = 20\ \mu m$, $\kappa r_0 = 10$, $\alpha = 0.2$, $\zeta = -1$, $E_0 = 10^4\ Vm^{-1}$.

effective contact area between different flow streams to get improved downstream mixing. Better mixing for higher values of wave amplitude can be verified by the respective concentration contours (Fig. 6.8(a) and Fig. 6.8(b)). The mixing efficiency along the channel length and the downstream concentration profile are shown in Fig. 6.9(a) and Fig. 6.9(b) respectively for $\alpha = 0.10,\ 0.20,\ 0,25$ with $n = 1.5$ and $\zeta_p = 1.0$. The mixing efficiency distribution along the streamwise direction shows that the downstream mixing efficiency for the constricted configuration is improved from 65% to 71% for the increment of wave amplitude from $\alpha = 0.10$ to $\alpha = 0.25$ (for $n = 1.5$ and $\zeta_p = 1.0$), whereas for the other configuration it varies from 58% (for $\alpha = 0.10$) to 64% (for $\alpha = 0.25$).

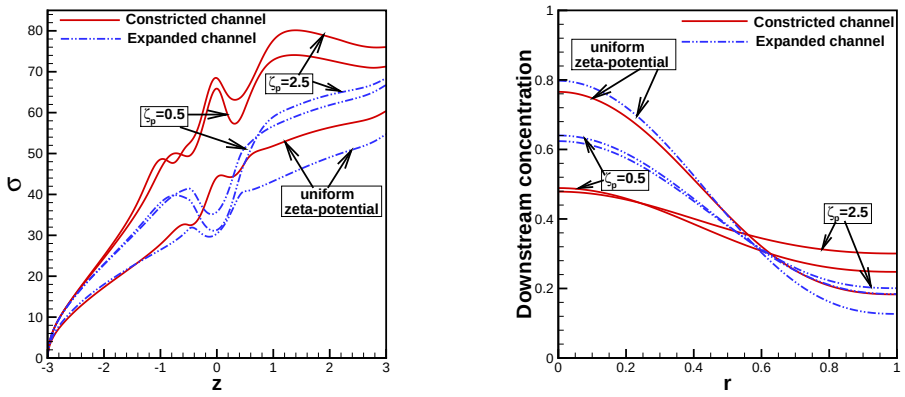

(a) (b)

Figure 6.12: Distribution of (a) mixing efficiency along the channel length and (b) downstream concentration profile for constricted expanded channels for different patch potential (ζ_p) with $n = 1.6$. Here $r_0 = 20\ \mu m$, $\kappa r_0 = 10$, $\alpha = 0.2$, $\zeta = -1$, $E_0 = 10^4\ Vm^{-1}$.

6.4.3 Effect of Overpotential Patch Strength

This section involves the effect of non-homogenous surface potential strength on mixing efficiency enhancement. The above mentioned discussions show mixing efficiency can be improved by the increment of n and α. In this section, our motivation is to improve downstream mixing by regulating the strength of the overpotential patch, placed in the constricted/ expanded zones of the cylindrical tube. Fig. 6.10 illustrates the flow line pattern for two configurations with different patch strength $\phi_p = 0.50$ and $\phi_p = 2.5$. With the increment of ϕ_p, the ions near the walls of potential heterogeneity achieves negative momentum to create stronger flow reversal which is observed in streamlines pattern. The size of the eddies, formed in the constricted/ expanded zone is expanded with the increment of ϕ_p. The average flow rate is decreased due to the increment of patch strength which in turn increases the retention time together with the contact area between solute species to get more diffusion flux which improves the downstream mixing. This phenomena can be verified by the concentration contours (Fig. 6.11) for both the configurations. It is important to notice that, the mixing efficiency at the downstream is higher for constricted configuration compared to the other (under same flow condition).

The parametric dependence of mixing efficiency, discussed above is summarized in Fig. 6.13. It is evident from the figure that mixing efficiency follows a proportional relationship with power-law index (n), wave amplitude (α) and potential patch strength (ϕ_p) irrespective of geometric configuration. Moreover, it can be observed that mixing efficiency is quiet better in case of constricted geometry as compared to the other.

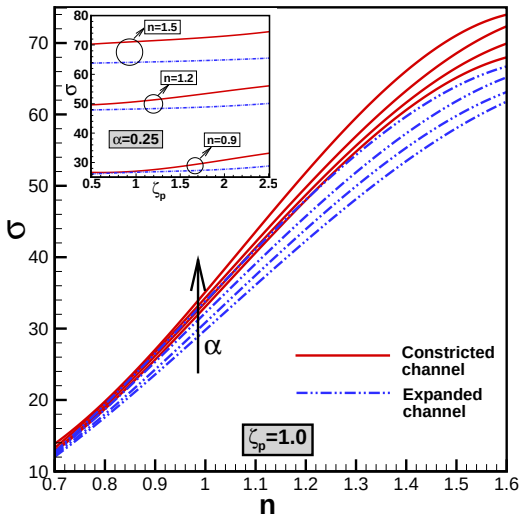

Figure 6.13: Variation of mixing efficiency at channel downstream for constricted and expanded channels as a function of power-law index (n) and wave amplitude (α) with a fixed value of over-potential patch strength $\zeta_p = 1$. The inset shows the dependence mixing efficiency as a function of overpotential patch strength (ζ_p) and power-law index (n) for a fixed wave amplitude $\alpha = 0.25$. Here $\kappa r_0 = 10$, $\zeta = -1$, $r_0 = 20\ \mu m$, $E_0 = 10^4\ Vm^{-1}$.

6.4.4 Pressure Drop and Mixing Enhancement Factor

Another important parameter to analyze the mixing capability of a passive micromixer is the pressure drop associated with the configuration. Since the overall performance of a micromixer is determined by the maximum mixing efficiency and minimum pressure drop, estimation of pressure drop is necessary besides calculating mixing efficiency to design a novel efficient and effective micromixer [194]. In this context we have calculated the average pressure drop (Δp) along the channel length which is defined as $\Delta p = p_{avg}^{inlet} - p_{avg}^{outlet}$ [17], where p_{avg}^{inlet} and p_{avg}^{outlet} denote the average pressure at upstream and downstream of the channel respectively. Fig. 6.14 illustrates the effect of power-law index (n), overpotential patch strength (ζ_p) and wave amplitude (α) for both the configurations. It is evident from Fig. 6.14 (a) and 6.14 (b) that the magnitude of the average pressure drop is higher for the constricted geometry as compared to the other for a wide range of parameters n, α and ζ_p, though the mixing efficiency is quiet better for the earlier one. It can also be reported that the increment of n and ζ_p causes higher average pressure drop for both the configurations but the increment of α shows a different characteristic. As the wave amplitude is increased, the average pressure drop in the constricted configuration becomes higher due to the narrower passage whereas in case of the expanded channel, the respective pressure drop is reduced with higher wave amplitude due to expanded channel area.

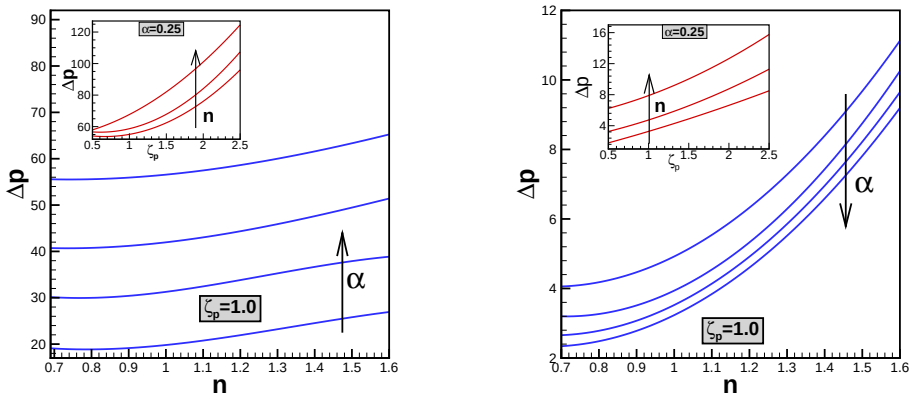

Figure 6.14: Variation of pressure drop (Δp) for (a) constricted, (b) expanded channel with the variation of power-law index (n) for different wave amplitude ($\alpha = 0.10, 0.15, 0.20, 0.25$) and for a fixed ζ_p ($= 1.0$). The insets show the variation of pressure drop (Δp) as a function of (n) and overpotential patch strength ($\zeta_p = 1.0, 2.0, 2.5$). Here $\kappa r_0 = 10$, $\alpha = 0.25$, $r_0 = 20\ \mu m$, $\zeta = -1$, $E_0 = 10^4\ Vm^{-1}$.

Increasing pressure drop may increase the difficulty in micromixing integration. Thus to design a novel micromixer, for optimum output (i.e. maximum mixing efficiency with minimum pressure drop), mixing enhancement factor (χ), the ratio of mixing efficiency (σ) and pressure drop (Δp) [71, 244] are evaluated. The effectiveness of the mixing performance with regard to the pressure drop is evaluated by mixing enhancement factor (χ) for different configurations. Higher value of χ signifies better overall performance of the system [151]. Fig. 6.15 depicts the parametric relationship between mixing enhancement factor (χ) and power-law index as a function of potential patch strength and wave amplitude. It can be observed that for a wide parameter range, expanded configuration gives better overall performance due to lower pressure drop, though the mixing efficiency is quite better for the other configuration. In addition, it is also noticed that, for constricted geometry, the mixing enhancement factor is increased both for shear thinning and Newtonian fluid (irrespective of ζ_p and α) due to the dominance of mixing efficiency over pressure drop (Fig. 6.15 (a)). As the power-law index increased (approximately $n = 1.4$), mixing performance factor graph becomes parallel to the horizontal axis for the constricted geometry. On the other hand, it is evident from Fig. 6.15 (b) that the mixing performance factor (χ) for the expanded configuration is increased upto $n = 1.2$ (approximately) and then it is decreased due to higher pressure drop. Therefor, from Fig. 6.15 it is evident that the expanded configuration is better in term of mixing performance factor as compared to the other, although the downstream mixing efficiency is better for constricted configuration.

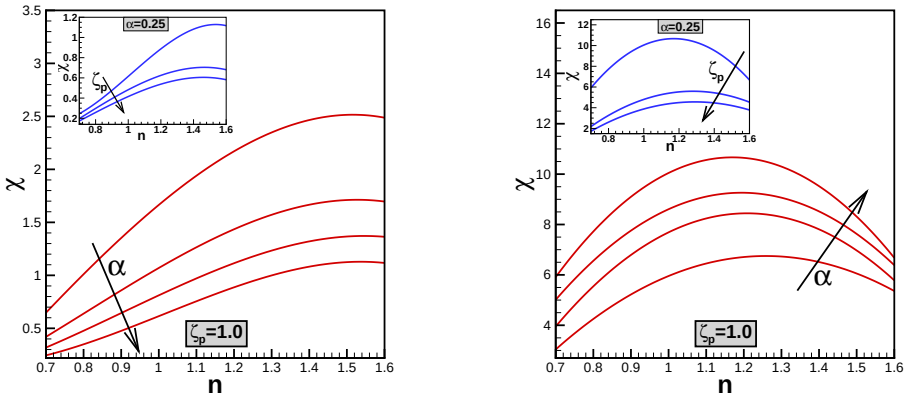

Figure 6.15: Variation of mixing performance factor ($\chi = \sigma/\Delta p$) for (a) constricted, (b) expanded channel with the variation of power-law index (n) for different wave amplitude ($\alpha = 0.10, 0.15, 0..20, 0.25$) and for a fixed ζ_p ($= 1.0$). The insets show the variation of mixing performance factor ($\chi = \sigma/\Delta p$) as a function of power-law index (n) and overpotential patch strength ($\zeta_p = 1.0, 2.0, 2.5$). Here $\kappa r_0 = 10$, $r_0 = 20\ \mu m$, $\alpha = 0.25$, $E_0 = 10^4\ Vm^{-1}$.

6.5 Conclusions

In this chapter, a comparative mixing enhancement and pressure drop is analyzed in a cylindrical tube, filled with power-law electrolyte with sudden constriction/ expansion. Results are presented in order to achieve an effective mixing enhancement with minimum pressure drop for a wide range of power-law index, wave amplitude and overpotential patch strength. The main findings of this chapter can be summarized as follows :

- It is found that the mixing efficiency is increased proportionally with power-law index irrespective of geometric configuration. In case of pseudoplastic fluid, the mixing efficiency difference for both the configurations are negligible, whereas for Newtonian and dilatant fluids mixing efficiency is higher in case of constricted geometry.

- As the wave amplitude of the constricted/ expanded zone is increased, the fluid experiences more stretched and folded paths which enhance effective diffusive flux to improve downstream mixing for both the cases.

- In case of higher overpotential patch strength, flow recirculation strength in the deflected zone is increased which causes improved mixing.

- Besides mixing efficiency, average pressure drop is an important parameter to evaluate the overall preformance of the system. It can be seen that the average pressure drop

(Δp) is increased with higher values of power-law index and overpotential patch strength irrespective of channel configuration and the magnitude of Δp is observed to be higher for the constricted one. It is also evident that the increment of wave amplitude create more pressure drop for the constricted channel, whereas in case of expanded channel a reverse characteristic is followed.

- However, the constricted configuration produces better mixing efficiency as compared to the other for a wide range of parametric values, but the constricted geometry is not the best choice from the point of view of mixing enhancement factor because of higher pressure drop. In case of expanded configuration, mixing efficiency is moderate with very lower pressure drop which is compatible to a integrate an efficient micromixer.

- Although the increment of power-law index causes effective mixing efficiency enhancement irrespective of channel geometry for a wide range of potential patch strength and wave amplitude, mixing enhancement factor does not increase after a certain power-law index due to the dominance of pressure drop increment over mixing efficiency enhancement.

Chapter 7

Summary and Future Scope

7.1 Overall Summary

This thesis dealt with the electrokinetic mixing and pressure drop in rectangular and circular micro/ nano channels for Newtonian and non-Newtonian electrolytes based on Poisson-Nernst-Planck model. Major contribution of the thesis includes:

- Combined effect of geometric modulation and surface heterogeneity on solute mixing in micro and nano domains.
- Impact of wall corrugation on flow reversal in absence of surface potential heterogeneity.
- Effect of power-law index on mixing enhancement in rectangular and circular corrugated channels.
- Effect of power-law index, potential heterogeneity and geometric modulation on pressure drop and mixing enhancement factor.

In Chapter 2, the electroosmotic flow and mixing of uncharged species of two different concentrations are studied in a nano-fluidic system. The channel is modulated with a non-conducting block, embedded on the lower wall of the channel with surface potential heterogeneity. The results are presented in terms of electric field lines, streamlines, mixing efficiency and concentration contours by solving a coupled set of non-linear PDE's involving Maxwell's equation for electric potential, Nernst-Planck equation for ion transport, Navier-Stokes equation for momentum transport and advection-diffusion equation for uncharged species transport. The simulated results are shown for the variation of block height, over-potential patch strength, external electric field and block location. The effective diffusion flux is increased due to the

increment of patch potential strength and block height which provides an improved mixing. On the other hand, it is concluded that higher external electric field strength increases the overall flow rate resulting a reduction in mixing efficiency. Last section of this chapter includes mixing of two different streams of fluid and it is concluded that maximum mixing efficiency is achieved along the downstream of the channel, when the block is placed close to the inlet.

In Chapter 3, a comparative study on EOF mixing and charge transport is conducted based on Poisson-Nernst-Planck model. Two different configurations are considered to create geometric and surface modulation. In the first configuration (Case I), a non conducting block with overpotential patch is embedded on the lower wall of the channel and two overpotential patches are placed on the upper wall asymmetrically. In Case II, two blocks with potential heterogeneity are placed on the lower wall and two overpotential patches are attached on the upper wall symmetrically at the same axial locations. An analytical estimation for pressure and velocity is made at the far away from heterogenous region. The simulated results concluded that a larger pressure drop is developed in Case II as a consequence of higher effective circulation strength due to the presence of block-patch. The fluid streams experience more stretched and folded paths in Case-II which causes better downstream mixing as compared to case-I.

In Chapter 4, a numerical simulation is performed for EOF mixing and flow reversal in a symmetric modulated microchannel. The side walls of this micromixer is composed of two sinusoidal wave functions. In the first section of this chapter, a parametric estimation for flow reversal is discussed in terms of wave amplitude, external electric field and ratio of EDL thickness to channel height. The flow reversal diagram revels that the critical wave amplitudes for flow reversal is increased with the increment of external electric field and solution strength. In the last section of the chapter, the criterion for mixing enhancement is discussed for a wide range of above mentioned parameters. An improved mixing is found with the increment of wave amplitudes and decrement in external electric field & solution strength.

In Chapter 5, a numerical study of electrokinetic mixing and pressure drop is presented in a wavy patterned microchannel with different phase shifts. The rheological behaviour of the electrolyte is described by power-law model. The wall zeta potential is assumed to vary sinusoidally with same wave length that of wall structures for this chapter. The first part of the chapter dealt with the parametric study on EOF mixing to choose the best choice of phase shift for achieving a good mixing with minimum pressure drop for Newtonian fluid. The discussions

for pseudoplastic (shear thinning) and dilatant (shear thickening) fluids are made using the best chosen phase shift ($\pi/2$) to observe the differences. The results depicted that the mixing efficiency remarkably increases with the increment of wavy nature of the wall and higher power-law index, but the pressure drop is found to be increased accordingly. Thus to achieve an effective and controllable mixing, mixing performance factor (ratio of mixing efficiency and pressure drop) is included along with the mixing efficiency. It is found that, higher values of power-law index is not always beneficial for the mixing enhancement factor. Mixing performance factor is found to decrease after a certain value of power law index (here $n = 1.3$) due to the dominance of pressure drop over mixing efficiency.

In Chapter 6, a comparative numerical study on non-Newtonian fluid (power-law) mixing is performed in a cylindrical channel with sudden constriction / expansion with surface potential heterogeneity. The overpotential patches are placed in the region of constriction / expansion zones. The simulated results are presented in terms of mixing enhancement factor and pressure drop. The result shows that the mixing efficiency is increased with the increment of power-law index and wave amplitudes for both these cases. It is important to mention here that, irrespective of flow controlling parameters (such as, patch potential strength, wave amplitude of the deflectrd zones and power-law index), constricted configuration gives better mixing as compared to the other, but a reverse characteristic is followed for mixing enhancement factor due to higher pressure drop in case of the earlier one. Hence, it is concluded that, for mixing purpose, constricted configuration is quite better, but for overall performance, i.e. for maximum possible mixing with minimum pressure drop, expanded structure is more suitable.

7.2 Future Scope

In this thesis, the study is restricted to binary monovalent symmetric electrolytes in DC electric field. However, the work can be extended to multiple ionic species in presence of AC electric field. In addition, the non-Newtonian mixing analysis is restricted to the power-law model in isothermal flow environment due to its simplicity. These works can also be extended for Casson, Bingham, Herschel-Bulkley, CarreauYasuda and generalized Maxwell model with non-isothermal flow conditions. We can highlight some of the proposed extensions of the work made in the thesis are as follows:

- One can directly extend the present model for multi-valent ions to study the combined

EOF-pressure driven flow mixing with non-zero wall temperature gradient and temperature dependent properties.

- The effect of hydrophobicity on mixing enhancement in semi active micromixers for different non-Newtonian models.
- The mixing enhancement due to the presence of conducting obstacles of different shapes under a combined effect of direct and alternating electric fields.
- The comparative study on flow enhancement due to slip effect in corrugated micro channels for different non-Newtonian models.
- The slippage and thermo-electrokinetc behaviour for multi phase flow.

Appendix A

Successive Over Relaxation (SOR)

The relaxation technique is a finite-difference method particularly suited for the solution of elliptic partial differential equations. Successive over-relaxation (SOR) is a technique which can be used in an attempt to accelerate any iteration procedure but we will propose it here primarily as a refinement to the Gauss-Seidel method. As we apply Gauss-Seidel iteration to a system of simultaneous algebraic equation, we expect to make several recalculations or iterations before convergence to an acceptable level is achieved. A major disadvantage of the otherwise attractive Gauss-Seidel method is that its convergence is too slow, especially when a large number of grid points are involved. The reason for the slowness is easy to understand; the method transmits the boundary condition information at a rate of one grid interval per iteration.

In the iterative solution of the algebraic equation or in the overall iterative scheme employed for handing nonlinearity, it is often desirable to speed up or to slow down the changes. This process is called over-relaxation or under-relaxation depending on whether the variable changes are accelerated or slowed down. An arbitrary correction to the intermediate values of the unknowns from any iteration procedure according to the form

$$u_{i,j}^{k+1'} = \omega u_{i,j}^{k+1} + (1-\omega) u_{i,j}^{k'} \tag{A.1}$$

is known as over-relaxation or successive over-relaxation (SOR).

Here, k denotes iteration level and $u_{i,j}^{k+1}$ is the most recent value of $u_{i,j}$ calculated from the Gauss-Seidel procedure, $u_{i,j}^{k'}$ is the value from the previous iteration as a adjusted by previous application of this formula if the over-relaxation is being applied successively and $u_{i,j}^{k+1'}$ is newly adjusted for $u_{i,j}$ at the $k+1$ iteration level. ω is the relaxation parameter whose value is usually found by trail-and-error experimentation for a given problem. For over-relaxation, generally the value of ω is bounded by $1 < \omega < 2$ and for under-relaxation, ω is bounded by $0 < \omega < 1$.

Appendix B

Tridiagonal Matrix Algorithm

Suppose we have to solve a linear system of algebraic equations

$$AV = D \tag{B.1}$$

where

$$A = \begin{bmatrix} b_1 & c_1 & & & & \\ a_2 & b_2 & c_2 & & & \\ & . & . & . & & \\ & & a_i & b_i & c_i & \\ & & . & . & . & \\ & & & a_{N-1} & b_{N-1} & a_{N-1} \\ & & & & a_N & b_N \end{bmatrix}$$

is a $N \times N$ tri-diagonal matrix,

$$V = \begin{bmatrix} v_1 \\ v_2 \\ . \\ v_i \\ . \\ v_{N-1} \\ v_N \end{bmatrix}$$

is the vector of unknowns and

$$D = \begin{bmatrix} d_1 \\ d_2 \\ . \\ d_i \\ . \\ d_{N-1} \\ d_N \end{bmatrix}$$

is the known vector. All elements in A, other than those shown, are zero.

The Thomas algorithm for solving $(B.1)$ consists of two parts. First $(B.1)$ is manipulated into the form

$$\begin{bmatrix} 1 & c_1^1 & & & & & \\ & 1 & c_2^1 & & & & \\ & & . & . & & & \\ & & & 1 & c_i^1 & & \\ & & & & . & . & \\ & & & & 1 & c_{N-1}^1 & \\ & & & & & 1 & \end{bmatrix} \begin{bmatrix} v_1 \\ v_2 \\ . \\ v_i \\ . \\ v_{N-1} \\ v_N \end{bmatrix} = \begin{bmatrix} d_1^1 \\ d_2^1 \\ . \\ d_i^1 \\ . \\ d_{N-1}^1 \\ d_N^1 \end{bmatrix}$$

i.e., the a_i coefficients have been eliminated and the b_i coefficients normalized to unity.

For the first equation

$$c_1^1 = \frac{c_1}{b_1}, \quad d_1^1 = \frac{d_1}{b_1} \tag{B.2}$$

and for the general equation

$$c_i^1 = \frac{c_i}{b_i - a_i c_{i-1}^1}, \quad d_i^1 = \frac{d_i - a_i d_{i-1}^1}{b_i - a_i c_{i-1}^1}$$

The equation are modified as in $(C.2)$. The second stage consists of a back substitution

$$v_N = d_N^1, \quad v_i = d_i^1 - v_{i+1} c_i^1$$

The Thomas algorithm is particularly economical, it requires only $5N - 4$ operations (multiplications and divisions). But to present ill conditioning, it is necessary that

$$|b_i| > |a_i| + |c_i|$$

Appendix C

Block Tridiagonal Matrix Algorithm

A block tri-diagonal system of equations can be written as

$$\overline{AV} = \overline{D} \tag{C.1}$$

where

$$\overline{A} = \begin{bmatrix} B_1 & C_1 & & & & \\ A_2 & B_2 & C_2 & & & \\ & . & . & . & & \\ & & A_i & B_i & C_i & \\ & & . & . & . & \\ & & & A_{N-1} & B_{N-1} & C_{N-1} \\ & & & & A_N & B_N \end{bmatrix}$$

is a block tri-diagonal matrix, each element being a third order square matrix. Let

$$V_1 = (0,0,0)^T, \quad V_N = (0,0,0)^T$$

$$\overline{V} = (V_2, V_3, ..., V_{N-1})^T$$

is the vector of unknowns vectors and

$$\overline{D} = (D_2, D_3, ..., D_{N-1})^T$$

is the vector of known vectors. The matrix equation $(C.1)$ can be solved using Varga's Algorithm.

The algorithm is as follows

$$V_n = -E_n V_{n+1} + J_n, \qquad 2 \le n \le N-1$$

where

$$E_n = (B_n - A_n E_{n-1})^{-1} C_n, \qquad 2 \le n \le N-1$$

$$J_n = (B_n - A_n E_{n-1})^{-1} (D_n - A_n J_{n-1}), \qquad 2 \le n \le N-1$$

$$E_1 = E_N = \begin{bmatrix} 0 & 0 & 0 \\ 0 & 0 & 0 \\ 0 & 0 & 0 \end{bmatrix}$$

$$J_1 = V_1, \quad J_N = V_N.$$

Bibliography

[1] Abramowitz M., Stegun I. A., Handbook of mathematical functions: with formulas, graphs, and mathematical tables, *New York: Dover publications* **55**, 886, 1972.

[2] Afzal A., Kim K. Y., Passive split and recombination micromixer with convergent-divergent walls, *Chemical Engineering Journal* **203**, 182–192, 2012.

[3] Ajdari A., Electro-osmosis on inhomogeneously charged surfaces, *Physics Review Letters* **75**, 266–275, 1995 .

[4] Ajdari A., Generation of transverse fluid currents and forces by an electric field: Electro-osmosis on charged-modulated and undulat surface, *Physical Review E* **53**, 4996–5005, 1996.

[5] Alam A., Afzal A., Kim K. Y., Mixing performance of a planar micromixer with circular obstructions in a curved microchannel, *Chemical Engineering Research and Design* **92** (3), 423–434, 2014.

[6] Alam A., Kim K. Y., Analysis of mixing in a curved microchannel with rectangular grooves, *Chemical Engineering Journal* **181-182**, 708–716, 2012.

[7] Alizadeh A., Zhang L., Wang M., Mixing enhancement of low-Reynolds electro-osmotic flows in microchannels with temperature-patterned walls, *Journal of Colloid and Interface Science* **431**, 50–63, 2014.

[8] Amsden A. A., The SMAC method: a numerical technique for calculating incompressible fluid flows, *Los Alamos Sci. Lab. Rep*, 1970.

[9] Anderson D. A., Tannehill J. C., Pletcher R. H., *Computational fluid mechanics and heat transfer*, CRC Press, 2012.

[10] Anderson Jr. J. D., *Computational Fluid Dynamics: The Basics and Apllications*, McGraw-Hill, 1995.

[11] Ansari M. A., Kim K. Y., Parametric study on mixing of two fluids in a three-dimensional serpentine microchannel, *Chemical Engineering Journal* **146**, 439–448, 2009.

[12] Arcos J. C., Mendez F., Bautista E. G., Bautista O., Dispersion coefficient in an electro-osmotic flow of a viscoelastic fuid through a microchannel with a slowly varying wall zeta potential, *Journal of Fluid Mechanics* **839**, 348–386, 2018.

[13] Auroux P. A., Iossifidis D., Reyes D. R., Manz A., Micro total analysis systems. 2. Analytical standard operations and applications, *Analytical Chemistry* **74** (12), 2637–2652, 2002.

[14] Azimi S., Nazari M., Daghighi Y., Developing a fast and tunable micro-mixer using induced vortices around a conducting flexible link, *Physics of Fluids* **29**, 032004, 2017.

[15] Babaie A., Sadeghi A., Saidi M. H., Combined electroosmotically and pressure driven flow of power-law fluids in a slit microchannel, *Journal of Non-Newtonian Fluid Mechanics* **166**, 792–798, 2011.

[16] Babaie A., Saidi M. H., Sadeghi A., Electroosmotic flow of power-law fluids with temperature dependent properties, *Journal of Non-Newtonian Fluid Mechanics* **185-186**, 49–57, 2012.

[17] Bag N., Bhattacharyya S., Electroosmotic flow of a non-Newtonian fluid in a microchannel with heterogenous surface potential, *Journal of non-Newtonian Fluid Mechanics* **259**, 48–60, 2018.

[18] Bandopadhyay A., Borgne T. L., Méheust Y., Dentz M., Enhanced reaction kinetics and reactive mixing scale dynamics in mixing fronts under shear flow for arbitrary Damköhler numbers, *Advances in Water Resources* **100**, 78–95, 2017.

[19] Bandopadhyay A., Tripathi D., Chakraborty S., Electroosmosis-modulated peristaltic transport in microfluidic channels, *Physics of Fluids* **28** (5), 052002, 2016.

[20] Banerjee A., Nayak A. K., Haque A., Weigand B., Induced mixing electrokinetics in a charged corrugated nano.channel: towards a controlled ionic transport, *Microfluid Nanofluid* **22**, 115, 2018.

[21] Bau H. H., Zhong J., Yi M., A minute magneto hydro dynamic (MHD) mixer, *Sensors and Actuators B* **79**, 207–215, 2001.

[22] Bera S., Bhattacharyya S., Electroosmotic flow in the vicinity of a conducting obstacle mounted on the surface of a wide microchannel, *International Journal of Engineering Science* **94**, 128–138, 2015.

[23] Bera S., Bhattacharyya S., Effects of geometric modulation and surface potential heterogeneity on electrokinetic flow and solute transport in a microchannel, *Theoretical and Computational Fluid Dynamics* **32** (2), 201–214, 2018.

[24] Beyssen D., Le Brizoual L., Elmazria O., Alnot P., Microfluidic device based on surface acoustic wave, *Sensors and Actuators B: Chemical* **118** (1-2), 380–385, 2006.

[25] Bhattacharyya S., Nayak A. K., Time periodic electro-osmotic transport in a charged micro/nano-channel, *Colloids and Surfaces A: Physicochemical and Engineering Aspects* **325** (3), 152–159, 2008.

[26] Bhattacharyya S., Zhang Z., Conlisk A. T., Electroosmotic flow in two-dimensional charged micro-and nano-channels. *Journal of Fluid Mechanics* **540**, 247–267, 2005.

[27] Bhattacharyya S., Nayak A. K., Combined effect of surface rougness and heterogeneity of wall potential on electroosmosis in microfluidic/nanofluidic channels, *Journal of Fluids Engineering* **132** (4), 041103, 2010.

[28] Bhattacharyya S., Bera S., Nonlinear Electroosmosis Pressure-Driven Flow in a Wide Microchannel With Patchwise Surface Heterogeneity, *Journal of Fluids Engineering* **135** (2), 021303, 2013.

[29] Bhattacharyya S., Gopmandal P. P., Baier T., Hardt S., Sample dispersion in isotachophoresis with Poiseuille counterflow, *Physics of Fluids* **25** (2), 022001, 2013.

[30] Bhattacharyya S., Bera S., Combined electroosmosis-pressure driven flow and mixing in a microchannel with surface heterogeneity, *Applied Mathematical Modelling* **39** (15), 4337–4350, 2015.

[31] Biddis E., Erickson D., Li D., Heterogeneous surface charge enhanced micromixing for elcetrokinetic flows, *Analytical Chemistry* **76**, 3208–3213, 2004.

[32] Bingham E. C., *Fluidity and Plasticity*, McGraw-Hill, 1922.

[33] Bird R. B., Stewart W. E., Lightfoot E. N., *Transport Phenomena*, Wiley, London, 1960.

[34] Böhme G., Müller D., Analysis of non-Newtonian effects in peristaltic pumping, *Journal of Non-Newtonian Fluid Mechanics* **201**, 107–119, 2013.

[35] Borgohain P., Arumughan J., Dalal A., Natarajan G., Design and performance of a three-dimensional micromixer with curved ribs, *Chemical Engineering Research and Design* **136**, 761–775, 2018.

[36] Borgohain P., Arumughan J., Dalal A., Natarajan G., Design and performance of a three-dimensional micromixer with curved ribs, *Chemical Engineering Research and Design* **136**, 761–775, 2018.

[37] Borgohain P., Choudhary D., Dalal A., Natarajan G., Numerical investigation of mixing enhancement for multi-species flows in wavy channels, *Chemical Engineering & Processing: Process Intensification* **127**, 191–205, 2018.

[38] Brody J. P., Yager P., Goldstein R. E., Austin R. H., Biotechnology at low Reynolds number, *Biophysical journal* **71**, 3430–3441, 1996.

[39] Cai G., Xue L., Zhang H., Lin J., A review on micromixers, *Micromachines* **8** (9), 274, 2017.

[40] Campo A. D., Greiner C., Alvarez I., Arzt E., Patterned Surfaces with Pillars with Controlled 3D Tip Geometry Mimicking Bioattachment Devices, *Advanced Materials* **19**, 1973–1977, 2007.

[41] Capretto L., Cheng W., Hill M., Zhang X., Micromixing within microfluidic devices, *In Microfluidics*, 27–68, Springer, Berlin, Heidelberg, 2011.

[42] Carneiro-da-Cunha M. G., Cerqueira M. A., Souza B. W. S., Teixeira J. A., Vicente A. A., Influence of concentration, ionic strength and pH on zeta potential and mean hydrodynamic diameter of edible polysaccharide solutions envisaged for multinanolayered films production, *Carbohydrate Polymers* **85**, 522–528, 2011.

[43] Chang C. C., Yang R. J., Computational analysis of electrokinetically driven flow mixing in microchannels with patterned blocks, *Journal of Micromechanics and Microengineering* **14** (4), 550–558, 2004.

[44] Chang C. C., Yang R. J., Electrokinetic mixing in microfluidic systems, *Microfluid Nanofluid* **3**, 501–525, 2007.

[45] Chang C. C., Wang C. Y., Electro-osmotic flow in a sector microchannel, *Physics of Fluids* **21**, 042002, 2009.

[46] Chang S. H., Electroosmotic flow in a dissimilarly charged slit microchannel containing salt-free solution, *European Journal of Mechanics-B/Fluids* **34**, 85–90, 2012.

[47] Chao Z., Zhang Y., Wang Y., Jakobsen J. P., Jakobsen H. A., Modelling of binary fluidized bed reactors for the sorption-enhanced steam methane reforming process, *The Canadian Journal of Chemical Engineering* **95** (1), 157–169, 2017.

[48] Chapman D. L., LI. A contribution to the theory of electrocapillarity, *The London, Edinburgh, and Dublin philosophical magazine and journal of science* **25** (148), 475–481, 1913.

[49] Cheaib F., Kekejian G., Antoun S., Cheikh M., Lakkis I., Microfluidic mixing using pulsating flows, *Microfluid Nanofluid* **65**, 399–416, 2004.

[50] Chen C. K., Cho C. C., Electrokinetically-driven flow mixing in microcannels with wavy surface, *Journal of Colloid and Interface Sciences* **312**, 470–480, 2007.

[51] Chen H., Fan Z. H., Two-dimensional protein separation in microfluidic devices, *Electrophoresis* **30** (5), 758–765, 2009.

[52] Chen C. K., Cho C. C., A combined active/passive scheme for enhancing the mixing efficiency of microfluidic devices, *Chemical Engineering Science* **63** (12), 3081–3087, 2008.

[53] Chen L., Electroosmotic Flow and DNA Electrophoretic Transport in Micro/Nano Channels, *PhD diss.* The Ohio State University, 2009.

[54] Chen L., Conlisk A. T., Effect of nonuniform surface potential on electroosmotic flow at large applied field strength, *Biomedical microdevices* **11** (1), 251–258, 2009.

[55] Chen L., Lee S., Choo J., Lee E. K., Contnuous dynamic flow micropumps for microfluidic manipulation, *Journal of Micromechanics and Microengineering* **18**, 013001, 2008.

[56] Chen L., Lee S., Lee M., Lim C., Choo J., Park J. K., Lee S., Joo S. W., Lee K. H., Choi Y. W., DNA hybridisation detection in a microfluidic channel using two fluorescently labeled nucleic acid probes, *Biosensors and Bioelectronics* **23** (12), 1878–1882, 2008.

[57] Chen X., Li T., A novel passive micromixer designed by applying an optimization algorithm to the zigzag microchannel, *Chemical Engineering Journal* **313**, 1406–1414, 2017.

[58] Chen X., Li T., Zeng H., Hu Z., A novel research on serpentine microchannels of passive micromixers, *Microsystem Technologies* **23** (7), 2649–2656, 2017.

[59] Chen X., Li T., Zeng H., Hu Z., Fu B., Numerical and experimental investigation on micromixers with serpentine microchannels, *International Journal of Heat and Mass Transfer* **98**, 131–140, 2016.

[60] Chen X., Shen J., Numerical analysis of mixing behaviors of two types of E-shape micromixers, *International Journal of Heat and Mass Transfer* **106**, 593–600, 2017.

[61] Cheng L. J., Guo L. J., Ionic current rectification, breakdown, and switching in heterogeneous oxide nanofluidic devices, *ACS Nano* **3** (3), 575–584, 2009.

[62] Chin C. D., Linder V., Sia S. K., Lab-on-a-chip devices for global health: Past studies and future opportunities, *Lab on a Chip* **7** (1), 41–57, 2007.

[63] Cho C. C., Chen C. L., Chen C. K., Electrokinetically-driven non-Newtonian fluid flow in rough microchannel with complex-wavy surface, *Journal of Non-Newtonian Fluid Mechanics* **173-174**, 13–20, 2012.

[64] Cho C. C., Chen C. L., Chen C. K., Flow characterictics and mixing performance of electrokinetically driven non-Newtonian fluid in contraction-expansion microchannel, *Rheologica acta* **51**, 925–935, 2012.

[65] Cho C. C., Chen C. L., Chen C. K., Mixing of non-Newtonian fluids in wavy serpentine microchannel using electrokinetically driven flow, *Electrophoresis* **33**, 743–750, 2012.

[66] Cho C. C., Chen C. L., Chen C. K., Mixing enhancement of electrokinetically-driven non-Newtonian fluids in microchannel with patterned blocks, *Chemical Engineering Journal* **191**, 132–140, 2012.

[67] Cho C. C., Chen C. L., Chen C. K., Characteristics of transient electroosmotic flow in microchannels with complex-wavy surface and periodic time-varying electric field, *Journal of Fluids Engineering* **135**, 021301, 2013.

[68] Cheri M. S., Latifi H., Moghaddam M. S., Shahraki H., Simulation and experimental investigation of planar micromixers with short-mixing-length, *Chemical engineering journal* **234**, 247–255, 2013.

[69] Chorin A. J., Shahraki H., A numerical method for solving incompressible viscous flow problems, *Journal of computational physics* **135** (2), 118–125, 1997.

[70] Chung A. J., Kim D. and Erickson D., Electrokinetic microfluidic devices for rapid, low power drug delivery in autonomous microsystems, *Lab on a Chip* **8** (2), 330–338, 2008.

[71] Chung C. K., Shih T. R., A rhombic micromixer with asymmetrical flow for enhancing mixing, *Journal of Micromechanics and Microengineering* **17** (12), 2495, 2007.

[72] Conlisk A. T., McFerran J., Zheng Z., Hansford D., Mass Transfer and Flow in Electrically Charged Micro- and Nano-channels, *Analytical Chemistry* **74** (9), 2139–2150, 2002.

[73] Conlisk A. T., The Debye-H*ü*ckel approximation: Its use in describing electroosmotic flow in micro-and nano cannels, *Electroporesis* **26** (10), 1896–1912, 2005.

[74] Courant R., Isaacson E., Rees M., On the solution of nonlinear hyperbolic differential equations by finite differences, *Communications on Pure and Applied Mathematics* **5** (3), 243–255, 1952.

[75] Czilwik G., Messinger T., Strohmeier O., Wadle S., Von Stetten F., Paust N., Roth G., Zengerle R., Saarinen P., Niittymki J., McAllister K., Rapid and fully automated bacterial pathogen detection on a centrifugal-microfluidic LabDisk using highly sensitive nested PCR with integrated sample preparation, *Lab on a Chip* **15** (18), 3749–3759, 2015.

[76] Das S., Chakraborty S., Analytical solutions for velocity, temperature and concentra- tion distribution in electroosmotic microchannel flows of a non-Newtonian bio-fluid, *Analytica Chimica Acta* **559** (1), 15–24, 2006.

[77] Datta S., Ghosal S., Patankar N. A., Electroosmotic flow in a Rectangular Channel with Variable Wall Zeta-potential: Comparison of Numerical Simulation with Asymptotic Theory, *Electrophoresis* **27**, 611–619, 2006.

[78] D'Avino G., Greco F., Maffettone P. L., Particle migration due to viscoelasticity of the suspending liquid and its relevance in microfluidic devices, *Annual Review of Fluid Mechanics* **49**, 341–360, 2017.

[79] Davis J. A., James R. O., Leckie J. O., Surface ionization and complexation at the oxide/water interface: I. Computation of electrical double layer properties in simple electrolytes, *Journal of colloid and interface science* **63** (3), 480–499, 1978.

[80] Dauyeshova B., Rojas-Solórzano L. R., Monaco E., Numerical simulation of diffusion process in T-shaped micromixer using Shan-Chen Lattice Boltzmann Method, *Computers & Fluids* **167**, 229–240, 2018.

[81] Deng S., The Parametric Study of Electroosmotically Driven Flow of Power-Law Fluid in a Cylindrical Microcapillary at High Zeta Potential, *Micromachines* **8** (12), 344, 2014.

[82] Duan C., Wang W., Xie Q., Review article: Fabrication of nanofluidic devices, *Biomicrofluidics* **7** (2), 026501, 2013.

[83] Eijkel J. C., Van Den Berg A., Nanofluidics: what is it and what can we expect from it?, *Microfluidics and Nanofluidics* **1** (3), 249–267, 2005.

[84] Erickson D., Li D., Influence of surface heterigeneity on electrokinetically driven microfluidic mixing, *Langmuir* **18** (5), 1883–1892, 2002.

[85] Erickson D., Towards numerical prototyping of labs-on-chip: modeling for integrated microfluidic devices, *Microfluidics and Nanofluidics* **1** (4), 301–318, 2005.

[86] Fair R. B., Digital microfluidics: is a true lab-on-a-chip possible ?, *Microfluidics and Nanofluidics* **3**, 245–281, 2017.

[87] Fan L. L., Zhu X. L., Zhao H., Zhe J., Zhao L., Rapid microfluidic mixer utilizing sharp corners structures, *Microfluidics and Nanofluidics* **21** (3), 36, 2017.

[88] Ferziger J. H., Peric M., *Computational methods for fluid dynamics*, Springer Science & Business Media, 2012.

[89] Fletcher C. A. J., *Computational Techniques for Fluid Dynamics*, Vol. I and II, Springer Ser. Comput. Phy. 2nd ed. Springer, Berlin, Heidelberg, New York, 1991.

[90] Fu L. M., Lin J. Y., Yang R. J., Analysis of electroosmotic flow with step change in zeta potential, *Journal of Colloid and Interface Science* **258**, 266–275, 2003.

[91] Fuest M., Boone C., Rangharajan K. K., Conlisk A. T., Prakash S., A Three-State Nanofluidic Field Effect Switch, *Nano letters* **15** (4), 2365–2371, 2015.

[92] Gao X., Li Y., Biofluid pumping and mixing by an AC electrothermal micropump embedded with a spiral microelectrode pair in a cylindrical microchannel, *Electrophoresis* **39**, 3156–3170, 2019.

[93] Ghia K. N., Hankey Jr W. L., Hodge J. K., Use of primitive variables in the solution of incompressible Navier-Stokes equations, *AIAA journal* **17** (3), 298–301, 1979.

[94] Ghosh U., Chakraborty S., Patterned-wettability-induced alteration of electro-osmosis over charge-modulated surfaces in narrow confinements, *Physical Review E* **85**, 046304–13, 2012.

[95] Glasgow I., Aubry N., Enhancement of microfluidic mixing using time pulsing, *Lab on a Chip* **3** (4), 114–120, 2003.

[96] Gonalvs J., Rousseau-Gueutin P., Revil A., Introducing interacting diffuse layers in TLM calculations: A reappraisal of the influence of the pore size on the swelling pressure and the osmotic efficiency of compacted bentonites, *Journal of colloid and interface science* **316** (1), 92–99, 2007.

[97] Goswami P., Chakraborty J., Bandopadhyay A., Chakraborty S., Electrokinetically modulated peristaltic transport of power-law fluids, *Microvascular Research* **103**, 41–54, 2016.

[98] Guta L., Sundar S., Navier-Stokes-Brinkman system for interaction of viscous waves with a submerged porous structure, *Tamkang journal of mathematics* **41** (3), 217–243, 2010.

[99] Gouy M., Sur la constitution de la charge électrique à la surface d'un électrolyte, *J. Phys. Theor. Appl.* **9** (1), 457–468, 1910.

[100] Hadigol M., Nosrati R., Nourbakhsh A., Raisee M., Numerical study of electroosmotic micromixing of non-Newtonian fluids, *Journal of Non-Newtonian Fluid Mechanics* **166**, 965–971, 2011.

[101] Hadigol M., Nosrati R., Raisee M., Numerical analysis of mixed electroosmotic/pressure driven flow of power-law fluids in microchannels and micropumps, *Colloids and Surfaces A: Physicochemical and Engineering Aspects* **374**, 142–153, 2011.

[102] Harlow F. H., Welch J. E., Numerical calculation of time-dependent viscous incompressible flow of fluid with free surface, *The physics of fluids* **8** (12), 2182–2189, 1965.

[103] Hattersley, S. M., Greenman, J., Haswell S. J., The application of microfluidic devices for viral diagnosis in developing countries, *In Microfluidic Diagnostics*, Humana Press, Totowa, NJ, 285–303, 2013.

[104] Hayase T., Humphrey J. A. C., Greif R., A consistently formulated QUICK scheme for fast and stable convergence using finite-volume iterative calculation procedures, *Journal of Computational Physics*, **98** (1), 108–118, 1992.

[105] Helmholtz H. V., Studien *ü*ber electrische Grenzschichten, *Annalen der Physik* **243** (7), 337–382, 1879.

[106] Herschel W. H., Bulkley R., Measurement of consistency as applied to rubber-benzene solutions, *Proc. Am. Soc. Test Mater.* **26**, 621–633, 1926.

[107] Himstedt H. H., Yang Q., Dasi L. P., Qian X., Wickramasinghe S. R., Ulbricht M., Magnetically activated micromixers for separation membranes, *Langmuir* **27**, 5574–5581, 2011.

[108] Hirt C. W., Nichols B. D., Romero N. C., SOLA: A numerical solution algorithm for transient fluid flows, *NASA STI/Recon Technical Report N* **75**, 32418, 1975.

[109] Hossain S., Lee I., Kim S. M., Kim K. Y., A micromixer with two-layer serpentine crossing channels having excellent mixing performance at low Reynolds numbers, *Chemical Engineering Journal* **327**, 268–277, 2017.

[110] Hsieh S. S., Lin J. W., Chen J. H., Mixing efficiency of Y-type micromixers with different angles, *International Journal of Heat and Fluid Flow* **44**, 130–139, 2013.

[111] Hsu J. P., Kuo Y. C., Tseng S., Dynamic interactions of two electrical double layers. *Journal of colloid and interface science* **195**, 388–394, 1997.

[112] Hu J. S., Chao C. Y. H., Numerical study of electroosmotic (EO) flow in microfabricated EO pump with overlapped electrical double layer (EDL), *International journal of refrigeration* **30**, 290–298, 2007.

[113] Huang K. R., Hong Z. H., Chang J. S., Microfluidic mixing on application of traveling wave electroosmosis, *European Journal of Mechanics B/Fluids* **48**, 153–164, 2014.

[114] Huikko K., Kostiainen R., Kotiaho T., Introduction to microanalytical systems: bioanalytical and pharmaceutical applications, *European journal of pharmaceutical sciences* **20** (2), 149–171, 2003.

[115] Hunter R. J., *Foundations of colloid science*, *Oxford University Press*, 2001.

[116] Jain M., Yeung A., Nandakumar K., Efficient micromixing using Induced-Charge Electroosmosis, *Journal of Microelectromechanical Systems* **18** (2), 376–384, 2009.

[117] Jain M., Nandakumar K., Optimal patterning of eterogeneous surface charge for improved electrokinetic micrimixing, *Computers and Chemical Engineering* **49**, 18-24, 2013.

[118] Jaluria Y., *Computational Heat Transfer*, Taylor Francis, New York, 2003.

[119] Jeon W., Shin C. B., Design and simulation of passive mixing in microfluidic systems with geometric variations, *Chemical Engineering Journal* **152**, 575–582, 2009.

[120] Jeon W., Shin C. B., Design and simulation of passive mixing in microfluidic systems with geometric variations. *Chemical Engineering Journal* **152** (2-3), 575–582, 2009.

[121] Jeong G. S., Chung S., Kim C. B., Lee S. H., Applications of micromixing technology. *Chemical Engineering Journal* **135** (3), 460–473, 2010.

[122] Johnson T. J., Ross D., Locascio L. E., Rapid microfluidic mixing, *Analytical chemistry* **74**, 45–51, 2002.

[123] Jung K. Y., Jung S. K., Myong R. S., Kim J. H., A Three-Dimensional Unstructured Finite Volume Method for Droplet Impingement in Aircraft Icing, *21st AIAA Computational Fluid Dynamics Conference* 2576, 2013.

[124] Jung S. K., Myong R. S., A second-order positivity-preserving finite volume upwind scheme for air-mixed droplet flow in atmospheric icing, *Computers & Fluids* **86**, 459-469, 2013.

[125] Kairi R. R., Narayana P. A. L., Murthy P. V. S. N., The effect of double dispersion on natural convection heat and mass transfer in a non-Newtonian fluid saturated non-Darcy porous medium, *Transport in porous media* **76** (3), 377-390, 2009.

[126] Kang S., Suh Y. K., Electroosmotic flows in an electric double layer overlapped channel with rectangle-waved surface roughness, *Microfluidics and nanofluidics* **7**, 337–352, 2009.

[127] Karnik R., Castelino K., Duan C. H., Majumdar A., Diffusion-limited patterning of molecules in nanofluidic channels, *Nano Letters* **6** (8), 1735–1740, 2006.

[128] Kee S. P., Gavriilidis A., Design and characterisation of staggered herringbone mixer, *Chemical Engineering Journal* **142**, 109–121, 2008.

[129] Kemna A., Binley A., Cassiani G., Niederleithinger E., Revil A., Slater L., Williams K. H., Orozco A. F., Haegel F. H., Hoerdt A., Kruschwitz S., An overview of the spectral induced polarization method for near-surface applications *Near Surface Geophysics* **10** (6), 453–468, 2012.

[130] Kim H. J., Beskok A., Quantification of chaotic strength and mixing in a micro fluidic system, *Journal of Micromechanics and Microengineering* **17**, 2197–2210, 2007.

[131] Kim H., Kwak H. S., Westerweel J., Assessment of mixing problem on the EOF with thermal effects, *Colloids and Surfaces A: Physicochemical and Engineering Aspects* **376**, 53–58, 2011.

[132] Ko C. H., Li D., Malekanfard A., Wang Y. N., Fu L. M., Xuan X., Electroosmotic flow of non-Newtonian fluids in a constriction microchannel, *Electrophoresis* **0**, 1–8, 2018.

[133] Kockmann N., Kiefer T., Engler M., Woias P., Convective mixing and chemical reactions in microchannels with high flow rates, *Sensors and Actuators B: Chemical* **117** (2), 495–508, 2006.

[134] Kumar V., Paraschivoiu M., Nigam K. D. P., Single-phase fluid flow and mixing in microchannels, *Chemical Engineering Science* **66** (7), 1329–1373, 2011.

[135] Koga Y., Kuriyama R., Sato Y., Hishida K., Miki N., Effects of Micormachining process on Electroosmotic flow mobility of Glass surfaces, *Micromachines* **4**, 67–79, 2013.

[136] Kostal V., Katzenmeyer J., Arriaga E. A., Capillary electrophoresis in bioanalysis, *Analytical chemistry* **80** (12), 4533–4550, 2008.

[137] Kumar V., Paraschivoiu M., Nigam K. D. P., Single-phase fluid flow and mixing in microchannels, *Chemical Engineering Science* **66** (7), 1329–1373, 2011.

[138] Kunti G., Bhattacharya A., Chakraborty S., Rapid mixing with high-throughput in a semi-active semi-passive micromixer, *Electrophoresis* **38**, 1310–1317, 2017.

[139] Lagally E., Scherer J., Blazej R., Toriello N., Diep B., Ramchandani M., Sensabaugh G., Riley L., Mathies R., Integrated portable genetic analysis microsystem for pathogen/infectious disease detection, *Analytical chemistry* **76** (11), 3162–3170, 2004.

[140] Le N. T. P., Xiao H., Myong R. S., A triangular discontinuous Galerkin method for non-Newtonian implicit constitutive models of rarefied and microscale gases, *Journal of Computational Physics* **273**, 160–184, 2014.

[141] Lee C. Y., Lee G. B., Lin J. L., Huang F. C., Liao C. S., Integrated microfluidic systems for cell lysis, mixing/pumping and DNA amplification, *Journal of Micromechanics and Microengineering* **15**, 1215–1223, 2005.

[142] Lee C. Y., Chang C. L., Wang Y. N., Fu L. M., Microfluidic mixing: A review, *International journal of molecular sciences* **12**, 3263–3287, 2011.

[143] Lee C. Y., Wang W. T., Liu C. C., Fu L. M., Passive mixers in microfluidic systems: A review, *Chemical Engineering Journal* **288**, 146–160, 2016.

[144] Lei Y., Wang W., Wu W., Li Z., Nanofluidic diode in a suspended nanoparticle crystal, *Applied Physics Letters* **96** (26), 263102, 2010.

[145] Leonard B. P., Stable and accurate convective modelling procedure based on quadratic upstream interpolation, *Computer methods in applied mechanics and engineering* **19**, 59–98, 1979.

[146] Leroy P., Revil A., Altmann S., Tournassat C., Modeling the composition of the pore water in a clay-rock geological formation (Callovo-Oxfordian, France), *Geochimica et cosmochimica acta* **71** (5), 1087–1097, 2007.

[147] Leroy P., Jougnot D., Revil A., Lassin A., Azaroual M., A double layer model of the gas bubble/water interface, *Journal of colloid and interface science* **388** (1), 243–256, 2012.

[148] Li X., Yin Z., Jiaan Y., Chang L., Su J., Liu Q., Transient electro-osmotic flow of generalized Maxwell fluids through a microchannel, *Journal of Non-Newtonian Fluid Mechanics* **187-188**, 43–47, 2012.

[149] Lim C. Y., Lam Y. C., Yang C., Mixing enhancement in microfluidic channel with a constriction under periodic electro-osmotic flow, *Biomicrofluidics* **4**, 014101, 2010.

[150] Lin C. H., Tsai C. H., Fu L. M., A rapid three-dimensional vortex micromixer utilizing self rotation effects under low Reynolds number conditions, *Journal of Micromechanics and Microengineering* **15**, 935–943, 2005.

[151] Lin Y., Yua X., Wang Z., Tu S. T., Wang Z. D., Design and evaluation of an easily fabricated micromixer with three-dimensional periodic perturbation, *Chemical Engineering Journal* **171**, 291–300, 2011.

[152] Lindner D., Microsystems for chemical and biological applications, *Mrs Bulletin* **26**, 333–336, 2001.

[153] Liu A. L., He F. Y., Wang K., Zhou T., Lu Y., Xia X. H., Rapid method for design and fabrication of passive micromixers in microfluidic devices using a direct-printing process, *Lab on a Chip* **5**, 974–978, 2005.

[154] Liu Y, Yang D., Effect of wall roughness on Electroosmotic flow in Microchannels, *Advanced Tribiology* **3**, 1087–1099, 2010.

[155] Lomax H., Pillian T. H., Zingg D. W., *Fundamentals of Computational Fluid Dynamics*, Springer-Verlag, 2001.

[156] Lu X., Liu C., Hu G., Xuan X., Particle manipulations in non-Newtonian microfluidics: A review, *Journal of colloid and interface science* **500**, 182–201, 2017.

[157] Luo W. J., Transient electro-osmotic flow induced by AC electric field in micro-channel with patchwise surface heterogeneities, *Journal of colloid and interface science* **295**, 551–561, 2006.

[158] Mahanta G., Shaw S., 3D Casson fluid flow past a porous linearly stretching sheet with convective boundary condition, *Alexandria Engineering Journal* **54** (3), 653–659, 2015.

[159] Maiti D. K., Dependence of flow characteristics of rectangular cylinders near a wall on the incident velocity, *Acta Mechanica* **222** (3-4), 273–286, 2011.

[160] Maiti D. K., Numerical study on aerodynamic characteristics of rectangular cylinders near a wall, *Ocean Engineering* **54**, 251–260, 2012.

[161] Maiti D. K., Bhatt R., Numerical study on flow and aerodynamic characteristics: Square cylinder and eddy-promoting rectangular cylinder in tandem near wall, *Aerospace Science and Technology* **36**, 5–20, 2014.

[162] Maiti D. K., Bhatt R., Interactions of Vortices of a Square Cylinder and a Rectangular Vortex Generator Under Couette Poiseuille Flow, *Journal of Fluids Engineering* **137** (5), 051203, 2015.

[163] Maiti D. K., Bhatt R., Alam M. M., Aerodynamic forces on square cylinder due to secondary flow by rectangular vortex generator in offset tandem: Comparison with inline, *Computers & Fluids* **134**, 157–176, 2016.

[164] *Malkin A. Y., Rheology fundamentals*, ChemTec Publishing, 1994.

[165] Mansur E. A., Ye M., Wang Y., Dai Y., A state of the art Review of Mixing in Microfluidic Mixtutres, *Chinese Journal of Chemical Engineering* **16** (4), 503–516, 2008.

[166] Mariotti A., Galletti C., Mauri R., Salvetti M. V., Steady and unsteady regimes in a T-shaped micro-mixer: Synergic experimental and numerical investigation, *Chemical Engineering Journal* **341**, 414–431, 2018.

[167] Martinez L., Bautista O., Escandon J., Mendez F., Electroosmotic flow of a Phan-Thien-Tanner fluid in a wavy-wall microchannel, *Colloids and Surfaces A: Physicochemical and Engineering Aspects* **498**, 7–19, 2016.

[168] Masilamani K., Ganguly S., Feichtinger C., Bartuschat D., Rude U., Effects of Surface roughness and electrokinetic heterogeneity on electroosmotic flow in microchannel, *Fluid Dynamics Research* **47**, 035505, 2015.

[169] Masliyah J. H., Bhattacharjee S., *Electrokinetic and colloid transport phenomena*, John Wiley & Sons, 2006.

[170] Matle S., Sundar S., A 2D Finite Element Study on the Flow Pattern and Temperature Distribution for an Isothermal Spherical Furnace with the Aperture, *Open Journal of Applied Sciences* **2** (04), 319, 2012.

[171] Matle S., Sundar S., Axi symmetric 2D simulation and numerical heat transfer characteristics for the calibration furnace in a rectangular enclosure, *Applied Mathematical Modelling* **36** (3), 878–893, 2012.

[172] Matta A., Narayana P. A. L., Hill A. A., Double-diffusive Hadley Prats flow in a horizontal porous layer with a concentration based internal heat source, *Journal of Mathematical Analysis and Applications* **452** (2), 1005–1018, 2017.

[173] Matteucci M., Christiansen T. L., Tanzi S., Stergaard P. F., Larsen S. T., Taboryski R., Fabrication and characterization of injection molded multi level nano and microfluidic systems, *Microelectronic Engineering* **111**, 294–298, 2013.

[174] Medina I., Toledo M., Méndez M., Bautista O., Pulsatile electroosmotic flow in microchannel with asymmetric wall zeta potentials ans its effect on mass transport enhancement and mixing, *Chemical Engineering Science* **184** 259–272, 2018.

[175] Meisel I., Ehrhard P., Electrically excited (Electroosmotic) flow in Micro channels for Mixing applications, *European Journal of Mechanics B/Fluids* **25**, 491–504, 2006.

[176] Min J. Y., Hasselbrink E., Kim S. J., On the efficiency of electrokinetic pumping of liquids through nanoscale channels, *Sensors and Actuators B: Chemical* **98** (2), 368–377, 2004.

[177] Mirbozorgi S. A., Niazmand H., Renksizbulut M., Electro-Osmotic Flow in Reservoir-Connected Flat Microchannels With Non-Uniform Zeta Potential, *Journal of Fluids Engineering* **128**, 1133–1143, 2006.

[178] Moctar A. O. El., Aubry N., Batton J., Electro-hydrodynamic micro-fluidic mixer, *Lab on a Chip* **3** (4), 273–280, 2003.

[179] Mondal A., Shit G. C., Electro-osmotic flow and heat transfer in a slowly varying asymmetric micro-channel with Joule heating effects, *Fluid Dynamics Research* **50** (6), 065502, 2018.

[180] Murthy S. K., Kumar B. R., Chandra P., Sangwan V., Nigam M., A study of double diffusive free convection from a corrugated vertical surface in a Darcy porous medium under Soret and Dufour effects, *Journal of Heat Transfer* **133** (9), 092601, 2011.

[181] Muthu P., Kumar B. R., Chandra P., Peristaltic motion in circular cylindrical tubes: effect of wall properties, *Indian Journal of Pure and Applied Mathematics* **32** (9), 1317–1328, 2001.

[182] Muthu P., Kumar B. R., Chandra P., On the influence of wall properties in the peristaltic motion of micropolar fluid, *The ANZIAM Journal* **45** (2), 245–260, 2003.

[183] Muthu P., Kumar B. R., Chandra P., Peristaltic motion of micropolar fluid in circular cylindrical tubes: Effect of wall properties, *Applied Mathematical Modelling* **32** (10), 2019–2033, 2008.

[184] Myong R. S., Theoretical description of the gaseous Knudsen layer in Couette flow based on the second-order constitutive and slip-jump models, *Physics of Fluids* **28** (1), 012002, 2016.

[185] Narayana M., Sibanda P., Motsa S. S., Narayana P. A. L., Linear and nonlinear stability analysis of binary Maxwell fluid convection in a porous medium, *Heat and Mass Transfer* **48** (5), 863–874, 2012.

[186] Narayana P. A. L., Sibanda P., Soret and Dufour effects on free convection along a vertical wavy surface in a fluid saturated Darcy porous medium, *International Journal of Heat and Mass Transfer* **53** (15-16), 3030–3034, 2010.

[187] Navier C. L. M. H., Memoiré sur les lois de mouvement des fluides, *Mémoires de l'Académie Royale des Sciences de l'Institut de France*, **6**, 389–416, 1823.

[188] Nayak A. K., An Analysis of Steady/Unsteady Electroosmotic flows Through Charged cylindrical nano channel, *Theoretical and Computational Fluid Dynamics* **24**, 3006–3017, 2013.

[189] Nayak A. K., Analysis of mixing for electroosmotic flow in micro/nano channels with heterogeneous surface potential, *International Journal of Heat and Mass Transfer* **75**, 135–144, 2014.

[190] Nayak A. K., Banerjee A., Weigand B., Mixing and charge transfer in a nanofluidic system due to a patterned surface, *Applied Mathematical Modelling* **54**, 483–501, 2018.

[191] Nayak A. K., Haque A., Banerjee A., Weigand B., Flow mixing and electric potential effect of binary fluids in micro/nano channels, *Colloids and Surfaces A: Physicochemical and Engineering Aspects* **512**, 145–157, 2017.

[192] Nayak A. K., Haque A., Weigand B., Analysis of electroosmotic flow and Joule heating effect in a hydrophobic channel, *Chemical Engineering Science* **176**, 165–179, 2018.

[193] Nekoubin N., Electroosmotic flow of power-law fluids in curved rectangular microchannel with high zeta potentials, *Journal of Non-Newtonian Fluid Mechanics* **260**, 54–68, 2018.

[194] Nezhad J. R., and Mirbozorgi S. A., An immersed boundary-lattice Boltzmann method to simulate chaotic micromixers with baffles, *Computers & Fluids* **167**, 206–214, 2018.

[195] Ng C., Chu H. C. W., Electrokinetic flows through a parallel-plate channel with slipping stripes on walls, *Physics of Fluids* **23**, 102002, 2011.

[196] Ng Chiu-On., Combined pressure-driven and electroosmotic flow of Casson fluid through a slit microchannel, *Journal of Non-Newtonian Fluid Mechanics* **198**, 1–9, 2013.

[197] Ng Chiu-On., Qi C., Electroosmotic flow of power-law fluid in a non-uniform microchannel, *Journal of Non-Newtonian Fluid Mechanics* **208-209**, 118–125, 2014.

[198] Nimafar M., Viktorov V., Martinelli M., Experimental comparative mixing performance of passive micromixers with H-shaped sub-channels, *Chemical engineering science* **76**, 37–44, 2012.

[199] Niu X., Lee Y. K., Efficient spatial-temporal chaotic mixing in microchannels, *Journal of Micromechanics and Microengineering* **13**, 454–462, 2003.

[200] Nouri D., Zabihi-Hesari A., Passandideh-Fard M., Rapid mixing in micromixers using magnetic field, *Sensors and Actuators A: Physical* **255**, 79–86, 2017.

[201] Oddy M. H., Santiago J. G., Mikkelsen J. C., Electrokinetic instability micromixing, *Analytical chemistry* **73**, 5822–5832, 2001.

[202] Oratega-Casanova J., Enhancing mixing at very low Reynolds number by heaving square cylinder, *Journal of Fluids and Structures* **65**, 1–20, 2016.

[203] Ottino J. M., *The kinematics of mixing, stretching and chaos*, Cambridge University Press, Cambridge, 1989.

[204] Ottino J. M., Wiggins S., Introduction: Mixing in Microfluidics, *Philosophical Transactions: Mathematical, Physical and Engineering Sciences*, 923–935, 2004.

[205] Pacheco J. R., Mixing enhancement in electroosmotic flows via modulation of electric fields, *Physics of Fluids* **20**, 093603, 2008.

[206] Panda S., Pyarajan S., *Encyclopedia of Microfluidics and Nanofluidics*, Springer US, Boston, MA, 940–947, 2008.

[207] Park J. M., Kim D. S., Kang T. G., Kwon T. H., Improved serpentine laminating micromixer with enhanced local advection, *Microfluidics and Nanofluidics* **4**, 513–523, 2008.

[208] Park S. Y., Russo C. J., Branton D., Stone H. A., Eddies in a bottleneck: An arbitrary Debye length theory for capillary electroosmosis, *Journal of Colloid and Interface Science* **297**, 832–839, 2006.

[209] Parsa M. K., Hormozi F., Experimental and CFD modeling of fluid mixing in sinusoidal microchannels with different phase shift between side walls, *Journal of Micromechanics and Microengineering* **24**, 065018, 2014.

[210] Patankar S., *Numerical heat transfer and fluid flow*, CRC press, 1980.

[211] Patankar S., Spalding D., A calculation procedure for heat, mass and momentum transfer in three-dimensional parabolic flows, *International Journal of Heat and Mass Transfer* **15** (10), 1787–1806, 1972.

[212] Peng R., Li D., Effects of ionic concentration gradient on electroosmotic flow mixing in a microchannel, *Journal of Colloid and Interface Science* **440**, 126–132, 2015.

[213] Peyret R., Taylor T. D., *Computational methods for fluid flow*, Springer Science & Business Media, 2012.

[214] Pham N., Radajewski D., Round A., Brennich M., Pernot P., Biscans B., Bonneté F., Teychené S., Coupling high throughput microfluidics and small-angle X-ray scattering to study protein crystallization from solution, *Analytical chemistry* **89** (4), 2282–2287, 2017.

[215] Philip J. R., Wooding R. A., Solution of the PoissonBoltzmann equation about a cylindrical particle, *The Journal of Chemical Physics* **52** (2), 953–959, 1970.

[216] Pletcher R. H., Tannehill J. C., Anderson D., *Computational Fluid Mechanics and Heat Transfer*, CRC Press, 2012.

[217] Prakash S., Zambrano H. A., Fuest M., Boone C., Rosenthal-Kim E., Vasquez N., Conlisk A. T., Electrokinetic transport in silica nanochannels with asymmetric surface charge, *Microfluidics and Nanofluidics* **19** (6), 1455–1464, 2015.

[218] Prakash S., Conlisk A. T., Field effect nanofluidics, *Lab on a Chip* **16** (20), 3855–3865, 2016.

[219] Probstien R. F., Physicochemical hydrodynamics: an introduction, *John Wiley & Sons* 2005.

[220] Ramirez J. C., Conlisk A.T., Formation of vortices near abrupt nano-channel height changes in electro-osmotic flow of aqueous solutions, *Biomedical microdevices* **8** (4), 325–330, 2006.

[221] Ramsey J. M., Jacobsen S. C., Knapp M. R., Microfabricated Chemical Measurement System, *Nature Medicine* **1** (10), 1093–1095, 1995.

[222] Ranjit N. K., Shit G. C., Joule heating effects on electromagnetohydrodynamic flow through a peristaltically induced micro-channel with different zeta potential and wall slip, *Physica A: Statistical Mechanics and its Applications* **482**, 458–476, 2017.

[223] Philip D., Chandra P., Flow of Eringen fluid (simple microfluid) through an artery with mild stenosis, *International journal of engineering science* **34** (1), 87–99, 1996.

[224] Rice C. L., Whitehead R., Electrokinetic flow in a narrow cylindrical capillary, *The Journal of Physical Chemistry* **69** (11), 4017–4024, 1965.

[225] Revil A., Transport of water and ions in partially water-saturated porous media. Part 2. Filtration effects *Advances in water resources* **103**, 139–152, 2017.

[226] Reynolds O., An experimental investigation of the circumstances which determine whether the motion of water shall be direct or sinuous, and of the law of resistance in parallel channels, *Philosophical Transactions of the Royal Society*, **174**, 935–982, 1883.

[227] Rusten H. K., Ochoa-Fernendez E., Chen D., Jakobsen H. A., Numerical investigation of sorption enhanced steam methane reforming using Li_2ZrO_3 as CO_2-acceptor, *Industrial & engineering chemistry research* **46** (13), 4435–4443, 2007.

[228] Sackmann E. K., Fulton A. L., Beebe D. J., The present and future role of microfluidics in biomedical research, *Nature* **507** (7491), 181, 2014.

[229] Sadeghi A., Saidi M. H., Veisi H., Fattahi M., Thermally developing electroosmotic flow of power-law fluids in a parallel plate microchannel, *International Journal of Thermal Sciences* **61**, 106–117, 2012.

[230] Sadr R., Yoda M., Zheng Z., Conlisk A. T., An experimental study of electroosmotic flow in rectangular microchannels, *Journal of fluid mechanics* **506**, 357–367, 2004.

[231] Sánchez R. A., Riboldi L., Jakobsen H. A., Numerical modelling and simulation of hydrogen production via four different chemical reforming processes: process performance and energy requirements, *The Canadian Journal of Chemical Engineering* **95** (5), 880–901, 2017.

[232] Sarkar A., Narva'ez A., Harting J., Quantification of the performance of chaotic micromixers on the basis of finite time Lyapunov exponents, *Microfluidics and Nanofluidics* **13** (1), 19–27, 2012.

[233] Sezavar D., Miri M., Investigating fluid mixing in electro-osmotic flow through passive micro-mixers having square and triangle barriers, *International Journal of Advanced Biological and Biomedical Research* **2** (12), 2940–2948, 2014.

[234] Shaw S., Murthy P. V. S., Pradhan S. C., The effect of body acceleration on two dimensional flow of Casson fluid through an artery with asymmetric stenosis, *The Open Conservation Biology Journal* **2**, 55–68, 2010.

[235] Shaw S., Mahanta G., Sibanda P., Non-linear thermal convection in a Casson fluid flow over a horizontal plate with convective boundary condition, *Alexandria Engineering Journal* **55** (2), 1295–1304, 2016.

[236] Shen H. H., Fan S. K., Kim C. J., Yao D. J., EWOD microfluidic systems for biomedical applications, *Microfluidics and Nanofluidics* **16** (5), 965–987, 2014.

[237] Shit G. C., Mondal A., Sinha A., Kundu P. K., Effects of slip velocity on rotating electro-osmotic flow in a slowly varying micro-channel, *Colloids and Surfaces A: Physicochemical and Engineering Aspects* **489**, 249–255, 2016.

[238] Shit G. C., Mondal A., Sinha A., Kundu P. K., Electro-osmotic flow of power-law fluid and heat transfer in a micro-channel with effects of Joule heating and thermal radiation, *Physica A: Statistical Mechanics and its Applications* **462**, 1040–1057, 2016.

[239] Shit G. C., Mondal A., Sinha A., Kundu P. K., Electro-osmotically driven MHD flow and heat transfer in micro-channel, *Physica A: Statistical Mechanics and its Applications* **449**, 437–454, 2016.

[240] Shyy W., Thakur S., Wright J., Second-order upwind and central difference schemes for recirculatingflow computation, *AIAA journal* **30** (4), 923–932, 1992.

[241] Siddiqui A. A., Lakhtakia A., Steady electro-osmotic flow of a micropolar fluid in a microchannnel [J], *Proceedings the Royal of Society A* **465**, 501–522, 2009.

[242] Singh K. P., Guo C., Current-voltage characteristics influenced by the nanochannel diameter and surface charge density in a fluidic field-effect-transistor, *Physical Chemistry Chemical Physics*, **19**, 15701, 2017.

[243] Sinha A., Mondal A., Shit G. C., Kundu P. K., Effect of heat transfer on rotating electroosmotic flow through a micro-vessel: haemodynamical applications, *Heat and Mass Transfer* **52** (8), 1549–1557, 2016.

[244] Solehati N., Bae J., Sasmito A. P., Numerical investigation of mixing performance in microchannel T-junction with wavy structure, *Computers & Fluids* **96**, 10–19, 2014.

[245] Solsvik J., Becker P. J., Sheibat-Othman N., Jakobsen H. A., Numerical Solution of the Drop Population Balance Equation Using Weighted Residual and Finite Volume Methods, *Journal of Dispersion Science and Technology* **37** (1), 80–88, 2016.

[246] Song H., Bennet D. J., Numerical study of enhancing the mixing effect in microchannels via transverse electroosmotic flow by placing electrodes on top and bottom of the channel, *Microsystem technologies* **17** (9), 1427–1437, 2011.

[247] Stern O., Theory of the electrical double layer.(In German.), *Electrochemistry* **30**, 508–516, 1924.

[248] Stokes G. G., On the theory of the internal friction of fluids in motion, and of the equilibrium and motion of elastic solids, *Transactions of the Cambridge Philosophical Society* **8**, 287–305, 1845.

[249] Stone H., Stroock A., Ajdari A., Engineering flows in small devices: microfluidics towards a lab-on-a-chip, *Ann. Rev. Fluid Mech.* **36**, 381–441, 2004.

[250] Stroock A. D., Weck M., Chiu D. T., Huck W. T. S., Kenis P. J. A., Ismagilov R. F., Whitesides G. M., Patterning electro-osmotic flow with patterned surface charge, *Physical Review Letters* **84**, 3314–3317, 2007.

[251] Sugioka H., Chaotic mixer using electro-osmosis at finite Peclet number, *Pysical Review E* **81**, 036306, 2010.

[252] Ta B. Q., Le Thanh H., Dong T., Thoi T. N., Karlsen F., Geometric effects on mixing performance in a novel passive micromixer with trapezoidal-zigzag channels, *Journal of Micromechanics and Microengineering* **25** (9), 094004, 2015.

[253] Tang G. H., He Y. L., Tao W. Q., Numerical analysis of mixing enhancement for micro-electroosmotic flow, *Journal of Applied Physics* **107**, 104906, 2010.

[254] Tang G. H., Ye P. X., Tao W. Q., Electroviscous effect on non-Newtonian fluid flow in microchannels, *Journal of Non-Newtonian Fluid Mechanics* **165**, 435–440, 2010.

[255] Tian F., Li B., Kwok D. Y., Tradeoff between Mixing and Transport for Electroosmotic Flow in Heterogeneous Microchannels with Nonuniform Surface Potentials, *Langmuir* **21**, 1126–1131, 2005.

[256] Toro E. F., *Solvers and Numerical Methods for Fluid Dynamics: A Practical Introduction*, Springer, 1999.

[257] Tripathi D., Jhorar R., Bég O. A., Shaw S., Electroosmosis modulated peristaltic biorheological flow through an asymmetric microchannel: mathematical model, *Meccanica* **53** (8), 2079–2090, 2018.

[258] Vasu N., De S., Electroosmotic flows of power-law fluids at high zeta potentials, *Colloids and Surfaces A: Physicochemical and Engineering Aspects* **368**, 44–52, 2010.

[259] Vennela N., Bhattacharjee, S., De S., Sherwood number in porous microtube due to combined pressure and electroosmotically driven flow, *Chemical engineering science* **66** (24), 6515–6524, 2011.

[260] Vaudelet P., Revil A., Schmutz M., Franceschi M., Bégassat P., Induced polarization signatures of cations exhibiting differential sorption behaviors in saturated sands *Water Resources Research* **47** (2), W02526, 2011.

[261] Versteeg H. K., Malalasekera W., *An introduction to computational fluid dynamics: the finite volume method*, Pearson Education, 2007.

[262] Ward K., Fan Z. H., Mixing in microfluidic devices and enhancement method, *Journal of Micromechanics and Microengineering* **25**, 094001, 2015.

[263] Watzig H., Kaupp S., Graf M., Inner surface properties of capillaeirs for electrophoresis, *TrAC Trends in Analytical Chemistry* **22** (9), 588–604, 2003.

[264] Wang D., Summers J. L., Gaskell P. H., Modelling of electrokinetically driven mixing flow in microchannels with patterned blocks, *Computers & Mathematics with Applications* **55**, 1601–1610, 2008.

[265] Wang L., Liu D., Wang X., Han X., Mixing enhancement of novel passive microfluidic mixers with cylindrical grooves, *Chemical engineering science* **81**, 157–163, 2012.

[266] Wang H., Iovenitti P., Harvey E., Masood S., Numerical investigation of mixing in microchannels with patterned grooves, *Journal of Micromechanics and Microengineering* **13**, 801–808, 2003.

[267] Wang J., Wang M., Li Z., Lattice Boltzmann simulations of mixing enhancement by the elcetro-osmotic flow in microcannels, *Modern Physics Letter B* **19**, 1515–1518, 2005.

[268] Wang M., Li Z., Gas mixing in microchannels using the direct simulation Monte Carlo method, *International Journal of Heat and Mass Transfer* **49**, 1696–1702, 2006.

[269] Wang M., Revil A., Electrochemical charge of silica surfaces at high ionic strength in narrow channels, *Journal of colloid and interface science* **343** (1), 381–386, 2010.

[270] Wang P. M., Wang J., Chen S., On applicability of Poisson-Boltzmann equation in micro- and nanoscale electroosmotic flows, *Commun. Comput. Phys.* **3** (5), 1087–1099, 2008.

[271] Weigl B. H., Bardell R. L., Cabrera C. R., Lab-on-a-chip for drug development, *Advanced drug delivery reviews* **55** (3), 349–377, 2003.

[272] West J., Karamata B., Lillis B., Gleeson J. P., Alderman J., Collins J. K., Lane W., Mathewson A., Berney H., Application of magnetohydrodynamic actuation to continuous flow chemistry, *Lab on a Chip* **2** (4), 224–230, 2002.

[273] Whitesides G., The lab finally comes to the chip ! *Lab on a Chip* **5**, 3125–3126, 2014.

[274] Wilkes N. S., Thompson C. P., An evaluation of higher-order upwind differencing for elliptic flow problems *In Numerical Methods in Laminar and Turbulent Flow*, 248–257, 1983.

[275] Wu J., Kodzius R., Cao W., Wen W., Extraction, amplification and detection of DNA in microfluidic chip-based assays, *Microchimica Acta* **181** (13-14), 1611–1631, 2014.

[276] Wu Z., Li D., Mixing and flow regulating by induced-charge electrokinetic flow in a microchannel with a pair of conducting triangle hurdles, *Microfluidics and Nanofluidics* **5**, 65–76, 2008.

[277] Wu Z. M., Zhao Z. J., Yang J. X., Liu L. P., Yang X. L., Frequency-modulation-type MI sensor with nanocrystalline ribbon core, *Sensors and Actuators A: Physical* **121**, 430–433, 2005.

[278] Xia Q., Zhong S., Liquid mixing enhanced by pulse width modulation in a Y-shaped jet configuration, *Fluid Dynamics Research* **45** (2), 025504, 2013.

[279] Xie F., Wang Y., Wang W., Li Z., Yossifon G., Chang H. C., Preparation of rhombus-shaped micro/nanofluidic channels with dimensions ranging from hundred nanometers to several micrometers, *Journal of nanoscience and nanotechnology* **10** (11), 7277–7281, 2010.

[280] Xu Y., Nanofluidics: A New Arena for Materials Science, *Advanced Materials* **30** (3), 1702419, 2008.

[281] Xu Z., Yang Y., Vadillo D., Ruan X., Fu X., A Mathematical model of mixing enhancement in microfluidic channel with a constriction under periodic electro-osmotic flow, *Applied Physics Letters* **100**, 0141907, 2012.

[282] Yang P. W., Chang Y. J., Huang H. F., Wall polymer depletion effects on electrokinetic diffusioosmosis of power-law liquids in cylindrical capillaries, *Microfluidics and nanofluidics* **17** (1), 149–165, 2014.

[283] Yanga Z., Matsumotoa S., Gotob H., Matsumotob M., Maeda R., Ultrasonic micromixer for microfluidic systems, *Sensors and Actuators A: Physical* **93** (3), 266–272, 2001.

[284] Yaralioglu G. G., Wygant I. O., Marentis T. C., Khuri-Yakub B. T., Ultrasonic mixing in microfluidic channels using integrated transducers, *Analytical chemistry* **76** (13), 3694–3698, 2004.

[285] Yu C. J., Tseng W. L., Online concentration and separation of basic proteins using a cationic polyelectrolyte in the presence of reversed electroosmotic flow, *Electrophoresis* **27** (18), 3569–3577, 2006.

[286] Zhang Y., Chao Z., Jakobsen H. A., Modelling and simulation of hydrodynamics in double loop circulating fluidizedbed reactor for chemical looping combustion process, *Powder Technology* **310**, 35–45, 2017.

[287] Zhao C., Zolkovskij E., Masliyah J. H., Yang C., Analysis of electroosmotic flow of power-law fluids in a slit microchannel, *Journal of Colloid and Interface Science* **326**, 503–510, 2008.

[288] Zhao C., Yang C., Advances in electrokinetics and their applications in micro/nano fluidics, *Microfluidics and Nanofluidics* **13**, 179–203, 2012.

[289] Zhao C., Yang C., Electrokinetics of non-Newtonian fluids: A review, *Advances in Colloid and Interface Sciences* **201-202**, 94–108, 2013.

[290] Zhao C., Yang C., Electroosmotic flows of non-Newtonian power-law fluids in a cylindrical microchannel, *Electrophoresis* **34** (5), 662–667, 2013.

[291] Zhao C., Zhang W., Yang C., Dynamic electroosmotic flows of power-law fluids in rectangular microchannels, *Micromachines* **8** (2), 34, 2017.

[292] Zheng Z., Hansford D., Conlisk A. T., Effect of multivalent ions on electroosmotic flow in micro-and nanochannels, *Electrophoresis* **24**, 3006–3017, 2003.

[293] Zhu Q., Deng S., Chen Y., Periodical pressure-driven electrokinetic flow of power-law fluids through a rectangular microchannel, *Journal of Non-Newtonian Fluid Mechanics* **203**, 38–50, 2014.

[294] Zimmerman W., Rees J., Craven T., Rheometry of non-Newtonian electrokinetic flow in a microchannel T-junction, *Microfluidics and Nanofluidics* **2** (6), 481–492, 2006.